THE UNIVERSITY *of* EDINBURGH

This thesis has been submitted in fulfilment of the requirements for a postgraduate degree (e.g. PhD, MPhil, DClinPsychol) at the University of Edinburgh. Please note the following terms and conditions of use:

This work is protected by copyright and other intellectual property rights, which are retained by the thesis author, unless otherwise stated.
A copy can be downloaded for personal non-commercial research or study, without prior permission or charge.
This thesis cannot be reproduced or quoted extensively from without first obtaining permission in writing from the author.
The content must not be changed in any way or sold commercially in any format or medium without the formal permission of the author.
When referring to this work, full bibliographic details including the author, title, awarding institution and date of the thesis must be given.

Satellite and UAV Remote Sensing of Debris-Covered Glaciers

Rosie Bisset

Thesis submitted for the degree of Doctor of Philosophy

The University of Edinburgh

2021

Abstract

Mountain glaciers play a crucial role in the global provision of water resources. The majority of these glaciers are retreating rapidly in response to anthropogenic climate change, posing serious risks to downstream communities, many of which are located in some of the most socio-economically vulnerable regions on Earth. Consequently, accurate simulations of the future behaviour of mountain glaciers are critical in facilitating effective planning and water resource management over the 21st century.

One fifth of the Earth's largest glaciers (> 2 km^2) are substantially covered by a layer of rocky material, known as supraglacial debris. This material alters the melt rates of the ice beneath, making the behaviour of debris-covered glaciers significantly harder to predict and limiting the ability of models to forecast effectively the impacts on downstream water resources.

This thesis aims to contribute towards an improved understanding of debris-covered glacier behaviour through the development and application of novel remote sensing techniques which utilise data collected by satellites and uncrewed aerial vehicles (UAVs). The major findings that stem from this thesis are presented as three results chapters.

The first results chapter (presented as Chapter 3) utilises recently-acquired satellite-derived datasets to estimate the surface-mass-balance gradients of the largest glaciers within five regions of High Mountain Asia. A key finding is that, on the ablation zones of debris-covered glaciers, there are distinctive reversed surface-mass-balance gradients which were previously concealed from geodetic studies of ice-surface lowering. More generally, this work emphasises the importance of quantifying the

distinctive contributions of ice-flow dynamics and surface mass balance towards the distributed mass changes of debris-covered glaciers, in order to better constrain their melt rates in glaciological models.

The second results chapter (Chapter 4) tests the application of high-resolution thermal UAV imagery to simulate spatially-distributed debris thicknesses and sub-debris melt rates on Llaca Glacier, a debris-covered glacier in the Peruvian Andes. The results demonstrate that appropriately-calibrated thermal UAV imagery can be used, in conjunction with meteorological data and thermal measurements within the debris layer, to provide more precise estimates of supraglacial debris thickness. Additionally, this work indicates large differences between the sub-debris melt rates simulated using UAV-derived and satellite-derived debris thicknesses, demonstrating the importance of further high-resolution data acquisition on debris-covered glaciers in order to parameterise better their complex melt patterns.

The final results chapter (Chapter 5) utilises high-resolution visible and thermal UAV imagery to explore the behaviour of supraglacial ice cliffs on Llaca Glacier. Surface energy balance modelling is used to quantify the contribution of ice-cliff backwasting towards overall melt rates on a portion of the glacier tongue. The findings show that aspect plays a crucial role in controlling the development of ice cliffs, with southwest-facing ice cliffs surviving preferentially over others. The results also show that ice-cliff backwasting contributes disproportionately towards the overall ablation of Llaca Glacier, demonstrating the importance of further high-resolution studies of tropical debris-covered glaciers in order to calibrate glacio-hydrological models effectively.

Overall, this thesis provides proofs-of-concepts for emerging methods that can be used to monitor debris-covered glaciers based on recently-available remote sensing datasets and UAV data-collection techniques. Future research to develop these techniques further, and apply them to multiple glaciers within different regions, will facilitate improved model calibration and better estimates of future runoff from debris-covered glaciers in mountain regions.

Lay summary

Mountain glaciers play a crucial role in the global provision of water resources. The majority of these glaciers are retreating rapidly in response to anthropogenic climate change, posing serious risks to downstream communities, many of which are located in some of the most socially and economically vulnerable regions on Earth. One fifth of the Earth's largest glaciers are substantially covered by a layer of rocky material, known as debris cover, which changes the behaviour of these glaciers and makes their evolution more difficult to predict. Making use of data recently collected by satellites and drones, this thesis tests the use of novel techniques to study debris-covered glaciers with greater levels of detail than was previously possible. The application of these techniques reveals previously-unreported patterns of glacier behaviour in High Mountain Asia and improves our understanding of the complex behaviour of tropical debris-covered glaciers in the Peruvian Andes. Future work now needs to be directed towards developing these techniques further and testing their applications in different regions, in order to contribute towards improved predictions of the future behaviour of debris-covered glaciers around the world.

Acknowledgements

The work in this PhD thesis was funded by the NERC E^3 DTP Studentship hosted at The University of Edinburgh, with additional funding support from SAGES (Scottish Alliance for Geoscience, Environment and Society) and CASCADA (a joint UK-Peruvian NERC/CONCYTEC project researching the impacts of glacial retreat on water resources in the Ancash region of Peru).

I would like to thank my principal supervisor, Rob Bingham, for his guidance and encouragement throughout my PhD. Whether presenting at conferences, writing papers, applying for grants or attempting to make sense of findings, his shared knowledge and experience have been invaluable. I am also particularly grateful to Pete Nienow for his added supervision and support during my PhD, and for giving me the opportunity to get involved in the CASCADA project, which brought some incredible fieldwork experiences and allowed me to be part of a great team. I would also like to thank to Dan Goldberg for all of his modelling wisdom and general support throughout my PhD.

Thank you to everyone that I collaborated with during my PhD: Ollie Wigmore, Moya MacDonald, Jemma Wadham, Raul Loayzo-Muro, Noel Gourmelen, Amaury Dehecq, Mattias Huss, Abdou Atto, Emmanuel Trouvé and Cat Fyffe. I am also grateful to Andrew Gray and Jack Gillespie (NERC FSF), Alan Hobbs and Colin Kay (NERC GEF) and David Redpath (Sky Tech) for providing key fieldwork equipment and valuable support. Thanks also to Calum Reay for his assistance in the field. I would also like to thank Anthony Newton and Andy Dugmore for their wise words and support during my PhD.

Thank you to the Drummond crew: Aythya, Boris, Charlie, Laura, Monika, Roslyn, Emma, Justine, Alex, Richard, Marina, Mikael and many others, for creating such a fun and friendly working environment with an endless supply of coffee and comedy, and thanks also to Fiona, Mariana and Sophie for all the added fun and support. The last four years really wouldn't have been the same without such a great bunch of people.

Finally, I would like to thank my mum, Julien, and close friends Anna, Myrto and Hannah, for all their support and love through the many ups and downs of the last four years.

This thesis is dedicated to my granny, Isobel Bisset, who inspired me to follow my interest in science and to never give up.

Declaration

I declare that this thesis has been composed solely by myself, and that it contains only my work except where otherwise specified, or where the work is explicitly indicated in the text to have formed part of a jointly-authored publication. This work has not been submitted for any other degree or professional qualification.

Rosie Bisset

December 2021

Contents

List of Figures

List of Tables

List of Abbreviations

ALOS	Advanced Land Observing Satellite
ASTER	Advanced Spaceborne Thermal Emission and Reflection Radiometer
CASCADA	CAscading impacts of peruvian glacier Shrinkage on biogeochemical Cycling and Acid Drainage in Aquatic ecosystems
DEM	Digital elevation model
DSM	Digital surface model
DTM	Digital terrain model
ELA	Equilibrium line altitude
GCP	Ground control point
GLOF	Glacial lake outburst flood
GNSS	Global Navigation Satellite System
GPR	Ground-penetrating radar
HMA	High Mountain Asia
LiDAR	Light Detection And Ranging
LW	Longwave
OBIA	Object-based image analysis
PPK	Post-processed kinematic
RGI	Randolph Glacier Inventory
RTK	Real-time kinematic
SfM	Structure-from-Motion
SRTM	Shuttle Radar Topography Mission
SW	Shortwave
SEB	Surface energy balance
SMB	Surface mass balance
TCP	Temperature calibration plate
TIR	Thermal infrared
UAV	Uncrewed aerial vehicle

List of Variables

Chapter 2

A	surface area	m^2
b	surface mass balance	m w.e. a^{-1}
d	debris thickness	m
E	total energy flux	W m^{-2}
ε	emissivity	-
h	ice thickness	m
k_{eff}	effective thermal conductivity	W m^{-2} K^{-1}
G_{ratio}	nonlinearity factor	-
L_f	latent heat of fusion	kJ kg^{-1}
l	length	m
M	melt rate	m s^{-1}
Q_c	ground heat flux	W m^{-2}
Q_{in}	incoming ice flux	m a^{-1}
Q_m	downward energy flux at base of debris layer	W m^{-2}
Q_{out}	outgoing ice flux	m a^{-1}
T_i	ice temperature	K
T_s	surface temperature	K
t	time	a
u	ice velocity	m a^{-1}
ρ_{ice}	density of ice	kg m^{-3}
ρ_{water}	density of water	kg m^{-3}
σ	Stefan-Boltzmann constant	W m^{-2} K^{-4}

Chapter 3

A	surface area	m^2
b	surface mass balance	m w.e. a^{-1}
h	ice thickness	m
l	length	m
ρ_{ice}	density of ice	kg m^{-3}
ρ_{water}	density of water	kg m^{-3}
Q	ice flux	m a^{-1}
Q_{in}	incoming ice flux	m a^{-1}

Q_{out}	outgoing ice flux	m a^{-1}
σ	standard deviation	-
t	time	a
u	ice velocity	m a^{-1}

Chapter 4

A	transfer coefficient	-
α	albedo	-
c_{air}	heat capacity of air	J kg^{-1} K^{-1}
c_{rock}	heat capacity of rock	J kg^{-1} K^{-1}
d	debris thickness	m
e_a	atmospheric vapour pressure	Pa
ε_{clear}	clear sky emissivity	-
ε_{eff}	effective emissivity of atmosphere	-
G_{ratio}	nonlinearity factor	-
K	debris thermal diffusivity	mm^2 s^{-1}
k_{eff}	effective thermal conductivity	Wm^{-2} K^{-1}
k_{vk}	von Kármán's constant	-
L_f	latent heat of fusion	kJ kg^{-1}
LW_{in}	incoming longwave radiation	W m^{-2}
P	atmospheric pressure	Pa
P_0	atmospheric pressure at sea level	Pa
Q_c	ground heat flux	W m^{-2}
Q_m	downward energy flux at base of debris layer	W m^{-2}
RH	relative humidity	%
R_n	net radiation flux	W m^{-2}
ρ_{air}	density of air	kg m^{-3}
ρ_{ice}	density of ice	kg m^{-3}
ρ_{rock}	rock density	kg m^{-3}
SW_{in}	incoming shortwave radiation	W m^{-2}
σ	Stefan-Boltzmann constant	W m^{-2} K^{-4}
T	debris temperature	K
T_{air}	air temperature	K
T_d	debris temperature at debris-ice interface	K
T_i	ice temperature	K
T_s	surface temperature	K
$T_{0.1m}$	debris temperature at 10 cm depth	K
$T_{0.2m}$	debris temperature at 20 cm depth	K
t	time	hr
u	wind speed	m s^{-1}

z	depth within the debris layer	m
z_d	depth of debris-ice interface	m
z_h	height of meteorological measurements	m
z_0	surface roughness length	m

Chapter 5

A	mean cliff azimuth	°
α_d	albedo of debris	-
α_i	albedo of ice	-
β	mean ice cliff slope	°
c_p	specific heat capacity of air at constant pressure	J kg^{-1} K^{-1}
e_a	atmospheric vapour pressure	kPa
$e_{s,a}$	saturation pressure of the atmosphere	kPa
$e_{s,i}$	atmospheric vapour at ice cliff face	kPa
ε	emissivity	-
H	sensible heat flux	W m^{-2}
h_c	ice cliff height	m
H_R	relative humidity	%
k_{vk}	von Kármán's constant	-
K_L	exchange coefficient for latent heat	-
K_s	exchange coefficient for sensible heat	-
L_a	longwave flux from the atmosphere	W m^{-2}
L_d	longwave flux from the debris	W m^{-2}
L_f	latent heat of fusion	kJ kg^{-1}
L_{in}	incoming longwave radiation	W m^{-2}
L_n	net longwave flux	W m^{-2}
L_{out}	outgoing longwave flux	W m^{-2}
LE	latent heat flux	W m^{-2}
L_v	latent heat of evaporation	J kg^{-1}
λ_f	frontal area density	-
M	ablation normal to the surface	m w.e.
P	atmospheric pressure	kPa
P_0	atmospheric pressure at sea level	kPa
Q_m	downward energy flux at base of debris layer	W m^{-2}
Re_*	roughness Reynold's number	-
R_v	gas constant for moist air	J kg^{-1}
ρ_0	standard density of air	kg m^{-3}
ρ_i	density of ice	kg m^{-3}
S_a	shortwave flux from the atmosphere	W m^{-2}
S_d	shortwave flux from the debris	W m^{-2}
S_{diff}	diffuse shortwave radiation from atmosphere	W m^{-2}
S_{dir}	direct shortwave radiation from atmosphere	W m^{-2}

S_n	net shortwave flux	W m^{-2}
σ	Stefan-Boltzmann constant	W m^{-2} K^{-4}
t	time	s
T_a	air temperature	K
T_s	surface temperature	K
u	wind speed	m s^{-1}
u_*	friction velocity	m s^{-1}
v	viscosity of air	m^{-2} s^{-1}
V_d	debris view factor	-
$V_{s,L}$	longwave sky view factor	-
W_D	wind direction	°
z	height of meteorological measurements	m
z_0	roughness length for a momentum profile	m
z_{0e}	roughness length for log profile of vapour pressure	m
z_{0T}	roughness length for a temperature profile	m

Chapter 1

Introduction

1.1 Motivation

Approximately 24 % of the global population live within or directly downstream from Earth's mountain regions (Immerzeel et al., 2020) (Figure 1.1). These regions are often described as 'water towers', as they supply a significant proportion of natural and anthropogenic water demands (Viviroli et al., 2007). The communities that depend the most on these water towers for drinking water, agriculture and energy production are predominantly located in the most socio-economically vulnerable regions on Earth (Immerzeel et al., 2020). Glaciers and snowpacks play a key role in storing and regulating the release of water resources from mountain regions to downstream populations (e.g. Bolch et al., 2017; Buytaert et al., 2017; Huss et al., 2017). However, with rising global temperatures and increasingly extreme climate events, glaciers and snow cover are shrinking rapidly, posing serious risks to downstream water availability (e.g. Jansson et al., 2003; Bradley et al., 2006; Huss and Hock, 2018). Research has shown that while some glaciated river basins have experienced an initial rise in meltwater runoff as glacial ablation and snowmelt production increase, the storage capacity of glaciers is rapidly diminishing, leading to an eventual decrease in downstream water availability (e.g. Barnett et al., 2005; Chevalier et al., 2011; Huss and Hock, 2018; McDowell et al., 2021). Since many large-scale glaciated catchments have already passed this tipping point, known as 'peak water', numerous regions are already experiencing diminishing water resources, with

a growing number of catchments projected to be impacted throughout the 21st century (e.g. Huss and Hock, 2018).

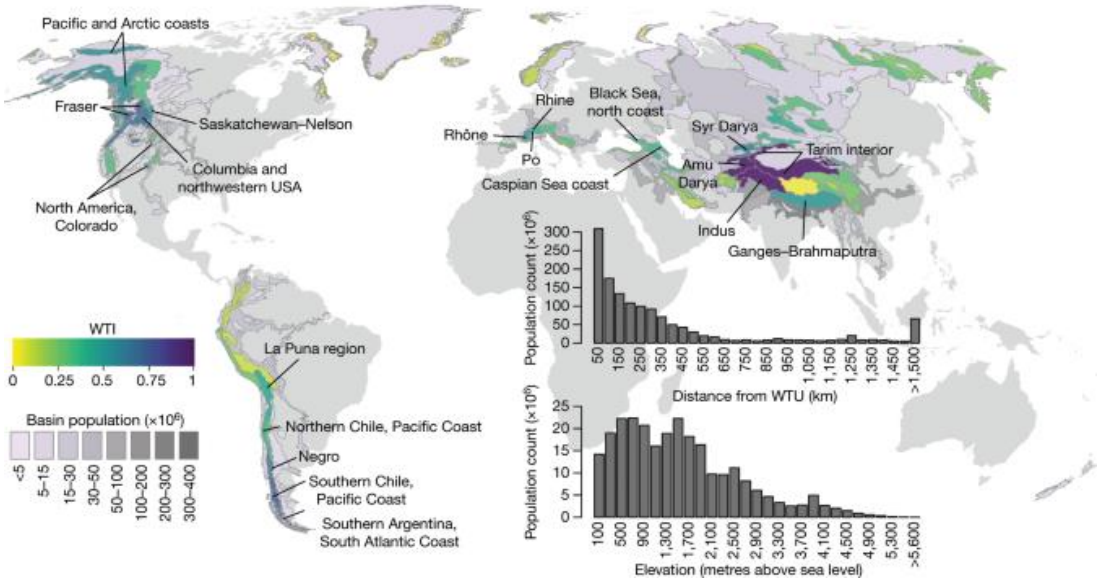

Figure 1.1: The global water tower index and the populations living downstream from global water towers. The water tower index (WTI: index defining importance of water-supplying role and downstream dependence of ecosystems and society) and the total population within each mountain-water-tower-dependent river basin are shown on the map. The bar graphs show the spatial and altitudinal distributions of the populations living within each river basin. Source: Immerzeel et al. (2020)

Debris cover exists on 44 % of the Earth's largest glaciers (covering > 2 km^2) and is prominent (covering > 1 km^2) on 15 % (Herreid and Pellicciotti, 2020). Supraglacial debris consists of materials such as rocks and sediment which originate from the glacial headwalls and are transported englacially to the surface of the ablation zone (Kirkbride and Deline, 2013; Rowan et al., 2015). Additionally, in some regions, supraglacial debris is derived from tephra fallout from volcanic eruptions (e.g. Kirkbride and Dugmore, 2003; Möller et al., 2016). This material modifies glacier melt rates by insulating the ice beneath and altering the surface albedo (e.g. Östrem, 1959; Mattson et al., 1993; Kayastha et al., 2000). Supraglacial ice cliffs and meltwater ponds, which are abundant on debris-covered glaciers, further alter the melt rates of debris-covered glaciers by acting as localised 'hot spots' of enhanced melting (e.g. Sakai et al., 2000; Reid and Brock, 2014; Buri et al., 2019). Despite recent advances,

there are still numerous gaps in our understanding of the complex behaviour of debris-covered glaciers (e.g. Watson et al., 2017; Pellicciotti and Buri, 2018; Huo et al., 2021). Further research is therefore critical in order to accurately project the future evolution of debris-covered glaciers and effectively predict the consequent impacts on downstream water resources.

1.2 Aims

The overall aim of this thesis is to use satellite and uncrewed aerial vehicle (UAV) remote sensing to investigate the complex behaviour of debris-covered glaciers and develop new techniques for monitoring these glaciers. More specifically, this gives rise to three key objectives, each of which respectively underpins the main studies undertaken for the thesis in Chapters 3, 4 and 5. This section provides a brief outline of each of these objectives and their specific motivations.

Thesis Objective 1: To quantify the surface mass balance gradients of the largest debris-covered glaciers in High Mountain Asia using a remote-sensing-based mass continuity approach.

The glacial surface mass balance (SMB) is defined as the difference between accumulation (the gain of snow and ice) and ablation (the loss of snow or ice) (Cuffey and Paterson, 2010). Supraglacial debris cover significantly impacts the SMB of mountain glaciers by altering the amount of energy that is received and absorbed at the ice surface (Cuffey and Paterson, 2010). Previous studies have used fieldwork to quantify surface measurements, using ablation stakes and snow pits to measure ablation and accumulation at discrete points on the ice surface (e.g. Benn et al., 2012; Azam et al., 2016; Anderson et al., 2021). Due to the remote, high-altitude settings of debris-covered glaciers, these in-situ measurements of SMB are limited in spatial coverage. Geodetic studies have utilised satellite data in order to provide valuable large-scale regional estimates of ice surface elevation change, which can be used to approximate overall glacier mass balances (e.g. Kääb et al., 2012; Brun et al., 2019; Shean et al., 2020). However, the surface lowering measured in these studies results

from a combination of SMB and ice flow dynamics, therefore spatially-distributed patterns of SMB are not resolved. By quantifying the dynamic contribution towards previously-observed ice surface elevation changes, we can isolate the SMB from overall patterns of ice surface lowering. This allows us to quantify the modified ablation rates of debris-covered glaciers and gain a better understanding of the role of supraglacial debris in controlling their behaviour.

Thesis Objective 2: To develop a method for simulating supraglacial debris thicknesses and sub-debris melt rates from high-resolution, UAV-acquired thermal infrared imagery.

Debris thickness is a key factor controlling the melt rate of debris-covered glaciers. A thin debris layer, less than a critical thickness (~3-8cm), accelerates sub-debris melt rates (e.g. Östrem, 1959; Nicholson and Benn, 2006). In contrast, debris exceeding the critical thickness supresses melt rates, inducing reduced ablation as debris thickness increases (e.g. Benn and Lehmkuhl, 2000; Azam et al., 2016). The thickness of the debris layer is often highly spatially heterogeneous (e.g. Nicholson and Mertes, 2017), therefore quantifying spatially-distributed debris thickness with high spatial precision is critical for accurately simulating the melt rates of debris-covered glaciers. Previous field-based studies have quantified debris thickness using methods such as manual excavation and ground-penetrating radar (GPR) (e.g. Zhang et al., 2011; McCarthy et al., 2017), but the spatial coverage of these studies is limited due to challenges associated with accessing and navigating debris-covered glaciers. Remote sensing has more recently been used to quantify debris thickness from thermal infrared (hereafter shortened to 'thermal') satellite imagery and meteorological data, using surface energy balance modelling (e.g. Foster et al., 2012; Rounce and McKinney, 2014). However, the resolution of currently available thermal satellite imagery is 60 metres or more, limiting the precision and accuracy of debris thickness estimates. By using high-resolution UAV-acquired thermal imagery, combined with high resolution digital elevation models (DEMs) (derived from visible UAV imagery) and meteorological data, we can calculate distributed debris thicknesses with high levels

of spatial precision. Using these simulated debris thicknesses, we can then simulate the spatially-distributed melt rates of debris-covered glaciers with greater accuracy and precision.

Thesis Objective 3: To investigate the characteristics and melt rates of supraglacial ice cliffs on a debris-covered glacier using high-precision UAV imagery.

Supraglacial ice cliffs are abundant on the surfaces of debris-covered glaciers. These features act as localised 'hot spots' of enhanced ablation, contributing significantly towards the overall melt rates of debris-covered glaciers (e.g. e.g. Sakai et al., 2000; Watson et al., 2017). Previous studies of supraglacial ice cliffs have demonstrated that the orientation of ice cliffs plays a key role in controlling their evolution (e.g. Sakai, Nakawo and Fujita, 2002; Kraaijenbrink et al., 2016). In the northern hemisphere, north-facing cliffs survive preferentially over south-facing cliffs, predominantly as a consequence of contrasting distributions of solar radiation across ice cliff surfaces (e.g. Thompson et al., 2016; Sakai et al., 2018; Buri et al., 2021). While supraglacial ice cliffs in northern hemisphere temperate regions such as High Mountain Asia and Alaska have received increasing attention in recent years, little is known about the behaviour of supraglacial ice cliffs in equatorial regions and the contribution of ice-cliff backwasting towards the overall mass loss of tropical-debris-covered glaciers. High-resolution visible UAV surveys provide the opportunity to investigate the characteristics of ice cliffs in detail and, in conjunction with thermal UAV imagery and meteorological data, simulate high-resolution spatially-distributed melt rates of ice cliffs on tropical debris-covered glaciers. Furthermore, these datasets can be used to examine ice flow dynamics and ice-surface lowering, as well as to explore the potential role of different factors in controlling ice-cliff evolution.

1.3 Thesis structure

To provide background to the overall thesis aims discussed above, Chapter 2 discusses the science surrounding debris-covered glacier and the techniques which have previously been used to monitor debris-covered glaciers. Additionally, this chapter

discusses the key principles of UAV remote sensing, focusing particularly on visible and thermal surveying. The chapter culminates with a summary of the key knowledge gaps from existing studies and the respective research goals that have motivated each original research chapter of the thesis.

Chapters 3, 4 and 5 detail the research that has been undertaken as part of this PhD in order to address each of the thesis objectives. These three chapters have been written in a format suitable for publication in peer-reviewed journals. Chapter 3 was published in *Remote Sensing* in 2020, Chapter 4 has been submitted for publication in *Journal of Glaciology* and Chapter 5 is in preparation for submission.

Chapter 6 synthesises the key progress associated with Chapters 3, 4 and 5. Recent studies of relevance to Chapter 3, which have been released since the publication of Chapter 3, are also discussed. Additionally, the limitations of chapters 3, 4 and 5 are discussed, while important directions for future research are highlighted within this section.

Chapter 7 concludes by summarising the key findings and implications of the research produced within this thesis. Scientific journal articles produced in association with this thesis are included in the Appendices.

Chapter 2

Background

This chapter begins, in Section 2.1, by introducing the two key regions of study within this thesis: High Mountain Asia and the Cordillera Blanca of the Peruvian Andes. This is followed, in Section 2.2, by a summary of current knowledge and recent progress in the field of debris-covered glaciology. Section 2.3 discusses the current techniques that are used to study the characteristics and behaviour of debris-covered glaciers. Section 2.4 provides an overview of UAV remote sensing, focusing particularly on the collection and handling of thermal and visible imagery. Section 2.5 closes this chapter with a summary of the key knowledge gaps that this thesis will centre around.

2.1 Introduction to regions of study

2.1.1 High Mountain Asia

High Mountain Asia is the Earth's largest reservoir of glacial ice outside the Polar Regions. It encompasses the Tibetan Plateau and its neighbouring mountain ranges, including the Himalaya, Karakoram, Pamir and Tien Shan. The glaciers in High Mountain Asia span across a total area of around 118,264 km^2, with debris-covered ice constituting approximately 10-11% of this area (RGI, 2017; Scherler et al., 2018). The meltwater produced by these glaciers flows into several key river basins, including the Indus, Ganges, Brahmaputra, Yellow and Yangtze (Figure 2.1). These

rivers supply water resources to downstream communities inhabited by more than 800 million people (Pritchard, 2019).

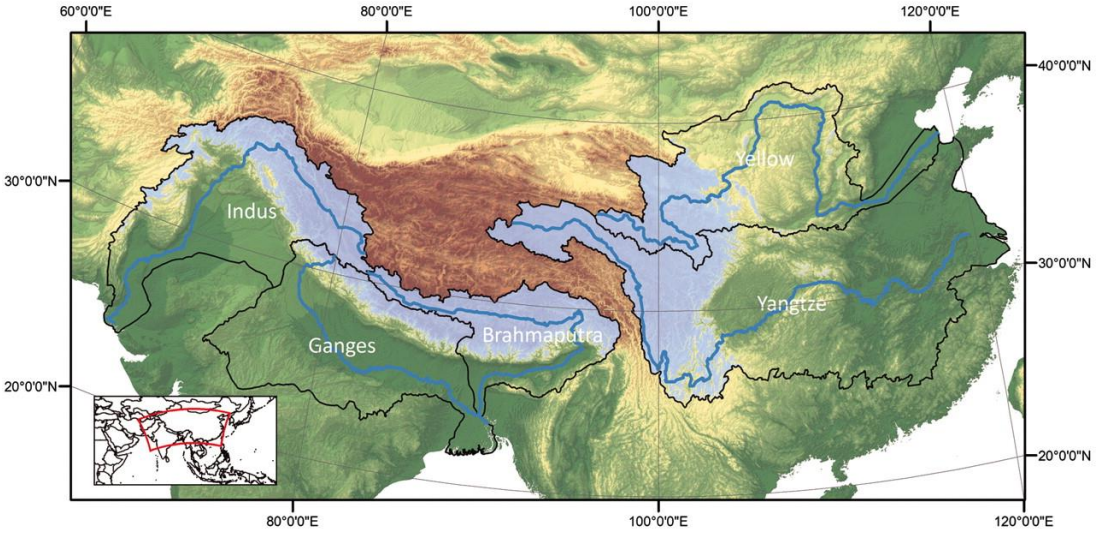

Figure 2.1. Major river basins of High Mountain Asia. Source: Immerzeel et al. (2010).

Over the past several decades, the glaciers within High Mountain Asia have shrunk in mass by approximately $-19.0 \pm 2.5\,\mathrm{Gt\,a^{-1}}$ (Shean et al., 2020), posing significant risks to downstream communities. While increased glacial melting has led to initial increases in downstream river discharges, the headwaters of the Brahmaputra are already reaching peak flow levels, with discharges already beginning to decline due to dropping glacial storage capacity (Huss and Hock, 2018). Other major river basins, such as the Indus, Tarim and Ganges, are expected to follow similar trajectories, with peak water flow projected to occur around the middle of the 21st century (Huss and Hock, 2018).

The glaciers of High Mountain Asia are the source of flood hazards, known as glacial lake outburst floods (GLOFs), which have been responsible for more than 6300 deaths in central Asia (Carrivick and Tweed, 2016). With increased levels of annual glacial ablation, the glacial lakes responsible for these floods are growing, leading to an increased likelihood of GLOF events (e.g. Allen et al., 2016; Shugar et al., 2020; Veh et al., 2020). This change is particularly pronounced in the Eastern Himalaya,

where GLOF hazard (linked to lake abundance and flood frequency) is at least 3 times greater than in any other region within High Mountain Asia (Veh et al., 2020).

The atmospheric circulation in High Mountain Asia is primarily dominated by the Indian summer monsoon and Westerly disturbances. The Indian monsoon is a seasonal weather phenomenon which occurs during the Northern Hemisphere summer due to a northward shift of the Intertropical Convergence Zone (e.g. Zhang, Chan and Ding, 2004; Yao et al., 2012). In southern Asia, warm air is drawn in from the Indian Ocean, producing continuous heavy precipitation over the Tibetan Plateau between June and September (e.g. Bookhagen and Burbank, 2010). On the other hand, westerly disturbances occur in the winter, when low-pressure systems originating from the Mediterranean and mid-west Atlantic Ocean are carried eastwards over High Mountain Asia, resulting in high precipitation rates (e.g. Charturvedi et al., 2014).

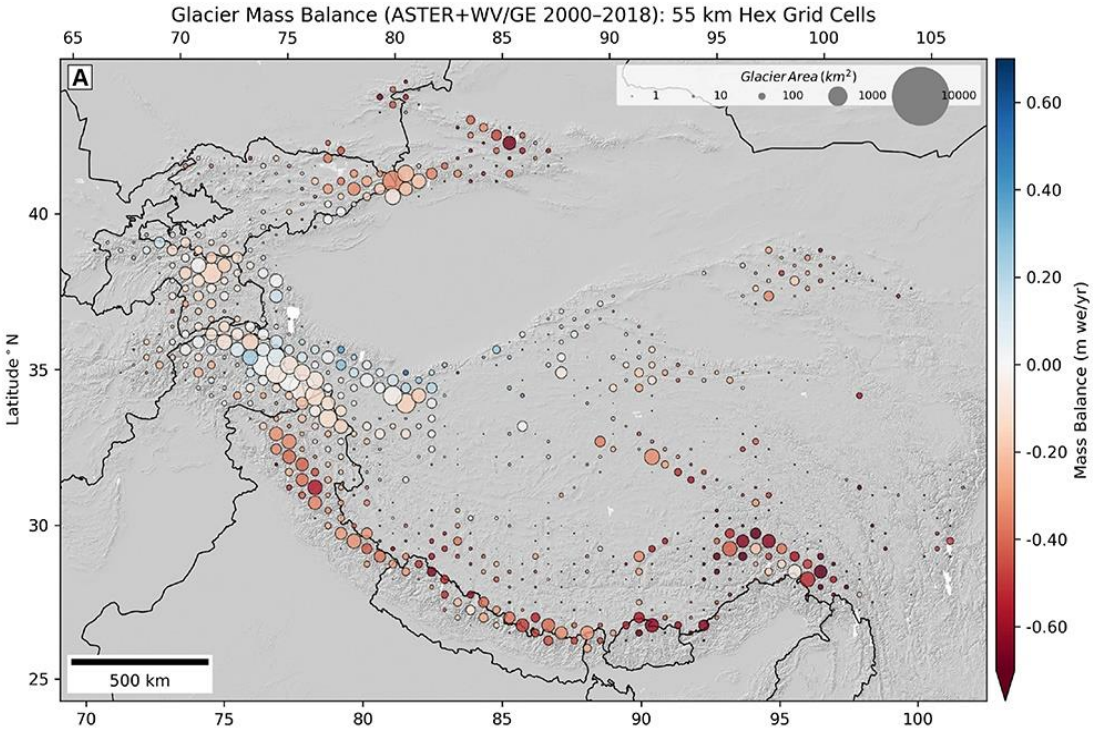

Figure 2.2. Mass changes of glaciers in High Mountain Asia. The sizes of the circles represent the total glacierized area within each cell. The colour scale represents the rate of mass loss (red) or gain (blue). Source: Shean et al. (2020).

The differential timing of the Indian monsoon and the westerly disturbances results in heterogeneous patterns of glacial accumulation across High Mountain Asia (e.g. Shean et al., 2020; Figure 2.2). Glaciers in the northwest of High Mountain Asia predominantly receive precipitation from westerly disturbances during the winter. These glaciers receive a larger proportion of overall precipitation as snowfall, leading to high glacial accumulation rates (e.g. Yao et al., 2012; Rowan et al., 2018; Farinotti et al., 2020). Conversely, glaciers in the southeast of High Mountain Asia predominantly receive precipitation brought by the summer monsoon and a smaller proportion of the overall precipitation falls as snow. As a result, glaciers in the northwest of High Mountain Asia have a more stable mass balance compared to those in the southeast (e.g. Kapnick et al., 2014). In particular, the glaciers in the Karakoram have very stable or even positive mass balances due to the colder air temperatures within the interior of the mountain belt (e.g. Yao et al., 2012). However, recent research indicates that this phenomenon, known as the 'Karakoram glacier Anomaly', is unlikely to persist over long timescales due to the significant future warming forecasted by current climate projections (Farinotti et al., 2020).

2.1.2 Cordillera Blanca, Peruvian Andes

The Cordillera Blanca is a mountain chain spanning a distance of ~ 200 km through the Ancash region of Peru, forming part of the wider Peruvian Andes range (Figure 2.3). Containing more than 25% of the total glacial area in the tropics, the Cordillera Blanca is home to the largest collection of tropical glaciers on Earth (RGI, 2017). Figures 2.4 – 2.9 show photographs of one of these glaciers (Llaca Glacier), where fieldwork was conducted for this thesis. The Río Santa river runs parallel to and southwest of the mountain range, delivering water resources to around a quarter of a million inhabitants of the Ancash region (Mark et al., 2010) (Figure 2.3). Almost half of these inhabitants live in the city of Huáraz, located directly downstream from the glaciers of the southern Cordillera Blanca.

The climate of Ancash is characterised by two main seasons: the wet season (between October and May) and the dry season (between May and September). While

there are large variations in precipitation between these two seasons, seasonal variations in air temperature are relatively small (Kaser et al., 2017). As a result, glacial accumulation predominantly occurs during the wet season, while glacial ablation takes place throughout the year, with ablation rates on glacier tongues being approximately one third higher in the wet season compared to the dry season (Kaser et al., 2017).

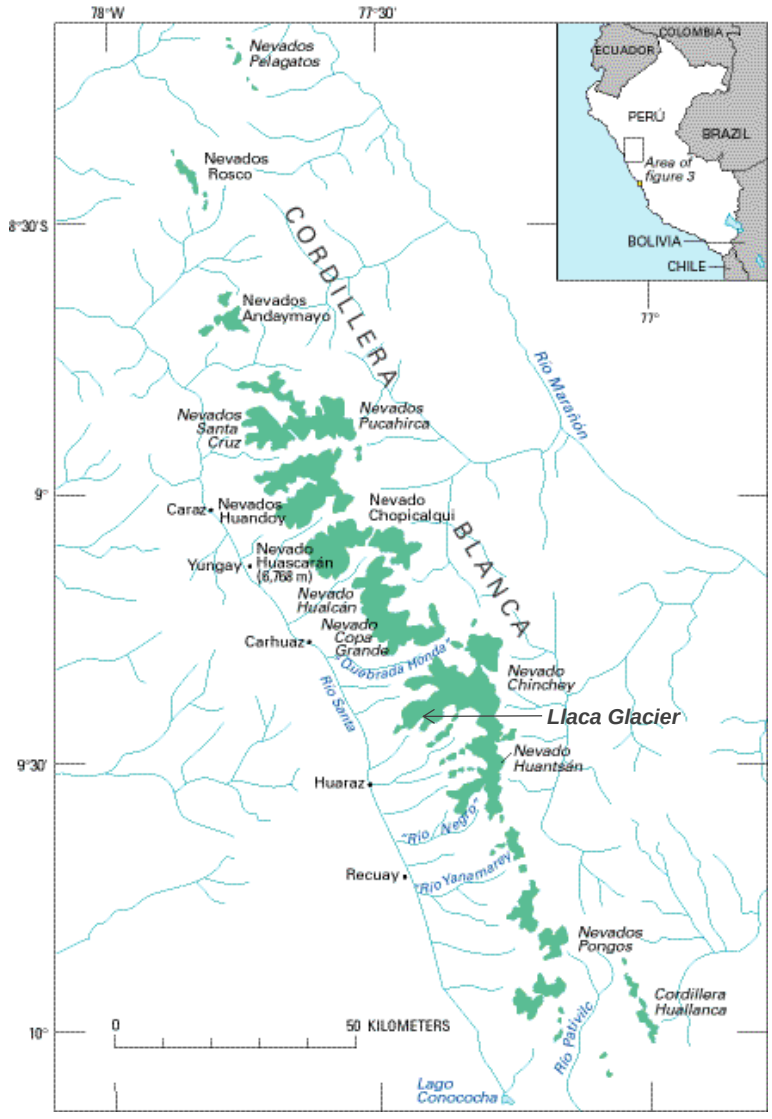

Figure 2.3. Glaciers of the Cordillera Blanca. The green shaded area shows the spatial coverage of the glaciers within this region. The location of Llaca Glacier, where fieldwork was conducted in 2019 as part of this thesis, is shown. Source: Adapted from USGS (1999).

2.1. INTRODUCTION TO REGIONS OF STUDY

The total area covered by glaciers within the Cordillera Blanca has decreased by over 30% between 1930 and 2014 (Schauwecker et al., 2014). Research indicates that glacial retreat has been accelerating over the last several decades, with the average rate of area loss between 2004 and 2010 being ~3.5 times that of between 1970 and 2003 (Burns and Nolin, 2014). Glacial retreat appears to be particularly pronounced in the southern Cordillera Blanca, where the median elevations of glaciers are lower on average (Burns and Nolin, 2014).

Glaciers play a key role in buffering seasonal river discharges in the Río Santa basin, storing and gradually releasing meltwater throughout the year. Baraer et al. (2017) found that of 9 watersheds investigated, 7 were likely already to have passed the critical transition point of peak stream discharges, and were already beginning to experience reduced river discharges. Hydrological model predictions indicate that a complete disappearance of the glaciers in the Cordillera Blanca will result in up to a 30% drop in annual discharges, with impacts most pronounced during the dry season (Baraer et al., 2017).

Killing almost 30,000 people between 1941 and 2005, GLOFs in the Cordillera Blanca significantly endanger downstream communities in Ancash (Carey et al., 2005). The most catastrophic GLOF event recorded within this region took place in December 1941, as a result of a breach in the moraine holding Lake Palcachocha. The GLOF produced a debris flow which destroyed around a third of the city of Huáraz and killed about 5000 inhabitants (Carey et al., 2005). Since then, the population of Huáraz has increased sixfold to approximately 120,000, with a large proportion of the town situated within the area that was previously impacted by the flood. Since 1941, efforts have been made to reduce the risks of GLOFs, such as draining lakes and constructing artificial dams (Carey et al., 2005). However, due to deglaciation, the number of glacial lakes in the Cordillera Blanca has been growing rapidly, posing progressively serious threats to downstream communities (Frey et al., 2018).

Figure 2.4. Llaca Glacier (background), where thesis fieldwork was conducted, and Llaca Lagoon (foreground) (August 2019).

Figure 2.5. Llaca Glacier terminus (August 2019).

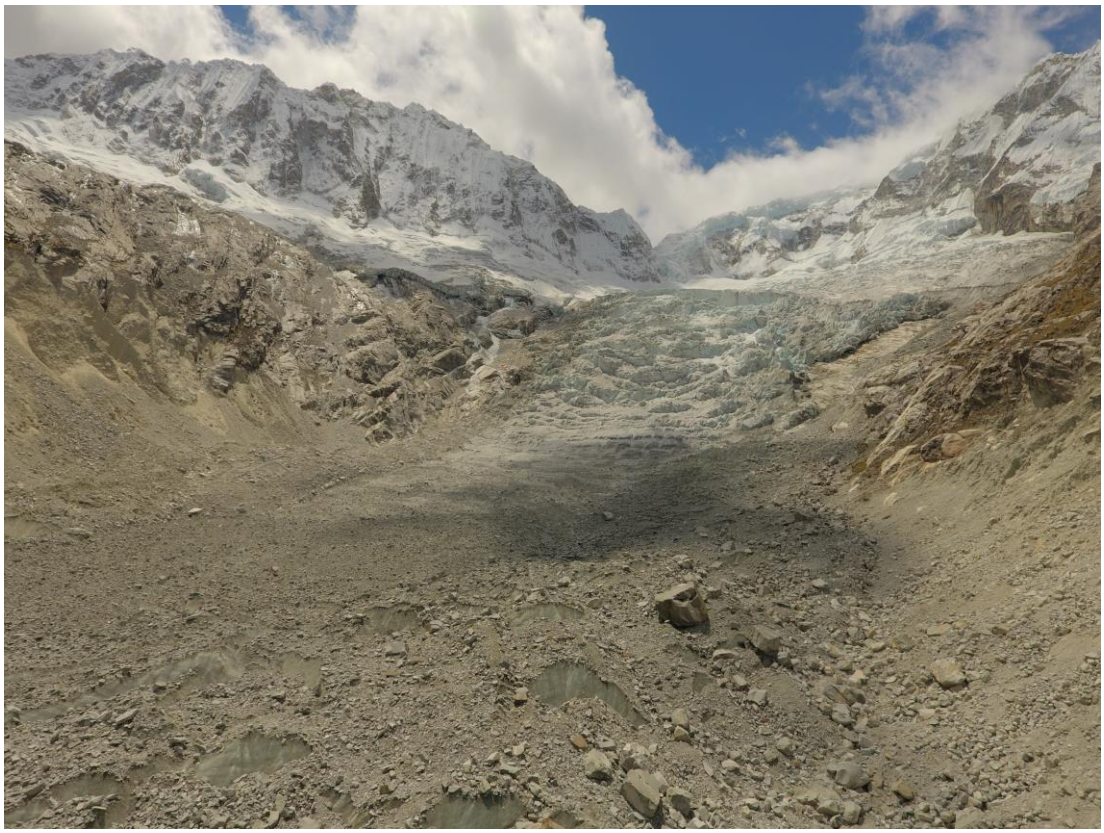

Figure 2.6. UAV-acquired image of the upper portion of the debris-covered tongue of Llaca Glacier (foreground) and the icefall (background) (August 2019).

Figure 2.7. Supraglacial ice cliff on the debris-covered tongue of Llaca Glacier (August 2019).

Figure 2.8. UAV-based thermal survey of Llaca Glacier tongue (August 2019).

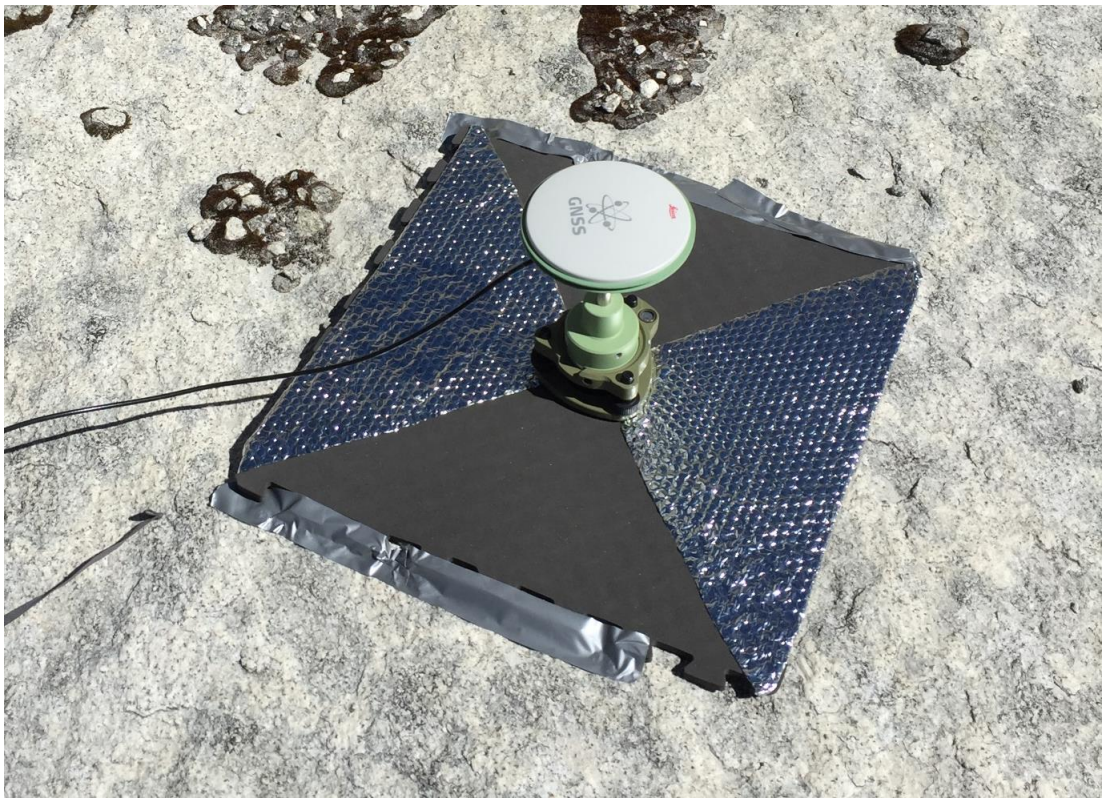

Figure 2.9. Ground control survey on Llaca Glacier (August 2019).

2.2 Debris-covered glaciers

2.2.1 Introduction

Around a fifth of Earth's largest glaciers (> 2 km^2) are substantially debris covered, with > 7 % and/or > 10 km^2 of their surfaces being debris-covered (Herreid and Pellicciotti, 2020). At present, ~ 10 – 11 % of the glacial ice surface in High Mountain Asia is blanketed with debris, while ~ 6.5 % of the glacierised area in the Cordillera Blanca is debris-covered, with debris being predominantly found within glacier ablation zones (RGI, 2017; Scherler et al., 2018). The proportion of the Earth's glacial ice blanketed by supraglacial debris is growing in response to climate change (Scherler et al., 2018), making debris cover an increasingly important factor to consider when projecting future glacier mass balances and downstream river discharges.

2.2.2 Supraglacial debris cover evolution

Supraglacial debris originates from glacial headwalls in areas of high-relief topography. The eroded material is transported englacially before re-emerging in the ablation zone, due to surface melting and emergent ice flow (Rowan et al., 2015). The thickness and extent of supraglacial debris cover is controlled by debris supply rates from glacial headwalls, ice flow dynamics and glacial ablation rates (e.g. Kirkbride and Deline, 2013; Gibson et al., 2017). When the mass balance of a glacier is negative, the equilibrium line altitude moves up-glacier, resulting in an expansion of the ablation zone. As a result, debris-carrying ice flow paths are shifted up-glacier and melting occurs over a greater area of the glacier tongue, leading to up-glacier expansion of supraglacial debris cover (Rowan et al., 2015). Eventually, debris-covered ice tongues can become detached from the main trunks of glaciers, leading to further acceleration of glacial retreat.

2.2.3 Sub-debris melt

Previous research has shown that supraglacial debris cover significantly impacts the ablation rates and melt patterns of glaciers. When the debris layer is less than a critical thickness of ~3-8cm, the melt rate at the ice surface is amplified

(Østrem, 1959; Kayastha et al., 2000). Conversely, when the supraglacial debris layer exceeds the critical thickness, the sub-debris melt rate is dampened, with increasing debris thickness leading to increasingly reduced melt rates (e.g. Nicholson and Benn, 2006; Lejeune et al., 2013). This empirical relationship between debris thickness and ablation rates was first established by Østrem (1959) and is commonly termed the Østrem curve (Figure 2.10).

On debris-free ice, ablation generally decreases continuously with increasing altitude, due to vertical air temperature gradients (e.g. Sherpa et al., 2017). However, field-based studies have observed that on debris-covered glacier tongues, this relationship between altitude and ablation is frequently reduced or even reversed (e.g. Benn et al., 2012; Azam et al., 2016). This reversed trend results from altitudinal thinning of the debris layer, leading to reduced insulation and enhanced melt rates (e.g. Benn and Lehmkuhl, 2000). Consequently, on debris-covered glaciers, the greatest ablation rates are often observed towards the upper portion of the ablation zone (e.g.; Banerjee and Shankar, 2013; Azam et al., 2016).

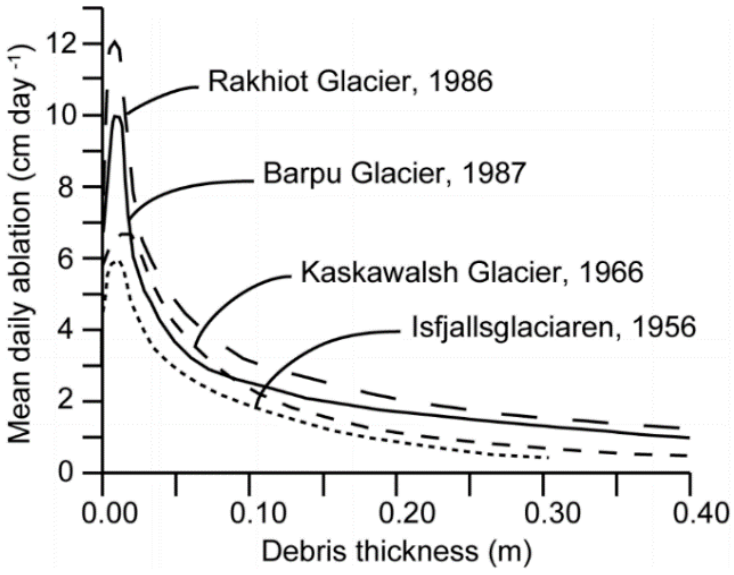

Figure 2.10. Field-based examples of the Østrem curve relationship between debris thickness and sub-debris ablation rates. Source: Nicholson et al. (2018), redrawn from Mattson et al. (1993).

In conjunction with debris thickness, other properties of supraglacial debris can also influence sub-debris melt rates. As the moisture content of the debris increases, the thermal conductivity of the debris layer also increases, consequently raising sub-debris melt rates (Nakawo and Young, 2017). Rock type can also influence the thermal conductivity of the debris layer, since different lithologies have different specific heat capacities (Nicholson and Benn, 2013). For example, limestone has a higher specific heat capacity than granite (Nicholson and Benn, 2013), resulting in higher thermal conductivities and greater sub-debris melt rates beneath limestone debris compared to beneath granite debris.

Debris grain size can also considerably influence sub-debris melt rates. Coarse debris has greater pore space, allowing greater heat transfer by ventilation (Nicholson and Benn, 2013). Consequently, the temperature of coarse debris quickly equilibrates with the air temperature. In contrast, the thermal response of finer debris is less rapid, due to slow processes of conduction through individual grains (Harris and Pederson, 1998). As a result, when debris grain size is smaller, there is a longer lag time between changes in air temperatures and consequent changes in debris temperatures within the debris layer (Harris and Pederson, 1998). These differences in the efficiency of heat transfer through the debris layer consequently influence the rate of sub-debris melting. Meltwater runoff can also wash fine-grained material out of the debris, thus increasing debris porosity, accelerating heat transfer through the debris layer and modifying sub-debris melt rates (Lambrecht et al., 2011).

2.2.4 Flow dynamics

Many glaciers in high mountain regions, both debris-covered and debris-free, are decelerating in response to climate-change-driven mass losses (e.g. Heid and Kääb, 2012; Neckel et al., 2017; Dehecq et al., 2019; Farinotti et al., 2020). Heid and Kääb (2012) observed an extensive and sustained reduction in ice flow velocities in mountain regions including Alaska (11%), Patagonia (20%), Caucasus (8%) and Pamir (43%). Similarly, Dehecq et al. (2019) found that in 9 of 11 areas in High Mountain Asia, glaciers exhibited continuous slowdown associated with ice thinning for the period

between 2000 and 2017. Meanwhile, in the few regions where glaciers were stable or even slightly gaining mass, glaciers accelerated during the same period (Dehecq et al., 2019). The deceleration that has been observed overall can be attributed to the reduction of gravitational driving stresses as widespread glacial thinning occurs. For example, Dehecq et al. (2019) found that 94% of the variability in flow velocity change between regions could be explained by changes in driving stress. With projections of continued glacier mass loss in the future (e.g. Radić et al., 2014; Shannon et al., 2019; Rounce et al., 2020), it is likely that the deceleration that has been observed will continue over the next several decades.

Research has shown that the lower reaches of debris-covered glaciers are frequently stagnant, with lower flow velocities than their debris-free counterparts (e.g. Scherler et al., 2011; Thompson et al., 2016; Bhushan et al., 2018). This stagnancy results from the inverse relationship between distance up-glacier from the terminus and supraglacial debris thickness (e.g. Quincey et al., 2009; Benn et al., 2012). As discussed in Section 2.2.2, the greatest melt rates on debris-covered glaciers occur in the upper portions of the debris-covered areas, where the debris layer is thin. As a result, ice-surface lowering is concentrated in this area, with lower thinning rates towards the terminus, causing a reduced ice surface slope (Benn et al., 2012). The gravitational driving stress is consequently reduced, resulting in low ice flow velocities (Benn et al., 2012). Topography also plays a role in determining the stagnancy of glaciers, since steep glacier beds can increase driving stress, acting against the slowdown of debris-covered ice tongues. Scherler et al. (2011) found that stagnant ice on debris-covered glaciers in High Mountain Asia can only exist on ice tongues with surface slopes of less than 8° (Scherler et al., 2011), therefore debris-covered tongues on slopes exceeding 8° are likely to remain active.

2.2.5 Supraglacial ice cliffs

Supraglacial ice cliffs are generally defined as exposed or thinly debris-covered ice surfaces present on debris-covered glaciers (Steiner et al., 2019). In general, ice cliffs have surface gradients of greater than ~30°, as debris material tends to

accumulate on ice surfaces shallower than ~30° (Herreid and Pellicciotti, 2018). Ice cliffs can exist in a variety of sizes, from only a few metres in dimensions to more than 100 metres in width and 30 metres in height (Steiner et al., 2019). These features can have a range of different geometries, most commonly crescent, circular or linear shapes (Herreid and Pellicciotti, 2018).

Research suggests that ice cliffs can contribute significantly towards the mass loss of debris-covered glaciers. For example, Thompson et al. (2016) found that ice cliffs were responsible for ~40% of the overall mass loss of Ngozumpa Glacier, the longest glacier in the Himalaya. Meanwhile, Brun et al. (2018) observed that between November 2016 and November 2017, ice cliffs on Changri Nup Glacier (Himalaya) were responsible for 24 ± 5 % of the total ablation on the glacier tongue, despite only covering ~7-8% of the total area. These cliffs were found to have a net melt rate 3.0 ± 0.6 times higher than the average melt rate of the debris-covered tongue (Brun et al., 2018).

Ice cliff ablation rates are greater on debris-covered glaciers compared to on debris-free glaciers. This is, in part, due to the conglomeration of fine debris particles on cliff surfaces, thus reducing the albedo and raising radiative absorption (Brock et al., 2010). In addition, the debris material which surrounds ice cliffs warms up during the daytime, emitting longwave radiation and raising ambient air temperatures through the process of convection (Brock et al., 2010). The bases of ice cliffs generally receive more longwave radiation from the surrounding debris, compared to the crests of ice cliffs, due to a decrease in the debris view factor from the cliff base towards the cliff crest (Buri and Pellicciotti, 2018).

Ice-cliff formation occurs through three principal mechanisms. Firstly, the slumping of debris down slopes on the surfaces of glaciers can lead to the exposure of sub-debris ice (Benn et al., 2001). Secondly, calving of ice into supraglacial ponds can result in the formation of cliffs around the perimeters of these lakes (Kirkbride and Warren, 1997, Benn et al., 2001). Thirdly, collapse of the roofs of englacial conduits can promote ice-cliff formation (Kirkbride, 1993; Sakai et al., 2002).

Ice cliffs can form in a wide range of orientations, but recent research suggests that aspect plays a strong role in ice-cliff survival. Research in the Himalaya demonstrates that cliffs facing north generally survive preferentially over south-facing cliffs (e.g. Sakai, Nakawo and Fujita, 2002; Kraaijenbrink et al., 2016; Buri and Pellicciotti, 2018; Steiner et al., 2019; Watson et al., 2017). South-facing cliffs (in the Northern Hemisphere) receive a higher volume of solar radiation, with the greatest amount of radiation being received at the tops of cliffs (Buri and Pellicciotti, 2018). While cliff bases may receive more longwave radiation emitted by adjacent debris, this is not sufficient to compensate for the low solar radiation receipt (Buri and Pellicciotti, 2018). As a result, melt rates increase from the cliff bases cliff crests, resulting in the flattening and reburial of ice cliffs. However, ice cliffs facing north (in the Northern Hemisphere) have a weaker base-to-crest solar radiation gradient, therefore cliffs backwaste with a more constant slope, enabling ice-cliff survival (Buri and Pellicciotti, 2018). Some north-facing cliffs may even have greater melt rates at their bases than their crests, leading to ice-cliff steepening (Buri and Pellicciotti, 2018).

Several studies in the Himalaya have found that diurnal meteorological patterns also play a role in controlling ice-cliff survival. These studies established that north-west facing cliffs have the longest life expectancy (e.g. Buri and Pellicciotti, 2018; Steiner et al., 2019). For example, Steiner et al. (2019) found that 53% of all cliffs on Langtang Glacier and 60% of all cliffs on Langshisha Glacier faced northwest. The melt season in this region occurs during the same period as the monsoon season, resulting in a frequent presence of thick cloud cover during the afternoons. As a result, the solar radiation receipt of cliffs with westerly aspects is lowered significantly, reducing the base-to-crest solar radiation gradient and enabling ice-cliff survival (Buri and Pellicciotti, 2018).

Some studies of debris-covered glaciers in the Himalaya have indicated that flow direction does not play a strong role in controlling ice cliff orientation since, regardless of the ice flow direction, ice cliffs predominantly have a north-west-facing aspect (Buri and Pellicciotti, 2018; Watson et al., 2017; Steiner et al., 2019). However, the findings from several studies indicate that ice flow may play some role in

controlling ice-cliff evolution. For example, Steiner et al. (2019) observed that cliffs near glacier termini were generally orientated perpendicular to the flow line. Furthermore, research indicates that higher densities of ice cliffs are present in areas of active ice flow (Watson et al., 2017) and areas of compressional flow (Kraaijenbrink et al., 2016; Steiner et al., 2019), such as glacier termini, tributary confluences and areas of curving ice flow direction. Strain rates are expected to be high in areas of compressional flow, promoting englacial-conduit formation and fracturing, which can result in a greater occurrence of ice cliffs (Kraaijenbrink et al., 2016; Steiner et al., 2019).

Ice cliffs are frequently located around the perimeters of supraglacial ponds. For example, Steiner at al. (2019) found that, for five glaciers analysed in the Himalaya, >50% of cliffs were adjacent to a pond during the wet season, while Kraaijenbrink et al. (2016) showed that ice cliffs which deviate from the optimum aspects for survival are frequently connected to supraglacial ponds. Research has shown that supraglacial ponds help to sustain adjoined ice cliffs through processes of thermoerosion and subaqueous melt (e.g. Miles et al., 2016). These ponds absorb a larger quantity of solar radiation than the surrounding debris-covered area and deliver this energy to the ice, thereby accelerating melt rates. The processes of thermoerosion and subaqueous melt are concentrated at ice cliff bases, enabling cliffs to sustain steep gradients which promote their survival (e.g. Buri et al., 2016; Miles et al., 2016; Miles et al., 2020). Additionally, cliffs connected to ponds are exposed to incoming longwave radiation emitted by the debris surrounding the ponds (Buri et al., 2016). This longwave radiation receipt is particularly high at cliff bases, therefore encouraging further steepening of ice cliff faces. Furthermore, the drainage of water from supraglacial ponds through englacial channels can lead to the formation of new supraglacial cliffs through the broadening of englacial channels, which leads to increased risk of channel roof collapse (e.g. Sakai et al., 2018).

2.2.6 Supraglacial meltwater ponds

The key processes suggested to contribute towards the formation and expansion of supraglacial ponds on debris-covered glaciers include (i) the collapse of englacial conduits, (ii) melting of adjacent ice at and beneath the waterline, and (iii) calving, promoted by thermal undercutting (e.g. Sakai et al., 2000, Benn et al., 2001., Miles et al., 2016). Supraglacial ponds are often transient, draining sporadically due to the opening and closing of structures as the ice flows (e.g. Reynolds, 2000). Research has shown that supraglacial ponds tend to be most abundant in areas with low surface gradients and velocities (e.g. Miles et al., 2016), with the largest ponds usually being found where the surface slope is $<2°$ (e.g. Reynolds, 2000). Watson et al. (2017) found that ponds adjacent to ice cliffs on Khumbu and Lobuche Glaciers (Himalaya) were deeper and more irregularly-shaped, compared to the shallower and more circular ponds independent from ice cliffs.

While supraglacial ponds promote higher melt rates on debris-covered glaciers through the delivery of energy to cliff bases, the melt rates beneath ice ponds are often relatively low in comparison. Sakai et al. (2000) found that the energy available for melting the ice beneath the debris layer at the bottom of a pond on Lirung Glacier (Himalayas) was negligible (1-4 W m^{-2}) in comparison to the energy received at the pond surface (110 to 240 W m^{-2}). Meanwhile, a study on Langtang Khola Glacier (Nepal) found that while bare ice in contact with a supraglacial pond had a simulated melt rate 2-4 cm d^{-1}, melt rates at the saturated debris zone beneath the pond were simulated to be less than 1 mm d^{-1} within the heavily debris-covered zone (Miles et al., 2016). The results of this study also demonstrated that majority of the energy absorbed by the pond was evacuated through englacial channels, providing the potential to melt ~2612 m^3 of ice (Miles et al., 2016).

Research has demonstrated that the coverage of supraglacial ponds on debris-covered glaciers is increasing over time. Since meltwater ponds buffer proglacial discharge by temporarily storing and releasing meltwater, ponds are likely to play an increasingly important role in regulating meltwater runoff in the future (Irvine-Fynn

et al., 2017), therefore impacting downstream freshwater availability and biodiversity (e.g. Pritchard et al., 2019; Jacobson et al., 2012). Additionally, the expansion of supraglacial pond coverage is likely to affect the volume of meltwater being produced by debris-covered glaciers, through the delivery of energy absorbed by ponds to their bordering ice cliffs. Furthermore, the increasing coverage of supraglacial ponds is likely to heighten the risk of GLOF events, posing dangers to downstream communities and infrastructure (e.g. Kattelmann, 2003; Rounce et al., 2016).

2.2.7 The 'debris cover anomaly'

Despite the well-known influence of supraglacial debris on glacier ablation rates, geodetic studies have observed similar rates of thinning on debris-covered and debris-free glaciers (Kääb et al., 2012; Gardelle et al., 2013; Brun et al., 2019). This inconsistency is known as the 'debris cover anomaly'. A factor which may be partially responsible for this anomaly is the presence of supraglacial ice cliffs and meltwater ponds on debris-covered glaciers. As discussed in Section 2.2.5, these features provide localised 'hot spots' of enhanced melting. These melt hotpots can contribute towards offsetting the reduction in melt rates due to insulation from the debris layer (Sakai et al., 1998; Brun et al., 2018; Miles et al., 2018). Debris-covered glacier dynamics may also be contributing towards the debris cover anomaly. As a result of the suppressed ablation rates on debris-covered tongues, there are reduced emergence velocities in the ablation areas of debris-covered glaciers. As a result, the resupply of ice from the accumulation area into the ablation area of these glaciers is slower, resulting in increased dynamic thinning which partially compensates for the reduced thinning resulting from ice-surface insulation (e.g. Banerjee, 2017; Nuimera et al., 2017; Yang et al., 2020). However, the contribution of flow dynamics towards glacial thinning in regions such as High Mountain Asia is poorly constrained, limiting the ability of glaciological models to forecast effectively the future mass balance of debris-covered glaciers.

2.3 Current techniques for monitoring debris-covered glaciers

2.3.1 Techniques for quantifying debris thicknesses

Supraglacial debris thicknesses have been quantified previously using field-based techniques and satellite remote sensing. Field-based techniques include: (i) the physical measurement of debris thickness by digging through the debris layer to the debris-ice interface, (ii) the use of ground-penetrating radar (GPR) to produce reflection profiles along linear transects across the glacier surface; and (iii) the surveying of the debris layer exposed above supraglacial ice cliffs.

While physical measurements of debris thickness can provide a high level of accuracy at discrete points, this technique is time-consuming and is often skewed towards smaller debris thicknesses (e.g. Zhang et al., 2011; McCarthy et al., 2017; Nicholson and Mertes, 2017). Furthermore, this technique provides only single-point measurements and, due to high spatial heterogeneities in debris thickness, can lead to inaccuracies in interpolation between data points (McCarthy et al., 2017). McCarthy et al. (2017) found that the use of GPR facilitates the collection of debris thickness measurements over a wider range of thicknesses (between 10 cm and at least 2.3 m). This technique also allows collection of debris thickness measurements more rapidly and with a greater spatial resolution compared to physical spot measurements (McCarthy et al., 2017). However, the high relief and surface roughness of debris-covered glacier surfaces still limits the speed and coverage of GPR surveys. Furthermore, this technique cannot be used to measure debris thicknesses of less than 10 cm and the interpretation of GPR data can be subjective (McCarthy et al., 2017). Cliff-top debris thicknesses have been measured using laser reflections (Nicholson and Benn, 2012) and Structure-from-Motion (SfM) based on terrestrial photogrammetry (Nicholson and Mertes, 2017; Nicholson et al., 2018). This method is relatively simple and cost-effective, and allows the measurement of spatially-heterogeneous debris thicknesses with high spatial precision (Nicholson and Mertes, 2017). The disadvantage of this technique is that measurements are limited to areas directly above

ice cliffs, where debris characteristics may be atypical (McCarthy et al., 2017), leading to poor spatial interpolation of debris thicknesses.

Previous studies have shown that thermal satellite imagery, in conjunction with meteorological data, can be used to simulate distributed supraglacial debris thicknesses, using surface energy balance (SEB) modelling (Foster et al., 2012; Rounce and McKinney, 2014; Schauwecker et al., 2015). A SEB describes the balance of energy inputs and energy outputs to a surface. The SEB of a debris-covered glacier surface is shown in Figure 2.11. As shown, the debris temperature increases from the ice-debris interface (where debris temperature is assumed to be 0 °C) to the surface of the debris layer. Thus, the thickness of the debris can be simulated from the surface temperature, provided that (i) there are sufficient meteorological data to simulate the energy fluxes shown in Figure 2.11, and (ii) there are suitable measurements of depth-dependent temperature within the debris layer to parameterise the thermal conductivity of the debris layer.

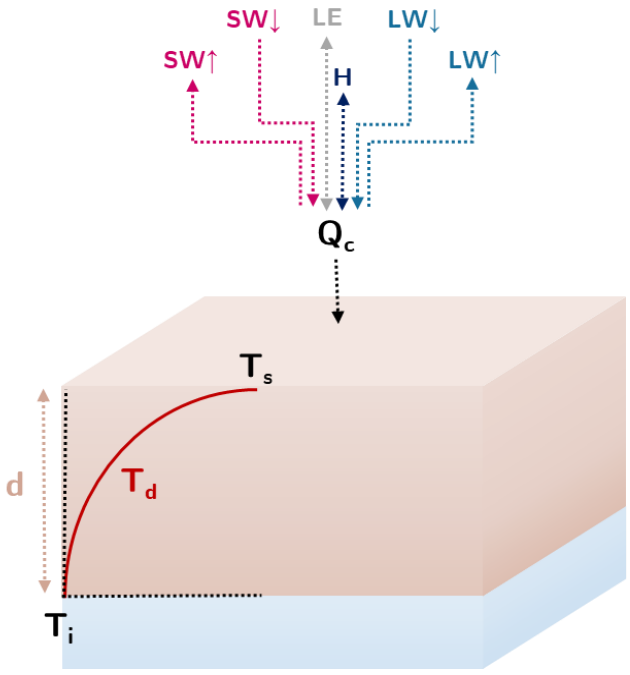

Figure 2.11. Surface energy balance of a debris-covered glacier. T_i, T_d and T_s represent the temperatures of the ice, debris and debris surface respectively. The red curve represents the depth-dependent debris temperature profile. SW↓ and SW↑ represent the incoming and outgoing shortwave radiation while LW↓ and LW↑ represent the incoming and outgoing longwave radiation. The turbulent heat fluxes are represented by H (sensible heat flux) and LE (latent energy flux).

The accuracy of debris thicknesses simulated using SEB modelling can be improved by accounting for several additional factors. Firstly, the effects of the local and surrounding topography on the energy fluxes can be considered. For example, by using DEMs to simulate the spatially-varying incoming shortwave radiation that reaches the surface, the effects of shadowing from local features (e.g. debris mounds) and the surrounding topography can be accounted for (e.g. Rounce and McKinney, 2014). Model accuracy can also be enhanced by considering the nonlinearity of the temperature gradient between the debris-ice interface and the debris surface. For example, Rounce and McKinney (2014) introduced an additional parameter to a debris-covered glacier SEB model, G_{ratio}, which represents the ratio of the linear temperature gradient in the upper 10 cm of the debris layer to the linear temperature gradient through the entire debris layer. The addition of this term converts the SEB model from its standard linear form

$$d = \frac{k_{eff}(T_s - T_i)}{Q_c} \tag{2.1}$$

into a nonlinear form

$$d = \frac{G_{ratio} k_{eff}(T_s - T_i)}{Q_c} \tag{2.2}$$

where k_{eff} is the effective thermal conductivity (W m^{-1} K^{-1}), T_s is the surface temperature (K), T_i is the ice temperature (K), Q_c is the ground heat flux (W m^{-2}) and G_{ratio} is the nonlinear approximation factor (dimensionless).

Non-SEB approaches have also been applied previously to surface temperature data to simulate supraglacial debris thickness. For example, Mihalcea et al. (2008) used a simplified method combining thermal satellite data (ASTER) with in-situ measurements of debris thickness to calculate the empirical relationship between debris thickness and surface temperature on Baltoro Glacier, Karakoram, Pakistan. Using this relation, Mihalcea et al. (2008) simulated spatially-distributed debris thicknesses across the glacier to produce a 90 m-resolution debris thickness map. An advantage of this method is its simplicity, and the fact that meteorological data are

not required. However, spatial variations in meteorological variables such as incoming shortwave radiation can lead to inaccuracy in simulated debris thicknesses.

Overall, the key advantage of simulating debris thicknesses using satellite data is that it can provide estimates of distributed debris thicknesses over larger spatial scales compared to field-based measurements. However, due to the relatively coarse resolution of currently available thermal satellite datasets ($>$ 60 m), the accuracy of debris thickness estimates can be impacted by the 'mixed-pixel effect' (Rounce and McKinney, 2014). The mixed-pixel effect describes the averaging of varying intra-pixel surface temperatures into a single value representing each pixel. Since the relationship between debris thickness and sub-debris melt rate is non-linear, this mixel-pixel effect impacts not only the precision of the simulated debris thicknesses, but also the accuracy of the sub-debris melt rates subsequently simulated using these debris thicknesses. As a simplified example, within a single 60 m pixel, both an ice cliff (with a debris thickness of 0 cm) and a thick layer of debris (40 cm) surrounding the ice cliff could be present. If the bare ice cliff covered 25 % of the pixel area, then a debris thickness of ~ 30 cm would be simulated for that pixel. Since the melt rate beneath a 30 cm layer of debris differs from the total melt rate beneath a bare ice cliff surrounded by a thicker 40 cm debris layer, the simulated melt rate for this pixel would be impacted. If similar variations are present within the extents of many pixels, which is a probable scenario due to the high spatial heterogeneity of debris thicknesses on debris-covered glaciers (e.g. Nicholson et al., 2018), then the mixel-pixel effect can accumulate, impacting upon the accuracy of melt models.

2.3.2 Techniques for measuring glacier mass changes

Previous studies have applied field and remote sensing techniques to measure the mass balances of debris-covered glaciers. The mass balance of a glacier is defined as the difference between accumulation and ablation (Cuffey and Paterson, 2010). If a glacier has a positive mass balance, total accumulation outweighs total ablation, resulting in overall mass gain. If the total ablation of a glacier outweighs the total accumulation, the glacier has a negative mass balance, therefore is undergoing mass

loss. Processes of accumulation include snowfall, avalanches, wind-blown accumulation, freezing rain, basal freeze-on, hoar deposition and internal accumulation (freezing of water within the firn layer or ice), while processes of ablation include melting, calving, sublimation, avalanches and wind-blown snow loss (Cuffey and Paterson, 2010).

Mass changes per unit area occur as a result of two contributions: (i) the surface mass balance (SMB) contribution, and (ii) the dynamic contribution. The SMB contribution is the balance of accumulation and ablation per unit area, while the dynamic contribution is the balance of incoming and outgoing ice fluxes per unit area (Cuffey and Paterson, 2010). Both of these processes contribute towards mass changes at any single point on a glacier. For example, if a greater volume of ice is flowing into a given area of the glacier than is flowing out, this will contribute towards a positive mass change within that given area. Therefore, even if there is net ablation occurring (the SMB contribution), the net mass balance of the area can be stable or positive if the dynamic mass gain is equal to or more than the net SMB contribution. The mass continuity equation describes the relationship between the key components of mass change for any given section of a glacier (Cuffey and Paterson, 2010).

$$b = \left(\frac{dh}{dt} - \frac{Q_{in} - Q_{out}}{A}\right) \times \frac{\rho_i}{\rho_w} \tag{2.3}$$

where b is SMB (m w.e. a^{-1}), h is ice thickness, t is time, Q_{in} and Q_{out} are incoming and outgoing ice fluxes (m a^{-1}), ρ_i is the density of ice and ρ_w is the density of water.

Ablation stakes and snow pits are commonly used to collect in-situ point measurements of ablation and accumulation on debris-covered glaciers (e.g. Mihalcea et al., 2006; Pratap et al., 2017; Shah et al., 2019). Since stakes and pits are transported along the glacier surface with dynamic ice flow, they can be used to measure ablation and accumulation directly and independently from dynamic mass changes. However, the remote locations, challenging surface conditions and expansive spatial extents of most debris-covered glaciers limit the number of measurements that can be collected, limiting the spatial scale of field studies using these techniques.

2.3. CURRENT TECHNIQUES IN DEBRIS-COVERED GLACIOLOGY

Geodetic remote sensing techniques, measuring ice surface elevation changes, have previously been used to estimate the mass balances of debris-covered glaciers (e.g. Kääb et al., 2012; Gardelle et al., 2012; Brun et al., 2017; Seehaus et al., 2019; Shean et al., 2020). Digital elevation models (DEMs) acquired by satellites during different years can be differenced in order to measure the raising or lowering of glacier surfaces. The measured surface elevation changes, in conjunction with assumed ice density, can be used to approximate the net mass balance of glaciers. Due to the extensive spatial coverage of satellite-derived DEMs, remote sensing facilitates the quantification of glacier mass changes across significantly greater spatial scales. However, since the measured surface-elevation changes result from the combination of dynamic changes and SMB contributions, geodetic techniques cannot be used to quantify spatially-distributed ablation and accumulation rates driven by climatic changes.

A handful of previous studies have estimated the separate contributions of SMB and ice flow dynamics towards spatially-distributed rates of mass loss (e.g. Gudmundsson and Bauder, 1999; Vincent et al., 2009; Berthier and Vincent, 2012). These studies have used surface ice velocity measurements to estimate ice fluxes and subtract the flux contributions from the overall mass balances to estimate distributed SMBs (eq. 2.3). While these studies effectively separate the signals of SMB and ice flow dynamics, they are limited in spatial scale (focusing on single glaciers), as the result of a lack, until relatively recently, of large-scale input datasets.

Surface energy balance modelling (discussed previously in this section) can be used to simulate spatially distributed melt rates on debris-covered glaciers (e.g. Nicholson and Benn, 2006; Reid and Brock, 2010; Reid et al., 2012; Lejeune et al., 2013; Fyffe et al., 2014; Rounce et al., 2015). The melt rate M (m s^{-1}) can be calculated from the conductive heat flux

$$M = \frac{Q_m}{\rho_i L_f} \tag{2.4}$$

where Q_m (W m^{-2}) is downward energy flux at the base of the debris layer and L_f is the latent heat of fusion (334 kJ kg^{-1}). Since the energy flux through the debris layer is predominantly via heat conduction, the downward heat flux is approximated as the conductive heat flux (Q_c), which is calculated as the sum of all ingoing and outgoing energy fluxes. While a sub-daily time-step is usually used, Nicholson and Benn (2006) demonstrated that the model still performs well when using daily mean meteorological variables to calculate the conductive heat flux. This method facilitates the simulation of sub-debris melt rates over longer timescales with greater computational efficiency.

2.3.3 Techniques for measuring the characteristics and melt patterns of supraglacial ice cliffs

Supraglacial ice cliffs have previously been mapped using a range of manual and automated methods (e.g. Han et al., 2010; Reid et al., 2012; Reid and Brock, 2017; Steiner et al., 2017; Watson et al., 2017; Herreid and Pellicciotti, 2018). While manual delineation can often yield more precise results, it can be time-consuming and subject to user biases and errors. Meanwhile, automated mapping methods offer the advantages of eliminating user biases and reducing mapping time. Additionally, objective automated mapping methods have been demonstrated to successfully identify small features that are undetected through manual delineation (Kneib et al., 2021). However, a disadvantage of automated methods is that they can miss abnormal ice cliffs which do not meet the criteria used for detection, or falsely detect other features with similar characteristics to ice cliffs. Therefore, manual validation and/or correction is usually required in order to ensure that the results are reliable.

A number of different automated techniques have been used previously to map supraglacial ice cliff coverage from satellite and UAV imagery. Due to the steeply-sloping nature of ice cliffs in comparison to their surroundings, surface slope thresholds have been applied to DEMs to detect cliff surfaces (e.g. Reid and Brock, 2017; Herreid and Pelliciotti, 2018). Kneib et al. (2021) utilised the unique spectral signatures of ice cliffs to detect ice cliffs on three glaciers in the Himalayas from multispectral satellite

imagery, using Spectral Curvature and Linear Spectral Unmixing techniques. Anderson et al. (2021) took advantage of the differences in image brightness between ice cliffs (which are covered with a thin layer of dark-coloured saturated debris) and the surrounding debris, using techniques of adaptive binary thresholding and Sobel edge delineation to detect supraglacial cliffs on the Kennicott Glacier (Alaska) from optical satellite imagery. Kraaijenbrink et al. (2016) applied object-based image analysis (OBIA) to high-resolution UAV data to semi-automatically classify supraglacial ice cliffs and ponds on Langtang Glacier, Nepal. This study also demonstrated that applying the OBIA technique to UAV imagery revealed approximately four times the number of supraglacial ponds identified from applying OBIA to 5m-resolution RapidEye satellite imagery (Kraaijenbrink et al., 2016), highlighting the benefits of using high-resolution imagery for detection of surface features. In future, with further development of automated mapping techniques and improvement in the resolution of satellite imagery, these techniques can be applied effectively to map ice-cliff coverage at a regional scale.

Previous studies have used in-situ measurements, remote sensing techniques, point models and grid-based models to measure the ablation of supraglacial ice cliffs (e.g. Han et al., 2010; Reid and Brock, 2014; Brun et al., 2016; Buri et al., 2016; Steiner et al., 2017; Wigmore et al., 2017; Brun et al., 2018; Anderson et al., 2021). Cliff ablation rates can be quantified in three different ways: backwasting rates, perpendicular melt rates and vertical melt rates (Figure 2.12).

In the field, repeat measurements of ablation stakes, installed either vertically or perpendicularly into the surfaces of ice cliffs, have been used to quantify vertical or perpendicular melt rates (e.g. Reid and Brock, 2014; Anderson et al., 2021). Alternatively, to estimate ice-cliff backwasting rates, markers can be placed several metres behind the top edges of ice cliffs, allowing repeat measurements of the distances between markers and cliff edges to be made (e.g. Han et al., 2010; Figure 2.12). The disadvantages of these field techniques are that (i) they can only produce individual point measurements of cliff ablation, (ii) they are limited in spatial scale, and (iii) accessing cliff faces and their surroundings is often dangerous.

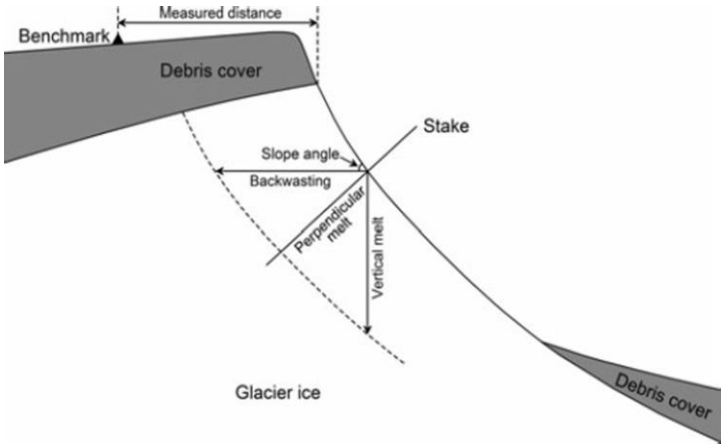

Figure 2.12. Schematic diagram of ice cliff ablation measurements. Source: Han et al. (2010).

Various remote sensing techniques, including geodetic methods and orthomosaic comparison, can be used to quantify the retreat rate of supraglacial ice cliffs. For example, Brun et al. (2018) used terrestrial photogrammetry (0.1 m precision), UAV photogrammetry (0.2 m precision) and satellite photogrammetry from Pléiades (2 m precision) to measure backwasting rates on the tongue of Changri Nup Glacier, Nepal. Meanwhile, Wigmore et al. (2017) used UAV-derived orthomosaics from 2014 and 2015 to estimate the backwasting rates of ice cliffs on Llaca Glacier, Cordillera Blanca, the same glacier studies here in Chapters 4 and 5. When using these remote-sensing-based methods, the imagery needs to be georectified first, in order to account for effects of ice flow on ice-cliff positions (Wigmore et al., 2017). Overall, using remote-sensing-based methods to quantify cliff backwasting rates can provide spatially-continuous data (as opposed to point-based data) across greater spatial scales than is possible using manual field techniques.

SEB modelling has also been used to estimate the backwasting rates of supraglacial ice cliffs on debris-covered glaciers. A simple model, which accounts for turbulent heat fluxes, in addition to shortwave and longwave radiation from the sky, was introduced by Sakai et al. (1998). This model was updated to account for the effects of shading from the surrounding topography, as well as the longwave radiation emitted onto cliffs from the surrounding debris (Sakai et al., 2002). In order to account for these effects, view factors, which describe the exposure of ice cliffs to the sky and

the surrounding debris, were calculated (Sakai et al., 2002). Han et al. (2010) further developed this approach to account for the effect of the cliff slope orientation on the exchange coefficient for calculating turbulent heat fluxes. This updated approach introduced a topographic-dependent roughness length, which is calculated based on wind direction and cliff slope orientation, in order to account for the fact that the exchange coefficient is one order of magnitude greater when the wind is perpendicular to a smooth surface, compared to when the wind is parallel to the surface (Han et al., 2010). Reid and Brock (2014) further improved this method by using hourly upwelling longwave radiation measurements recorded by a weather station to calculate the debris surface temperature, which was then used to calculate the longwave radiation emitted by the surrounding debris, as opposed to assuming that the debris temperature is equal to the air temperature. This study also proposed the use of an adjusted roughness parameter which accounts for variations in aerodynamic roughness along the base-to-crest profiles of ice cliffs (Reid and Brock, 2014). Steiner et al. (2015) and Buri et al. (2016a) further optimised the parameterisation of longwave and shortwave fluxes, while Buri et al. (2016a) introduced the first grid-based model of ice cliff backwasting, calculating spatially-distributed melt estimates across ice cliff faces, as opposed to previous studies which produced point-based estimates. While results of this gridded model show good agreement with observations, the results are based on a static cliff geometry which does not change over time in response to ablation. Therefore, Buri et al. (2016b) introduced a 3-dimensional model which simulates cliff evolution through time, accounting for the effects of atmospheric forcing, ponds adjacent to ice cliffs and reburial of cliffs by debris. To further develop our understanding of ice-cliff evolution, Buri et al. (2016b) state that further high-resolution cliff monitoring is required to gather information on a greater number of cliffs, representing a wider range of sites around the world, over longer (multi-annual) timescales.

2.4 UAV-based remote sensing

This section provides an overview of UAV-based remote sensing, focusing on the techniques used to generate 3D models and maps which are highly valuable for the study of debris-covered glaciers. As Chapters 4 and 5 of this thesis centre around the use of visible and thermal UAV data to study debris-covered glaciers, this section will focus on the collection and handling of visible and thermal UAV imagery.

2.4.1 UAV image acquisition

In order to collect UAV imagery suitable for developing maps and 3D models, UAVs are flown in a grid-like pattern whilst on-board sensors capture images of the ground at regular intervals (Figure 2.13). The resolution of the UAV imagery produced is determined by the ground sampling distance, which describes the distance on the ground between the centre points of each pair of sequential pixels (Lloyd, 2013). The optimal UAV flight altitude can be calculated based on the required ground sampling distance, in conjunction with the resolution, angle and focal length of the sensor being used (Figure 2.13). The optimal flight velocity can be determined based on the required 'frontlap' (overlap between consecutive images in the direction of flight) and the frequency of image capture (Figure 2.13). Meanwhile, the ideal spacing between parallel consecutive flight lines can be calculated based on

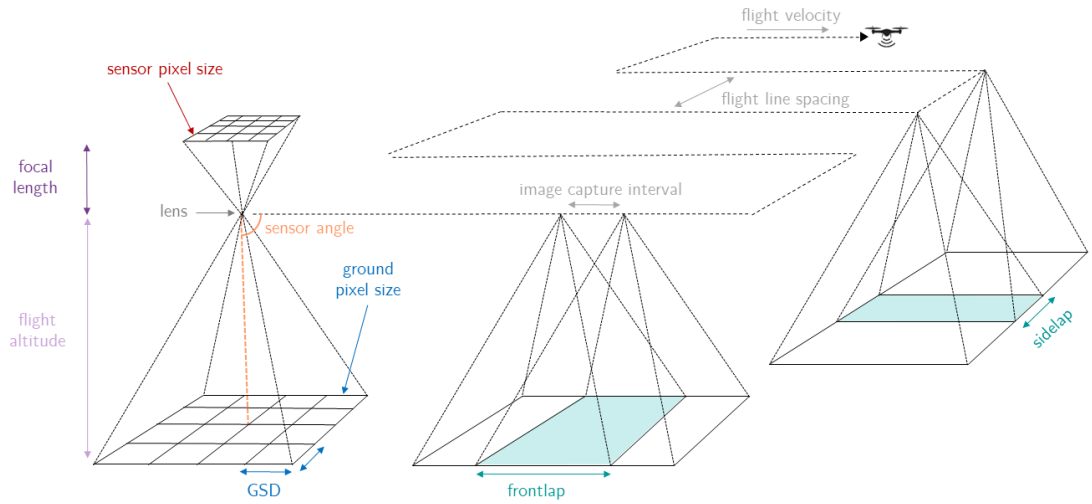

Figure 2.13. Schematic diagram of UAV flight parameters and on-board sensor properties.

the required 'side lap' (overlap between consecutive images perpendicular to the direction of flight).

A range of flight planning applications, such as DroneDeploy, UGCS and DJI Go, can be used to pre-programme flight parameters and select the spatial coverage of surveys. Some flight planning applications, such as UGCS, offer terrain correction while others can only be programmed to keep the UAV at a fixed altitude relative to the launch point. If the option of terrain correction is available, a DEM can be uploaded to the software and used to alter the flight altitude continuously over the course of the survey. Many off-the-shelf UAVs (e.g. DJI Phantom, DJI Mavic) have built-in sensors, such as visible and thermal cameras, as well as built-in GNSS receivers. For more niche survey requirements, custom-made UAVs, with specialised sensors and equipment, can be used.

UAV-mountable thermal cameras can be used to measure surface temperatures. Thermal cameras can be classified by two different types of detectors: cooled and uncooled (Kelly et al., 2019). As cooled thermal cameras have a greater sensitivity and accuracy, these sensors are most frequently used for remote sensing applications (Ribeiro-Gomes et al., 2017). However, these sensors are large and expensive, and have a high energy consumption, making them unsuitable for UAV-based thermal surveying. As a result, uncooled thermal cameras, which are lighter, cheaper and easier to fit to UAVs, are most commonly used for UAV-based data collection (Ribeiro-Gomes et al., 2017). Uncooled thermal cameras have an array of microbolometers, which change electrical resistance in response to the absorption of incoming thermal infrared radiation. As these sensors are not cooled, their thermal measurements are more sensitive to changes to the temperature of the camera sensor, body and lens (Maes et al., 2017). As a result, manufacturer-reported temperature accuracy can be up to $\pm$ 5 °C for uncooled cameras (Kelly et al., 2019). Thermal cameras can also be classified as either radiometric or non-radiometric. Radiometric thermal cameras measure the intensity of an infrared signal and calculate the absolute surface temperature, based on adjustable parameters such as emissivity, humidity and target-sensor distance (Lloyd, 2013). Meanwhile, non-

radiometric thermal cameras simply provide scene temperatures, which are represented by digital numbers as opposed to absolute temperature values (Lloyd, 2013). The use of low-cost non-radiometric cameras can be sufficient for some applications such as feature detection or object counting, where only relative thermal maps are required, while for other applications, where absolute surface temperatures are required, a radiometric camera is more suitable.

2.4.2 Georeferencing UAV imagery

In order to use UAV imagery for photogrammetric applications, high levels of spatial accuracy and precision are required. While all UAVs have on-board GNSS receivers for navigation, these systems typically have absolute horizontal and vertical accuracies of ~1 m and ~ 3 m respectively. Therefore, ground control surveys are usually required in order to georeference the UAV imagery accurately (James et al., 2017). For these surveys, ground control points (GCPs, i.e. points on the ground for which the coordinates are known) are used. During a ground control survey, GCP targets are distributed across the surface of the survey area. The centre point of each GCP target needs to be easily recognisable from the UAV images, therefore, depending on the type of sensor being used, different materials or colours may be optimal. The coordinates of each GCP are accurately measured in-situ using a GNSS receiver (James et al., 2017). Subsequently, following image acquisition, the GCP targets within the survey area are identified within the UAV imagery, and their GNSS-derived coordinates are used to adjust the positioning of the imagery in order to provide sub-centimetre-scale spatial accuracy (James et al., 2017).

In recent years, some UAVs have been fitted with an additional precision GNSS device, which can georeference images with cm-to-mm scale accuracy. The advantage of using this type of UAV is that it removes the need to conduct a ground control survey, significantly reducing the time required to conduct detailed surveys and reducing risks associated with dangerous conditions on the ground (Mulakala, 2019). These UAVs may have a post-processed kinematic (PPK) or a real-time kinematic (RTK) receiver on-board. Both PPK and RTK receivers collect

location data from satellites, but only RTK receivers are able to collect location data in real time from a nearby ground station (Mulakala, 2019). Since the location data received from satellites is affected by errors resulting from factors such as tropospheric delay, a maximum accuracy of ~1 metre can be obtained (Mulakala, 2019). Therefore, when a PPK UAV is used, satellite data from a GNSS receiver are collected and used to apply post-flight corrections which improve the location accuracy to a sub-cm scale (Tomaštík et al., 2019). Meanwhile, UAVs with RTK receivers instantaneously correct satellite signal errors during UAV flights using the real-time data received from the ground station, gaining a georeferencing accuracy of a few centimetres (Tomaštík et al., 2019). While using an RTK UAV can be quicker than using a PPK UAV, as post-processing is not required, PPK UAVs are more reliable and provide greater flight flexibility as they are not affected by signal strength between the UAV and the ground station (Mulakala, 2019). Therefore, RTK UAVs can work well in bare areas of flat terrain where the signal is unobstructed, while PPK UAVs are more suitable for longer flights in mountainous or forested areas.

2.4.3 Generating maps and 3D models

In order to generate maps and models from UAV-derived images, post-processing is required in order align, merge and georeference the imagery. These operations can be performed using photogrammetry software such as Agisoft or Pix4D. Due to the overlap between consecutive UAV images, features within the images are captured multiple times from different angles. Photogrammetric software automatically identifies, matches and aligns these features, producing a point cloud which is georeferenced using the ground-control-survey-derived coordinates associated with each individual image (Ludwig et al., 2020). Additionally, the user can identify GCPs from the aligned imagery and assign their measured coordinates, which are used by the software to automatically adjust the spatial positioning of the imagery (Ludwig et al., 2020). Using the point cloud produced, the photogrammetric software generates an orthorectified map known as an orthomosaic, which can

contain many different types of imagery: e.g. thermal imagery can be used to construct thermal orthomosaics.

In order to map the 3D structure of the surface of a survey area, Structure-from-Motion (SfM) Photogrammetry or Light Detection And Ranging (LiDAR) can be used. The SfM technique can be performed using different types of UAV imager, utilising the point correspondence between multiple overlapping images in order to triangulate and extract the 3D positions of points within the imagery (Mlambo et al., 2017). This technique can be used to create a map of the Earth's surface elevation including all objects on the surface, known as a digital surface model (DSM). Meanwhile, UAV-mounted LiDAR systems operate by sending out laser pulses and measuring the timing and intensity of returning pulses which have been reflected by the ground (Wallace et al., 2012). Since it is possible for some of the transmitted laser beams to travel through gaps in forest canopies and other vegetation to reach the ground beneath and return to the UAV (Wallace et al., 2012), LiDAR can be used not only to generate DSMs, but also topographic models of the bare Earth, known as digital terrain models (DTMs). Therefore, while SfM photogrammetry is relatively low-cost in comparison to LiDAR, the optimum technique for use depends on the application.

2.4.4 Calibrating UAV imagery

Depending on the on-board sensor used, calibration and/or correction procedures may need to be applied to UAV imagery to make it suitable for use in scientific applications. In particular, thermal UAV imagery is impacted by a range of external factors and sensor-related effects, including atmospheric attenuation, sensor bias, sensor drift, sensor stabilization, image vignetting and radiometric calibration (Kelly et al., 2019; Aragon et al., 2020). Therefore, several corrections and calibrations must be applied in order to improve the accuracy of UAV-derived thermal imagery.

As discussed in Section 2.4.1, thermal cameras can be described as either radiometric or non-radiometric. When a non-radiometric camera is used, an

empirical line calibration can be performed in order to convert the camera digital numbers within the images to actual surface temperature values (Wang and Myint, 2015). This technique involves the use of temperature calibration plates (TCPs), covering a wide range of temperatures, which are installed within the survey area. In-situ measurements of the TCP temperatures are performed regularly throughout the UAV survey and the linear relationship between the camera digital numbers of the TCPs (recorded by the non-radiometric thermal camera on-board the UAV) and the measured TCP temperatures is used to calculate surface temperatures for each pixel across the survey area (Kelly et al., 2019). Due to the simplicity and effectiveness of this method, empirical line correction is the most widely-used method for handling non-radiometric UAV imagery (Wang and Myint, 2015). However, a disadvantage of this technique is the assumption that the relationship between digital number and surface temperature is linear, while in fact most digital cameras use a curvilinear function to transform electromagnetic radiation to digital signals (Wang and Myint, 2015). Therefore, when possible, it is optimal to use a radiometric thermal camera in order to eliminate uncertainties associated with an empirical line calibration.

The flux of thermal infrared radiation received by a radiometric thermal camera is dependent not only on the surface temperature of the target, but also the surface emissivity of the target (Vollmer and Möllmann, 2017). Using a user-defined emissivity value, thermal cameras convert the measured thermal radiation flux to a surface temperature value, based on the Stefan-Boltzmann law,

$$E = \varepsilon \sigma T^4 \tag{2.5}$$

where E is the total energy flux (W m^{-2}), ε is the emissivity (dimensionless), $\sigma = 5.67 \times 10^{-8}$ W m^{-2} K^{-4} is the Stefan-Boltzmann constant and T is the absolute surface temperature (K). While the camera performs this calculation using a single emissivity value, surface emissivity values are likely vary considerably spatially. In order to account for emissivity variations, surface emissivity measurements can be made

and/or multiple emissivity values can be assigned for different surface materials (Kelly et al., 2019).

Previous studies have demonstrated that atmospheric effects can result in significant differences between actual surface temperatures and those measured by thermal infrared sensors (e.g. Meier et al., 2011; Hammerle et al., 2017). For UAV-mounted thermal cameras, these atmospheric effects include atmospheric attenuation of thermal radiance between the surface and the sensor, as well as upwelling thermal radiation originating from particles in the atmosphere (Maes et al., 2017). Both of these effects are primarily dependent on atmospheric water content and the distance from the surface to the sensor. To minimise the impacts of these factors on the surface temperatures recorded, thermal cameras convert measured values of at-sensor radiance to surface radiance, based on user-defined values for humidity, air temperature and sensor-target distance. However, while single user-defined values are used to represent these parameters, these parameters are likely to vary during single surveys, therefore limiting the accuracy of surface temperature values within thermal imagery. As a solution, radiative transfer models can be used to apply atmospheric corrections to the imagery based on the changing sensor-target distance, in order to minimise the impacts of atmospheric effects on final surface temperature values (Berni et al., 2009).

As mentioned previously, the lightweight uncooled thermal cameras that are predominantly used for UAV-based data collection have lower accuracy due to the impact of thermal radiation emitted by the camera interior (Maes et al., 2017). Additionally, non-uniformity in the response signal across the sensor can contribute towards a reduction in the accuracy of surface temperature values within thermal imagery. For example, distortion caused by the lens optics can result in 'vignetting' of thermal images (Meier et al., 2011). Vignetting describes the phenomenon where the central portion of an image is brighter (or in the case of thermal imagery, the surface temperatures are higher) compared to the outside regions of the image. Measured temperatures need to be calibrated in order to account for the effects of thermal radiation emitted by the camera interior and as well as the heterogeneous response of individual microbolometers within the camera (Kelly et al., 2019). The

radiometric calibrations and non-uniformity corrections performed by thermal cameras should, at least partially, account for these effects but, since information about the algorithms used by camera manufacturers is proprietary, the extent to which these effects are accounted for is poorly understood (Budzier et al., 2015).

Some thermal cameras have been found to warm up slowly after being switched on, causing unstable temperature measurements during the beginning of a thermal survey (Kelly et al., 2019). Additionally, due to external factors such as air temperature and wind speed, the temperature of the sensor can change, causing the temperatures recorded by the camera to drift (Ribeiro-Gomes et al., 2017; Kelly et al., 2019). To minimise these effects, Kelly et al. (2019) recommend a camera stabilization time of at least 15 minutes before beginning data collection, as well as to add a custom-built wind shield around the thermal camera and reduce the UAV flight velocity in order to minimise wind-related effects.

2.5 Summary

In chapter has introduced the key regions of study, reviewed our current understanding of debris-covered glaciers, highlighted some of the key knowledge gaps in this field, discussed the techniques that are currently used to monitor debris-covered glaciers and introduced the principles of UAV surveying relevant to this thesis. Overall, the chapter has highlighted that while understanding of debris-covered glaciers and techniques used to monitor them have advanced significantly over the past few decades, there are some key areas where further research is required. These research areas include:

(i) The 'debris cover anomaly':
Geodetic studies have observed similar thinning rates on debris-covered and debris-free glaciers in High Mountain Asia, despite the well-known influence of debris on ablation rates.

(ii) Debris thickness model precision:

Current satellite-based techniques for simulating supraglacial debris thickness produce maps with relatively coarse resolution, resulting in poor parameterisation of debris in glaciological models.

(iii) Ice-cliff evolution on debris-covered glaciers:
The temporal evolution of ice cliffs and the mechanisms controlling their development are not well understood, particularly in low latitude regions such as the Cordillera Blanca.

Chapters 3-5 of this thesis respectively address each of these research areas by:

(a) Using a mass continuity approach incorporating remote sensing datasets in order to understand better the contribution of ice-flow dynamics towards the patterns of ice thinning observed by geodetic studies of High Mountain Asia (Chapter 3).

(b) Conducting high-resolution thermal UAV surveys on a tropical debris-covered glacier in order to simulate spatially-distributed debris thicknesses and sub-debris ablation rates with greater levels of precision than currently possible (Chapter 4).

(c) Using high-resolution visible UAV data to investigate the characteristics and melt rates of supraglacial ice cliffs in the Cordillera Blanca, as well as the key factors controlling their evolution (Chapter 5).

Chapter 3

Reversed Surface-Mass-Balance Gradients on Himalayan Debris-Covered Glaciers Inferred from Remote Sensing

This chapter investigates the use of a mass continuity approach, in conjunction with satellite remote sensing datasets, to quantify the spatially-distributed surface mass balance of glaciers in High Mountain Asia. Within this chapter, the role of debris cover in controlling altitudinal ablation gradients is also explored.

This work was published in *Remote Sensing* in 2020 – see Appendix 1 for a copy of the published journal article. This work was conducted in collaboration with researchers from the School of GeoSciences (University of Edinburgh) and the Laboratory of Hydraulics (ETH Zurich).

Paper Details: Bisset, R.R., Dehecq, A., Goldberg, D., Huss, M., Bingham, R.G., Gourmelen, N. (2020) Reversed Surface-Mass-Balance Gradients on Himalayan Debris-Covered Glaciers Inferred from Remote Sensing. *Remote Sensing*. 12(10), 1563. https://doi.org/10.3390/rs12101563

Author contributions: I designed the study with input from A. Dehecq, N. Gourmelen and D.N. Goldberg. I performed the processing, analyses and interpretation, with contributions from A. Dehecq, N. Gourmelen, D.N. Goldberg,

R.G. Bingham and M. Huss. The paper was written by myself and edited by all co-authors.

3.1 Abstract

Meltwater from the glaciers in High Mountain Asia plays a critical role in water availability and food security in central and southern Asia. However, observations of glacier ablation and accumulation rates are limited in spatial and temporal scale due to the challenges associated with fieldwork at the remote, high-altitude settings of these glaciers. Here, using a remote-sensing-based mass-continuity approach, we compute regional-scale surface mass balance of glaciers in five key regions across High Mountain Asia. After accounting for the role of ice flow, we find distinctively different altitudinal surface-mass-balance gradients between heavily debris-covered and relatively debris-free areas. In the region surrounding Mount Everest, where debris coverage is most extensive, our results show a reversed mean surface-mass-balance gradient of -0.22 ± 0.18 m w.e. a^{-1} $(100m)^{-1}$ on the low-elevation portions of glaciers, switching to a positive mean gradient of 1.21 ± 0.41 m w.e. a^{-1} $(100m)^{-1}$ above an average elevation of 5520 ± 50 m. Meanwhile, in West Nepal, where debris coverage is minimal, we find a continuously positive mean gradient of 1.18 ± 0.40 m w.e. a^{-1} $(100m)^{-1}$. Equilibrium line altitude estimates, derived from our surface-mass-balance gradients, display a strong regional gradient, increasing from northwest (4490 ± 140 m) to southeast (5690 ± 130 m). Overall, our findings emphasise the importance of separating signals of surface mass balance and ice dynamics, in order to constrain better their contribution towards the ice thinning that is being observed across High Mountain Asia.

3.2 Introduction

The glaciers in High Mountain Asia collectively form the largest glacierised area outside the Polar Regions, covering an estimated ~118,264 km^2 (RGI, 2017). Meltwater from these glaciers feeds into major river basins including the Indus,

Ganges, Brahmaputra, Yellow and Yangtze, providing water resources to 221 ± 59 million people living in central and southern Asia (Pritchard, 2019). Furthermore, the melt rates of the glaciers in High Mountain Asia modify the frequency and magnitude of glacial-lake outburst floods, posing significant threats to downstream communities (Richardson and Reynolds, 2000; Veh et al., 2019; Veh et al., 2020). Quantifying and improving our understanding of glacier surface-mass-balance distribution across High Mountain Asia is critical for effective prediction and mitigation of these impacts.

Glacier surface mass balance (hereafter SMB) is defined as the difference between accumulation and ablation, negative where there is net melt. Many of the glaciers in High Mountain Asia are characterised by supraglacial debris cover of varying thickness and extent, which plays an important role in modifying SMB through its impact on glacier ablation rates. Field-based studies have shown that a thin layer of supraglacial debris, less than a critical thickness of ~3-8 cm, enhances glacier melt rates (e.g. Kayastha et al., 2000) through a reduction in the ice-surface albedo, as first demonstrated experimentally (Östrem, 1959) and more recently constrained from surface energy balance modelling (e.g. Lejeune et al., 2013; Rounce et al., 2015). In contrast, debris cover exceeding the critical thickness has the opposite effect, reducing ablation by insulating the ice surface (e.g. Kayastha et al., 2000; Nicholson and Benn, 2006; Wagnon et al., 2007; Azam et al., 2014; Pratap et al., 2015; Vincent et al., 2016). Other properties of supraglacial debris, such as moisture content, rock type and grainsize, can alter the thermal conductivity of the debris layer, consequently modifying the relationship between debris thickness and surface melt rates (e.g. Nakawo and Young, 1981; Lambrecht et al., 2011; Nicholson and Benn, 2012). Ablation rates on heavily debris-covered glaciers are extremely difficult to measure, due to the challenges associated with drilling stakes through the debris layer, as well as the large heterogeneity of local ablation rates (e.g. Mihalcea et al., 2006; Vincent et al., 2016).

Previous geodetic studies of ice-surface-elevation change have shown that, collectively, the glaciers in High Mountain Asia are losing mass rapidly (Kääb et al., 2012; Gardelle et al., 2013; Brun et al., 2017; Shean et al., 2020), with a total annual

mass change of $-19.0 \pm 2.5\,\mathrm{Gt\,a^{-1}}$ between 2000 and 2018 (Shean et al., 2020). However, despite the well-known importance of debris cover, geodetic studies have identified no clear relationship between supraglacial debris cover and rates of ice thinning in High Mountain Asia (Kääb et al., 2012; Gardelle et al., 2013; Brun et al., 2019). One factor which is likely to be contributing to this anomaly is the presence of supraglacial features on debris-covered ice, such as ice cliffs and meltwater ponds. These features enhance localised melt rates and therefore partially offset the effects of reduced surface melting on ice thinning rates in debris-covered areas (Sakai et al., 1998; Brun et al., 2018; Miles et al., 2018). Another factor that is hypothesised to play a role in the debris anomaly is the reduced emergence velocity of debris-covered glaciers (Nuimura et al., 2011; Banerjee, 2017), leading to greater rates of ice-surface lowering compared to clean-ice glaciers. This surface lowering counteracts against the reduced ice-thinning rate in debris-covered areas, therefore potentially contributing towards the similar rates of thinning which have been observed on both debris-free and debris-covered glaciers (Nuimura et al., 2011; Banerjee, 2017; Nuimura et al., 2017).

The previously-observed ice-surface-elevation changes are a result of a combination of both SMB and ice dynamics, as well as other processes such as basal melting, internal accumulation and calving (for lake-terminating glaciers) (Cuffey and Paterson, 2010). Therefore, producing regional distributed SMB observations is critical for separating signals of climate and ice flow dynamics and better constraining the region-wide influence of debris cover in glaciological models. Several studies have shown that using the mass conservation principle, it is possible to disentangle these contributions towards ice-surface-elevation changes (Nuimura et al., 2011; Berthier et al., 2012; Nuimura et al., 2017; Brun et al., 2018; Rounce et al., 2018). Here, we present a methodology to calculate SMB for a larger sample of glaciers across multiple regions, using recently-produced spatially-extensive remote sensing datasets, based on the principle of mass conservation. All of the terms of the mass conservation principle are estimated from remote-sensing datasets (Dehecq et al., 2015; Brun et al., 2017) and simulated ice-thickness data (Farinotti et al., 2019). After isolating the contribution

of SMB towards ice thinning, we investigate the contrasting altitudinal patterns of SMB on debris-covered and clean-ice glaciers at a regional level.

3.3 Materials and methods

3.3.1 Overview

Using a mass-continuity approach, we combined existing remote-sensing observations and simulated datasets to derive spatially-distributed estimates of mean SMB over a total glaciated area of ~2000 km^2 within the Pamir-Karakoram-Himalaya. Our computations were performed for 25 glaciers within these regions. We divided each glacier into sections of ~2 km in length (Figure 3.S1). For each section, we computed the ingoing and outgoing ice fluxes from existing feature-tracking-derived ice velocities (Dehecq et al., 2015) and simulated ice thickness (Farinotti et al., 2019) (see Section 3.3.2). We calculated mean elevation change for each section from previously-derived geodetic measurements (Brun et al., 2017) and, based on mass continuity, constrained the contribution of SMB. Using surface digital elevation models (Farr et al., 2007) and existing simulated debris-thickness maps (Kraaijenbrink et al., 2017), we analysed the dependence of SMB on elevation and debris thickness. We used breakpoint analyses to determine the elevations of transition points between different altitudinal SMB gradients for each glacier, and applied weighted regression models to determine the altitudinal SMB gradients below and above these elevations.

Our mean SMB estimates were generated for the period 2000-2015, which aligns with the periods of the input datasets (see Section 3.3.2). We carried out our analyses for five regions within High Mountain Asia (Figure 3.1), which were chosen based on mutual availability of ice-surface velocity and elevation-change data, and to cover a range of meteorological and environmental conditions. The mean percentage debris cover for each region, computed from an existing global debris-cover-extent dataset (Scherler et al., 2018), is shown in Figure 3.1. The largest glaciers within each region were included in our analyses (Figure 3.S1), as smaller glaciers ($<$ ~ 10 km in length) do not provide a sufficient number of measurements to compute SMB

gradients. The glacier-wide coverage of our SMB calculations was dependent on the availability of ice velocity data, which was often limited in coverage in high-altitude accumulation areas. We used our final SMB results to investigate the influence of supraglacial debris cover on altitudinal SMB gradients at a regional scale.

3.3.2 Data

The ice velocities used in this study cover the period 1999-2015 at 120 m resolution and were previously produced using semi-automated feature tracking, applied to Landsat multispectral satellite imagery (Dehecq et al., 2015). The existing ice-surface-elevation change dataset used in this study was derived from differencing

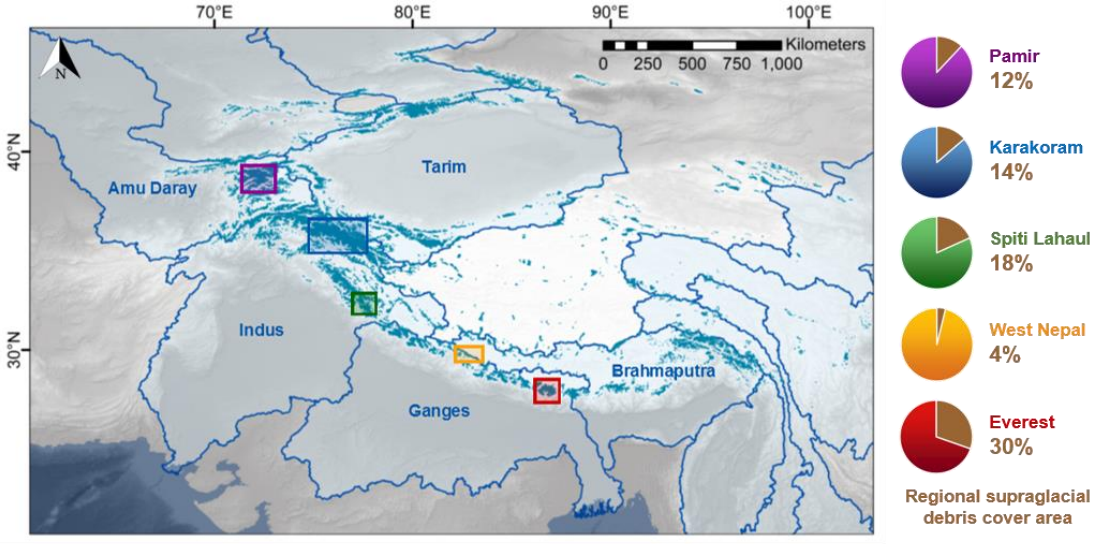

Figure 3.1 Regions of study across High Mountain Asia. Coloured boxes show the five regions for which surface mass balance is computed: Pamir (purple), Karakoram (blue), Spiti Lahaul (green), West Nepal (orange) and Everest (red). Pie charts on right show the mean percentage of ice covered by debris (computed from an existing debris cover distribution dataset for 2013-2017 (Scherler et al., 2018) for the glaciers analysed within each of the five study regions. Turquoise shaded areas show the glaciers from the Randolph Glacier Inventory v6.0 (RGI, 2017). Blue outlined areas show the major river basins (The Global Runoff Data Centre, 2020) which drain meltwater from the glaciers in High Mountain Asia.

of digital elevation models produced from ASTER optical satellite stereo imagery (Brun et al., 2017), and provides coverage for 2000-2016 at a 30 m resolution. We note that we used this ice-surface-elevation dataset (Brun et al., 2017) rather than the recently-released compilation (Shean et al., 2020), because the former aligns more closely with the temporal coverage of the ice velocity dataset. As a consequence, the

SMB dataset which we produced in this study is representative of the mean SMB for the period 2000-2015, which is covered by both the ice velocity and ice-surface-elevation change datasets. The existing simulated ice thicknesses used in this study are part of a global dataset, which was produced using an ensemble of models based on ice-thickness inversion from surface characteristics (Farinotti et al., 2019). The surface elevation data used in this study are from SRTM 1 Arc-Second Global digital elevation data, collected in 2000 (Farr et al., 2007). The existing debris thickness dataset used in this study has a 30 m resolution and was simulated from thermal infrared Landsat 8 satellite imagery (2013-present) (Kraaijenbrink et al., 2017). This dataset was selected for use as it is the only regional dataset providing consistent coverage of debris thickness across all five study regions.

3.3.3 Computing cross-sectional ice fluxes

Cross-sectional ice fluxes were computed from ice velocities (Dehecq et al., 2015) and ice thicknesses (Farinotti et al., 2019). Cross-sectional transects between each glacier section were demarcated with two points at the lateral edges of the glacier, with transects distributed at intervals of approximately 2 km along the length of each glacier. A spacing of approximately 2km was chosen as a compromise between providing a sufficient number of data points to establish trends, and averaging over a sufficiently long along-flow distance to prevent large correlations and potentially strong correlation of velocity errors. Each transect was divided into 20 segments of equal length. The normal velocity and ice thickness were interpolated to the midpoint of each segment and multiplied to compute flux. The resulting values were summed to compute total ice flux perpendicular to each transect. These calculations were carried out twice for every transect, using median velocities for two periods (1999-2003 and 2013-2015), and the results averaged. These periods align with the temporal coverage of Landsat 7 (before the Scan Line Corrector failure) and Landsat 8 (Dehecq et al., 2015). The equation for ice flux Q_t, where t is 1999-2003 or 2013-2015, is thus

$$Q_t = \sum_{i=1}^{n=20} u_i h_i l_i \tag{3.1}$$

where i is the index of the segment, u_i is the normal velocity interpolated to segment i, h_i is the thickness interpolated to the segment and l_i is the length of the segment. The calculated mean values of Q_t for each transect were used to quantify the ingoing and outgoing ice fluxes (Q_{in} and Q_{out}) for each section between every adjacent pair of transects (or group of 3+ transects, where tributaries are present). Depth-averaged velocity depends on the fraction of basal sliding which is unknown. Since the surface velocities are high for the observed glaciers, we assume that internal deformation makes a negligible contribution and hence assume that ice-surface velocity approximates to depth-averaged velocity. In order to test the impact of this assumption, we produced an additional set of surface-mass-balance estimates for the Gechongkang Glacier, based on a depth-averaged velocity equal to 90% of the surface velocity.

3.3.4 Producing sectional surface mass balance estimates

The ice-surface area between each pair of transects was digitised and quantified using glacier outlines from the Randolph Glacier Inventory v6.0 (RGI, 2017). The mean annual ice-surface-elevation change was calculated for each glacier section using glacier-wide elevation-change maps derived from digital elevation model differencing (Brun et al., 2017). The mean annual SMB between each pair/group of transects was computed using the mass-continuity method, as used by previous studies (Nuimura et al., 2011; Berthier et al., 2012; Nuimura et al., 2017; Brun et al., 2018; Rounce et al., 2018):

$$b_j = \left(\frac{dh_j}{dt} - \frac{Q_{in_j} - Q_{out_j}}{A_j}\right) \times \frac{\rho_{ice}}{\rho_{water}} \quad (3.2)$$

where b is the mean SMB in glacier section j, $\frac{dh}{dt}$ is the mean ice-surface-elevation change, A is the surface area of the section, while ρ_{ice} is the density of ice (920 kg m^{-3}) and ρ_{water} is the density of water (1000 kg m^{-3}).

3.3.5 Statistically approximating altitudinal gradients

For each glacier, we used breakpoint analysis to detect transition points between contrasting altitudinal SMB gradients and to determine the elevation at which the transition point occurs. We used linear regression models, weighted by SMB uncertainties (discussed in Section 3.3.7), to estimate the altitudinal SMB gradients below and above computed breakpoint elevations. These gradients were compared to previously-simulated SMB gradients from a regionally-calibrated global glacier model used to estimate global glacier runoff changes (Huss and Hock, 2018). We computed mean regional breakpoint elevations as the arithmetic average of breakpoint elevations for each individual glacier within the region. Similarly, we computed mean regional altitudinal gradients above and below the breakpoint elevation using the arithmetic averages of the gradients for each glacier within each region. Using our collective dataset of sectional SMB values for each region, we used arithmetic averages to approximate the mean regional SMB, partitioned by elevation bands. For each glacier section, mean surface elevation and mean debris thickness were computed from digital elevation models (Farr et al., 2007) and a simulated debris-thickness dataset (Kraaijenbrink et al., 2017) respectively.

3.3.6 Estimating equilibrium line altitudes

From our generated SMB results, we calculated the equilibrium line altitude (ELA) for each region, which describes the mean elevation at which accumulation and ablation are in balance (Cuffey and Paterson, 2010). Using our regional elevation-dependent SMB gradients, for each region we calculated the ELA value as the elevation at which SMB is equal to zero. We took the arithmetic mean of the ELA values for all glaciers analysed within each region to estimate mean regional ELAs. We compared our regional ELA values to previous estimates (Scherler et al., 2011; Kaäb et al., 2012; Gardelle et al., 2013).

3.3.7 Assessing uncertainties

We assessed uncertainty in SMB through linear error propagation from errors in input data sets, as described by (Foresta et al., 2016). The error propagation involved assessment of errors for all flux estimates via Equation 1. The uncertainties associated with the thickness and velocity components are 25% and 5-10 m a^{-1} respectively. To estimate the error of flux, ε_{Q_t}, it was assumed that both velocity and thickness uncertainty have multivariate Gaussian distributions, and that each have exponentially decaying autocorrelations with a length scale of $L = 2$ km. (This was based on the autocorrelation of elevation differences from a previous geodetic study (Gardelle et al., 2013); but overall uncertainties were not found to depend strongly on L.) Furthermore, thickness and velocity uncertainties were assumed to be independent. Error in Q_t is thus given by

$$Q = \sum_{i=1}^{n}(u_i \Delta h_i) l_i + (h_i + \Delta h_i)\Delta u_i l_i \tag{3.3}$$

where Δh_i and Δu_i are error in the interpolated velocity and thickness at a given segment i in the calculation of Q_t. As this is a nonlinear expression of Δh_i and Δu_i, linear propagation cannot be applied. Therefore, we approximated this expression as

$$\varepsilon_{Q_t} = \sum_{i=1}^{n}(u_i \Delta h_i) l_i + (h_i + 3\sigma_{h_i})\Delta u_i l_i \tag{3.4}$$

where σ_{h_i} is the standard deviation of the error. Although this replaces a random error (Δh_i) by a nonrandom term $(3\sigma_{h_i})$, there is a 99.8% probability that the error term lies within the $\pm 3\sigma$ interval (Abramowitz and Stegun, 1965).

Error was then propagated from the flux and elevation change estimates to SMB errors. The uncertainties in the computed breakpoint elevations were approximated as the standard error computed from the weighted breakpoint analyses. The uncertainties in the computed altitudinal SMB gradients were approximated as the standard errors associated with the coefficients of the weighted regression models.

3.3.8 Validating against previous findings

In order to validate our results, we firstly directly compared our computed SMB gradients to gradients previously calculated from in-situ measurements for the benchmark Chhota Shigri Glacier, in the Spiti Lahaul region. This glacier was selected for validation purposes due to data availability, meeting the minimum size requirements for inclusion in our analyses, and the existence of a record of altitudinally-varying ablation stake measurements covering a similar period to that of our study (Wagnon et al., 2007; Azam et al., 2016). We are not aware of additional field-based altitudinal SMB gradients for any of the other glaciers included in our analyses and, since small glaciers provide an insufficient number of data points to compute reliable SMB gradients from our approach, we were unable to directly compare to smaller glaciers for which previous gradients have been estimated from in-situ measurements. Therefore, we made additional comparisons to previously-computed gradients for glaciers within the vicinity of the glaciers in our analyses. These gradients were based on in-situ measurements at the Abramov Glacier in the Pamir (Barandun et al., 2015), as well as the Polkalde Glacier (Sherpa et al., 2017; Wagnon et al., 2013) and Changri Nup Glacier (Sherpa et al., 2017) in the Everest region. For further validation, we compared our computed regional ELA values to previous values (Scherler et al., 2011; Kääb et al., 2012; Gardelle et al., 2013) which were estimated using different approaches: e.g. from snowline altitudes (Gardelle et al., 2013).

3.4 Results

3.4.1 Regional surface mass balance results

The mean regional SMB results, partitioned by elevation band, indicate distinctly different elevation-dependent SMB patterns in West Nepal, in comparison to those observed in the other four regions (Figure 3.2). The results show that in West

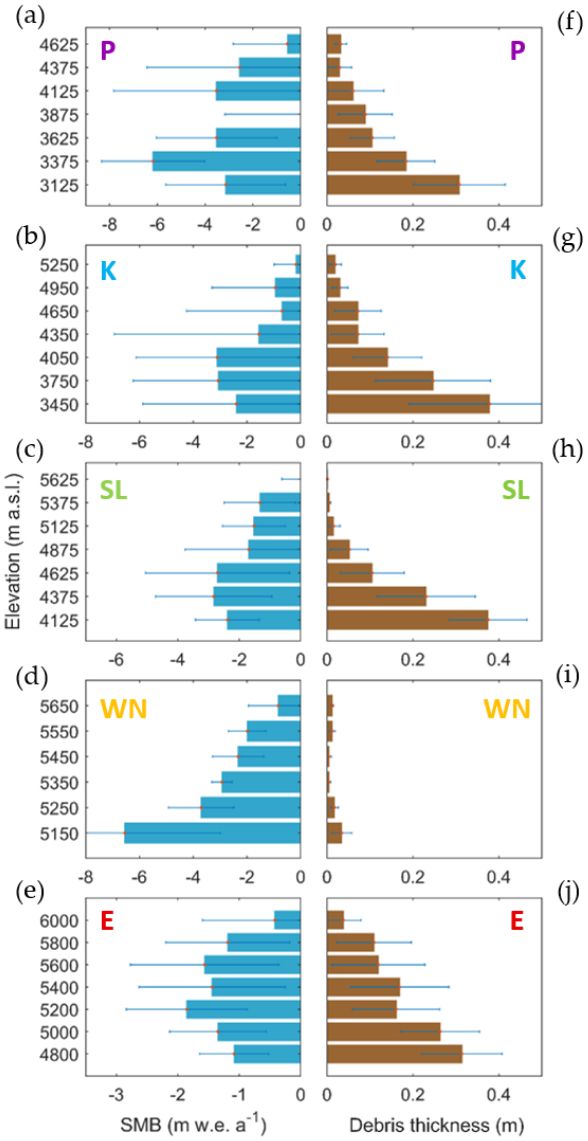

Figure 3.2. Regional elevation-dependent trends in SMB and debris thickness. (a)-(e) Regional mean surface mass balance, binned by elevation, for Pamir (P), Karakoram (K), Spiti Lahaul (SL), West Nepal (WN) and Everest (E). Horizontal bars represent standard error values. (f)-(j) Corresponding mean debris-thickness values (Kraaijenbrink et al., 2017).

Nepal, the lowest mean SMB values (i.e. greatest average melt rates) occur at the

lowest elevations (see Figure 3.2). In this region, the debris cover distribution is very low (see Figure 3.1) and the mean simulated debris thickness is < 3.5 cm in all elevation bands (Figure 3.2).

Contrastingly, our results indicate that in the Pamir, Karakoram, Spiti Lahaul and Everest regions, the lowest mean SMB values do not occur at the lowest elevations. Instead, the lowest mean SMB values occur at mid-elevations (Figure 3.2). Within all four of these regions, there is a considerably higher debris cover distribution compared to West Nepal (see Figure 3.1). In addition, the mean debris thickness is greatest in the lowest elevation band (simulated by Kraaijenbrink et al. (2017) as >30 cm) and decreases consistently with elevation.

3.4.2 Altitudinal surface mass balance gradients

Figure 3.S2 presents the individual SMB observations for every region. At a regional level, West Nepal shows a strong ($R^2 = 0.65$), linear altitudinal SMB gradient (Figure 3.S2). Meanwhile, in the Everest, Spiti Lahaul, Karakoram and Pamir regions, no clear linear altitudinal gradients were detected at a regional scale ($R^2 = 0.14$ or less; Figure 3.S2). However, breakpoint analysis of SMB gradients at a glacier-specific scale, revealed that breakpoints in altitudinal SMB profiles commonly occur within the Everest, Spiti Lahaul, Karakoram and Pamir regions (Table 3.S1). Below the elevations where these breakpoints occur, reversed altitudinal SMB gradients (where SMB decreases with increasing elevation) were commonly found. More specifically, convex breakpoints in altitudinal SMB gradients were detected for 15 out of 18 of the analysed glaciers within these four regions. Of the 15 glaciers where breakpoints were detected, 13 show negative altitudinal SMB gradients below their breakpoint elevation. Conversely, in the West Nepal region, where debris cover is very minimal (Figure 3.1), breakpoints were not detected for six of the seven analysed glaciers. Positive altitudinal gradients were found for all seven glaciers within this region.

Figure 3.3 shows examples of the segmented altitudinal SMB gradients for the glaciers we analysed in the Everest region, with the corresponding debris-thickness values shown for each SMB data point. All five glaciers transition from negative

altitudinal-SMB gradients of between -0.54 ± 0.19 and -0.06 ± 0.10 m w.e. a^{-1} $(100m)^{-1}$ at low elevations to positive altitudinal-SMB gradients of between 1.01 ± 0.39 and 1.56 ± 0.49 m w.e. a^{-1} $(100m)^{-1}$ at high elevations. The elevations at which convex breakpoints were detected range from 5180 ± 40 m a.s.l. (Ngozumpa Glacier) to 5920 ± 40 m a.s.l. (Gechongkang Glacier). As shown in Figure 3.3, debris thickness decreases from low elevations to high elevations for every glacier within this region.

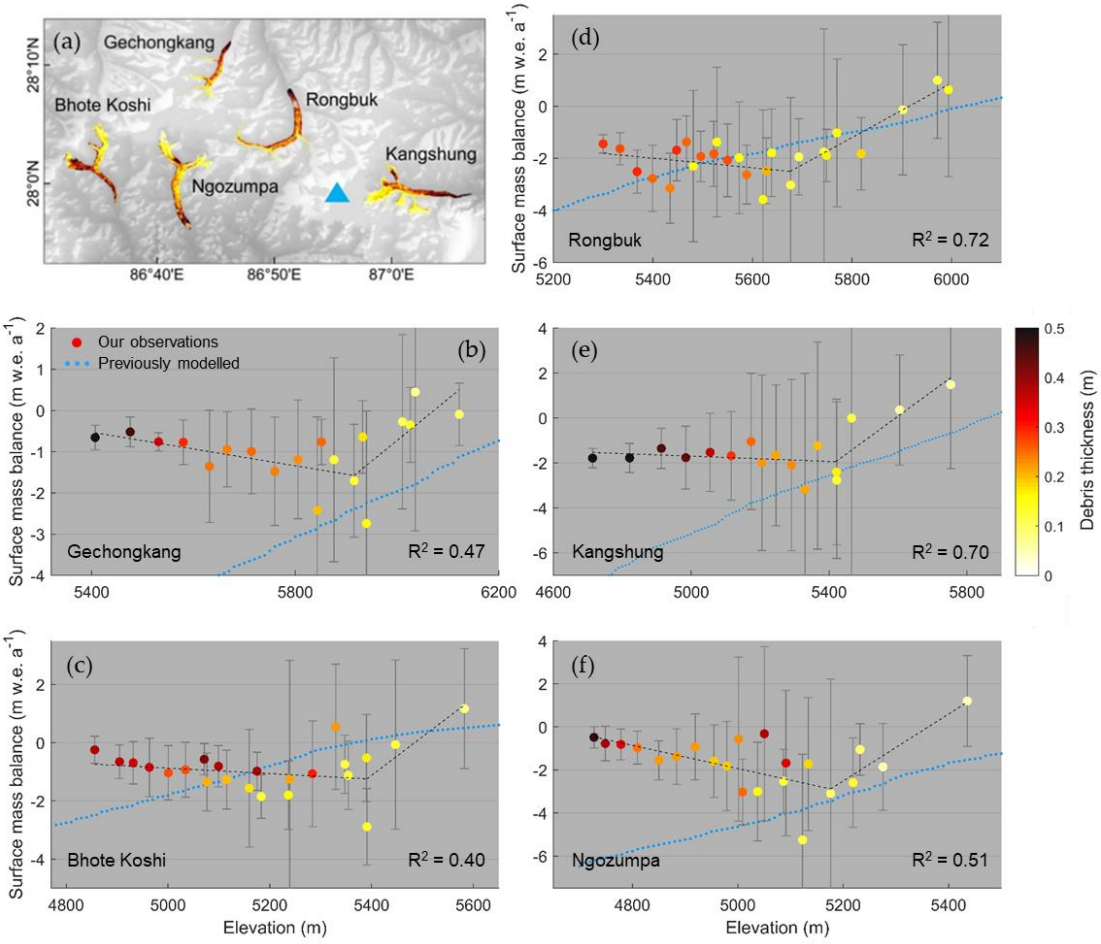

Figure 3.3. Elevation-dependent trends in SMB and debris thickness in the Everest region. (a) Locations of the five largest glaciers surrounding Mount Everest (blue triangle). (b-f) Altitudinal surface-mass-balance trends for these glaciers. Vertical bars represent (1σ) uncertainties in the computed SMB values, estimated using a linear propagation of errors. Corresponding debris thickness values (Kraaijenbrink et al., 2017) are represented on all panels with the colour scale on right. Dotted black lines represent our computed altitudinal SMB gradients, with corresponding R^2 values of the combined linear trends shown. The values of these gradients and their uncertainties are shown in Table 3.S1. Blue dotted lines represent previously-simulated SMB gradients from a regionally-calibrated global glacier model ignoring the effect of supraglacial debris (Huss and Hock, 2018).

Table 3.1 shows the mean regional breakpoint elevations and SMB gradients, which were computed from the glacier-specific results for each region. In the Pamir, Karakoram, Spiti Lahaul and Everest regions, we found regional mean SMB gradients of between -1.87 ± 2.57 and -0.17 ± 0.30 m w.e. a^{-1} $(100m)^{-1}$ below breakpoint elevations, with a transition to mean gradients of between 0.81 ± 0.34 and 1.21 ± 0.41 m w.e. a^{-1} $(100m)^{-1}$ above breakpoint elevations (Table 3.1). The results show that the regional breakpoint elevation varies considerably between regions. The lowest mean regional breakpoint elevation of 3680 ± 290 m a.s.l. is found in the Pamir while the highest breakpoint elevation of 5520 ± 50 m a.s.l. is found in the Everest region.

Table 3.1. Regional mean altitudinal SMB gradients and breakpoint elevations. The mean elevations at which convex breakpoints in the elevation-dependent SMB trends were detected from breakpoint analyses are displayed for each region, excluding West Nepal, where breakpoints were absent for the majority of glaciers (Table 3.S1). For the Pamir, Karakoram, Spiti Lahaul and Everest regions, where breakpoints were detected for the majority of glaciers (Table 3.S1), we display the mean altitudinal SMB gradients below and above the breakpoint elevation. These gradients represent the average of glacier-specific gradients computed from breakpoint analyses (Table 3.S1) within each region, and exclude glaciers where breakpoints were not detected. For these regions, we also report the mean R^2 values arising from the breakpoint analyses, excluding glaciers where breakpoints were not detected. For West Nepal, where breakpoints were not detected for the majority of glaciers, we display the mean continuous altitudinal gradient (and its associated R^2 value), which represents the average of the glacier-specific gradients computed from linear regression, excluding the single glacier for which a breakpoint was not detected. Error values reported are the mean standard error values associated with the gradients computed from linear regression (for West Nepal) and breakpoint analyses (for the other four regions).

Region	Mean breakpoint elevation (m)	Mean elevation-dependent SMB gradient (m w.e. a^{-1} $(100m)^{-1}$)		
		Below breakpoint elevation	Above breakpoint elevation	R^2 value
Pamir	3680 ± 280	-1.87 ± 2.57	1.01 ± 0.88	0.47
Karakoram	3860 ± 220	-1.04 ± 2.08	1.05 ± 0.59	0.22
Spiti Lahaul	4890 ± 100	-0.17 ± 0.30	0.94 ± 0.55	0.63
West Nepal	Not found	1.18 ± 0.41		0.74
Everest	5520 ± 50	-0.21 ± 0.18	1.21 ± 0.41	0.56

Our results also indicate considerable intra-regional variability in both the breakpoint elevation and the magnitude of the reversed gradients within each of the Everest, Spiti Lahaul, Karakoram and Pamir regions, with the latter ranging over as

much as two orders of magnitude (Table 3.S1). This variability precludes any clear region-wide elevation-dependent SMB gradients in these regions (as opposed to in West Nepal, Fig A2). We do see more conformity in above-breakpoint mass-balance gradients, however (Fig. A2).

3.4.3 Equilibrium line altitudes

From our regional mean altitudinal SMB gradients (Table 3.1), we estimate regional ELA values of between 4490 ± 140 m (Pamir) and 5700 ± 60 m (Everest), as shown in Figure 4. Our ELA values generally increase from the northwest to the southeast of the mountain belt. The exception to this trend is that we observe a slightly higher ELA in West Nepal than in Everest to its southeast. A comparison of our ELA values against previous estimates (Scherler et al., 2011; Kääb et al., 2012; Gardelle et al., 2013) is shown in Figure 3.4. The uncertainty range of all of our estimated ELA values fall within the error bounds of the ELA values previous estimated from snow line altitudes (Gardelle et al., 2013).

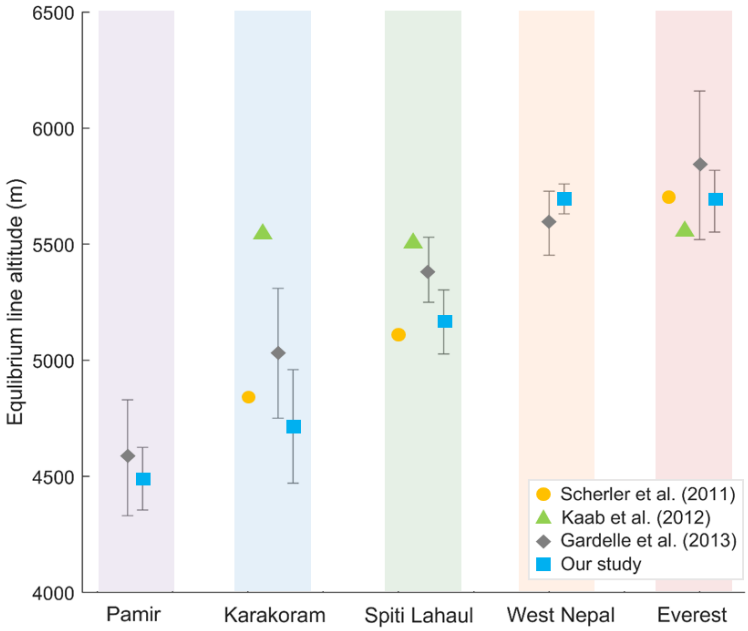

Figure 3.4. Regional equilibrium line altitudes in Pamir-Karakoram-Himalaya. Coloured symbols show regional mean equilibrium line altitudes (ELAs) calculated by previous studies (Scherler et al., 2011, Kääb et al., 2012; Gardelle et al., 2013) and our study. Coloured shaded areas enclose the ELA values for each of the five study regions, from northwest (left) to southeast (right).

3.5 Discussion

3.5.1 Influence of supraglacial debris cover

The reversed altitudinal SMB gradients observed at low elevations in the Pamir, Karakoram, Spiti Lahaul and Everest regions (Table 3.1; Figure 3.3) are likely attributable to the effects of supraglacial debris cover. As discussed previously, numerous field-based studies have shown that supraglacial debris cover significantly influences glacier melt rates: a thin layer of debris enhances melt rates while a thicker layer of debris (exceeding a critical thickness of ~ 3-8 cm) reduces melt rates (e.g. Östrem, 1959; Kayastha et al., 2000; Nicholson and Benn, 2006; Shea et al., 2015). Near the termini of the glaciers in our analyses, where debris-cover is thickest, the ice surface is likely to be insulated the most. As a result, the ablation rate is reduced and the SMB is raised (Figure 3.3). As elevation increases up-glacier from the snout, debris thickness decreases, therefore reducing the insulation effect. As a result, melt rates are enhanced up-glacier from the terminus, therefore contributing towards the reversed SMB gradients (Figure 3.3). Furthermore, as the debris thins to below the critical thickness, the albedo effect is likely to dominate, therefore further enhancing melt rates and contributing towards the lowest mean SMB values being observed at mid-elevations (Figure 3.2).

The strong region-wide linear correlation between elevation and SMB for the relatively debris-free glaciers in West Nepal (Table 3.2; Figure 3.S2), suggests that where debris cover is largely absent, SMB is dominated by altitudinal climatic gradients. As a result, the lowest mean SMB values (i.e. greatest melt rates) occur at the lowest elevations in this region (Figure 3.2). The absence of negative altitudinal-SMB gradients in West Nepal also provides further evidence that the negative gradients observed in the Pamir, Karakoram, Spiti Lahaul and Everest regions can be attributed to supraglacial debris cover.

The intra-regional variations in breakpoint elevations and altitudinal gradients observed within the Pamir, Karakoram, Spiti Lahaul and Everest regions (Figure 3.3; Table 3.S1) seem to preclude any strong region-wide relationships between elevation

and SMB (Figure 3.S2), despite strong correlation at the scale of individual glaciers. This variation could potentially arise from variations in supraglacial debris coverage. Differences in debris thickness distribution, as well as local debris properties such as lithology, grainsize and moisture content, may be contributing towards the contrasting breakpoint elevations and magnitudes of reversed altitudinal SMB gradients observed within these regions. Supraglacial ice cliffs and ponds can also influence the SMB of debris-covered glaciers by creating localised areas of enhanced melting (Sakai et al., 1998; Banerjee, 2017; Brun et al., 2018; Miles et al., 2018). Therefore, it is possible that these features could also partially explain the heterogeneity observed between debris-covered glaciers. However, this is only speculative, and further detailed investigations of relationships between debris characteristics and altitudinal SMB gradients are required to gain a better understanding of these variations in reversed gradients.

3.5.2 Contribution of glacier dynamics

Our results enabled us to separate the relative contributions of SMB and ice dynamics towards ice-surface thinning. There is a considerable difference between our SMB estimates (black dotted line, Figure 3.5) and observed ice-surface-elevation change (white dotted line). This difference represents the ice emergence velocity calculated from the mass convergence/divergence. At low elevations, where we observe a low ablation rate, the emergence velocity is also low (Figure 3.5), as also indicated by previous studies (e.g. Rowan et al., 2015; Anderson and Anderson, 2016; Banerjee, 2017; Brun et al., 2018). This can be explained by the low slope and velocity gradient that are characteristic of the stagnant tongues of debris covered glaciers. Further up-glacier near the breakpoint elevation, where melt rates are high, the emergence velocity is also high (see Figure 3.5). This is a consequence of the mass convergence at the transition between the stagnant tongue and the steeper debris-free part of the glacier. The reversed SMB gradient in the lower part of the glacier likely helps to maintain this mass convergence, by causing an inflexion of the glacier surface at its middle elevation. As a consequence, the surface elevation change, which is the sum of these two opposite processes of melt and emergence, shows a smooth trend along the length

of the glacier, as observed by geodetic studies. Our results demonstrate the importance of ice dynamics in explaining the apparent contradiction between the reversed altitudinal SMB gradients expected on debris-covered ice and the relatively stable/positive altitudinal ice-surface-elevation-change gradients observed by geodetic studies.

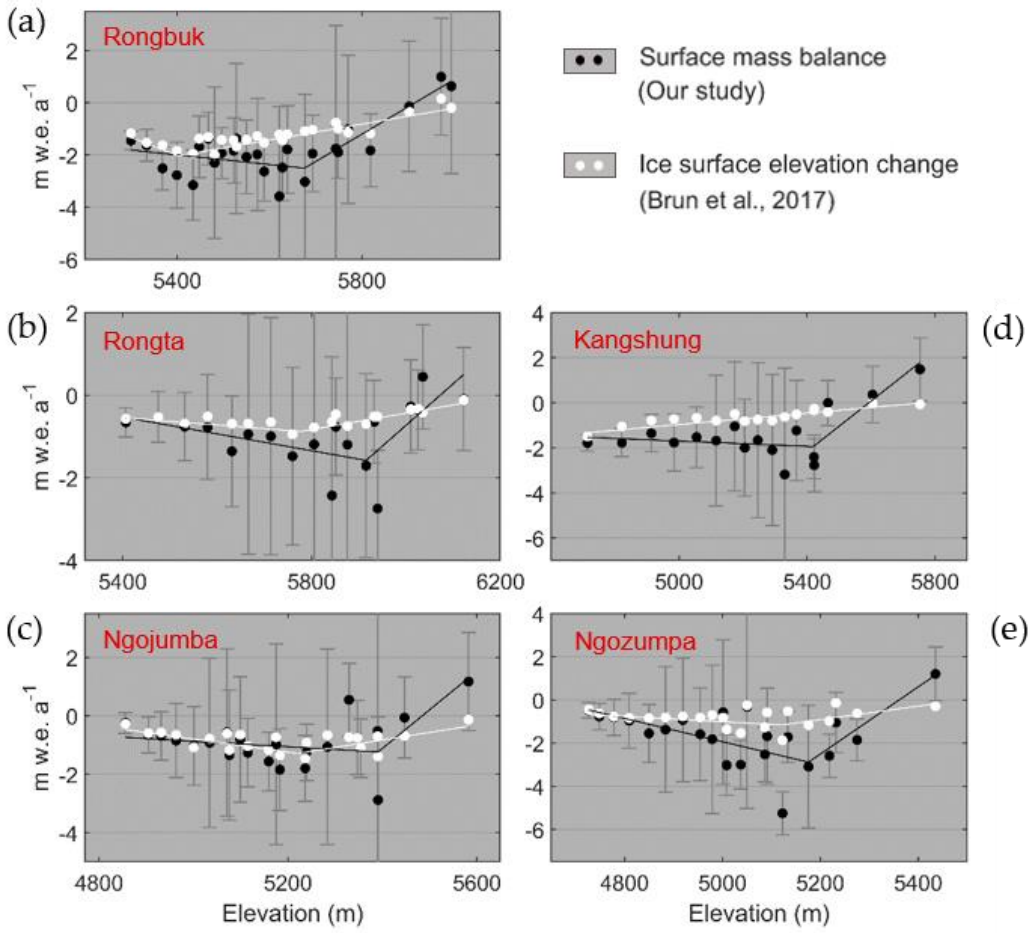

Figure 3.5. Comparison of surface mass balance and ice-surface-elevation change. (a)-(e) show the contrasting altitudinal patterns of SMB (black) and ice-surface-elevation change (white) for the five largest glaciers surrounding Mount Everest. Each point represents the mean SMB / ice-surface-elevation change value computed for each ~2km sub-section of each glacier. Vertical bars represent (1σ) uncertainties in the computed SMB values, estimated using a linear propagation of errors.

3.5.3 Role of glacier surging

Referring to a recent inventory of surging glaciers (Sevestre and Benn, 2015), all of the glaciers which we have analysed in the Pamir and Karakoram are surge-type

glaciers or have been exhibiting large velocity change during the study period. Surging behaviour can result in temporal variability in ice thickness and velocity (e.g. Meier and Post, 1969; Paul, 2020), therefore it is likely that this behaviour may be complicating the SMB trends and contributing towards the generally weaker R^2 values in the Pamir and Karakoram. An implicit assumption of our study is that the ice fluxes are in balance with the SMB gradient, but this is not the case for surging glaciers. Further investigation is required in the future in order to isolate signals of glacier surging, allowing us to gain more accurate representations of altitudinal SMB gradients in regions where surge-type behaviour is occurring.

3.5.4 Validation of SMB gradients with previous in-situ measurements

For the benchmark Chhota Shigri Glacier in Spiti Lahaul, we computed an above-breakpoint altitudinal SMB gradient within 7-12% of the gradients previously measured in the field on the debris-free portion of this glacier (see Table 3.2). For Kangshung and Ngozumpa Glaciers in the Everest region, we computed above-

Table 3.2. Comparison of altitudinal SMB gradients with previous field-based findings. The altitudinal SMB gradients computed above the breakpoint elevation for selected glaciers within the Spiti Lahaul, Everest and Pamir regions are shown. Gradients previously estimated by field-based studies (Wagnon et al., 2007; Wagnon et al., 2013; Barandun et al., 2015; Azam et al., 2016; Sherpa et al., 2017) for debris-free ice in the ablation area are also shown for glaciers within these regions. The measurement periods and elevation ranges associated with each gradient are indicated. The initials provided after each SMB gradient represent Chhota Shigri (CS), Kangshung (K), Ngozumpa (N), West Changri Nup (WCN), Pokalde (P), Fortambek (F) and Abramov (A). WCN is located ~10 km east of N and ~15 km west of K. P is located ~15 km southeast of N and ~15 km southwest of K. A is located ~70 km northwest of F.

	Measurement period	Elevation range (m)	Altitudinal surface-mass-balance gradient (m w.e. a^{-1} $(100m)^{-1}$)		
			Spiti Lahaul	Everest	Pamir
Our study	2000-2016	4570-5180	0.74 ± 0.14 (CS)	-	-
		5420-5750	-	1.12 ± 0.24 (K)	-
		5180-5230	-	1.56 ± 0.49 (N)	-
		3400-4020	-	-	0.74 ± 0.90 (F)
Azam et al. (2016)	2002-2014	4400-5200	0.66 ± 0.09 (CS)	-	-
Wagnon et al. (2007)	2002-2006	4400-4900	0.69 (CS)	-	-
Sherpa et al. (2017)	2010-2015	5330-5690	-	1.47 (WCN)	-
	2009-2015	5430-5690		1.37 (P)	
Wagnon et al. (2013)	2009-2012	5500-5600	-	1.51 (P)	-
Barandun et al. (2015)	2011-2015	3720-4400	-	-	1.02 ± 0.05 (A)

breakpoint altitudinal gradients with differences of between 3% and 26% compared to previously-derived gradients for clean ice on West Changri Nup and Pokalde Glaciers, which are both located in between Kangshung and Ngozumpa Glaciers. For Fortambek Glacier in the Pamir, we computed an above-breakpoint gradient 27% lower than the field-based gradient for the Abramov Glacier, located approximately 70 km northwest of Fortambek Glacier. As shown in Figure 3.4, the ELA values estimated from our SMB gradients are comparable to those calculated by previous studies (Scherler et al., 2011; Kääb et al., 2012; Gardelle et al., 2013), and follow a similar northwest-southeast increasing trend.

3.5.5 Limitations and future directions

While the ensemble approach used to simulate ice thickness minimises errors in the input ice thickness dataset, there are still considerable uncertainties associated with ice thickness inversion (Farinotti et al., 2019). These uncertainties are likely to have an impact on the accuracy of our results and we have accounted for these errors where possible. However, the improvement of ice thickness estimations in the future will increase the potential of this approach to produce better-resolved estimates of distributed SMB.

Our approach is also part limited by the inability to sample SMB in high-altitude accumulation areas, due to larger uncertainties in ice velocities associated with feature-tracking in snow-covered areas (Dehecq et al., 2015). Additionally, it is difficult to resolve accurately the SMB gradients of small glaciers $<\tilde{}$ 10 km in length, due to poorer signal-noise relationships and a lack of sufficient data points to accurately predict SMB gradients. The coverage of high-altitude areas and smaller glaciers can be improved in the future with the improvement of optical-satellite-imagery resolution (Millan et al., 2019) and the enhancement of feature-tracking algorithms.

There are also some uncertainties associated with the depth-dependence of ice velocities used to compute SMB, which can vary in space over a single glacier. Testing our depth-averaged velocity assumption for Gechongkang Glacier indicated that

changing the depth-averaged velocity from 100% to 90% of the surface velocity, resulted in an average change of 0.05 m w.e. a^{-1} in our absolute SMB values (equivalent to an average change of 5%). Gechongkang glacier was selected for testing purposes as we produced a high number of sectional SMB estimates for this large glacier, making it optimal for comparison between different sets of SMB estimates. While the effects of this assumption are relatively small, the associated uncertainties can be reduced in future with better knowledge of spatially-distributed depth-dependences of mountain glacier velocities.

We recognise that there are some significant uncertainties associated with the debris-thickness model used in this study, associated with the coarse resolution of thermal infrared satellite imagery, as well as high temporal and spatial variabilities in surface temperatures and vertical debris-temperature profiles (Foster et al., 2012; Rounce et al., 2018). A further limitation is that since we compute the mean debris thickness for each glacier section, we do not account for small-scale variations in debris thickness, which have been demonstrated to often be highly heterogeneous (e.g. Nicholson and Benn, 2018). These local-scale variations lead to the formation of supraglacial features, which result in significant variations in melt rates over small spatial scales (Brun et al., 2018; Miles et al., 2018). As previously discussed, it is likely that these localised melt variations may be contributing towards the heterogeneity in our SMB gradients. It is also possible that the debris cover distribution and thickness may have evolved over the course of our study period (Kirkbride and Deline, 2013; Rowan et al., 2015). However, significant changes generally occur over multi-decadal timescales (Rowan et al., 2015), therefore it is unlikely that the position of the transition zone between thin debris (below the critical thickness) and thicker debris shifted significantly during our study period.

A significant challenge associated with our approach is the highly branching nature of the glaciers that we analysed. Due to the presence of many glacier tributaries, only a semi-automated approach was possible, involving manual matching of ingoing/outgoing ice fluxes with corresponding glacier tributary sections. The development of a fully-automated approach, for example using flow lines to assign

fluxes to corresponding tributary sections, would allow a greater spatial coverage of distributed SMB and an expansion of our approach to further regions across High Mountain Asia.

Due to the uncertainties associated with the datasets produced in this study, we advocate that further field-based data acquisition is critical in order to validate remote-sensing-based observations thoroughly, and to facilitate accurate upscaling of SMB estimates over wider spatial scales.

3.6 Conclusions

In this paper, we have presented an approach for producing spatially-distributed estimates of glacial surface mass balance from remote-sensing observations, based on the principle of mass continuity. We applied our approach to the largest glaciers within five key regions of the Pamir-Karakoram-Himalaya. Each glacier was divided into sections of approximately 2 km in length and, using satellite-derived ice velocities and simulated ice thicknesses, we computed the ingoing and outgoing ice fluxes for each of these sections. Using geodetic measurements, we calculated mean sectional ice-surface-elevation changes and subsequently isolated the contribution of surface mass balance towards ice thinning rates using mass continuity. Using breakpoint analyses and regression models, we produced estimates of altitudinal surface-mass-balance gradients and equilibrium line altitudes for each of the five study regions. Our results show reversed altitudinal surface-mass-balance gradients in the lower-elevation portions of debris-covered glaciers, with a transition to positive surface-mass-balance gradients at higher elevations. In contrast, our results show continuously positive altitudinal surface-mass-balance gradients on debris-free glaciers. This demonstrates that there are important differences in altitudinal ablation trends between debris-covered and debris-free glaciers which were not previously visible from geodetic mass balance datasets. These differences in surface mass balance are likely offset by differences in ice dynamics, leading to similar thinning rates for debris-covered and clean-ice glaciers being observed by remote sensing. Our results show a regional equilibrium-line-altitude spatial gradient, with values increasing from the

northwest to the southeast. In future, with the generalisation and refinement of ice-velocity measurements and glacier thickness datasets, our operational approach can be developed and applied to glacierised mountain regions worldwide, providing the opportunity to uncover regional-scale surface-mass-balance patterns in areas where scale and location create challenges in field-based data acquisition.

3.7 Supplement

Table 3.S1. Glacier-specific altitudinal SMB gradients and breakpoint elevations for all glaciers analysed. Glacier-specific results of the breakpoint analysis of elevation-dependent SMB are displayed for every glacier analysed within each of the five study regions. For each glacier, the elevation at which a breakpoint in elevation-dependent SMB occurs is shown, as well as the altitudinal SMB gradient for ice at elevations below and above the breakpoint elevation. Error values reported are the standard errors associated with the breakpoint analysis and altitudinal SMB regression trends. The RGI codes for each glacier are shown, as well as the elevation ranges and areas covered by each glacier, as reported by the Randolph Glacier Inventory v6.0.

Glacier	RGI 6.0 ID	Area (km^2)	Elevation range (m)	Breakpoint elevation (m)	Elevation-dependent SMB gradient (m w.e. a^{-1} $(100m)^{-1}$)		
					Below B.P. elevation	Above B.P. elevation	R^2
Pamir							
Fortambek	13.19750	40.2	2930-6283	3400 ± 210	-2.04 ± 2.28	0.74 ± 0.90	0.27
Grumm-Grzhimaylo	13.13574	152.1	3615-6814	4020 ± 400	-1.77 ± 4.85	1.17 ± 1.12	0.24
Fedchenko	13.54431	663.7	2908-7392	3620 ± 240	-1.80 ± 0.58	1.13 ± 0.61	0.90
Garmo	13.19758	129.4	2976-6712	Not found	0.32 ± 0.13		0.34
Karakoram							
Hispar	14.04477	495.6	3110-7794	4230 ± 120	-0.62 ± 0.34	1.34 ± 0.72	0.23
Biafo	14.00005	559.8	3045-7148	3560 ± 310	-1.65 ± 4.00	1.50 ± 0.91	0.29
Baltoro	14.06794	809.1	3385-8569	3790 ± 230	-0.84 ± 1.89	0.30 ± 0.14	0.15
Siachen	14.07524	1078.0	3596-7579	Not found	-0.48 ± 0.06		0.75
Spiti Lahaul							
Samudra Tapu	14.15613	80.0	4237-6098	4750 ± 220	0.27 ± 0.48	0.97 ± 0.32	0.48
Bara Shigri	14.15447	112.4	3931-6309	5460 ± 90	0.02 ± 0.03	1.26 ± 0.75	0.58
Tichu Glacier	14.16068	24.8	4154-5875	4770 ± 50	-0.02 ± 0.08	0.78 ± 0.37	0.49
Sara Umga	14.16065	33.2	3835-5994	Not found	0.31 ± 0.10		0.39
Chhota Shigri	14.15990	16.8	4280-5764	4570 ± 50	-0.93 ± 0.59	0.74 ± 0.14	0.96
West Nepal							
CN5O257E0002	15.11019	20.8	5032-6333	Not found	0.59 ± 0.17		0.75
CN5O257D0011	15.11003	28.6	5185-6635	Not found	1.41 ± 0.53		0.59
CN5O257D0018	15.10994	29.9	5107-6501	Not found	2.36 ± 0.86		0.78
CN5O257D0003	13.26906	6.5	5355-6466	Not found	0.71 ± 0.25		0.74
CN5O257D0006	15.11011	7.2	5285-6399	Not found	0.47 ± 0.17		0.80
CN5O257D0001	13.26909	3.6	5387-6222	Not found	1.54 ± 0.45		0.75
CN5O257D0005	13.26904	7.2	5308-6252	5590 ± 20	0.03 ± 0.41	4.73 ± 1.02	0.98
Everest							
Rongbuk	15.09991	73.2	5155-7947	5680 ± 40	-0.18 ± 0.13	1.05 ± 0.20	0.72
Ngozumpa	15.03473	61.1	4702-8181	5180 ± 40	-0.54 ± 0.19	1.56 ± 0.49	0.51
Kangshung	15.09803	64.4	4587-8799	5420 ± 50	-0.06 ± 0.10	1.12 ± 0.24	0.70
Bhote Koshi	15.03422	27.2	4787-6550	5390 ± 70	-0.09 ± 0.09	1.33 ± 0.71	0.40
Gechongkang	15.09921	47.1	5328-7927	5920 ± 40	-0.20 ± 0.39	1.01 ± 0.39	0.47

3.7. SUPPLEMENT

Table 3.S2. Regional ELA estimates. Estimated ELAs (and standard errors) computed in this study are shown for each of the five study regions. Other previous estimates for these regions are also shown.

	ELA estimates (m)			
	Our study	Gardelle et al. (2013)	Kääb et al. (2012)	Scherler et al. (2011)
Pamir	4490 ± 140	4580 ± 250	-	-
Karakoram	4720 ± 240	5030 ± 280	5540	4845
Spiti Lahaul	5170 ± 140	5390 ± 140	5500	5103
West Nepal	5700 ± 60	5590 ± 138	-	-
Everest	5690 ± 130	5840 ± 320	5550	5700

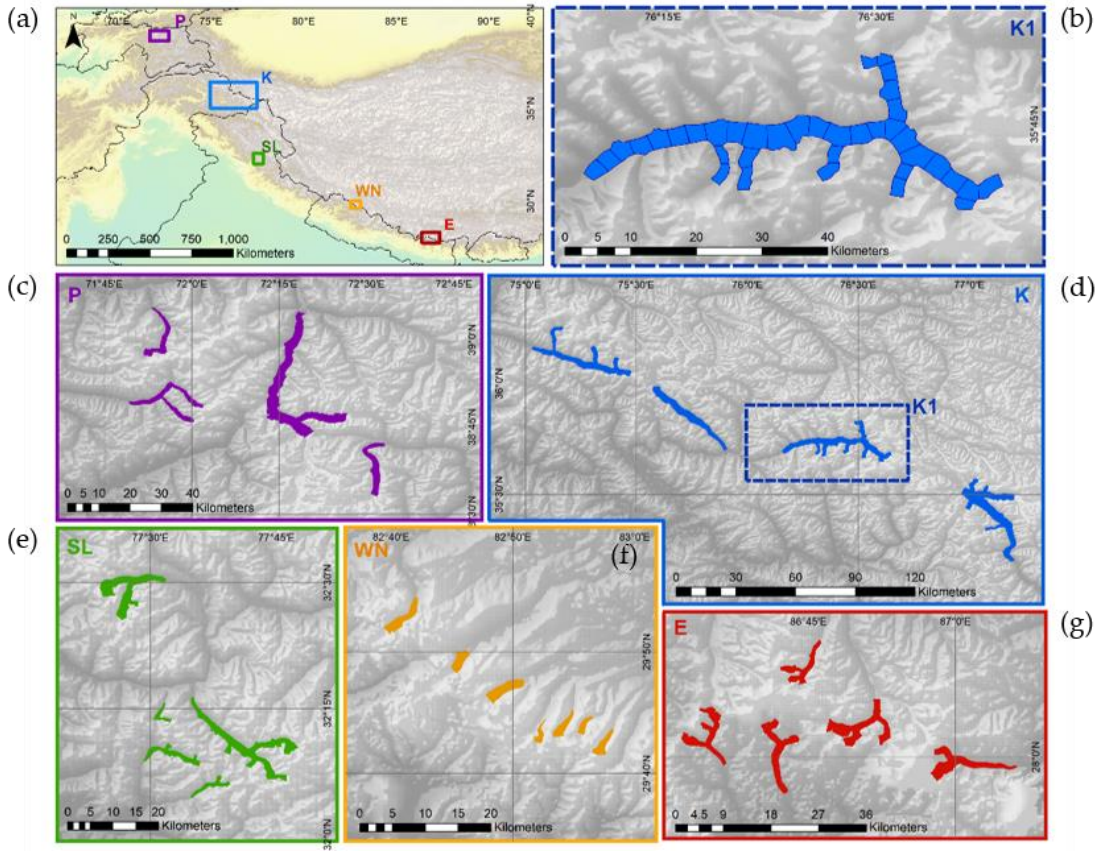

Figure 3.S1 Detailed breakdown of study sites and glacier sampling method. The coloured areas in (c)-(g) show the glacier areas which were monitored in each of the five study regions shown in (a). Labels P, K, SL, WN and E denote Pamir, Karakoram, Spiti Lahaul, West Nepal and Everest. (b) shows an example of the flux gates (black cross-sectional lines) used for Baltoro Glacier, shown in subset K1 in (d). For the area between each set of two or more flux gates (depending on the presence of tributaries), SMB is computed using the mass continuity method. Background DEMs are from Shuttle Radar Topography Mission.

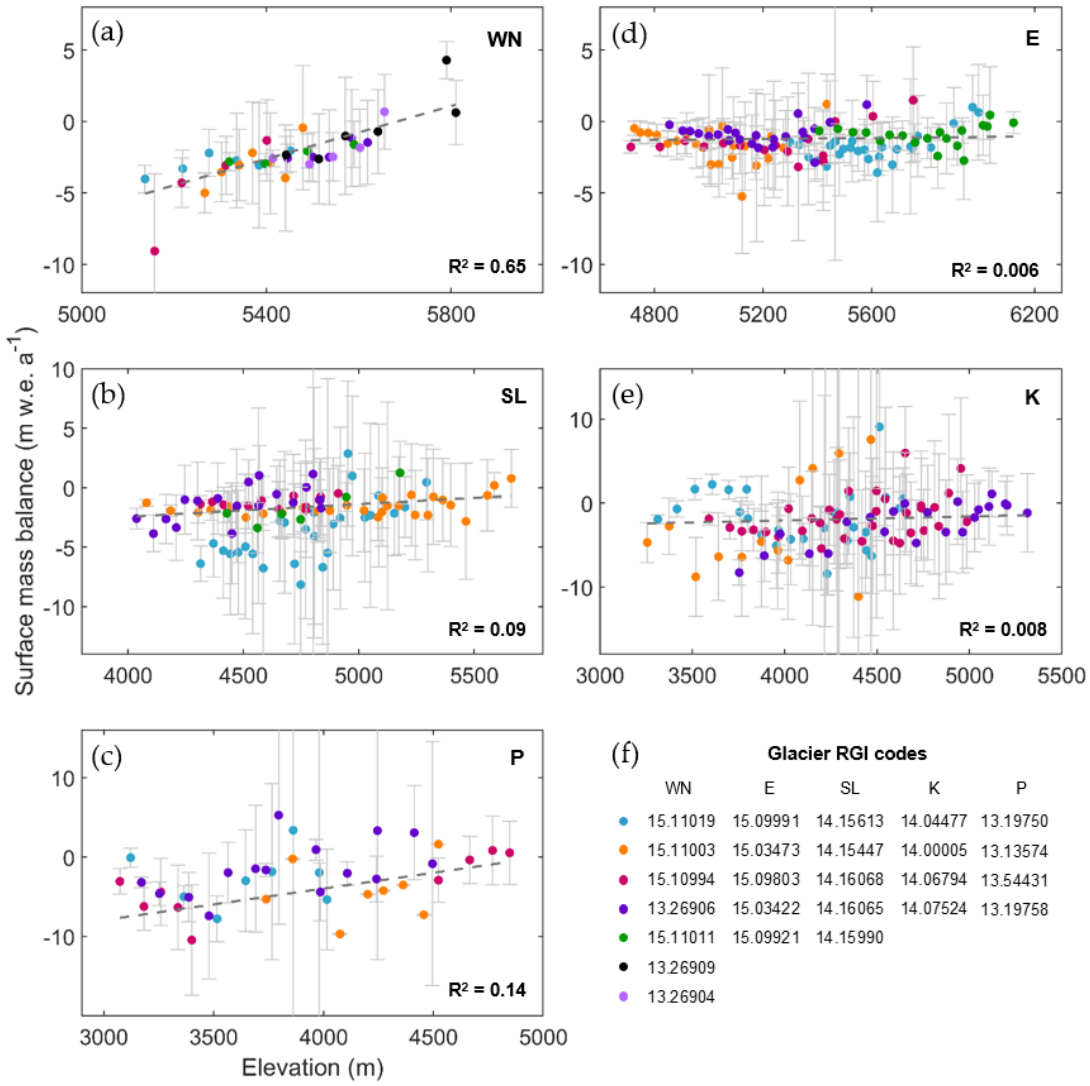

Figure 3.S2 Detailed breakdown of glacier-specific SMB observations within each region. Elevation-dependent SMB observations for every glacier analysed within West Nepal (WN), Everest (E), Spiti Lahaul (SL), Karakoram (K) and Pamir (P) are shown in (a)-(e). Each glacier within each region is shown in a different colour. RGI codes for each glacier and its corresponding colour are shown within the legend in (f). Error bars show uncertainties associated with SMB estimates. Dashed grey lines show regional simple linear regression trends, which were calculated from all points combined within each region and weighted by SMB uncertainties. The R^2 values associated with each linear regression trend are also shown.

Chapter 4

Using thermal UAV imagery to simulate distributed debris thicknesses and sub-debris melt rates at Llaca Glacier, Cordillera Blanca, Peru

This chapter tests the use of UAV-derived thermal imagery to simulate the spatially-distributed thickness of the supraglacial debris layer. Additionally, using the debris thickness produced, distributed sub-debris melt rates are simulated for a portion of Llaca Glacier tongue, to investigate the potential role of debris cover in modifying downstream hydrological discharge. This work was conducted in partnership with the project CASCADA (CAscading impacts of peruvian glacier Shrinkage on biogeochemical Cycling and Acid Drainage in Aquatic ecosystems), funded by the Newton Fund, the Natural Environmental Research Council (NERC) and Consejo Nacional de Ciencia, Tecnología e Innovación Tecnológica (CONCYTEC). Additionally, this work involved collaboration between The University of Edinburgh, Victoria University of Wellington, Universidad Peruana Cayetano Heredia and the University of Bristol.

Paper details: Bisset, R.R., Nienow, P.W., Goldberg, D.N., Wigmore, O., Loayza-Muro, R.A., Wadham, J.L., Macdonald, M.L., Bingham, R.G. (2021) Using thermal

UAV imagery to simulate distributed debris thicknesses and sub-debris melt rates at Llaca Glacier, Cordillera Blanca, Peru. *Journal of Glaciology* (in review).

Author contributions: I designed the study, with support from P.W. Nienow, D.N. Goldberg and R.G. Bingham. I planned and conducted the UAV surveys, with advice from O. Wigmore and field support from M.L. Macdonald. and R.A. Loayza-Muro. I processed and analysed the data and wrote the manuscript, which was edited by all co-authors.

4.1 Abstract

Supraglacial debris cover regulates the melt rates of many glaciers in mountainous regions around the world, thereby modifying the availability and quality of downstream water resources. However, the influence of supraglacial debris is often poorly parameterised within glaciological models, due to the absence of a technique to provide high-precision, spatially-continuous measurements of debris thickness. Here, we use high-resolution UAV-derived thermal imagery, in conjunction with local meteorological data, visible UAV imagery and vertically-profiled debris temperature time-series, to simulate the spatially-distributed debris thickness across a portion of Llaca Glacier in the Cordillera Blanca of Peru. Based on our results, we simulate daily sub-debris melt rates over a 3-month period during 2019. We demonstrate that, by effectively calibrating the radiometric thermal imagery and accounting for temporal and spatial variations in meteorological parameters during UAV surveys, thermal UAV data can be used to better represent the highly heterogeneous patterns of debris thickness and sub-debris melt on debris-covered glaciers. Additionally, our results indicate a mean sub-debris melt rate nearly three times higher than the mean melt rate simulated from satellite-derived debris thicknesses, emphasising the importance of acquiring further high-precision debris thickness data for the purposes of investigating glacier-scale melt processes and calibrating regional melt models.

4.2 Introduction

More than a quarter of the Earth's tropical glaciers are located in the Cordillera Blanca mountain range of Peru (RGI 6.0, 2017; Figure 4.1). The meltwater from these Peruvian glaciers feeds into the Rio Santa river basin, providing water resources to ~250,000 people living in the Ancash region of Peru (Mark et al., 2010). The glaciers of the Cordillera Blanca have shown consistently negative mass balances and significant reductions in spatial coverage over the past decades. For example, Silverio and Jaquet (2017) reported that the total area covered by these glaciers shrunk by 46% between 1930 and 2017, while Veettil (2018) indicated an area loss of 33.5% between 1975 and 2016. Rabatel et al. (2012) found an average mass balance of -0.76 m w.e. a^{-1} between 1976 and 2010, while Seehaus et al. (2019) reported a mass balance of -0.236 ± 0.042 m w.e. a^{-1} between 2000 and 2016. Glacial retreat in the Cordillera Blanca is impacting agriculture and drinking water supplies in the region not only by modifying the quantity of water available, but also negatively impacting the water quality via acid rock drainage due to enhanced weathering of metal- and sulphide-rich bedrock (Fortner et al., 2011; Guittard et al., 2017; Mark et al., 2017). Many of the glaciers within this region are mantled with a layer of supraglacial debris (Seehaus et al., 2019), which originates from glacial headwalls and is transported englacially to the ablation zone, where it re-emerges due to surface melting and emergent ice flow (Kirkbride and Deline, 2013; Rowan et al., 2015). Supraglacial debris is likely to be impacting both the retreat rate and the melt rate of these glaciers, thereby influencing downstream water toxification and long-term water resource depletion.

A key factor controlling the melt rate of debris-mantled glaciers is the supraglacial debris thickness. Previous studies have shown that if the debris layer is thinner than a critical thickness, sub-debris melt rates are enhanced while, if the debris layer is thicker than the critical thickness, sub-debris melt rates are reduced through ice-surface insulation (e.g. Östrem, 1959; Nicholson and Benn, 2006; Vincent et al., 2016; Anderson et al., 2021). Furthermore, supraglacial ice cliffs and

meltwater ponds, which are often abundant on debris-covered glaciers, create localised areas of enhanced ablation, further complicating the melt patterns on debris-covered glaciers (e.g. Sakai et al., 2000; Buri et al., 2016; Steiner at al., 2018). As the thickness of the debris layer and the presence of supraglacial features can change significantly over small spatial scales (e.g. Zhang et al., 2016; McCarthy et al., 2017; Nicholson et al., 2018), precisely mapping the debris thickness distribution is critical for effectively simulating their melt rates and meltwater contribution. Other debris characteristics, including moisture content, grain size and lithology can affect the relationship between debris thickness and sub-debris melt rate, by altering the thermal conductivity of the supraglacial debris (e.g. Nakawo and Young, 1981; Nicholson and Benn, 2012). Therefore, it is also important to quantify the thermal conductivity of the debris layer in order to effectively simulate sub-debris glacial melt rates with a high degree of accuracy.

Debris thickness can been measured *in situ* by manual excavation through the debris layer to the debris-ice interface (e.g. Reid et al., 2012). However, such measurements are limited in scale, due to the challenges associated with accessing and navigating the surface of debris-covered glaciers. More recently, structure-from-motion via terrestrial photogrammetry has been used to quantify the debris thickness exposed above ice cliffs (Nicholson and Mertes, 2017), while ground-penetrating radar (GPR) has been used to quantify debris thicknesses over glacier surface transects (McCarthy et al., 2017). While these techniques have yielded greater spatial coverage compared to manual excavations, neither provide spatially-complete, three-dimensional debris thickness observations. Additionally, since cliff-top debris thicknesses can differ considerably from surrounding debris thicknesses, the accuracy of debris thicknesses interpolated between observation sites is sometimes poor (McCarthy et al., 2017).

In order to provide spatially-distributed estimates of debris thickness, several previous studies have used surface energy balance modelling, combined with thermal satellite data, to derive the thermal resistance of the debris (e.g. Nakawo and Rana, 1999; Zhang et al., 2011). Since the thermal resistance is equal to the thermal

conductivity divided by the debris thickness, in-situ measurements of debris thermal conductivity can then been used, in conjunction with meteorological data, to simulate the thickness of the debris layer (e.g. Foster et al., 2012; Rounce and McKinney, 2014). Mihalcea et al. (2008a) used a different approach to simulate debris thickness from thermal satellite imagery, which involved finding the correlation between field-derived debris thickness and satellite-derived surface temperature and subsequently using this relationship to simulate glacier-wide debris thicknesses. While this method offers reduced model complexity, it does not account for spatial variations in meteorological conditions such as incoming shortwave radiation, which can significantly modify the relationship between surface temperature and debris thickness. Additionally, while the use of thermal satellite imagery enables debris thicknesses to be simulated across entire glaciers or regions, the resolution of satellite-derived thermal imagery is relatively coarse (> 60 m). As a result, sub-pixel variations in debris thickness cannot be detected, while the presence of supraglacial ice ponds and ice cliffs can lead to underestimation of debris thickness values (Rounce and McKinney, 2014).

Imagery collected by uncrewed aerial vehicles (UAVs) offers significantly greater spatial precision compared to satellite imagery. In recent years, a number of studies have used UAVs to collect high-resolution visible imagery of debris-covered glaciers in the Himalaya, in order to investigate their surface characteristics (e.g. Immerzeel et al., 2014; Kraaijenbrink et al., 2016). In the Cordillera Blanca, visible UAV surveys of Llaca Glacier were conducted in 2014 and 2015 (Wigmore and Mark, 2017). Comparison of the data collected from these surveys showed spatially-variable rates of ice loss, with the highest rates occurring where supraglacial ice cliffs and meltwater ponds were present (Wigmore and Mark, 2017). The use of UAVs to collect thermal imagery of a debris-covered glacier was demonstrated for the first time at Lirung Glacier in the Central Himalaya (Kraaijenbrink et al., 2018). The results showed high levels of spatial and temporal heterogeneity in the glacier's surface temperature, highlighting the potential drawbacks of using coarser-resolution thermal satellite data to simulate supraglacial debris thickness. The study also

demonstrated that while UAVs facilitate the collection of high-resolution thermal imagery, it is important to account for factors such as surface emissivity variations and sensor bias to derive reliable absolute surface temperatures (Kraaijenbrink et al., 2018).

Here, we test the use of UAV-derived radiometrically-calibrated thermal imagery, combined with local meteorological data, visible UAV imagery and thermal measurements taken within the debris layer, to produce centimetre-scale maps of distributed debris thickness for a portion of Llaca Glacier tongue (Figure 4.1). Following calibration of the thermal imagery, we simulate the thermal conductivity

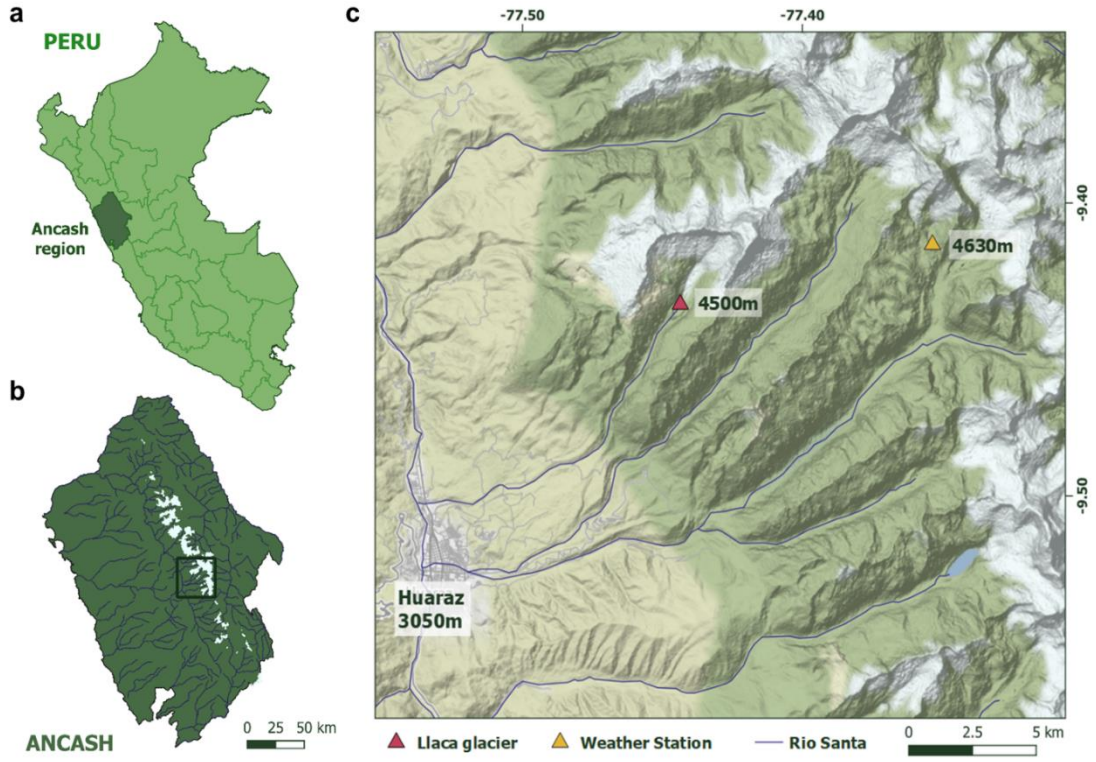

Figure 4.1. Map of the study site location. (a) Location of the Ancash region within Peru (dark green shading). (b) Location of panel (c) within Ancash. The ice-covered areas within the Ancash region are shown by the white shaded areas in (b) and (c), while the rivers are shown by the dark blue lines. The coloured triangles in (c) show the locations of Llaca Glacier (red) and the Cuchillacocha weather station (installed by Bridgewater State University) where the meteorological data used within this study were collected (yellow).

of the debris layer using a time-series of debris temperature measurements collected at varying depths within the debris layer. Spatially-distributed debris thicknesses are

estimated using a surface energy balance modelling approach which accounts for the changes in meteorological conditions over the duration of the thermal UAV surveys. Additionally, a simpler method for simulating debris thickness from UAV-derived surface temperatures, using a field-derived polynomial relation between debris thickness and surface temperature, is tested. Using the high-resolution debris thickness maps produced in this study, daily spatially-distributed melt rates are simulated over the duration of a 3-month period in 2019. The results are compared to melt rates simulated based on satellite-derived debris thicknesses in order to investigate the impact of debris thickness parameterisation accuracy on the simulated melt rates of debris-covered glaciers.

4.3 Methods

Figure 4.2 shows the workflow developed for this study, demonstrating schematically the links between the data acquisition, data processing and simulation steps of the methods, as described below.

4.3.1 Study site

Llaca Glacier (9°25'33''S, 77°26'15'') is located in the central Cordillera Blanca, a 200-km-long mountain chain situated within the wider Peruvian Andes range (Figure 4.1). Covering an area of ~ 5.1 km^2, the glacier extends from ~ 4460 to ~ 6090 m a.s.l (RGI 6.0, 2017). The debris-covered tongue of the glacier has an area of ~ 0.22 km^2 and ranges in elevation from ~ 4460 m to ~ 4620 m a.s.l.. The meltwater from Llaca Glacier contributes to the supply of water for the Ancash region, which is inhabited by approximately 250,000 people. Llaca Glacier was selected as the site for this study due to its relative accessibility in comparison to other glaciers in the region and has previously been surveyed in 2014 and 2015 (Wigmore et al., 2017).

4.3.2 UAV-based data collection

4.3.2.1 Thermal imagery acquisition

A standard DJI Phantom 4 UAV was fitted with a custom-built thermal camera system, comprising a a FLIR Vue Pro R 640 (13 mm FOV) thermal camera and a U-BLOX GNSS GPS chip. This was used to collect ~15,000 radiometric thermal images across a total survey area of approximately 0.25 km^2 (Figure 4.3a). The Phantom 4 was chosen because, unlike most commercially-available drones, it is capable of flying at high altitudes of up to 6,000 m a.s.l. Standard Phantom 4 propellers were used. The Vue Pro R camera was selected due to its ability to collect radiometrically-calibrated thermal images at high thermal precision (30 mK / 0.03 °C). The built-in visible camera was removed from the Phantom 4 in order to reduce weight and allow greater flight times.

The UAV-based thermal imagery collection was conducted within two survey zones (Z_{T1} and Z_{T2}) with differing launch point altitudes (LP_1: 4537 m a.s.l. and LP_2: 4576 m a.s.l.)(Figure 4.3a), in order to ensure that the UAV maintained a safe altitude above the sloping glacier surface, since terrain correction was not used for the UAV flights. In total, four thermal UAV surveys (S_{T1} - S_{T4}) were conducted, each at different times of day on 18-19 August 2019 (Table 1). S_{T1}, S_{T2} and S_{T4} were launched LP_1 and conducted within the bounds of Z_{T1}, while S_{T3} was launched from LP_2 and conducted over the entire extent of Z_{T2}. S_{T1}, which covered an area of 94,000 m^2, was conducted between 16.25 and 17.20 on 18 August 2019. S_{T2} was conducted between 9.30 and 10.00 on 19 August and covered an area of 87,000 m^2. The largest of the four surveys, S_{T3}, was conducted between 10.55 and 12.50 on 19 August and covered an area of 137,000 m^2. The final survey, S_{T4}, was conducted between 14.25 and 15.45 on 19 August and covered an area of 72,000 m^2.

The UAV was flown using an automated gridded flight plan, created using DroneDeploy flight planning software. As the option for terrain correction was not currently available with open-source flight planning software, the flight paths were along horizontal planes with a consistent altitude of 70 m relative to the launch

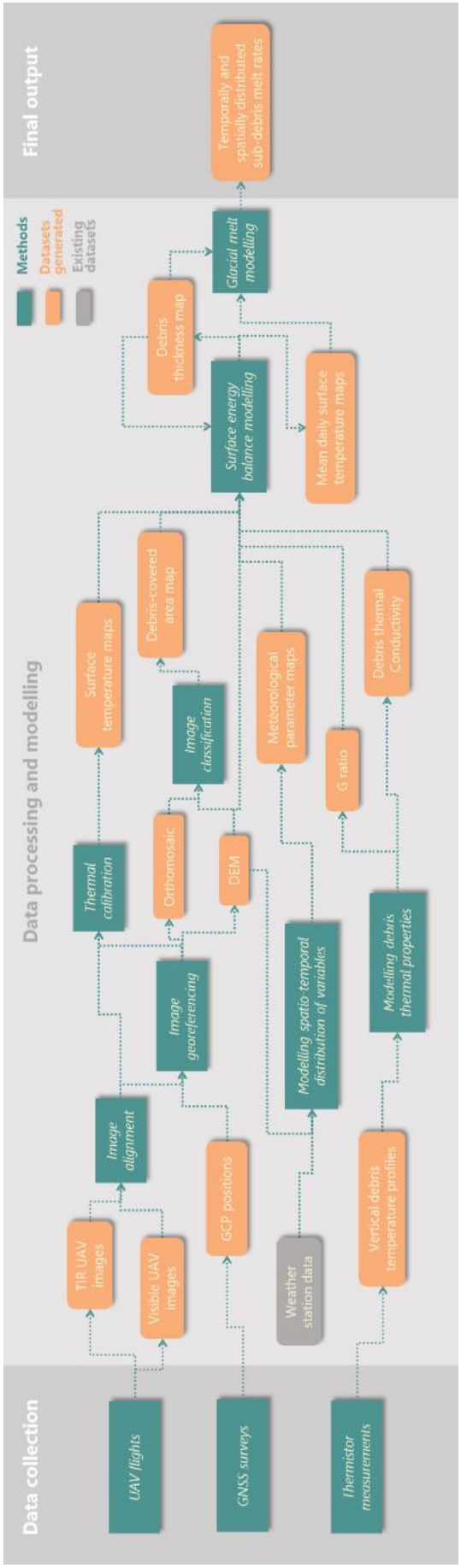

Figure 4.2. Workflow used in this study for simulating spatially-distributed, temporally-varying sub-debris melt rates.

point altitude. This flight altitude was chosen in order to provide a balance between obtaining high-resolution imagery (~ 5 cm) and providing coverage of a sufficiently large area (250,000 m^2 in total). The use of a consistent altitude relative to the launch altitude resulted in variations in the exact pixel spatial resolution and image overlap since the altitude above ground level (AGL) varied with surface topography. Since the surface elevation range of the complete survey area (~ 120 m) exceeded the average above-surface flight altitude (70 m), two separate launch points were used (Figure 4.3a).

A flight speed of 7 m s^{-1} and an image capture interval of 1 second were used, in order to provide a forward image overlap of 90 %. The flight lines, which ran perpendicular to the glacier flow direction, were spaced 7 m apart in order to provide an 80 % lateral image overlap. During each of the four thermal surveys, the UAV was returned to its launch point multiple times to conduct battery changes. At an altitude close to sea level, the DJI Phantom 4 can fly for ~ 25 minutes between battery changes. However, due to the high altitude of Llaca Glacier (approximately 4500 m a.s.l.), the air is considerably thinner and a significantly greater amount of power is required to create lift. Consequently, the average flight time between battery changes was roughly halved to ~ 12 minutes.

Many UAV-mountable thermal cameras, including the Vue Pro R 640 used in this study, use uncooled microbolometers, which are sensitive to changes in the temperature of the sensor, body and lens. While radiometric cameras apply corrections to account for these effects, Kelly et al. (2019) highlight the need to allow time for the camera to stabilise after activation. For this reason, the camera was turned on ~20 minutes prior to the start of each survey, while a couple of extra flight lines were added to the start of each survey to allow the camera to adjust to meteorological conditions experienced during flight.

For calibration purposes, images of 40 x 40 cm anodised aluminium calibration targets (Figure 4.3b) were collected with the Vue Pro R camera from an altitude of 10 m, at the beginning and end of every flight. Meanwhile, the

temperatures of these panels were also recorded using an Apogee thermal infrared (TIR) radiometer for subsequent comparison against the UAV-acquired temperatures.

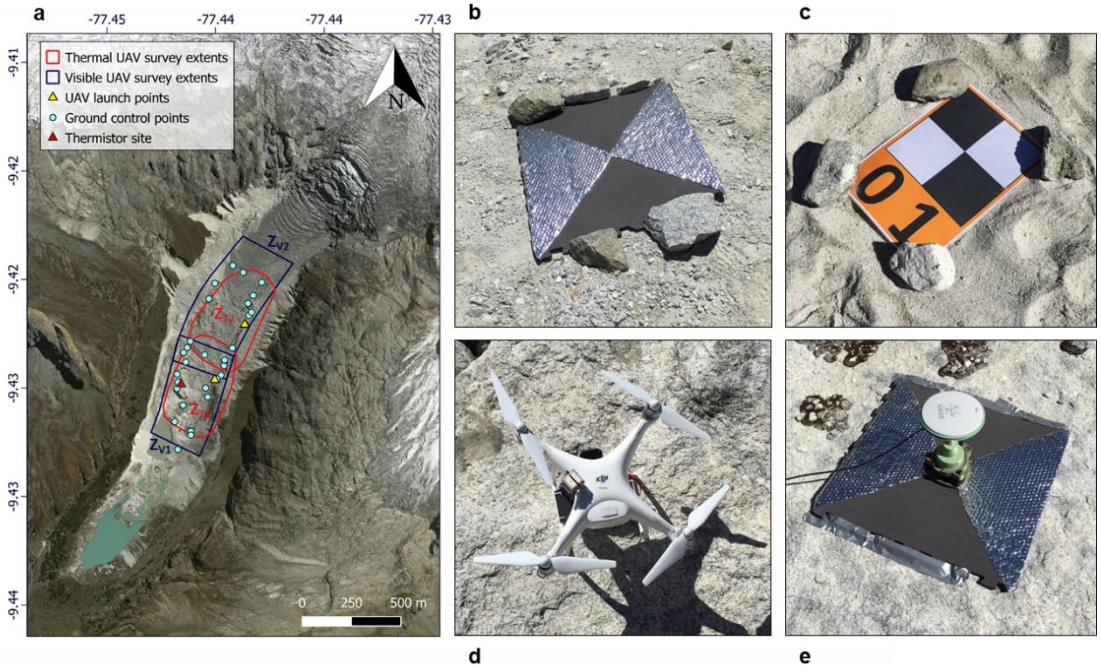

Figure 4.3. UAV survey setup at Llaca Glacier. (a) Extents of the thermal and visible UAV surveys, and locations of the two UAV launch points ground control points where GNSS data were collected and site where thermistors were installed within the debris layer. (b) and (c) Photographs of the materials used as ground control points for the thermal and visible UAV surveys respectively. (d) The custom-built UAV that was used to collect thermal imagery. (e) GNSS antenna setup for measuring the GPS position of each ground control point.

4.3.2.2 Visible imagery acquisition

Using a second DJI Phantom 4 UAV, with a built-in visible camera, 950 visible images of the glacier tongue were collected, covering a total survey area of ~325,000 m^2. Visible UAV data collection was also conducted using an automated gridded flight plan created using DroneDeploy flight planning software. An average flight altitude of 85 m was chosen, to allow the collection of high spatial resolution (2.5 cm) imagery, whilst providing coverage of a relatively large survey area. A flight speed of 5 ms^{-1} and an image capture interval of 1 second were used in order to

provide 90% forward overlap between images, while flight lines were spaced 45 m apart to allow 80% lateral image overlap.

Similar to the thermal UAV surveys, the UAV-based visible imagery collection was divided into two survey zones (Z_{V1} and Z_{V2}), with corresponding launch points LP_1 and LP_2 respectively (Figure 4.3a). In total, two visible UAV surveys (S_{V1} and S_{V2}) were conducted (one for each of the two visible survey zones). S_{V1} was conducted between 9.20 and 10.10 on 21 August 2019 and S_{V2} was conducted 10.50 and 12.20 on the same day (Table 1). Due to the slightly lighter weight of the visible camera, in comparison to the thermal camera, a slightly longer flight time of ~15 minutes could be achieved between battery changes. At the beginning of S_{V2}, there was a technical camera error, which resulted in the camera changing from a nadir 0° angle to an oblique 90° angle, resulting in a small data gap within the visible imagery.

Table 4.1. UAV survey information.

Survey name	Survey date	Survey time	Survey area (m^2)	Survey zone	Launch point
S_{T1}	18 August 2019	16:25 - 17:20	94,000	Z_{T1}	LP1
S_{T2}	19 August 2019	09:30 - 10:00	87,000	Z_{T1}	LP1
S_{T3}	19 August 2019	10:55 - 12:50	137,000	Z_{T2}	LP2
S_{T4}	19 August 2019	14:25 - 15:45	72,000	Z_{T1}	LP1
S_{V1}	21 August 2019	09:20 - 10:10	150,000	Z_{V1}	LP1
S_{V2}	21 August 2019	10:50 - 12:20	211,000	Z_{V2}	LP2

4.3.3 Ground-based data collection

4.3.3.1 Ground control data acquisition for UAV surveys

In order to georeference the thermal and visible UAV imagery, two corresponding ground control surveys were conducted. The thermal ground control

survey was carried out on 17 August 2019 (one day before the first thermal UAV survey) and the visible ground control survey was carried out on 20 August 2019 (one day before the visible UAV surveys). For each of the two ground control surveys, ground control point (GCP) targets were distributed across the UAV survey areas, with the greatest concentration of points around the perimeters of the UAV survey areas (Figure 4.3a). The GCP targets were fixed to flat surfaces using tape and rocks (Figure 4.3b-c).

For the thermal ground control survey, 20 ground control point (GCP) targets were assembled, each consisting of a 60 cm foam square with two triangles of insulated aluminium foil attached to the surface (Figure 4.3b). Foam and aluminium were chosen due to their contrasting emissivity values of ~0.6 and ~0.1 respectively, making their central point clearly distinguishable from the UAV-mounted thermal camera. For the visible ground control survey, 22 ground control point (GCP) targets, each consisting of a 30 cm x 30 cm checkboard square (Figure 4.3c), were set out across the glacier surface.

For each of the two ground control surveys, a Leica GNSS system was used to measure the GPS position of each GCP target with high (sub-cm) spatial accuracy. A fixed-location GNSS reference station was set up in a flat area ~20 m in front of the glacier terminus, in order to collect continuous GPS measurements over the complete ~8-hour duration of each ground control survey. Meanwhile, using a GNSS rover, the precise location of the centre of each GCP target was measured over a period of 5-10 minutes per target (Figure 4.3e).

4.3.3.2 Vertical debris temperature profile measurements

In order to measure vertical changes in debris temperature within the debris layer, a vertical profile of 5 thermistors, each connected to a DataHog2 data logger, was installed within the debris layer near the western margin of the glacier (Figure 4.3a). The thermistor probes were placed at depths of 5, 10, 20, 30 and 40 cm, with the 40 cm probe at the debris-ice interface. Once adjusted to local environmental conditions, the thermistors recorded temperatures at repeat intervals of 10 minutes

between 17 August 2019 00:00 and 19 August 2019 16:00. These measurements were used to simulate the thermal properties of the debris layer for integration within the surface energy balance model (Figure 4.2).

4.3.3.3 In-situ surface temperature and debris thickness measurements

An Apogee TIR radiometer was used to collect a sequence of ground-based TIR measurements at 22 points across the glacier surface, with varying supraglacial debris thicknesses. At each measurement point, three emitted TIR measurements of the debris surface were taken. Subsequently, a pit was dug through the debris layer to the debris-ice interface and the depth of the debris layer was measured. These 22 measurements were taken in close succession over a total duration of 1 hour 40 minutes (13.25 – 15.05) on 21 August, in order to minimise biases associated with temporal changes in meteorological conditions.

In order to validate the debris thickness model, an additional set of debris thickness measurements were taken, in conjunction with high-precision GPS positions measured with the Leica GNSS System. Unfortunately, due to a technical glitch with the pre-programmed UAV flights, several of these measurements were just outside the bounds of the thermal UAV survey. As a result, only three of the coupled GPS-debris thickness measurements could be used for validation of the debris thickness model.

4.3.4 UAV data processing

4.3.4.1 Producing surface temperature maps, DEMs and orthomosaics

To produce maps of surface temperature, the radiometric TIR images were processed using Pix4Dmapper software, which was selected due to its compatibility with the radiometric jpeg files collected by the Vue Pro R camera. To produce DEMs and orthomosaics, the visible images were processed using Agisoft Metashape Software. This software contains proprietary implementations of common structure-from-motion (SfM) photogrammetric workflows, and includes feature recognition, image matching, bundle block adjustment, point cloud densification and ultimately

the generation of high resolution digital surface models (DSMs) and orthomosaics. To provide accurate georeferencing, the thermal and visible GCP targets were identified within the thermal and visible UAV images and linked to the known coordinates recorded during the thermal and visible ground control surveys. To account for the effects of emissivity on the amount of TIR energy emitted by the debris surface, an emissivity value of 0.94 was assumed when converting emitted TIR values measured by the Vue Pro R to surface temperatures (Salisbury and D'Aria, 1992).

4.3.4.2 Calibrating UAV-derived surface temperature maps

Images of a blackbody calibrator (a target object with an emissivity close to 1), captured in the lab using the same Vue Pro R camera that was used in the field, were used to calibrate the surface temperature maps to account for sensor bias (Figure 4.S4). These thermal images were captured for blackbody temperatures between 5 °C and 60 °C, at 5 °C intervals. The equation of the best-fit line between measured temperature and actual temperature was used to calibrate the surface temperature values collected by the thermal camera.

The surface temperatures derived from UAV-mounted TIR cameras can be influenced by atmospheric attenuation of thermal radiance (Maes et al., 2017). Since the UAV flights were conducted across horizontal planes with constant flight heights of 4607 m a.s.l. (S_{T1}, S_{T2} and S_{T4}) and 4646 m a.s.l. (S_{T3}), the flight height above ground level (AGL) varied with surface topography. Consequently, the effect of atmospheric attenuation on measured surface temperatures is likely to have changed over the duration of the thermal UAV surveys. Since the flight height AGL is a function of elevation, a surface-altitude-dependent correction factor was applied to the thermal imagery in order to account for the effects of differential atmospheric attenuation on recorded surface temperatures. The surface-altitude-dependent correction factor was calculated based on differences between actual and recorded surface temperatures of exposed ice cliff surfaces, similar to the calibration approach used by Kraaijenbrink et al. (2018). It was assumed that exposed areas of ice cliffs

have a surface temperature of 0°C. This assumption was validated using spot measurements of surface temperature collected in the field with an Apogee TIR radiometer. Using a series of ice cliffs distributed from the lowermost to the uppermost part of each thermal UAV survey, the linear relation between the glacier surface elevation and the measured-actual ice cliff temperature difference was computed and subsequently used to correct the surface temperatures within the thermal orthomosaics (Figure 4.S4). Since the flight altitude AGL decreased continuously over the duration of each UAV survey (as the UAV gradually travelled up-glacier between sequential cross-sectional flight lines), it was assumed that this correction would also (at least partially) account for time-dependent sensor-related biases.

The accuracy of surface temperatures recorded by thermal cameras can be impacted by distortion caused by the lens optics, known as 'vignetting', where surface temperatures are slightly enhanced in the central region of each image and reduced in the outer portions of each image. It was assumed that, due to the continuously high overlap between subsequent images collected by the Vue Pro R camera, camera vignetting effects would be minimised by the averaging of temperature values during the image-stitching process and that any remaining vignetting effects, which may lower temperature values, were removed by the sensor bias correction.

4.3.5 Generating debris thickness maps

4.3.5.1 Simulating debris thermal properties

The effective conductivity of the debris was estimated at depths of 5, 10, 20, 30 and 40 cm within the debris layer, using the thermistor time-series (64-hour period following adjustment of thermistors to local environmental conditions; Section 4.3.3.2). Following the methods of Conway and Rasmussen (2000), debris thermal diffusivity K was approximated as the gradient between the first derivative of debris temperature T (K) with respect to time t (hr) and the second derivative of debris temperature with respect to depth z (m):

$$K = \frac{\dot{T}}{T''} = \frac{\left(\frac{\partial T}{\partial t}\right)}{\left(\frac{\partial^2 T}{\partial z^2}\right)} \quad (4.1)$$

Using the approximated thermal diffusivity values, the effective thermal conductivity k_{eff} was computed at each depth within the debris layer, assuming a rock density ρ_{rock} of 2700 kg m^{-3} and a heat capacity c_{rock} of 750 J kg^{-1} K^{-1} (Clark, 1966):

$$k_{eff} = K\rho_{rock}c_{rock} \quad (4.2)$$

The overall k_{eff}, which was used in the SEB model (discussed in Section 4.3.5.3), was calculated by treating the debris layer as a series of conductors corresponding to specific layers within the overall debris layer, each with different conductivities. These specific layers were: 0 – 5 cm depth (assigned the 5 cm simulated k_{eff}), 5 – 10 cm (assigned an average of the 5 and 10 cm k_{eff} values), 10 – 15 (assigned the 10 cm k_{eff}), 15 – 25 cm (assigned the 20 cm k_{eff}), 25 – 35 cm (assigned the 30 cm k_{eff}) and 35 – 40 cm (assigned the 40 cm k_{eff}). The overall k_{eff} was calculated as the arithmetic average of the k_{eff} values assigned to these layers, accounting for the relative depth of each layer. The arithmetic average was used in order to minimise skewing of the results due to a single layer with a very small or large k_{eff}.

In order to account for the nonlinearity of the vertical temperature gradient, we estimated a nonlinearity factor G_{ratio}, after Rounce and McKinney (2014). Due to the lower reliability of the thermistor measurements closest to the surface, the equation for G_{ratio} was adjusted slightly to incorporate the vertical temperature gradients for 10-20 cm and 10-40 cm depth, instead of the gradients for 0-10 cm and 0-40 cm depth used by Rounce and McKinney (2014).

$$G_{ratio} = \frac{T_{0.1m} - T_{0.2m}}{T_{0.1m} - T_d} \cdot \frac{z_d - 0.1}{0.1} \quad (4.3)$$

where $T_{0.1m}$ and $T_{0.2m}$ are the temperatures 10 cm and 20 cm below the surface, T_d is the temperature at the debris-ice interface and d is the depth of the layer.

4.3.5.2 Parameterising the spatial and temporal distribution of meteorological variables

Since the thermal UAV surveys were conducted over periods of up to 2 hours, it was necessary to account for the changing spatial distribution of incoming shortwave radiation (SW_{in}) over the duration of each survey. Firstly, the 10 cm DEM of the glacier tongue (produced from the visible UAV imagery) was joined with the ALOS 30 m DEM of the surrounding topography. The resulting joined DEM was used to simulate the spatial distribution of solar radiation across the glacier surface for 5-minute periods at 30-minute intervals over the duration of each thermal survey. Through interpolation, a SW_{in} distribution map was produced for every 5-minute period of each thermal UAV survey. Each map was divided by its maximum value to produce fractional SW_{in} maps for every 5-minute period. The SW_{in} measurements recorded by Cuchillacocha weather station (Figure 4.1) at 30-minute intervals were also interpolated to each 5-minute period within each survey. Based on the assumption that SW_{in} measured at the weather station was equal to the maximum radiation across Llaca Glacier tongue, each simulated fractional SW_{in} map for every 5-minute period was multiplied by the corresponding weather-station-derived SW_{in} value for the same period, to produce weather-station-adjusted maps of SW_{in} for every 5-minute period. Each of the thermal survey areas were split into cross-sectional segments corresponding to 5-minute flight time blocks and each segment was assigned the spatially-distributed simulated SW_{in} values associated with the corresponding 5-minute flight time block. Finally, all cross-sectional segments were merged to produce a spatially-distributed map of SW_{in}, adjusted for temporal changes in SW_{in}.

Weather station observations of air temperature (T_{air}) and relative humidity (RH) were used to simulate the temporal variations in incoming longwave radiation, LW_{in}, over the duration of the thermal UAV surveys, using the Stephan-Boltzmann law:

$$LW_{in} = \varepsilon_{eff} \sigma {T_{eff}}^4 \tag{4.4}$$

where ε_{eff} is the effective emissivity of the atmosphere, σ is the Stefan-Boltzmann constant (5.67 x 10^{-1} W m^{-2} K^{-4}) and T_{eff} is the effective air temperature. T_{eff} is represented by T_{air} at screen level. As there were clear weather conditions with no clouds during the thermal UAV surveys, the clear sky emissivity (ε_{clear}) was approximated using a parameterisation introduced by Dilley and O'Brian (1998) (equation 5). This approach has been found to provide the best parameterisation of LW_{in} over melting glaciers (Juszak and Pelliciotti, 2013).

$$\varepsilon_{clear} = \frac{a_{DO} + b_{DO}\left(\frac{T_{air}}{273.16}\right)^6 + c_{DO}\sqrt{\frac{4.65 e_a}{25 T_{air}}}}{\sigma {T_{air}}^4} \quad (4.5)$$

where e_a is the atmospheric vapour pressure (Pa), which was approximated from the altitude-corrected T_{air} and RH recorded at Cuchillacocha weather station (Figure 4.1), using the Magnus formula (Bell, 1996). a_{DO}, b_{DO} and c_{DO} are parameters from Dilley and O'Brien (1998) which have fixed values of 59.38, 113.7 and 96.96, respectively. Using this method, simulated LW_{in} values were produced at 30-minute intervals (corresponding to the frequency of weather station observations of T_{air} and RH), which were interpolated to produce simulated LW_{in} values for every 5-minutes of each thermal UAV survey. Each of these LW_{in} values was assigned to each of the corresponding cross-sectional segments of the thermal survey areas associated with each 5-minute flight time block of each survey. The cross-sectional segments produced were merged together to produce maps of LW_{in} which account for temporal variations in LW_{in} over the course of the thermal UAV surveys.

To account for altitudinal variations in T_{air} across the survey area, a spatially-dependent altitudinal correction was applied, using the UAV-derived DEM of the glacier tongue and a mean lapse rate derived from differences between values recorded at Cuchillacocha weather station (4630 m a.s.l.) and another weather station located further down the valley (3920 m a.s.l.). To account for temporal variations in T_{air}, wind speed and G_{ratio} over the duration of the thermal UAV surveys, the weather station observations (30-minute intervals) and calculated G_{ratio} (10-minute intervals) were again interpolated to every 5-minute flight time block of

each thermal UAV survey. The resulting values were assigned to the cross-sectional segments corresponding to each 5-minute flight time block of each thermal survey, to produce temporally-corrected maps of T_{air}, wind speed and G_{ratio} for incorporation within the debris thickness model.

4.3.5.3 Producing simulated debris thickness maps

Using the calibrated UAV-derived surface temperatures, alongside the spatially and temporally distributed meteorological variables parameterised in Section 4.3.5.2, debris thickness maps were produced using surface energy balance modelling, which has previously been used to simulate debris thickness from coarser-resolution thermal satellite imagery (e.g., Foster et al., 2012; Rounce and McKinney, 2014). As the surface temperature data collected between 11.55 and 12.50 on 19 August (during survey S_{T3}) were most optimal for simulating debris thickness (as discussed further in Section 4.5.1), these data were used to calculate debris thickness across survey zone Z_{T2} (Figure 4.3a), which covers an area of ~137,000 m^2.

Firstly, the ground heat flux Q_c (W m^{-2}) was calculated as:

$$Q_c = R_n + H + LE \tag{4.6}$$

where R_n is the net radiation flux (W m^{-2}), H is the sensible heat flux (W m^{-2}) and LE is the latent heat flux (W m^{-2}). The net radiation flux was calculated as:

$$R_n = SW_{in}(1 - \alpha) + \varepsilon\left(LW_{in} - \sigma {T_s}^4\right) \tag{4.7}$$

where SW_{in} is the incoming shortwave radiation (W m^{-2}), α is the albedo (dimensionless), ε is the emissivity (dimensionless), LW_{in} is the incoming longwave radiation (W m^{-2}), σ is the Stephan-Boltzmann constant (5.67×10^{-8} W m^{-2} K^{-4}) and T_s is the surface temperature (K). Debris emissivity and albedo values of 0.94 and 0.3, respectively, were assumed (Salisbury and D'Aria, 1992; Nicholson and Benn, 2012).

The sensible heat flux was calculated as:

$$H = \rho_{air}\left(\frac{P}{P_0}\right)c_{air}Au(T_{air} - T_s) \quad (4.8)$$

where ρ_{air} is the density of air (1.29 kg m^{-3}), P is the atmospheric pressure (Pa), P_0 is the atmospheric pressure at sea level (101 325 Pa), c_{air} is the specific heat capacity of air (1010 J kg^{-1} K^{-1}), A is the transfer coefficient (dimensionless), u is the wind speed recorded at the weather station (m s^{-1}) and T_{air} is the air temperature. The atmospheric pressure was computed using the barometric pressure formula and the transfer coefficient was calculated as:

$$A = \frac{{k_{vk}}^2}{\ln\left(\frac{z_h}{z_0}\right)\ln\left(\frac{z_h}{z_0}\right)} \quad (4.9)$$

where k_{vk} is the von Kármán's constant (0.41), z_h is the height of meteorological measurements (2 m) and z_0 is the surface roughness length, for which a value of 0.016 m was assumed (Rounce et al., 2014).

The latent heat flux was assumed to be zero, based on the assumption that the debris was dry.

The debris thickness d was calculated using a nonlinear model (Rounce and McKinney, 2014):

$$d = \frac{G_{ratio}k_{eff}(T_s - T_i)}{Q_c} \quad (4.10)$$

where T_i is the temperature at debris-ice interface (assumed to be 273.15 K based on the thermistor measurements).

The three in-situ coupled GPS-debris-thickness measurements within the bounds of the thermal UAV survey were used as a guide to ensure that realistic debris thicknesses were being simulated. Negative simulated debris thickness values and values more than three median absolute deviations (MADs) from the mean were assigned as no data values.

4.3.5.4 Omitting supraglacial ice cliffs and ponds from the model

Cliffs and ponds were not included in the model since the simulation approaches used to estimate debris thickness cannot be applied to areas beneath supraglacial ponds or on the surface of supraglacial ice cliffs. Cliffs were semi-automatically classified using the DEM and orthomosaic derived from the visible UAV survey. Firstly, areas with a surface slope of $>40°$ were isolated. To eliminate false detection areas, which primarily occur along the edges of large boulders where the surface gradient is high, areas with a maximum inter-pixel difference (between central pixel and surrounding pixels) of more than 40, in the brightness of the greyscale orthomosaic, were removed. Interconnected areas of less than 1 m^2 were also removed, in order to eliminate any remaining small rocks from the areas classified as ice cliffs. Finally, any boulder edges which were not successfully eliminated during the previous steps were removed manually from the ice-cliff-classified areas. As supraglacial ponds were relatively rare in comparison to ice cliffs, these features were classified using manual digitisation. Once ice cliffs and ponds had been classified, the areas covered by these features were removed from the model.

4.3.5.5 Alternative approach for mapping debris thickness from UAV-derived surface temperatures

A simpler empirical method for simulating debris thickness from UAV-derived surface temperature data was also tested. This approach involved using the 22 TIR measurements collected between 13.25 and 15.05 on 21 August, alongside the debris thickness measurements acquired at each of the 22 sites, to find the second order polynomial relation between debris thickness and surface temperature on Llaca Glacier. Based on this relation, debris thickness was simulated from the calibrated surface temperature maps derived from UAV TIR imagery of Llaca Glacier tongue. This alternative approach is based on the assumption that the relation between surface temperature and debris thickness does not change significantly within the day, which is unlikely to be true. Furthermore, this approach does not take into account the spatially and temporally varying meteorological parameters that impact surface temperature. Therefore, this alternative method was only used for the

purpose of testing how well debris thickness could be approximated using a simplified approach with fewer data requirements, as well as to allow comparison to the debris thicknesses simulated using the surface energy balance approach. A similar method was used by Mihalcea et al (2008) to calculate debris thickness from thermal satellite imagery (ASTER), based on the correlation between field-based debris thickness measurements and satellite-derived surface temperatures.

4.3.6 Simulating daily sub-debris melt rates

Distributed daily sub-debris melt rates were simulated based on the simulated debris thickness (derived from the surface energy balance modelling approach), following the method of Nicholson and Benn (2006). This method uses mean daily meteorological data, assuming that the daily mean temperature profile through the debris layer is linear and that net changes in heat storage are negligible on diurnal timescales. This method was chosen as it significantly reduces the computational resources needed to run the model and has been demonstrated to yield reliable sub-debris ablation rate estimates despite model simplification (Nicholson and Benn, 2006). Firstly, the distributed average daily surface temperatures were solved for iteratively, based on the polynomial:

$$-\varepsilon\sigma {T_s}^4 - \left(\rho_{air}\left(\frac{P}{P_0}\right)c_{air}Au + \frac{k_{eff}}{d}\right)T_s + SW_{in}(1-\alpha) + \rho_{air}\left(\frac{P}{P_0}\right)c_{air}AuT_{air} + \frac{k_{eff}T_i}{d} + \varepsilon\, LW_{in} = 0 \qquad (4.11)$$

Data from the Cuchillacocha weather station (Figure 4.1) were used to calculate mean daily meteorological parameters. Mean daily LW_{in} was calculated from T_{air} and RH (equations 4 and 5), while the spatial variability of meteorological parameters was accounted for using the following approaches. The spatial distribution of SW_{in} was simulated over a 24-hour period every 10 days between the 5 July and 5 October. Through interpolation, maps of average SW_{in} distribution were produced for every day during this 3-month period. For each day, the corresponding map of SW_{in} distribution was divided by its mean value, before being multiplied by the mean SW_{in} recorded at the weather station on that day. To account for spatial variations in T_{air}, the UAV-derived DEM was used to produce a map of altitude-

dependent T_{air}, using an environmental lapse rate of 6.5 °C km^{-1}. u and LW_{in} were assumed to be spatially-homogeneous.

Using the resulting surface temperature map, the ground heat flux was computed using equation 6 and the distributed daily melt rate M (m s^{-1}) was computed as:

$$M = \frac{Q_m}{\rho_{ice} L_f} \tag{4.12}$$

where Q_m is downward energy flux at the base of the debris layer (equal to Q_c), ρ_{ice} is the density of ice (assumed to be 900 kg m^{-3}) and L_f is the latent heat of fusion (334 kJ kg^{-1}). Negative values of M were set to 0, while values more than three standard deviations from the median were set to no data values.

In order to investigate the impact of differing simulated debris thicknesses on simulated sub-debris melt rates, the model was run for a second time using debris thicknesses simulated from satellite data (Rounce et al., 2021) and the results were compared to the sub-debris melt rates simulated in this study.

4.4 Results

4.4.1 Vertical debris temperature profiles

The debris temperatures recorded by the thermistors at depths of 5, 10, 20, 30 and 40 cm (40 cm being the debris-ice interface) are shown in Figure 4.4. The variation in debris temperature decays with increasing depth, with an average range in daily temperature of 17.9 °C at 5 cm depth compared to 0.7 °C at the debris-ice interface (40 cm depth). As depth into the debris layer increases, the times of the diurnal peaks and troughs in debris temperature are increasingly lagged. For example, there is a lag of 6.83 hours between the average time of peak daily debris temperature at a depth of 5cm (14:17) and at a depth of 40cm (21:07).

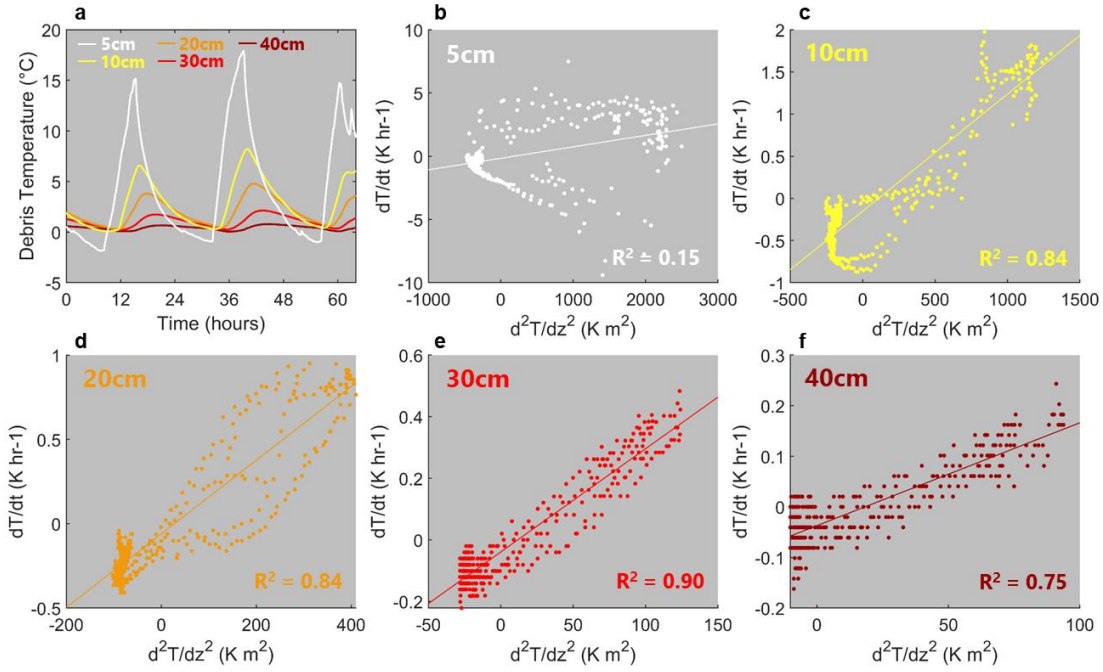

Figure 4.4. Thermal properties of the supraglacial debris layer at Llaca Glacier, derived from thermistors located at depths of 5, 10, 20, 30 and 40 cm (with the debris-ice interface being at 40 cm depth) within the debris layer. (a) shows the direct measurements that were recorded by each of the thermistors between 17 August 00:00 and 19 August 16:00, with lines colour-coded according to the debris thicknesses shown in (b)-(f). (b)-(f) show the relationship between the second derivative of debris temperature with respect to depth (d^2T/dz^2) and the first derivative of debris temperature with respect to time (dT/dt), derived from the time-series recorded by each of the thermistors. The gradient of this relationship, which was used to approximate the thermal diffusivity, is shown for each of the thermistors in (b)-(f), along with the R^2 value associated with each gradient.

4.4.2 Thermal conductivity

The effective thermal conductivity of the debris decreases by 0.963 W m^{-1} K^{-1} from near the surface of the debris layer (5 cm depth) to 30 cm depth (Table 2). However, the thermal conductivity appears to decrease below 30 cm, with a thermal conductivity 0.519 W m^{-1} K^{-1} lower at the ice-debris interface (40cm depth) than at 30 cm depth. R^2 associated with the gradients between $\frac{\partial T}{\partial t}$ and $\frac{\partial^2 T}{\partial z^2}$ are generally high (Figure 4.4c-f), except for at 5 cm depth, where the R^2 value is considerably lower (Figure 4.4b).

Table 4.2. Debris thermal properties on Llaca Glacier tongue. Thermal diffusivity and effective conductivity values, simulated from the thermistor measurements, are shown for each depth within the debris layer.

Debris thickness (cm)	Thermal diffusivity (mm^2 s^{-1})	Effective thermal conductivity (W m^{-1} K^{-1})
5	0.252	0.357
10	0.386	0.547
20	0.606	0.860
30	0.931	1.320
40	0.565	0.801

4.4.3 Simulated debris thickness

Figure 4.5 shows the debris thickness simulated across Llaca Glacier using the main workflow outlined in Figure 4.2. The results indicate a mean debris thickness of 0.20 m, with a variance of 0.03 m, across the survey area. Debris thickness generally decreases up-glacier, with the lowest debris thicknesses being found in the uppermost portion of the survey area, where the debris layer was ~ 1-7 cm thick. Over > 90% of the survey area (excluding supraglacial ice cliffs and ponds), the debris layer is thicker than the critical thickness required to reduce sub-debris melt rates through insulation of the ice surface (Östrem, 1959). Comparison against the three usable manually-acquired debris thickness measurements, coupled

with accurate GPS locations, within the survey area indicates good agreement between measured and simulated values, with differences of < 6 % between simulated and measured debris thickness values (Figure 4.5b).

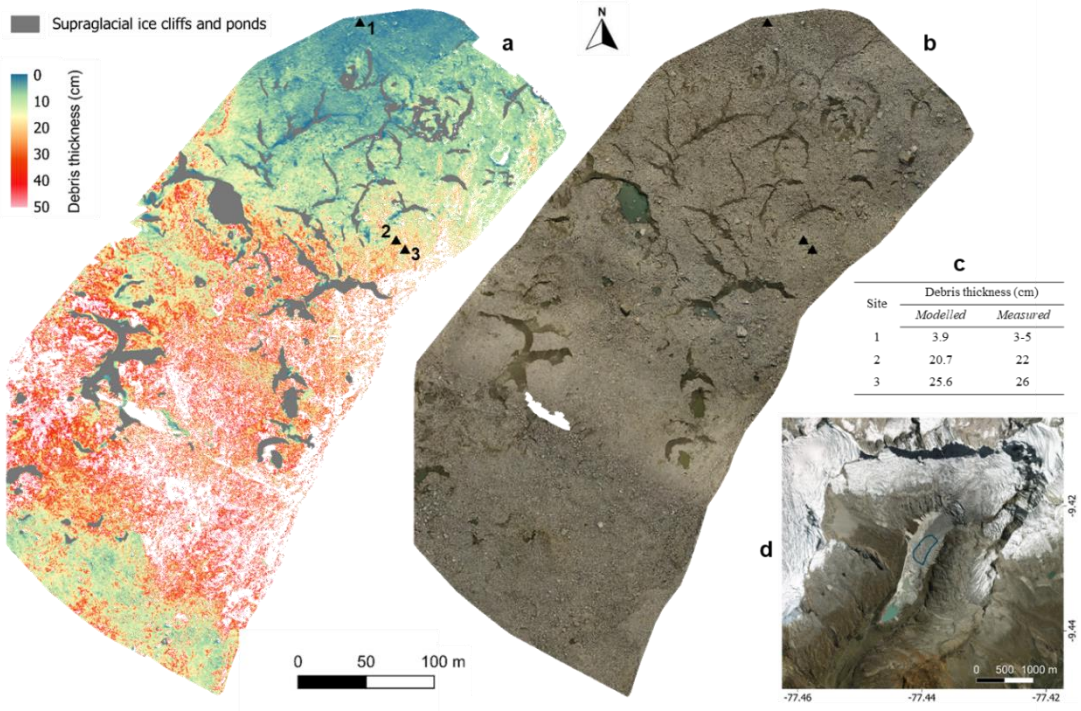

Figure 4.5. Spatially-distributed map of simulated debris thickness. Simulated debris thicknesses are shown in (a), with black triangles showing the locations of the in-situ debris thickness measurements within the survey area. White areas show the presence of no data values, where simulated values were negative or more than three MADs outside the mean (discussed in 2.5.3). Grey areas show the presence of supraglacial ice cliffs and ponds, which were not included in the model (discussed in 2.5.4). RGB orthomosaic for the simulated area is shown in (b). A comparison between the simulated and measured debris thicknesses at these three sites is shown in (c), while (d) shows the spatial coverage of the debris thickness map and RGB orthomosaic shown in (a) and (b), respectively.

4.4.4 Surface temperature

The results show that the spatial heterogeneity in surface temperatures is greatest during the middle of the day compared to early morning and late afternoon (Figure 4.S1). More specifically, the surface temperatures derived from the thermal imagery collected between 11.55 and 12.50 (survey S_{T3}) show a variance of 35.8 K across the survey area, while the surface temperatures derived from the thermal surveys of 16.25-17.20 (S_{T1}), 9.30-10.00 (S_{T2}) and 14.25-15.45 (S_{T3}) show lower

variances of 14.2, 23.6 and 21.8 °C, respectively, across their survey areas. Meanwhile, the surface temperatures from S_{T3} have a standard deviation of 6.0, while the surface temperatures from S_{T1}, S_{T2} and S_{T4} have lower standard deviations of 3.8, 4.9 and 4.7 °C, respectively. Note that some of the differences in variance may be partially attributable to different areas being covered by thermal surveys conducted at different times of day (as described in Section 4.3.2.1).

4.4.5 Simulated sub-debris melt rates

The results indicate a mean sub-debris melt rate of 0.49 cm d^{-1} across the total survey area, over the entire 3-month model period between 5 July and 5 October (Figures 4.6-4.7), with high levels of spatial heterogeneity ranging from 0.00 cm d^{-1} to 1.91 cm d^{-1} across the study area (Figures 4.5d,4.6). Sub-debris melt rates also generally increase up-glacier through the survey area (Figure 4.6). Maximum sub-debris melt rates decrease as a function of debris thickness, with mean melt

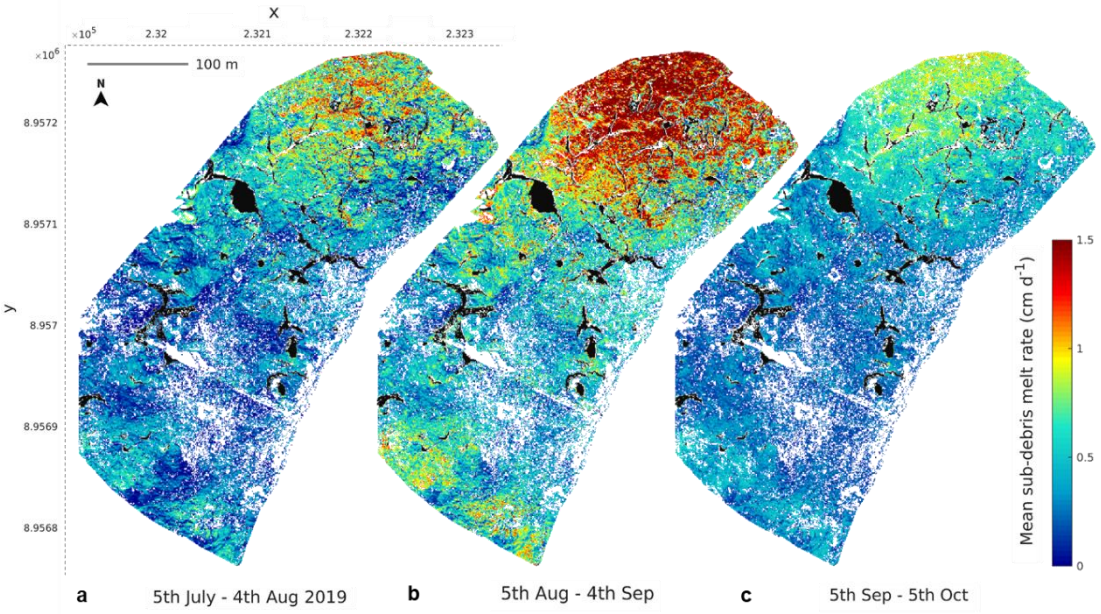

Figure 4.6. Spatially-distributed simulated sub-debris melt rates on Llaca Glacier tongue. Maps of the mean simulated melt rates (across the area shown in Figure 4.4c) are shown for three 31-day periods: 5 July – 4 August (a), 5 August – 4 September (b) and 5 September – 5 October (c). These values were simulated backwards and forwards in time from the date of thermal UAV data collection, 19 July 2019. Black shaded areas show the presence of supraglacial ice cliffs and ponds (which were not included in the model) and white areas show the presence of no data values.

rates for the 93-day period of up to nearly 2 cm d^{-1} for thin debris layers of a few mm, compared to mean melt rates of up to ~0.5 cm d^{-1} where debris is 30 cm thick (Figure 4.7c). Figure 4.7b shows that mean sub-daily melt rate for the period 5 July – October has a skewed distribution, with a modal melt rate of ~0.25 cm d^{-1}.

There are high levels of temporal variability in the sub-debris melt rates on Llaca Glacier tongue, with simulated mean daily melt rates for the whole survey area ranging from 0.00 to 1.18 cm d^{-1} between 5 July and 5 October 2019 (Figure 4.7a). The results indicate that sub-debris melt rates are generally slightly greater during the middle of the three-month simulation period (see moving average in Figure 4.7a), with mean daily sub-debris melt rates of 0.69 cm between 5 August and 4 September, compared to 0.40 and 0.38 for the periods of 5 July – 4 August

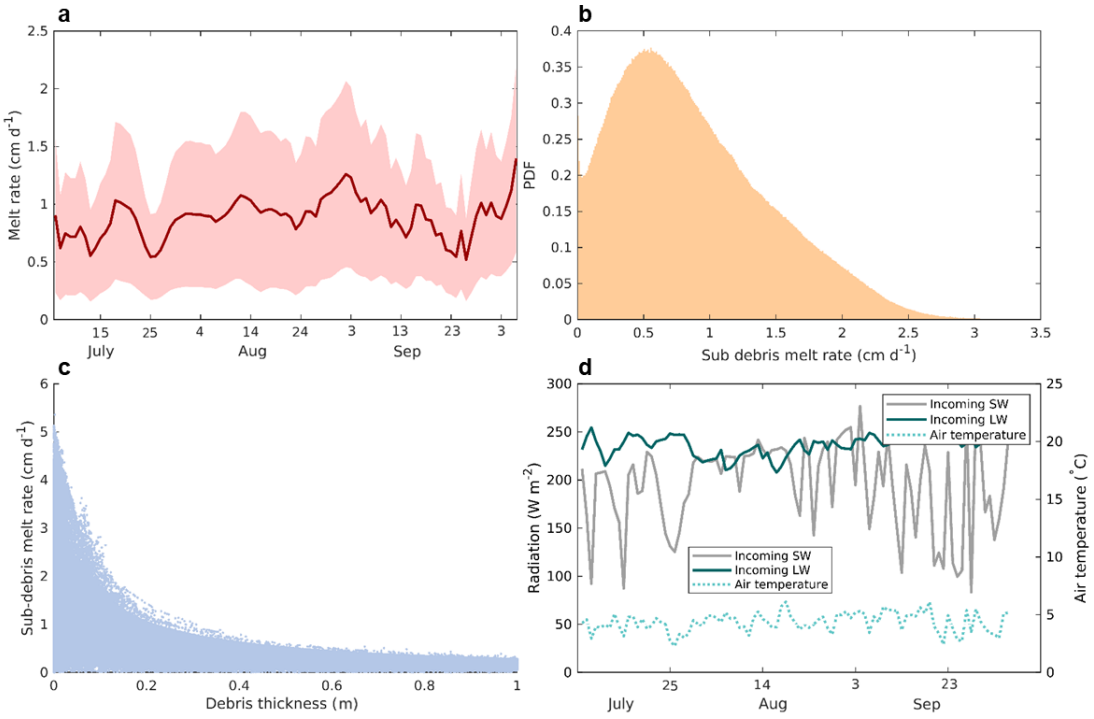

Figure 4.7. Simulated sub-debris melt rates on Llaca Glacier tongue between 5 July and 5 October 2019. (a) Temporal variations in the average sub-debris daily melt rates (red line with standard deviation shaded) and the 20-day moving average (yellow line) for the area shown in Figure 4.5c. (b) Probability density function (PDF) for the mean sub-debris melt rates of the period 5 July - 5 October for the survey area shown in Figure 4.5c. (c) Mean simulated sub-debris melt rates for the same area and period shown as a function of simulated debris thickness. (d) Mean daily air temperature and incoming shortwave (SW) radiation recorded at Cuchillacocha weather station and the mean daily simulated incoming longwave (LW) radiation between 5 July and 5 October).

and 5 Sep – 5 Oct, respectively (Figure 4.6). Over the duration of the three-month simulation period, the mean incoming SW and LW radiation fluxes are 195 and 185 W m^{-2}, respectively (Figure 4.7d). The ranges in mean daily incoming SW and LW radiation are 194 and 11 W m^{-2}, respectively, over the 93-day period, while the range in mean daily air temperature is 3.8 °C.

4.5 Discussion

4.5.1 Simulating debris thickness from thermal UAV imagery

The results of this study demonstrate that thermal UAV imagery can be used to effectively simulate spatially-distributed supraglacial debris thicknesses. The results also demonstrated that, while high levels of precision can be gained from using such imagery, a number of calibrations and corrections are critical to ensure that (a) the thermal imagery is calibrated to account for biases associated with UAV-mounted thermal sensors, (b) the thermal imagery is corrected to account for the changing sensor-surface distance over the course of the thermal UAV flights (if terrain correction is not used), (c) the temporal changes in meteorological parameters over the course of the thermal surveys are accounted for, and (d) the spatial variations in meteorological parameters across the thermal survey area are accounted for. We recommend that future studies take the aforementioned steps in order to maximise the accuracy of debris thickness maps derived from thermal UAV imagery.

The results also show that thermal imagery acquired near the middle of the day is optimal for simulating debris thicknesses, due to (a) high spatial heterogeneity in surface temperatures, and (b) relatively low temporal variations in the simulated G_{ratio} and meteorological variables. As shown in Table S2, survey S_{T3} yielded a variance in surface temperatures 50 - 150 % greater, and a standard deviation 20 – 60 % greater, than the other three surveys. As a result, it is easiest to distinguish between different debris thicknesses using thermal imagery collected during S_{T3}, which was conducted during the middle of the day (10.55 – 12.50). In contrast,

debris-thickness-driven differences in surface temperatures are less pronounced in the early morning, since debris has not yet heated up sufficiently, resulting in cooler and more homogeneous debris temperatures (further demonstrated in Figure 4.4a). During the late afternoon, the debris has cooled significantly since the middle of the day (Figure 4.4a), again partially obscuring some of the debris-thickness-driven differences in surface temperatures. Furthermore, during the early morning and late afternoon, temporal variations in meteorological variables are high (Figure 4.S1a,b,d,e), making it difficult to account for variability in meteorological parameters within the duration of the thermal UAV surveys, thereby impacting the accuracy of calculated debris thicknesses. Additionally, the G_{ratio} factor is highly unstable during the early morning (Figure 4.S1c), making it more difficult to account for the complex and changeable debris temperatures. We therefore recommend that future studies collect thermal imagery near the middle of the day (e.g. between approximately 11.00 and 13.00), when surface temperature variations are greatest and temporal meteorological variability is likely to be relatively low (Figure 4.S1).

Figure 4.8 demonstrates the improved level of detail obtained using UAV-derived surface temperatures to calculate debris thickness, compared to the use of thermal imagery derived from satellites. As demonstrated in Figure 4.5a, there are large variations in debris thickness over relatively small spatial scales, which can only be distinguished using the thermal UAV imagery, and not from the highest-resolution satellite imagery currently available (Figure 4.8). This provides further evidence that glaciological models which use satellite-derived debris thicknesses as input data are likely to be affected by 'inter-pixel mixing effects', as described by Rounce and McKinney (2014). Our UAV results indicate a mean debris thickness of 0.20 m across the survey area, which is 71 % less than the mean debris thickness simulated from thermal satellite data for the same area (0.70 m) (Rounce et al., 2021). This suggests that debris thicknesses on Llaca Glacier may be significantly

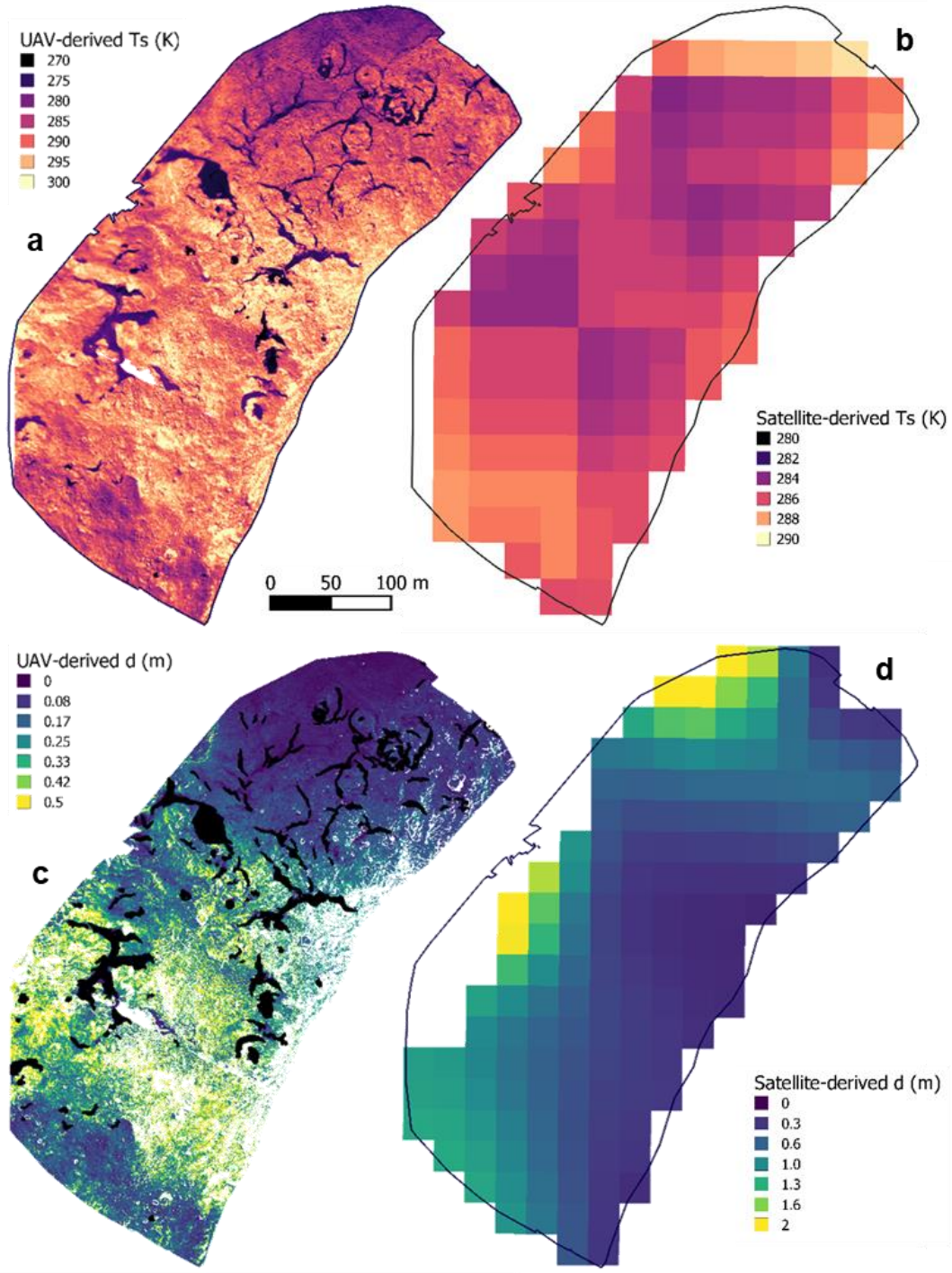

Figure 4.8. Comparison between UAV and satellite-derived surface temperature information and simulated debris thicknesses. (a) Calibrated surface temperatures derived from thermal UAV imagery, acquired between 10.55 and 12.50 on 19 August 2019. (b) Surface temperatures derived from the thermal band of the Landsat 7 satellite, acquired at 15.03 on 19 August 2019. (c) Debris thicknesses simulated in this study from thermal UAV imagery. Black shaded areas show the presence of ice cliffs and white areas show the presence of no data values. (d) Debris thicknesses simulated by Rounce et al. (2021). The black line surrounding each of the 4 maps shows the same reference area on Llaca Glacier, as shown in Figure 4.5c.

overestimated by satellite-based models, with significant impacts on simulated sub-debris melt rates (as discussed further in Section 4.5.2). Further evidence is therefore required in order to confirm whether this could be indicative of a wider pattern.

The results also indicate that using a simpler method to calculate debris thickness, based on the polynomial relationship between surface temperature and debris thickness, similar spatial patterns of debris thickness can be detected in areas where the debris layer is less than ~20 cm in depth (Figure 4.S3). However, when debris exceeds a thickness of around 20 cm, the polynomial-relation-based model appears to significantly underestimate debris thickness (Figure 4.S2; Table 4.S2). A potential explanation for this is that the polynomial relation method used to calculate debris thickness is based on a higher number of measurements at points where debris thickness is below 20cm (Figure 4.S2), while there is only one measurement with a debris thickness of 25 cm, which may provide a poor representation of surface temperature for thicker debris. Additionally, the polynomial relation method does not account for the contribution of spatial variations in meteorological conditions towards the debris surface temperatures observed. As a result, the debris thickness accuracy is likely to be lower compared to the results derived from the surface energy balance modelling approach.

4.5.2 Simulating sub-debris melt rates from UAV-derived debris thickness maps

This study demonstrates that by using high-resolution maps of debris thickness derived from thermal UAV data, greater-precision estimates of sub-debris melt rates can be produced. As shown in Figure 4.6, high levels of spatial heterogeneity in ice surface melt rates over sub-metre scales can be detected across the survey area on Llaca Glacier tongue. Inputting the derived debris thicknesses simulated by Rounce et al. (2021) (which are more than three times greater than our estimates) into our sub-debris melt model, we estimated a mean simulated melt rate of 0.17 cm d^{-1}, a value 65 % less than simulated in our study (0.49 cm d^{-1}). This indicates that since the debris thicknesses simulated from satellite data appear to be

considerably overestimated for Llaca Glacier tongue, this would lead to significant underestimation of sub-debris melt rates as a consequence. We therefore advocate for further high-precision studies of debris thickness, with better model validation, in order to better understand the uncertainties associated with satellite-derived debris thicknesses and more accurately calibrate regional-scale models of debris thickness and sub-debris melt rates.

4.5.3 Thermal properties of supraglacial debris

As shown by numerous previous studies (e.g. Conway and Rasmussen, 2000; Nicholson and Benn, 2012), our results further confirm that, during the daytime, the temperature of the supraglacial debris on Llaca Glacier is lowest at the debris-ice interface and increases towards the surface of the debris layer (Figure 4a). The increasingly lagged peaks in debris temperature from the surface to the base of the debris layer indicate that, with increased debris thickness, there will be an augmented delay time in the melt response to meteorological forcing at Llaca Glacier.

The depth-averaged thermal conductivity of the debris layer at Llaca Glacier (0.78 W m^{-1} K^{-1}) appears to be slightly lower than the values generally reported by previous studies in the Himalaya. For example, at Ngozumpa Glacier in Nepal, Nicholson and Benn (2012) found thermal conductivities of $0{\cdot}95 \pm 0{\cdot}10$ W m^{-1} K^{-1} and $1{\cdot}29 \pm 0{\cdot}13$ W m^{-1} K^{-1} for dry debris in winter and summer respectively. This lower thermal conductivity could potentially be attributed to greater debris porosity, which results in more air being trapped within the debris layer and less heat being transferred downwards through the debris layer (Juen et al., 2012).

As a result of its relatively low thermal conductivity, the debris layer on Llaca Glacier is likely to be providing a greater insulative effect on the ice below than on glaciers where the debris thermal conductivity is greater. This suggests that the debris is having a relatively high inhibiting effect on melt rates at Llaca Glacier, in comparison to some of the well-studied glaciers in the Himalaya. This could be indicative of a higher regional importance of debris cover in controlling glacier melt

rates in the Cordillera Blanca. However, further evidence is required in order to better understand the role of debris cover in controlling glacial melt rates and downstream hydrology in the Ancash region of Peru.

4.5.4 Model sensitivity and limitations

The sensitivity analysis results (Table S3) indicate that simulated debris thicknesses are most sensitive to incoming shortwave radiation and albedo. While incoming solar radiation recorded in the nearby valley is likely to be similar to Llaca Glacier (as there were cloud-free conditions during the thermal surveys), future studies could further minimise model uncertainties by gathering meteorological data on site. Additionally, ground-based pyranometer measurements of albedo could be collected and surface classification of albedo could be divided into a greater number of categories (e.g. corresponding to different debris lithologies). The model is relatively sensitive to surface temperature (Table S3), emphasising the importance of accurately calibrating the surface temperatures derived from UAV-mounted thermal cameras. While various calibration procedures were performed to correct for the effects of sensor biases, sensor drift, atmospheric signal attenuation and surface emissivity variations, future efforts could be made to further improve these calibration procedures. The model is also moderately sensitive to the nonlinear approximation factor. Since the parameterisation of the nonlinear approximation factor is affected by the debris temperatures recorded by the thermistors, setting up sequences of thermistors at multiple locations of varying debris thicknesses would help to ensure the accuracy of this parameter.

A key limitation associated with this study is the scarcity of debris thickness data suitable for validation (as discussed in Section 4.3.3.3), which results in some remaining uncertainty in the reliability of debris thicknesses simulated from thermal UAV data. In future, further thermal UAV surveys of debris-covered glaciers, coupled with a greater number of in-situ debris thickness measurements within surveyed areas, would be highly beneficial for establishing this technique as a viable method for obtaining high-precision estimates of supraglacial debris thickness with

improved levels of accuracy. Furthermore, the collection of ablation-stake measurements at debris-thickness simulation sites would enable validation of simulated sub-debris melt rates produced using UAV-derived simulated debris thicknesses.

4.6 Conclusions

This study has presented an approach for simulating high-resolution, spatially-distributed supraglacial debris thicknesses and sub-debris melt rates from UAV-derived thermal imagery, in conjunction with local meteorological data, visible UAV imagery and vertically-profiled debris temperature measurements. We have demonstrated that by (a) effectively calibrating the radiometric thermal imagery, (b) accounting for the temporal variations in meteorological parameters over the UAV survey duration, (c) parameterising the spatial distribution of meteorological parameters across the survey area, and (d) simulating the thermal conductivity of the debris layer, surface energy balance modelling can be used effectively to simulate the debris thickness and sub-debris melt rates of debris-covered glaciers. We have also demonstrated that by obtaining high-resolution (10 cm) UAV imagery, as opposed to using coarser ($>$ 60 m) satellite imagery, the highly spatially-heterogeneous debris thickness across Llaca Glacier tongue can be significantly better represented, facilitating higher-precision sub-debris melt simulations. Our findings have indicated that the mean debris thickness across the survey area on Llaca Glacier tongue is ~ 71 % lower than the satellite-derived estimate, indicating that the accuracy of satellite-derived debris thicknesses are likely to be poor in some places. Further sub-debris melt simulation has indicated that this overestimation of debris thicknesses would have resulted in a ~ 65 % underestimation of sub-debris melt rates across the survey area. Our results also indicated that the debris layer on Llaca Glacier has an ~18 – 40 % lower thermal conductivity compared to the debris on previously-studied glaciers in the Himalaya, suggesting that the inhibiting effect of debris on melt rates may vary considerably between glaciers and/or regions. Overall, the results of this study emphasise the need for further high-precision

UAV/ground-based studies of the thermal properties of supraglacial debris in the Cordillera Blanca, as well as in other mountain regions around the world, in order to better calibrate debris thicknesses within glaciological models and improve the accuracy of hydrological predictions.

4.7 Supplement

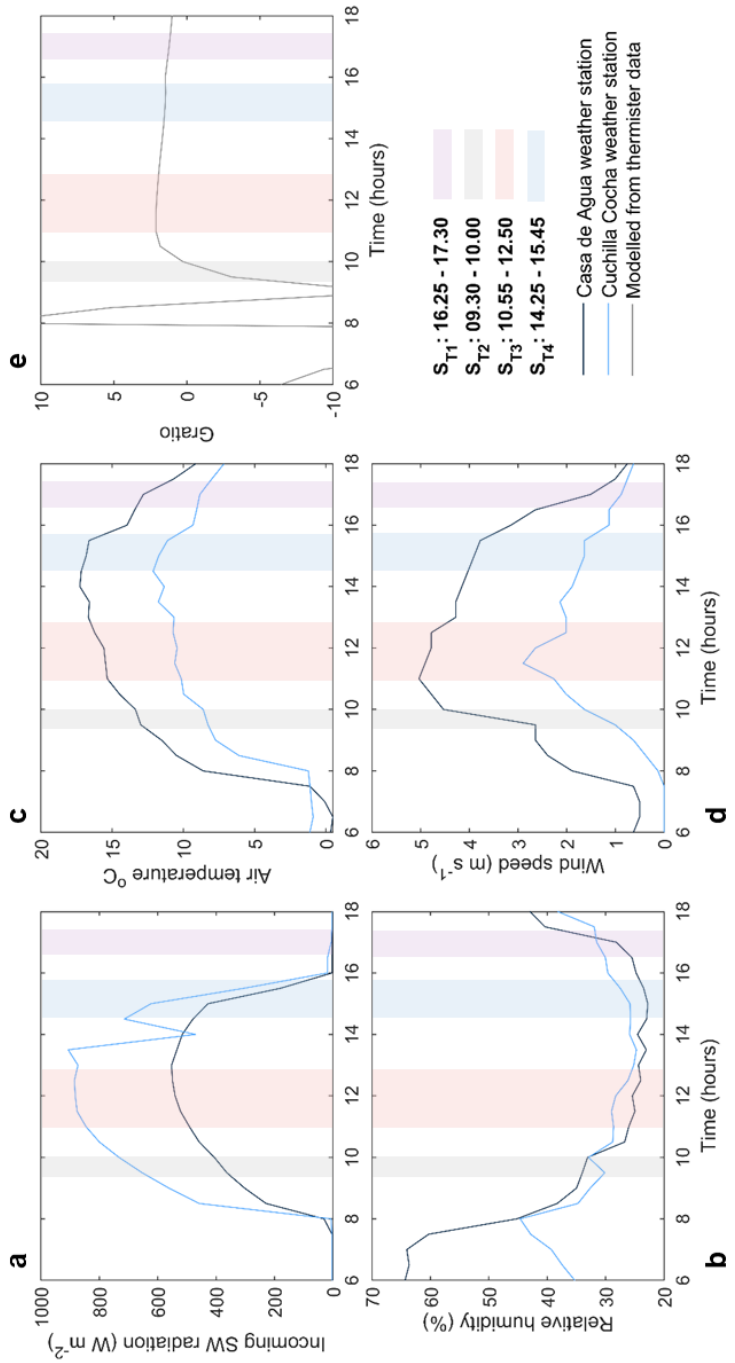

Figure 4.S1. Meteorological variability and G_{ratio} variability during the thermal UAV surveys. (a)-(d) show the mean incoming shortwave radiation, air temperature, relative humidity and wind speed, respectively, recorded at the Casa de Agua (navy line) and Cuchillacocha (blue line) weather stations, with an average of the values recorded on 18 and 19 August (when the four thermal UAV surveys were conducted) shown. (e) shows the mean G_{ratio} factor (grey line), simulated from the thermistor time series, for 18-19 August 2019. The shaded areas on each of the five plots shows the time periods over which thermal UAV surveys were conducted. Note that the survey S_{T1} was conducted on 18 August while surveys S_{T2}, S_{T3} and S_{T4} were conducted on 19 August.

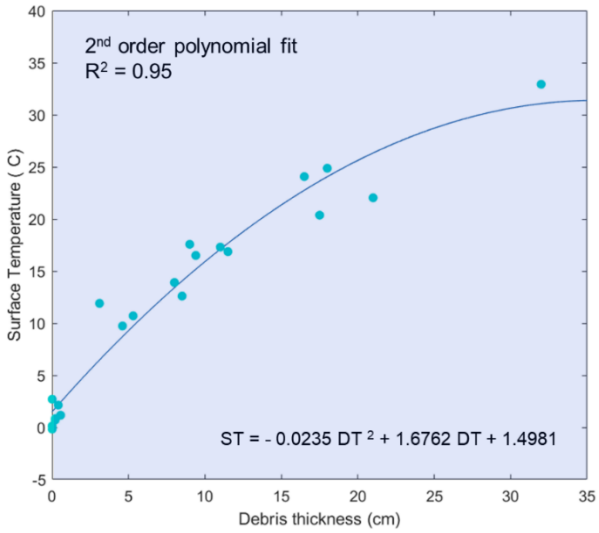

Figure 4.S2. Ground-based surface temperature and debris thickness measurements. The blue points show the mean surface temperature (measured in-situ with an Apogee TIR radiometer) and corresponding debris thickness (measured in-situ by manual excavation) at each of the 20 measurement sites. The dark blue line shows the 2nd order polynomial fit between debris thickness and surface temperature. The equation of the polynomial and the associated R^2 value are shown.

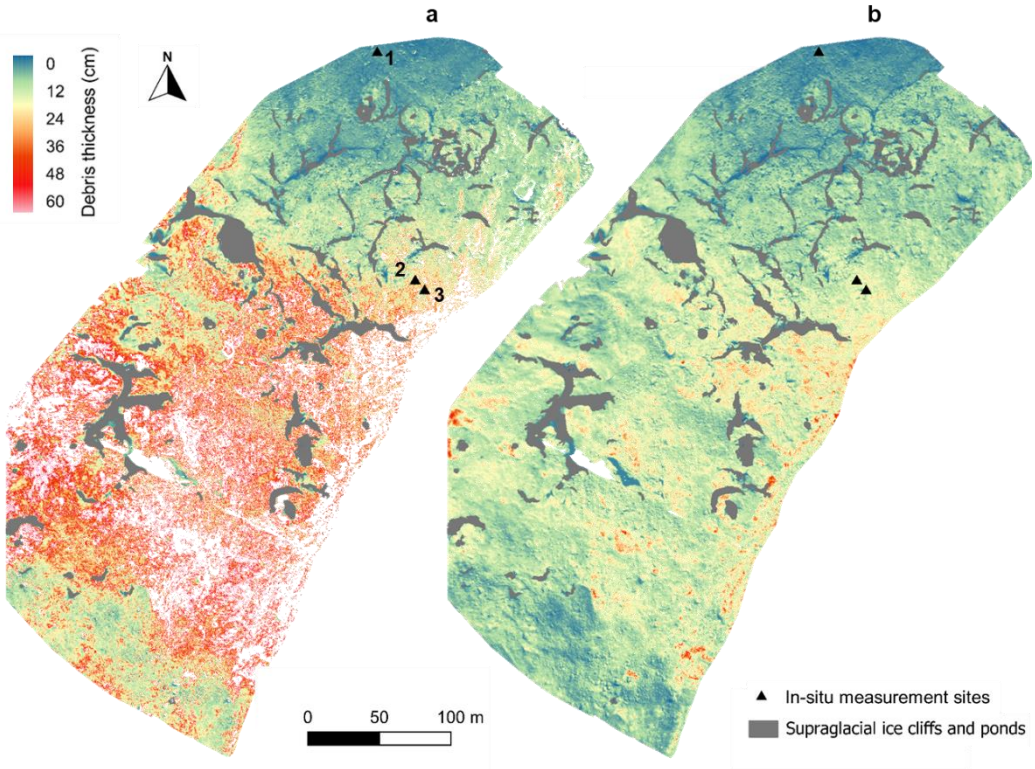

Figure 4.S3. Surface energy balance vs empirical relation model results. The spatially-distributed debris thickness values calculated from (a) the surface energy balance model, and (b) the empirical relation between debris thickness and surface temperature (derived from in-situ measurements of surface temperature and debris thickness).

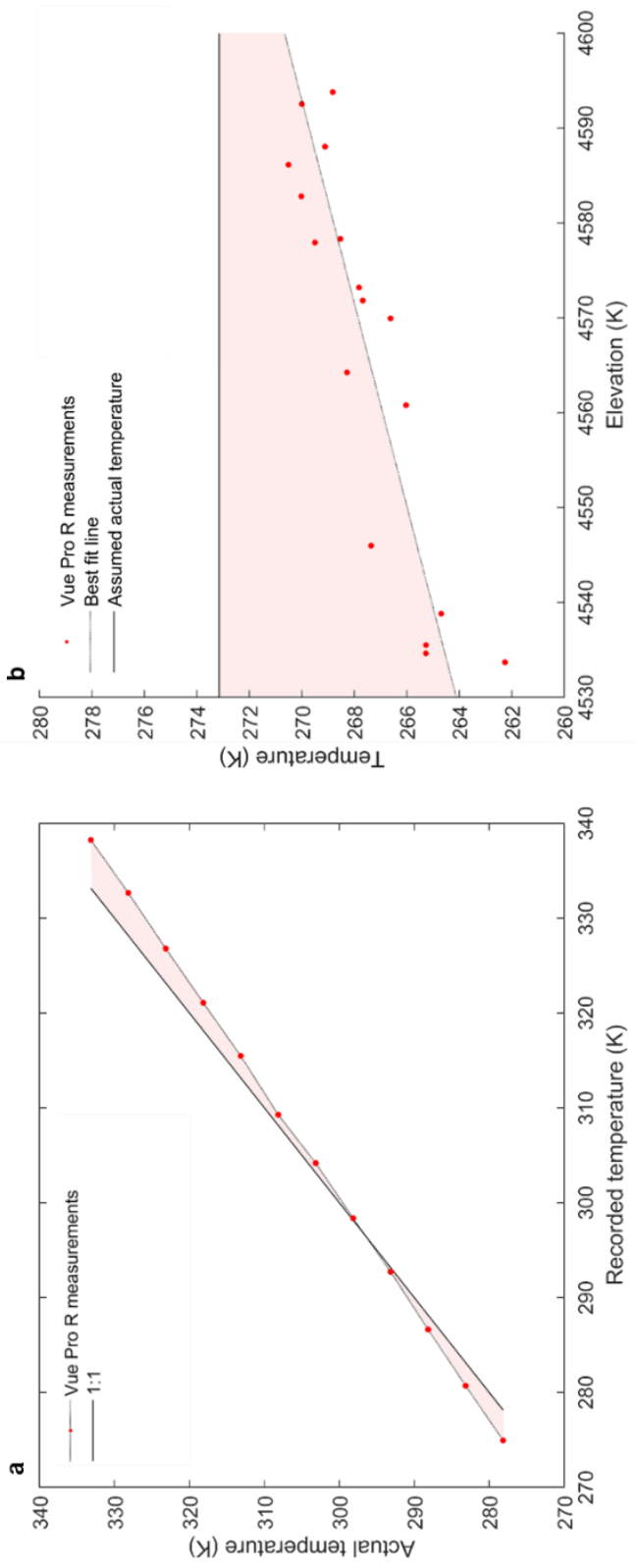

Figure 4.S4. Vue Pro R measurements used for calibration of surface temperature values. The pink shaded area in (a) shows differences between the actual blackbody temperatures and those recorded by the Vue Pro R camera used in this study. These differences were used to calibrate the thermal imagery to account for the effects of sensor bias. The pink shaded area in (b) shows the altitude-dependent differences between the best fit line for altitude-dependent exposed-ice-cliff temperatures recorded by the Vue Pro R camera and actual exposed-ice-cliff surface temperatures, which were assumed to be 0 °C. These differences were used to apply an altitude-dependent correction factor to the sensor-bias-corrected thermal imagery to account for the effects of atmospheric attenuation and sensor drift.

4.7. SUPPLEMENT

Table 4.S1. Thermal UAV survey comparison. For each of the four thermal UAV surveys, the variances and standard deviations in recorded surface temperatures (°C) are given. Note that while each of the four surveys cover different areas, similar materials (ice, rock, water) are present within all of the survey areas.

Survey	Date	Time period	Variance	St. dev.
S_{T1}	18/8/19	16.25 - 17.30	14.2	3.8
S_{T2}	19/8/19	09.10 - 10.00	23.6	4.9
S_{T3}	19/8/19	10.55 - 12.50	35.8	6.0
S_{T4}	19/8/19	14.25 - 15.45	21.8	4.7

Table 4.S2. Debris thickness model comparison. At each of the three locations where debris thickness was measured in-situ, a comparison of the calculated debris thickness values produced from the empirical model and the surface energy balance model is shown.

Debris thickness (cm)		
Measured in the field	Simulated	
	Empirical relation	SEB model
~26	17.7	25.6
~22	17.3	20.6
~3-5	5.3	3.9

Table 4.S3. Model sensitivity analysis results. Changes in the mean simulated debris thickness in response to changes in input parameter values are shown.

	Input parameter change	Mean change in d (m)
T_s	+1°C -1°C	0.035 -0.029
k_{eff}	+0.1 $Wm^{-2}K^{-1}$ -0.1 $Wm^{-2}K^{-1}$	0.025 -0.025
G_{ratio}	+0.4 -0.4	0.033 -0.033
SW_{in}	+10% -10%	-0.039 +0.052
LW_{in}	+10% -10%	-0.019 0.021
T_{air}	+1°C -1°C	-0.014 0.017
u	+1 $m\ s^{-1}$ -1 $m\ s^{-1}$	0.020 -0.033
α	+0.1 -0.1	0.074 -0.053
ε	+0.02 -0.02	0.004 -0.004
z_0	+0.006 -0.006	0.011 -0.016

4.7.1 Sensitivity analysis

The debris thickness model used in this study may be affected by uncertainties associated with input parameters. Surface temperature (T_s) inputs are likely to be affected by thermal camera accuracy and calibration accuracy, while effective conductivity (k_{eff}) and nonlinear approximation factor (G_{ratio}) inputs may be impacted by thermistor accuracy. Meteorological inputs, including incoming shortwave and longwave radiation (SW_{in} and LW_{in}), air temperature (T_{air}) and wind speed (u), may be impacted by instrument accuracy, as well as uncertainties associated with the transferability of measurements recorded at the weather stations to meteorological conditions on Llaca glacier tongue. Inaccuracies in the albedo (α) and emissivity (ε) values assigned to different surface materials could also potentially impact model outputs, as could the surface roughness length (z_0) assigned to the glacier surface.

4.7. SUPPLEMENT

The sensitivity analysis (Table S3) indicates that the model is most sensitive to incoming shortwave radiation and albedo. While incoming solar radiation recorded in the nearby valley is likely to be similar to Llaca Glacier (as there were cloud-free conditions during the thermal surveys), future studies could further minimise model uncertainties by gathering meteorological data on site. Additionally, ground-based pyranometer measurements of albedo could be collected and surface classification of albedo could be divided into a greater number of categories (e.g. corresponding to different debris lithologies).

The model is relatively sensitive to surface temperature (Table S3), emphasising the importance of accurately calibrating the surface temperatures derived from UAV-mounted thermal cameras. While various calibration procedures were performed to correct for the effects of sensor biases, sensor drift, atmospheric signal attenuation and surface emissivity variations, future efforts could be made to further improve these calibration procedures. For example, since the anodised aluminium panels used for quality control appeared to have relatively unstable surface temperatures, which varied considerably over short timescales and across their length, the use of calibration targets consisting of other materials and/or a portable calibration blackbody may help to improve calibration accuracy in the future. The model is also moderately sensitive to the nonlinear approximation factor. Since the parameterisation of the nonlinear approximation factor is affected by the debris temperatures recorded by the thermistors, setting up sequences of thermistors at multiple locations of varying debris thicknesses would help to ensure the accuracy of this parameter.

Chapter 5

The evolution and melt contribution of supraglacial ice cliffs on a low-latitude debris-covered glacier

This chapter investigates the characteristics and evolution of supraglacial ice cliffs on a tropical debris-covered glacier in the Peruvian Andes. This chapter explores similarities and differences between ice cliffs on the relatively understudied tropical glaciers and the debris-covered glaciers in High Mountain Asia which have received increased attention in recent years. Additionally, the high-resolution sub-debris melt maps produced in chapter 2 are used to investigate the potential contribution of supraglacial ice cliffs towards the overall mass loss of Llaca Glacier. This work was conducted in partnership with the project CASCADA (CAscading impacts of peruvian glacier Shrinkage on biogeochemical Cycling and Acid Drainage in Aquatic ecosystems), funded by the Newton Fund, the Natural Environmental Research Council (NERC) and Consejo Nacional de Ciencia, Tecnología e Innovación Tecnológica (CONCYTEC). Additionally, this work involved collaboration between The University of Edinburgh, Victoria University of Wellington, Universidad Peruana Cayetano Heredia and the University of Bristol.

Publication information: Following co-author reviews, this chapter will be submitted for publication as follows: Bisset, R.B., Goldberg, D.N., Nienow, P.W., Wigmore, O., Loayza-Muro, R.A., Wadham, J.L., Macdonald, M.L. Bingham, R.G. (in preparation) The evolution and melt contribution of supraglacial ice cliffs on a low-latitude debris-covered glacier.

Author contributions: I designed the study, with support from D.N. Goldberg, P.W. Nienow and R.G. Bingham. I planned and conducted the UAV surveys, with advice from O. Wigmore and field support from M.L. Macdonald. and R.A. Loayza-Muro. I processed the UAV data from 2019. UAV data from 2014 and 2015, which was previously acquired and processed by O. Wigmore, was also used. I designed and conducted the simulations within this study, with support from D.N. Goldberg.

5.1 Abstract

Like many tropical glaciers around the world, the glaciers of the Cordillera Blanca are retreating rapidly, threatening future drinking water availability, food security and energy production in the Ancash region of Peru. A large proportion of the glaciers in this region are partially blanketed by a layer of supraglacial debris, with numerous supraglacial ice cliffs present on their tongues. Previous research has demonstrated that the rapid backwasting of supraglacial ice cliffs contributes a significant proportion of the overall mass loss from debris-covered glaciers. While ice cliffs in regions such as High Mountain Asia have received increasing attention over the past decade, little is known about the behaviour of supraglacial ice cliffs in the tropics and their contribution towards overall rates of mass loss. Here, we use multi-temporal, high-resolution UAV data, collected over the tongue of Llaca Glacier, Cordillera Blanca (Peru), to investigate ice cliff characteristics and explore the factors driving their evolution. Additionally, we simulate the hourly backwasting rates of supraglacial ice cliffs over a 15-day period in August 2019 and examine the radiative fluxes that drive these backwasting rates. We find that, in line with glaciers in the northern hemisphere, ice-cliff survival is strongly controlled by aspect,

which influences the spatial distribution of radiative fluxes across cliff surfaces. The results also indicate that, while there is little evidence to suggest that ice-cliff survival on Llaca Glacier is driven by diurnal meteorological patterns, ice flow dynamics may play a role in controlling ice-cliff development. We estimate that, across our survey area, ice-cliff backwasting contributed ~20 % of overall ablation during the 15-day simulation period, despite covering only 5 % of the surface area. Overall, our results highlight the importance of further research into the complex dynamics of supraglacial ice cliffs in low-latitude regions in order to more accurately simulate the future evolution of and mass loss of tropical debris-covered glaciers

5.2 Introduction

Glacial meltwater from the Cordillera Blanca plays a vital role in meeting downstream water demands within the Ancash region of Peru, particularly during the dry season when precipitation is low (Mark and Seltzer, 2017). A significant proportion of the glaciers within this region are blanketed by a layer of supraglacial debris, which is well known to modify glacial melt rates (e.g. Östrem, 1959; Nicholson and Benn, 2006). There is emerging evidence that supraglacial ice cliffs on debris-covered glaciers play a significant role in further altering glacial melt, with recent studies demonstrating that supraglacial ice cliffs melt more rapidly than the debris-covered ice surrounding them, thereby contributing towards a significant proportion of the ablation of debris-covered glaciers (e.g. Thompson et al., 2016; Brun et al., 2018; Buri and Pellicciotti, 2018). Ice cliffs on the surfaces of debris-covered glaciers also have greater melt rates than those on debris-free glaciers, due to the gathering of fine debris particles on cliff surfaces, lowering surface albedo and increasing radiative absorption (Brock et al., 2010). Additionally, debris adjacent to ice cliffs heats up during the day, emitting longwave radiation and elevating the ambient air temperature by means of convection (e.g. Brock et al., 2010; Buri et al., 2016; Reid and Brock, 2017).

Recent studies of supraglacial ice cliffs on debris-covered glaciers have primarily focussed on High Mountain Asia and have shown that cliff orientation

plays a key role in controlling their evolution. In these regions of the northern hemisphere, north-facing ice cliffs survive preferentially over the course of the melt season, while south-facing ice cliffs are prone to disappear through flattening and reburial (e.g. Kraaijenbrink et al., 2016; Thompson et al., 2016; Watson et al., 2017; Buri and Pellicciotti, 2018; Sakai et al., 2018; Steiner et al., 2019). This pattern is predominantly driven by variations in the quantity of incoming solar radiation across cliff faces, which impact net radiation gradients (e.g. Buri and Pellicciotti, 2018; Buri et al., 2021). North-facing cliffs receive a relatively uniform net radiation flux across their surfaces, allowing cliffs to backwaste evenly and retain steep surface slopes, while south-facing cliffs generally receive the greatest net radiation fluxes towards their crests, resulting in a positive base-to-crest backwasting gradient which drives progressive flattening and ultimate reburial of cliffs (e.g. Thompson et al., 2016; Sakai et al., 2018; Buri et al., 2021).

Previous research has demonstrated that supraglacial ponds and hydrological drainage channels can also play a role in the development of supraglacial ice cliffs. Cliffs adjacent to supraglacial ponds undergo thermoerosion and/or subaqueous melt, which is most concentrated near their bases, allowing cliffs to maintain or steepen their surface slopes and backwaste evenly (e.g. Buri et al., 2016; Miles et al., 2016; Miles et al., 2020). Furthermore, the presence of adjacent ponds exposes cliff bases to a greater quantity of longwave radiation emitted by debris bordering the cliff-pond system, further steepening cliff surfaces (Buri et al., 2016). Additionally, the drainage of water from supraglacial ponds through the englacial system can widen englacial channels and increase the risk of conduit roof collapse, which can lead to the formation of new supraglacial ice cliffs and ponds (e.g. Sakai et al., 2000; Miles et al., 2016). Previous studies have also found few clear links between ice-flow dynamics and ice-cliff survival, with cliffs predominantly facing north, regardless of glacier flow direction (e.g. Watson et al., 2017; Buri and Pellicciotti, 2018; Steiner et al., 2019; Buri et al., 2021). However, some studies have found a greater prevalence of ice cliffs near tributary confluences and in areas of active ice flow (e.g. Watson et

al., 2017; Steiner at al., 2019), indicating that ice-flow dynamics could contribute towards ice-cliff evolution.

While supraglacial ice cliffs in mid/high-latitude regions such as High Mountain Asia and Alaska have received growing research attention in recent years (e.g. Buri and Pellicciotti, 2018; Anderson et al., 2021; Sato et al., 2021), little is known about the evolution of ice cliffs on low-latitude glaciers and their contribution towards glacier ablation. Here, we use high-resolution UAV imagery to examine the behaviour of supraglacial ice cliffs on the debris-covered tongue of Llaca Glacier, Cordillera Blanca, Peru. Using 10 cm digital elevation models (DEMs) of the glacier surface, acquired in 2014, 2015 and 2019, we investigate the physical characteristics and evolution of ice cliffs, as well as the general evolution of the glacier tongue between 2014 and 2019. Additionally, we simulate hourly ice-cliff backwasting rates for a 15-day period in August 2019 and investigate the radiative fluxes which play a role in driving ice-cliff backwasting and evolution.

5.3 Methods

5.3.1 Study site

Situated within the central Cordillera Blanca of Peru, Llaca Glacier (9°25'33''S, 77°26'15'') covers a total surface area of ~ 5.1 km^2 and spans from ~ 4460 to ~6090 m a.s.l. (RGI 6.0, 2017). The meltwater from Llaca Glacier feeds into the Rio Santa river basin, which supplies water resources to downstream communities in the Ancash region. The tongue of Llaca glacier, which extends over an area of ~ 0.22 km^2, is mantled with a layer of supraglacial debris. Llaca Glacier was selected as the site for this study in order to build upon previous work conducted on this glacier (Wigmore et al., 2017; Chapter 4 of this thesis).

5.3.2 High-resolution mapping of ice-surface-elevation change and ice flow

Analyses of ice-surface-elevation change patterns and ice-flow dynamics were performed using high-resolution orthomosaics (5 cm) and digital elevation models

(DEMs) (10 cm) of Llaca Glacier tongue (Figure 5.1), derived from visible UAV imagery collected in 2014 (23 July) and 2015 (28 July) (Wigmore et al., 2017) and 2019 (21 August) (see Thesis Section 4.3.2.2). These datasets cover an area of ~ 220,000 m^2 of the debris-covered ice tongue. For a full description of the methods used to generate these datasets, see Wigmore et al. (2017) and Thesis Sections 4.3.2.2, 4.3.3.1 and 4.3.4.1. The 2014, 2015 and 2019 DEMs were differenced in order to quantify temporal changes in the surface elevation of Llaca glacier tongue. In order to map patterns of ice flow between 2014 and 2019, manual feature tracking was performed based on 57 large boulders which could be distinguished clearly within both the 2014 and 2019 orthomosaics. Cubic spline interpolation was used to

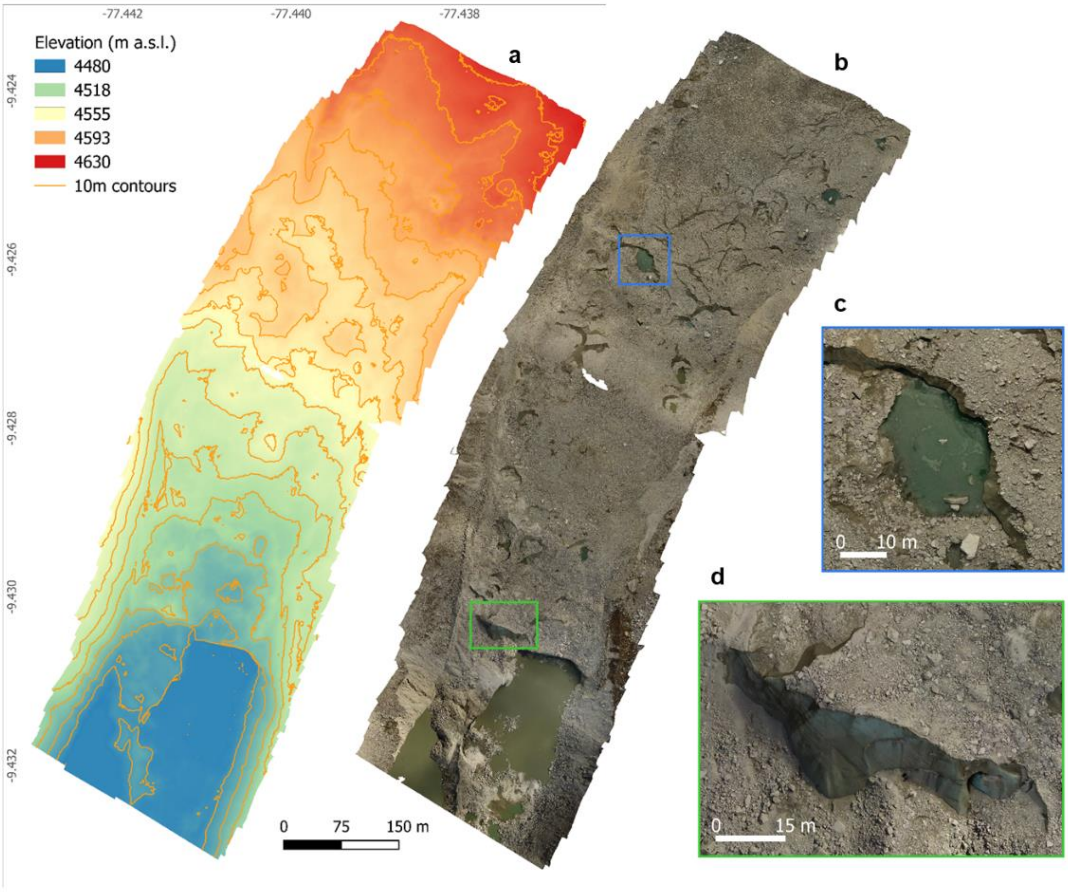

Figure 5.1. UAV-derived datasets from 2019. (a) and (b) show the 10 cm DEM and 5 cm orthomosaic, respectively, which were generated from visible UAV imagery collected on 21 August 2019. (c) and (d) show examples of supraglacial ponds and cliffs, the locations of which are shown by the blue and green rectangles in (b), which can be analysed in detail using these UAV-derived datasets.

generate gridded maps of ice surface flow speed and direction from the feature-tracking-derived surface velocity vectors.

5.3.3 Analysing ice-cliff distribution and physical characteristics

The spatial distributions of supraglacial ice cliffs and ponds were mapped for 2014, 2015 and 2019, based on the UAV-derived DEMs and orthomosaics. Ice cliffs were delineated semi-automatically based on physical characteristics such as surface slope (full description of the cliff-detection method available in Section 4.3.5.4 of this thesis). Due to their relatively low abundance, supraglacial ponds were mapped manually using the orthomosaics of Llaca Glacier tongue. The three-dimensional surface areas of supraglacial ice cliffs, as well as the overall glacier tongue, were calculated using the 10 cm DEMs for 2014, 2015 and 2019. Only supraglacial ice cliffs on top of the glacier surface were included in the analyses, while frontal ice cliffs were excluded.

Gridded maps of the surface slope and aspect of supraglacial ice cliffs were produced for 2014, 2015 and 2019, using the 10 cm DEMs. For each of these years, the mean slope, aspect and elevation of each ice cliff were calculated. In order to investigate altitudinal patterns in ice-cliff characteristics, the total area covered by ice cliffs was binned into 100 elevation bands, for each of which the mean slope and aspect were calculated. Based on these mean values, linear regression and breakpoint analyses were used to analyse altitudinal trends. To investigate the relationship between ice-cliff aspect and solar radiation receipt, the distribution of incoming shortwave radiation across ice-cliff faces was mapped using the 10 cm DEMs of the ice tongue in 2014, 2015 and 2019, overlaid onto the ALOS 30 m DEM of the surrounding topography. The shortwave radiation maps, which include direct and diffuse radiation, were generated over three 24-hour periods corresponding to the dates of the UAV surveys from which the DEMs were derived (00:00 to 24:00 on 23 July 2014, 28 July 2015 and 21 August 2019). Average diurnal trends in incoming solar radiation in the month preceding each of the three surveys were examined using meteorological data recorded by the Cuchilla Cocha weather station, located in

the nearby (9.5 km) Quilcayhuanca Valley at an altitude of 4630 m a.s.l. (location marked in Figure 4.1c).

5.3.4 Simulating backwasting rates of supraglacial ice cliffs

Spatially-distributed backwasting rates of ice cliffs were estimated using an energy balance model which accounts for the effects of surrounding terrain on longwave and shortwave energy fluxes, based on the grid-based model introduced by Buri et al. (2016). Because surface temperature data were only available for a smaller subset of the visible survey area (covering an area of ~ 137,000 m^2), ice-cliff backwasting could only be simulated across this reduced area. Hourly backwasting rates were simulated over a 15-day period from 12-26 August 2019, selected specifically to correspond closely with collection of the UAV data used in this study (Table 4.1).

The ablation M normal to the ice surface (m w.e.) for each horizontal grid square was calculated as:

$$M = \frac{Q_m \Delta t}{\rho_i L_f} \tag{5.1}$$

where Q_m is the energy flux available for melt, Δt is the model time-step (here being 3600 s), ρ_i is the ice density (900 kg m^3) and L_f is the latent heat of fusion (334 kJ kg^{-1}) (Buri et al., 2016). The use of a longer model time-step (1 day) was also tested; however, comparison of the results to those of the hourly model indicated that melt rates are poorly parameterised using daily averaged meteorological data (discussed further in Section 5.5.4).

The energy flux (Q_m) was calculated as:

$$Q_m = L_n + S_n + H + LE \tag{5.2}$$

where S_n and L_n are the net shortwave and longwave radiation fluxes, H is the sensible heat flux and LE is the latent heat flux (all units are in W m^{-2}) (Buri et al.,

2016). When the net energy flux was negative, a melt rate of 0 m w.e. h^{-1} was assumed.

In order to estimate the contribution of supraglacial ice cliffs towards the overall ablation of Llaca Glacier tongue (excluding ablation beneath supraglacial ponds), the simulated cliff ablation rate for each pixel was multiplied by its three-dimensional surface area to calculate volume loss. The volume losses corresponding to each pixel were summed to estimate total volume loss through ice-cliff backwasting across the survey area. Distributed sub-debris melt rates simulated in Thesis Chapter 4 were used to estimate the contribution of sub-debris ablation towards overall ablation within the survey area. To estimate the three-dimensional surface area of the ice surface beneath the debris, the UAV-derived DEM was downsampled to a resolution of 5 m in order to minimise the effects of individual rock surfaces on calculated surface areas. The surface area calculated for each 5 m pixel was multiplied by pixel-specific melt rates to calculate the volume loss for each pixel and volume loss values were summed to calculate the volume loss through sub-debris melting across the survey area. The contribution of ablation beneath and around the margins of supraglacial ponds, which cover less than 1% of the survey area, was excluded from these analyses as there was insufficient data to simulate pond-driven melt rates.

5.3.5 Simulating longwave and shortwave energy fluxes onto ice cliffs

When simulating the net longwave radiation (L_n) at ice-cliff surfaces, we accounted for longwave radiation emitted from the atmosphere onto the ice cliffs (L_a), from the debris onto the ice cliffs (L_d), and from the ice cliffs into the atmosphere (L_{out}) (Buri et al., 2016):

$$L_n = L_d + L_a - L_{out} \tag{5.3}$$

All longwave fluxes are in W m^{-2}. The longwave energy emitted by the surrounding debris was calculated as:

$$L_d = V_d \varepsilon \sigma {T_d}^4 \quad (5.4)$$

where V_d is the debris view factor (dimensionless), ε is the emissivity (a value of 0.94 was assumed (Salisbury and D'Aria, 1992)), σ is the Stefan-Boltzmann constant (5.67×10^{-8} W m^{-2} K^{-4}) and T_d is the inverse distance weighted (IDW) mean surface temperature of the debris surrounding each ice-cliff-covered pixel. To estimate T_d, the mean hourly surface temperature was simulated from a 10 cm resolution debris thickness map, derived from thermal UAV imagery (Thesis Section 4.3.5.3), in conjunction with weather station data, using the surface energy balance modelling approach of Nicholson and Benn (2006). While this approach does not account for the impacts of nonlinear temperature gradients within the debris layer on debris surface temperature, the impacts on the simulated melt rates were found to be minimal (< 3 %) (Section 5.5.4). A distance of 10 m was used in the IDW calculations of mean debris temperature surrounding the ice cliffs. This distance was considered sufficient since sensitivity analyses showed that changing the IDW distance from 10 to 20 m resulted in less than 0.1 K change in the IDW mean surface temperature calculated for each ice-cliff-covered pixel.

The longwave radiation emitted by the atmosphere was calculated as:

$$L_a = V_{s,L} L_{in} \quad (5.5)$$

where $V_{s,L}$ is the longwave sky view factor and $L_{\downarrow}$ is the incoming longwave radiation recorded at the weather station (W m^{-2}) (Buri et al., 2016). L_{in} was simulated using the parameterisation of Dilley and O'Brien (1998). A clear sky emissivity was used within this parameterisation, since clear sky conditions were observed in the field throughout the model period.

The net shortwave radiation (S_n) was calculated as:

$$S_n = (1 - \alpha_i)(S_{dir} + S_{diff} + S_d) \quad (5.6)$$

where α_i is the albedo of ice (assumed here to be 0.1 (Reid and Brock, 2014)), S_{dir} and S_{diff} are the incoming direct and diffuse shortwave radiation from the

atmosphere, respectively (W m^{-2}), and S_d is the shortwave radiation reflected by the debris onto the ice cliffs (W m^{-2}) (Buri et al., 2016). The 10 cm UAV-derived DEM of the glacier tongue, overlaid on the 30 m ALOS DEM of the surrounding area, was used to simulate the spatial distribution of S_{dir} and S_{diff} for each hour of the day. The resulting shortwave distribution maps were divided by their mean values, before being multiplied by the corresponding hourly incoming shortwave radiation values that were recorded at the weather station, in order to adjust for temporal changes in the strength of incoming solar radiation. The shortwave radiation reflected by the debris onto the cliffs (S_d) was calculated by:

$$S_d = V_d \alpha_d S_{in} \tag{5.7}$$

where α_d is the albedo for debris (assumed here to be 0.3 (Nicholson and Benn, 2012)) and S_{in} is the mean daily incoming shortwave radiation recorded by the weather station. The debris view factor was calculated from the UAV-derived DEM overlaid on the ALOS DEM.

5.3.6 Simulating turbulent energy fluxes onto ice cliffs

The sensible and latent heat fluxes were calculated using the bulk aerodynamic method of Han et al. (2010), which accounts for the effects of slope orientation on the exchange coefficients. Both the latent and sensible exchange coefficients were calculated for a neutral boundary layer with logarithmic profiles for temperature and wind speed.

The sensible heat flux was calculated as:

$$H = K_s P (T_a - T_s) u \tag{5.8}$$

where K_s is the exchange coefficient for sensible heat (dimensionless), P is the atmospheric pressure (kPa), T_a is the air temperature (K), T_s is the surface temperature (assumed to be 273.15 K on bare ice) and u is the wind speed (m s^{-1}) (Han et al., 2010). The air temperature and wind speed values recorded at the Cuchilla Cocha weather station were used, with air temperature being adjusted for

altitude within the model. The sensible heat exchange coefficient was calculated from:

$$K_s = \frac{c_p k^2 \rho_0}{P_0 \ln\left(\frac{z}{z_0}\right) \ln\left(\frac{z}{z_{0T}}\right)} \quad (5.9)$$

where c_p is the specific heat capacity of air at constant pressure (1004 J kg^{-1} K^{-1}), k is von Kármán's constant (0.41), ρ_0 is the standard density of air (1.29 kg m^{-3}), P_0 is the atmospheric pressure at sea level (101.3 kPa), z is the screen height for meteorological measurements (2 m), z_0 is the roughness length for a momentum profile (m) and z_{0T} is the roughness length for a temperature profile (m) (Han et al., 2010). z_0 was calculated as:

$$z_0 = 0.5 h_c \lambda_f \quad (5.10)$$

where h_c is the height of the cliff (m) and λ_f is the frontal area density, which was calculated as:

$$\lambda_f = 0.05 sin\beta (1 + \cos(A - W_D)) \quad (5.11)$$

where β is the mean ice-cliff slope (°), A is the mean cliff azimuth (°) and W_D is the wind direction (°) (Han et al., 2010). The mean height, slope and aspect of each ice cliff were calculated from the 10 cm DEM. z_{0T} was calculated as:

$$z_{0T} = \frac{e^{\frac{0.317 - 0.183 ln^2(Re_*)}{1000}} z_0}{Re_*^{0.565}} \quad (5.12)$$

where Re_* is the roughness Reynolds number, which was calculated as:

$$Re_* = \frac{u_* z_0}{v} \quad (5.13)$$

where u_* is the friction velocity (m s^{-1}) and v is the viscosity of air (1.35 x 10^{-5} m^{-2} s^{-1}) (Han et al., 2010). The friction velocity was obtained by:

$$u_* = \frac{uk}{\ln\left(\frac{z}{z_0}\right)} \quad (5.14)$$

The latent heat flux was calculated as:

$$LE = K_L(e_a - e_{s,i})u \tag{5.15}$$

where K_L is the exchange coefficient for latent heat (dimensionless), e_a is the atmospheric vapour pressure (kPa) and $e_{s,i}$ is the vapour pressure at the ice-cliff face, which is assumed to be the saturated vapour pressure at 273.15 K (0.611 kPa) (Han et al., 2010). The latent heat coefficient was calculated as:

$$K_L = \frac{0.623 L_v k^2 \rho_0}{P_0 \ln\left(\frac{z}{z_0}\right) \ln\left(\frac{z}{z_{0e}}\right)} \tag{5.16}$$

where L_v is the latent heat of evaporation (2.514 x 10^6 J kg^{-1}) and z_{0e} is the roughness length for logarithmic profile of vapour pressure (m), which was assumed to be equal to z_{0T}. The atmospheric vapour pressure was calculated as:

$$e_a = e_{s,a} \frac{H_R}{100} \tag{5.17}$$

where H_R is the relative humidity (as measured at the weather station) and $e_{s,a}$ is the saturation pressure of the atmosphere (kPa), which was calculated from the Clausius-Clapeyron relation:

$$e_{s,a} = 0.611 e^{\frac{L_v}{273 R_v} - \frac{L_v}{R_v T_a}} \tag{5.18}$$

where R_v is the gas constant for moist air (461 J kg^{-1}) (Salby, 1996).

5.4 Results

5.4.1 Ice-surface-elevation changes and flow dynamics

The results show a mean annual ice surface lowering of 1.43 m a^{-1} (Figure 5.2a) and a mean annual volume loss of 293,000 m^3 a^{-1} across the survey area on Llaca Glacier tongue between 2014 and 2019. Assuming an ice density of 850 ± 60 kg m^{-3}, this is equivalent to a mean annual mass loss of 249 ± 18 kilotonnes per year. For the same area, between 2014 and 2015, the results indicate a mean ice-

surface lowering of 0.76 m a^{-1}, 47 % lower than between 2014 and 2019 (Figure 5.2b) (Wigmore et al., 2017). The results also indicate high spatial heterogeneity in ice-surface-elevation change across the glacier tongue between 2014 and 2015 (with a standard deviation of 2.58 m a^{-1}) (Wigmore et al., 2017), while averaged patterns of surface elevation change over the entire 2014-2019 period are considerably less heterogeneous (with a standard deviation of 1.29 m a^{-1}).

In comparison to satellite-derived ice-surface-elevation change estimates for the period between 2013 and 2016 (Seehaus et al., 2019), our UAV-derived results indicate a significantly greater variability in mean surface-elevation change between 2014 and 2019 over the same area, despite being averaged over a greater time period (Figure 5.2c). More specifically, our results indicate a range of ice-surface-elevation change values 357 % greater, as well as a standard deviation 64 % greater, than indicated by the results of Seehaus et al. (2019) for the same area. Our results also suggest a 37% greater rate of ice surface lowering between 2014 and 2019, compared to the rate of ice loss observed by Seehaus et al. (2019) between 2013 and 2016 (Figure 5.2c).

The results of our surface feature tracking between 2014 and 2019 demonstrate that ice flow velocity increases up-glacier (Figure 5.3), with ice flowing approximately 6 times faster in the upper portion of the glacier tongue (~16-20 m a^{-1}) compared to near the glacier terminus (~ 2-4 m a^{-1}). We also find that the ice-flow direction shifts from south-westerly in the upper portion of the glacier tongue towards more southerly flow near the terminus (Figure 5.3). The flow direction is more variable near the glacier terminus (~ 165° - 210°) in comparison to the uppermost part of the study area (~ 240° - 250°). In contrast, the flow velocity is less variable near the terminus (3.0 - 3.5 m a^{-1}) in comparison to the uppermost part of the study area (13.2 – 20.9 m a^{-1}).

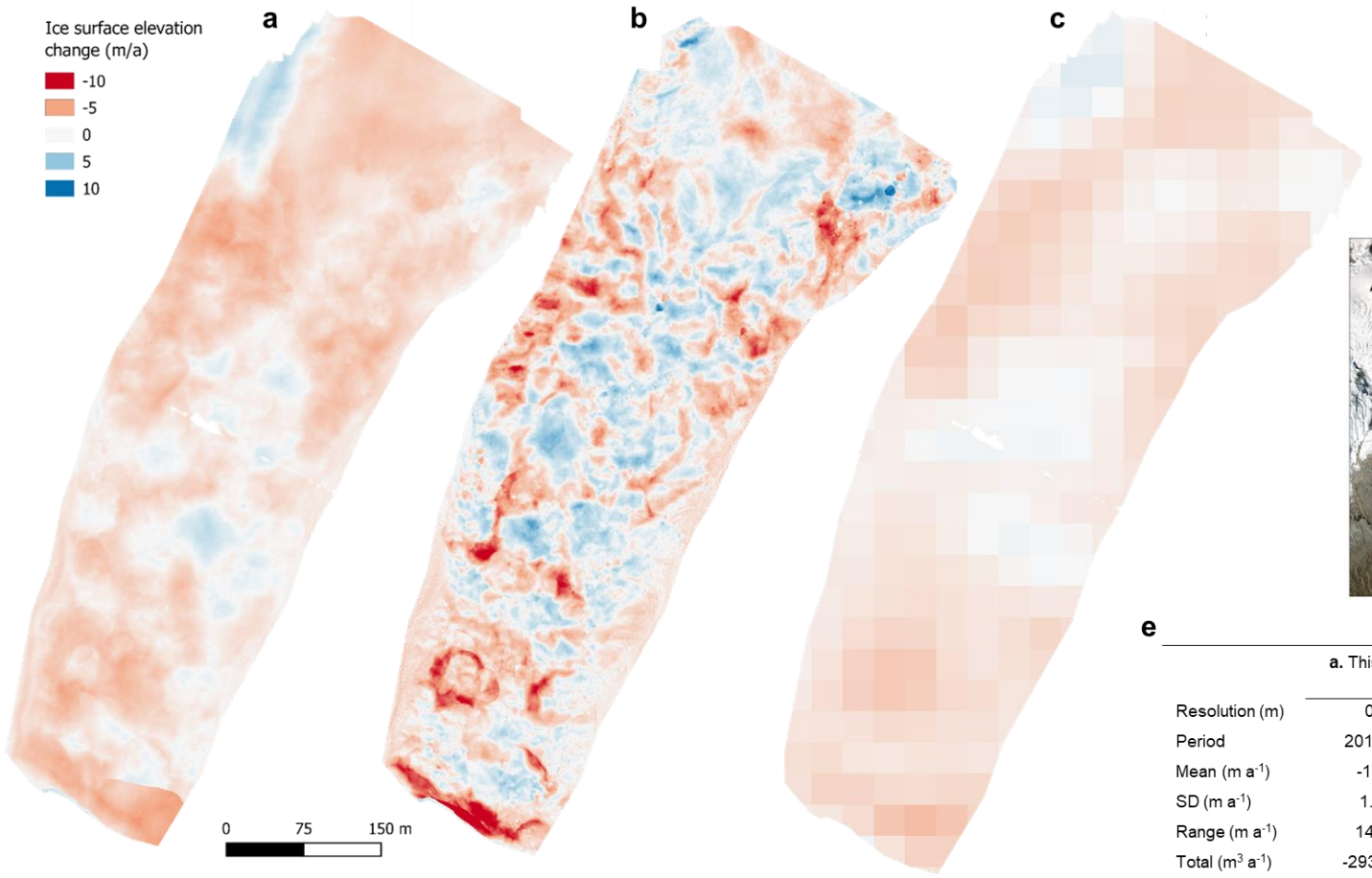

e

	a. This study	b. Wigmore et al. (2017)	c. Seehaus et al. (2019)
Resolution (m)	0.1	0.1	30
Period	2014-19	2014-15	2013-16
Mean (m a^{-1})	-1.43	-0.76	-1.05
SD (m a^{-1})	1.29	2.58	0.80
Range (m a^{-1})	14.21	29.71	4.65
Total (m^3 a^{-1})	-293,000	-156,000	-215,000

Figure 5.2. Ice-surface-elevation change patterns. (a) Surface-elevation changes between 2014 and 2019, calculated from UAV data collected by Wigmore et al. (2017) in 2014 and collected by this study in 2019. (b) Surface-elevation changes between 2014 and 2015, calculated from UAV data collected by Wigmore et al. (2017). (c) Satellite-derived surface elevation changes between 2013 and 2016, from Seehaus et al., 2019. (d) Comparison of the ice-surface-elevation change maps shown in (a-c). The red shaded area in (d) shows the spatial coverage of the maps shown in (a-c).

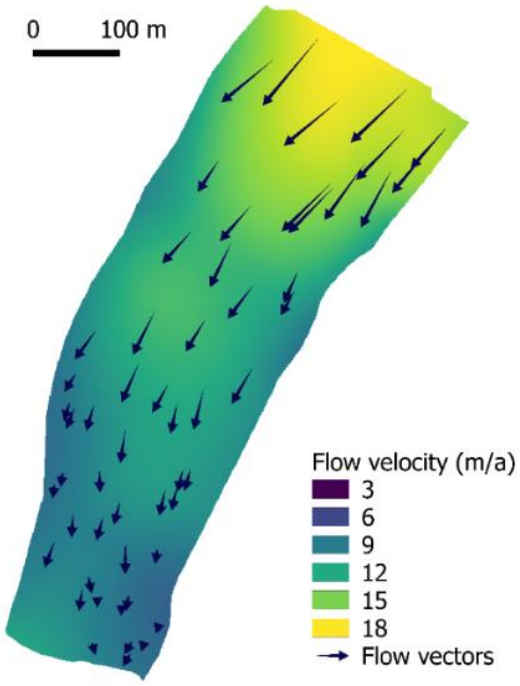

Figure 5.3. Glacier surface-flow map. The start and end positions of each surface feature that was manually tracked between 2014 and 2019 are shown by each arrow. The interpolated ice flow velocities for the study area (shown in Figure 5.2d) is shown by the colour scale.

5.4.2 Supraglacial ice-cliff and pond distribution

The three-dimensional surface area covered by supraglacial ice cliffs within the study area is lowest in 2019 (8,700 m^2), compared to 2014 (11,300 m^2) and 2015 (10,400 m^2) (Figure 5.4c). Ice cliffs covered 4.6%, 4.4% and 3.8% of the total surface area of Llaca Glacier tongue in 2014, 2015 and 2019, respectively. There appear to be no clear patterns in the spatial distribution of supraglacial ice cliffs. However, there is a noticeable absence of ice cliffs near the centre of the uppermost part of the survey area, which is consistent in all three survey years (2014, 2015 and 2019) (Figure 5.4a).

The surface area covered by supraglacial ponds in 2019 (2,000 km^2) is approximately two times greater than in both 2014 and 2015 (Figure 5.4c). There are no obvious spatial patterns in supraglacial pond distribution although it appears that the largest ponds in 2014 were located in the lower half of the survey area, compared to 2019, when the largest ponds were located in the upper half of the

survey area. There is also an absence of supraglacial ice ponds in the same uppermost area of the survey already noted as not hosting supraglacial ice cliffs either (Figure 5.4a-b).

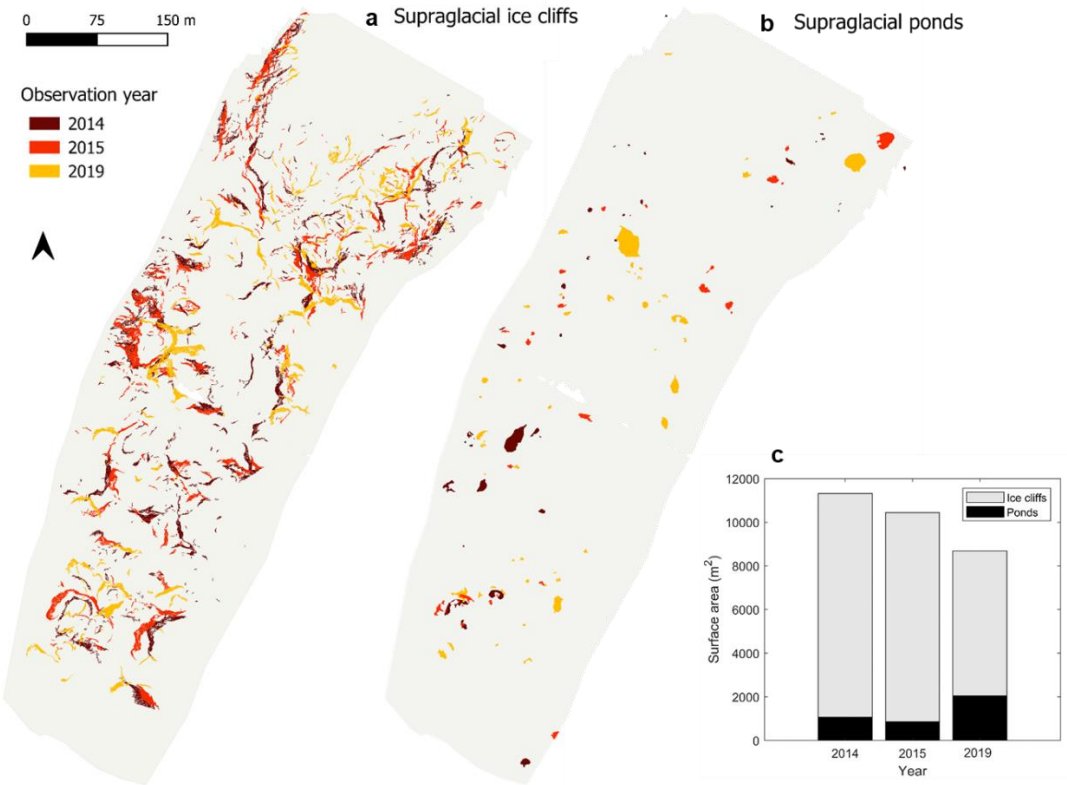

Figure 5.4. Spatial distribution of supraglacial ice cliffs and ponds. (a) Supraglacial ice cliffs on Llaca Glacier tongue in 2014, 2015 and 2019. (b) Supraglacial ponds in 2014, 2015 and 2019. The grey shaded area in (a) and (b) corresponds to the survey coverage shown in Figure 2d. (c) Comparison of the surface area covered by cliffs and ponds between different years.

5.4.3 Supraglacial ice cliff characteristics

The results show that ice cliffs had mean surface slopes of 51.4° in 2014, 50.5° in 2015 and 51.9° in 2019 (Figure 5.5a,c,e). In all three years, at least 85% of ice-cliff covered pixels (10 x 10 cm) had a slope value of between 40° and 60°. The most common ice-cliff surface slopes were 46° in both 2014 and 2015 and 50° in 2019. The results also indicate that supraglacial ice cliffs on Llaca Glacier tongue most frequently face in a south-westerly direction (Figure 5.5b,d,f). In 2014, 2015 and 2019, 44.6 %, 45.2 % and 45.0 % of cliff-covered pixels, respectively, correspond to

aspects of between 180° and 270°. The most common three degrees of cliff aspect were 208°-211° in 2014, 195°-198° in 2015 and 186°-189° in 2019. Cliff aspects observed in 2019 were more concentrated towards the south south-west, with 18.9%

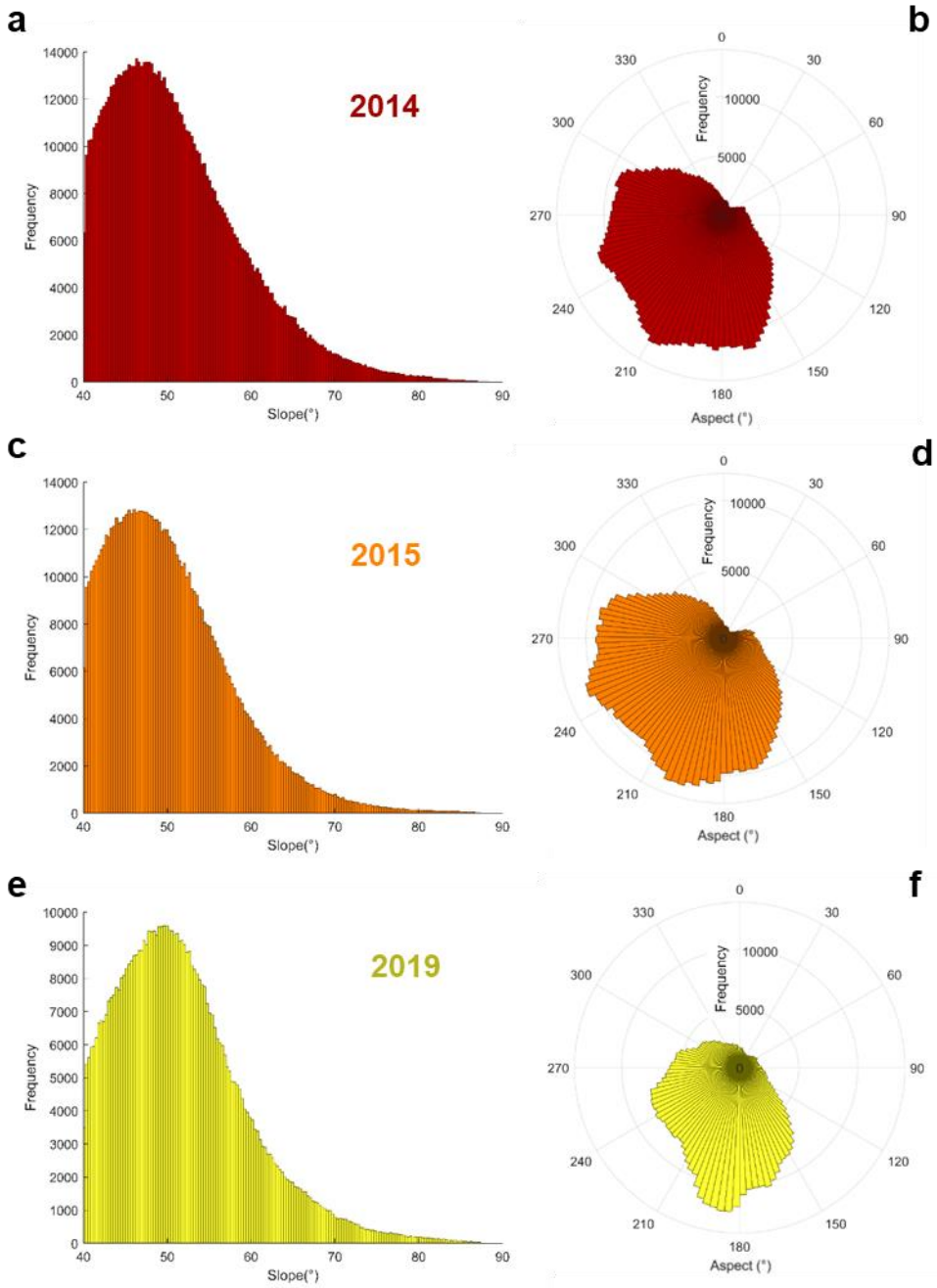

Figure 5.5. Histograms of ice cliff surface slope and aspect. (a), (c) and (e) show the frequency of ice-cliff-covered pixels in relation to surface slope between 40° and 90°, while (b), (d) and (f) show the frequency of ice-cliff covered pixels in relation to surface aspect. Each pixel included within these histograms represents a 10 cm x 10 cm area of the overall ice-cliff-covered area.

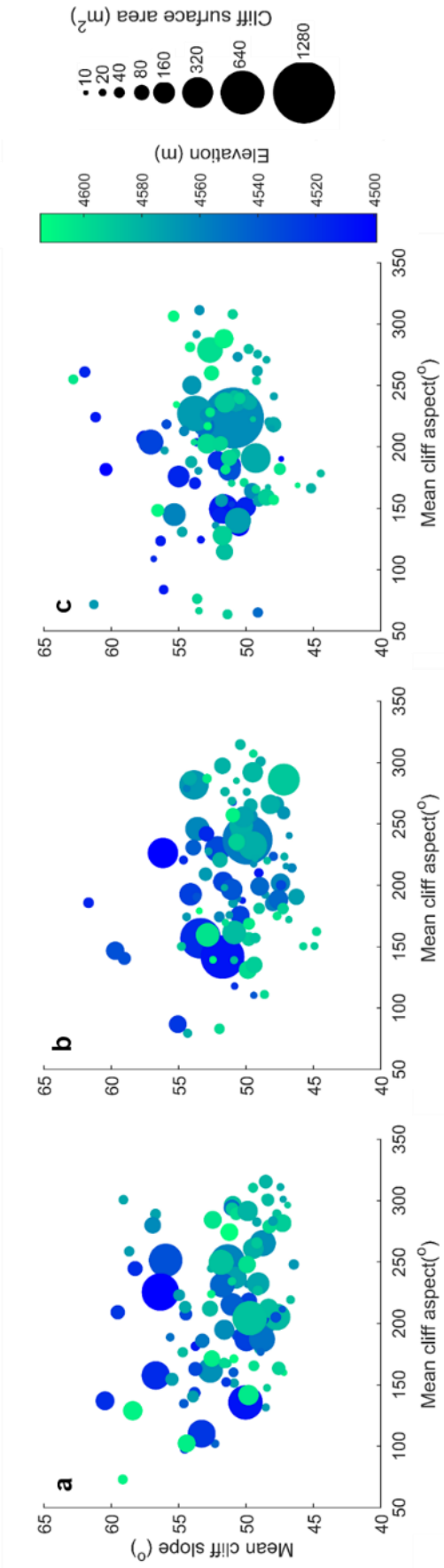

Figure 5.6. Ice-cliff-specific characteristics for the 100 largest ice cliffs surveyed in (a) 2014, (b) 2015 and (c) 2019. The surface area of each cliff is shown by circle size, in addition to the mean elevation (colour scale), aspect (x-axis) and surface slope (y-axis).

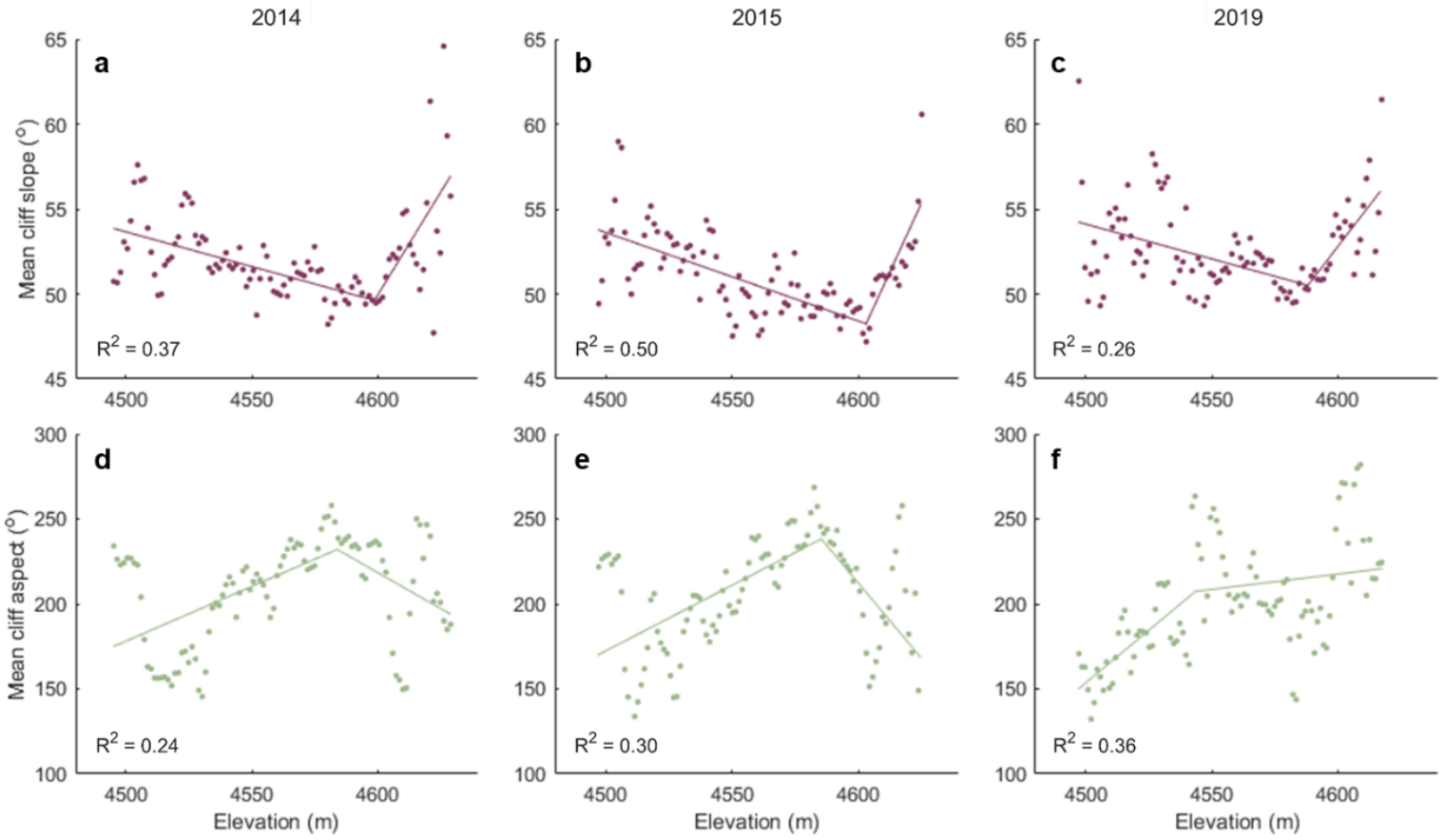

Figure 5.7. Altitudinal trends in ice-cliff slope and aspect. Mean ice-cliff slope (a-c) and aspect (d-f), binned by elevation (100 bins), are shown by the coloured points. Linear regression trends produced from breakpoint analyses are shown by the coloured lines, with corresponding adjusted R^2 values also shown.

of pixels between 180° and 210°, compared to 15.7% and 16.0% in 2014 and 2015 respectively (Figure 5.5b,d,f).

Figure 5.6 shows that, while the total surface area covered by ice cliffs is lowest in 2019, the surface area of the largest cliff is greatest (1,245 m^2) in 2019, while the largest cliffs have surface areas of 836 m^2 and 395 m^2 in 2014 and 2015, respectively. The mean surface slope of the largest cliff is similar in all three years, ranging by only 1.2° (from 49.7° to 50.9°). In all three years, the largest cliff has a south-west-facing mean aspect (204.4° in 2014, 237.1° in 2015 and 223.5° in 2019). In all three years, none of the largest 100 cliffs (Figure 5.6) have a mean north-facing aspect, with a complete absence of cliffs with mean aspects of between 320° and 60°. Additionally, cliffs facing northeast and northwest tend to be relatively small (Figure 5.6). Similarly, cliffs with particularly low or high mean slopes also tend to be relatively small. In 2019, the largest five ice cliffs account for 29% of the total cliff surface area, compared to 18% in 2014 and 25% in 2015.

Altitudinal changes in ice-cliff surface slope and aspect appear to follow similar trends in 2014, 2015 and 2019 (Figure 5.7). Mean surface slope generally decreases with elevation over the lowermost ~ 75 % of the survey area while, in the uppermost portion of the survey area, the ice-cliff slope appears to increase with elevation (Figure 5.7a-c). In all three years, the steepest ice-cliff surface slopes ($>$ ~ 55°) appear to be found either near the terminus or near the top of the survey area. Meanwhile, in all three years, mean ice-cliff aspect increases with elevation within the lower portion of the glacier tongue, from south/southeast to southwest/west (Figure 5.7d-e). However, this trend dissipates in the uppermost portion of the survey area, where there is a wider spread of aspects, from roughly southeast to west.

Our results show that, in all three years (2014, 2015 and 2019), cliff surfaces facing north receive the greatest quantity of incoming shortwave radiation, while cliff surfaces facing directly south receive the least shortwave radiation (Figure 5.8a). Data recorded at the nearby weather stations, during the month before the visible

UAV data were collected (21 August 2019), show that a greater proportion of the total incoming shortwave radiation is received after solar noon compared to before solar noon (Figure 5.8b). In the month preceding UAV data collection, the Cuchillacocha weather station recorded a mean incoming shortwave radiation flux of 159 W m^{-2} in the 12 hour period preceding solar noon, while a greater mean incoming shortwave radiation flux of 256 W m^{-2} was recorded during the 12 hour period following solar noon.

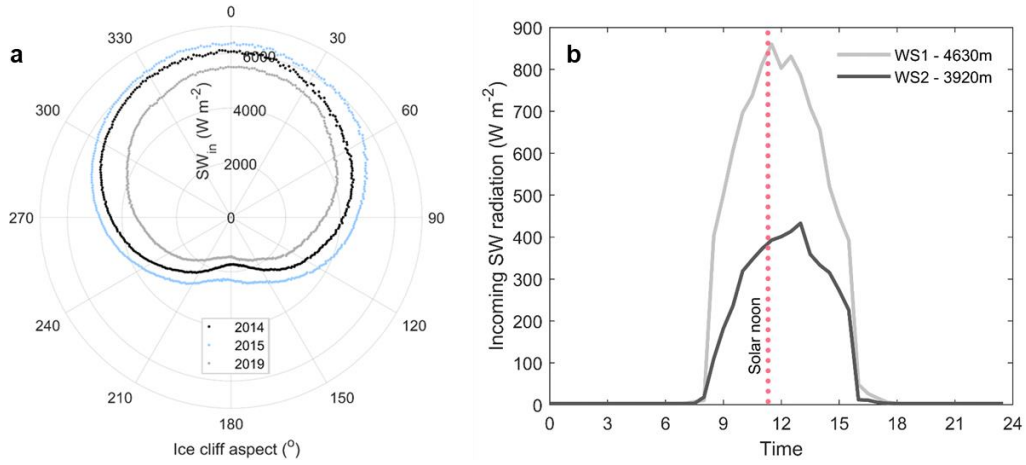

Figure 5.8. Patterns of incoming shortwave radiation. (a) Mean incoming shortwave radiation received by ice-cliff surfaces on Llaca Glacier, binned for each degree of aspect, for 2014, 2015 and 2019. (b) Mean diurnal patterns in incoming shortwave radiation recorded by the Cuchillacocha weather station (WS1: 4630 m a.s.l.) and the lower-elevation Casa de Agua weather station (WS2: 3920 a.s.l.) in the month preceding 19 August 2019 (when the UAV data were collected). Dotted red line shows the average time of solar noon during the month preceding 19 August.

5.4.4 Ice-cliff backwasting rates

Simulated ice-cliff backwasting from 12-26 August 2019 (Figure 5.9) was responsible for 20 % of overall ablation across the survey area, despite ice cliffs covering only 5 % of the survey's surface area. Simulated ice-cliff backwasting occurred at a mean rate of 0.14 cm h^{-1} over this period, with strong diurnal cycles in backwasting rate which peaked between 9:00 and 14:00 each day (Figure 5.9). The

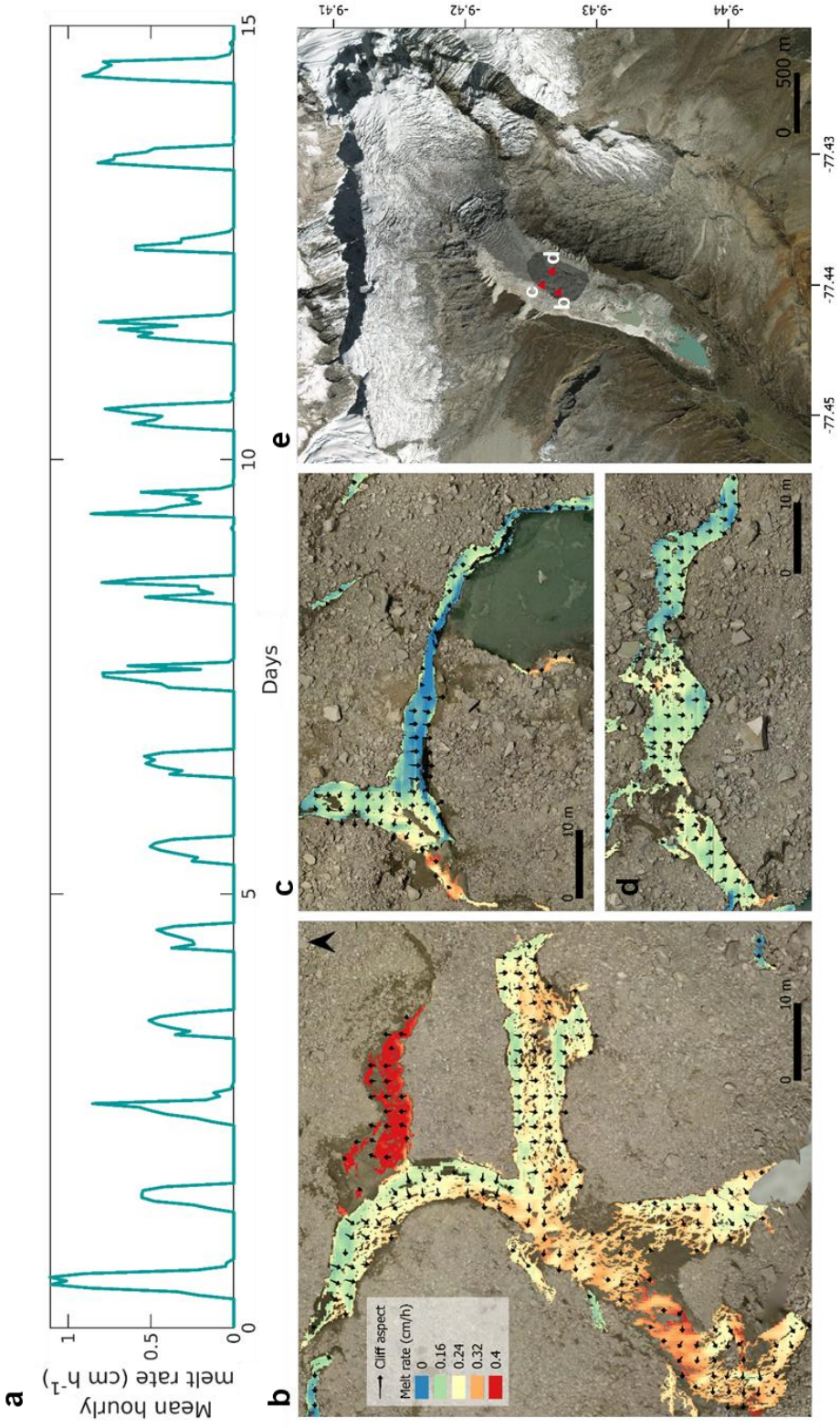

Figure 5.9. Simulated ice-cliff backwasting. (a) Mean hourly melt rate of all ice cliffs within the survey area on Llaca Glacier between 12 and 26 August 2019. (b), (c) and (d) Spatially-distributed melt rates on the three largest ice cliffs within the survey area. The directions in which ice cliffs face are shown by the black arrows. In (e), the location of these cliffs are shown by red triangles (with corresponding panel letters), while the grey shaded area shows the spatial coverage of the cliff backwasting model.

maximum mean hourly cliff backwasting rate across the survey area (0.89 cm h^{-1}) occurred on 12 August at 14:00.

The model results also indicate that ice-cliff backwasting rates are highly spatially heterogeneous (Figure 5.9), with mean melt rates having a variance of 0.19 cm h^{-1}. Additionally, backwasting rates often vary significantly across the surfaces of individual ice cliffs, particularly where ice cliffs have complex geometry with multiple limbs orientated in different directions. The north-facing components of ice cliffs have the greatest backwasting rates, while the south-facing parts have the lowest backwasting rates. This pattern is exemplified in Figures 5.9b-d, which display the distributed melt rates of the three largest ice cliffs within the survey area. There are no clearly-distinguishable gradients in backwasting rates from the bases to crests of ice cliffs within the survey area.

5.4.5 Radiative fluxes at ice-cliff surfaces

Figure 5.10 shows the temporal variations in the radiative fluxes at ice-cliff surfaces over the 15 day simulation period. The results indicate positive mean net shortwave and sensible energy fluxes of 106 and 93 W m^{-2}, respectively. By contrast, negative mean net longwave and latent energy fluxes of -103 and -81 W m^{-2}, respectively, are simulated for the same period. There are strong diurnal cycles in net shortwave, sensible and latent energy fluxes at ice-cliff surfaces, with mean hourly fluxes peaking at maximum values of 583, 499 and 27 W m^{-2}, respectively. Meanwhile, the results indicate low temporal variations in the net longwave flux, which ranges from a minimum mean hourly flux of -114 Wm^{-2} to a maximum mean hourly flux of -84 Wm^{-2}.

Breaking down the individual components of the net longwave flux shows that, overall, 44 % more longwave radiation is emitted onto ice-cliff faces from the atmosphere than from the surrounding debris (Figure 5.10b). The mean hourly flux of longwave radiation emitted by the debris onto ice cliffs ranges by a total of 57 W m^{-2}, while the longwave radiation from the atmosphere ranges by a total of only 24

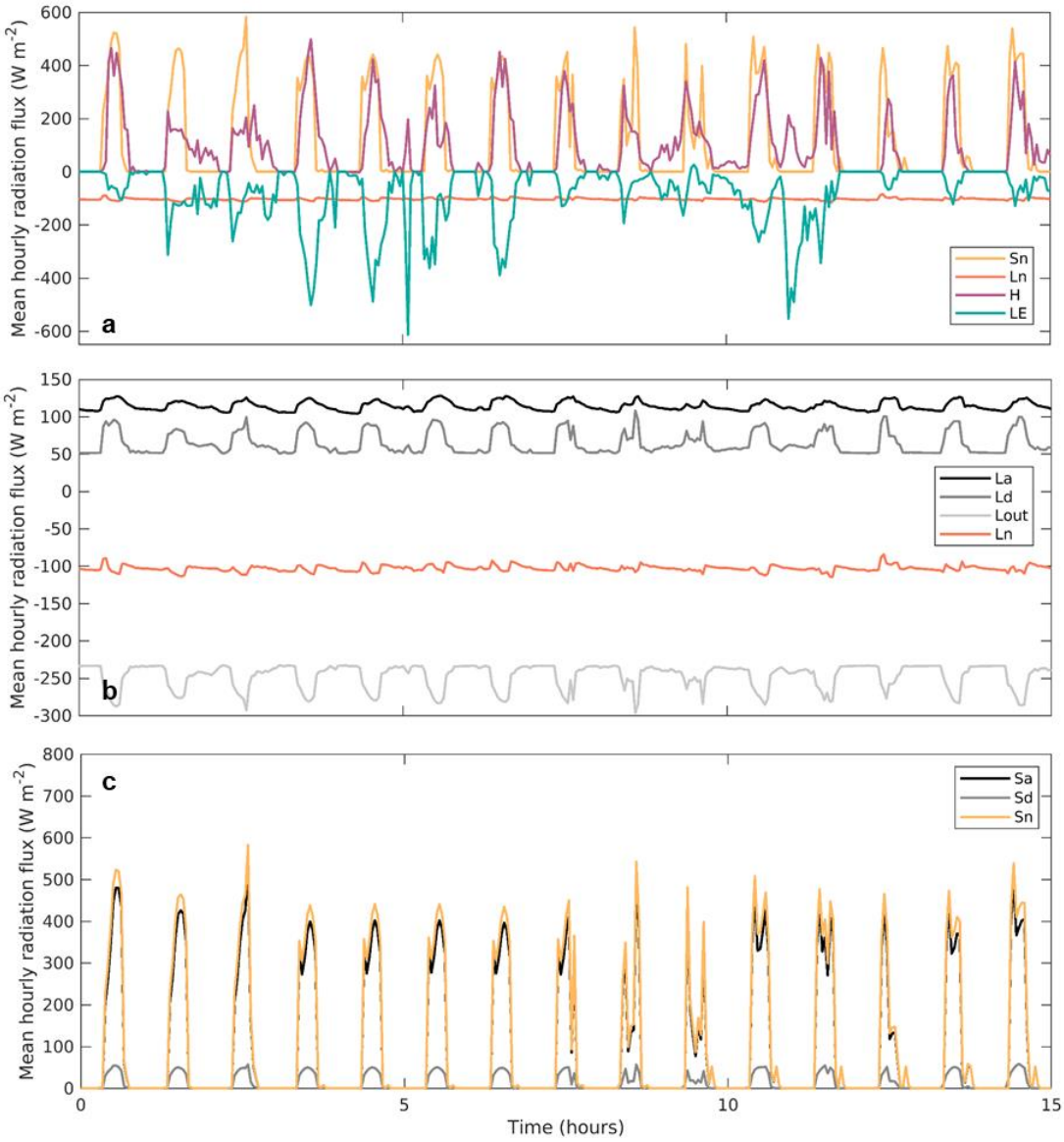

Figure 5.10. Simulated mean hourly radiative fluxes on ice cliff faces between 12 and 26 August 2019. (a) Net shortwave (S_n), longwave (L_n), sensible (H) and latent (LE) fluxes. (b) and (c) show the individual components of the longwave and shortwave fluxes, respectively, including the longwave flux from the atmosphere onto ice cliffs (L_a), the longwave flux emitted by the debris onto ice cliffs (L_d), the outgoing longwave flux emitted by ice cliffs (L_{out}), the shortwave flux from the atmosphere that is absorbed by cliffs (Sa) and the shortwave flux reflected by the debris that is absorbed by cliffs (L_d).

W m^{-2}. Throughout the 15-day period, the mean outgoing longwave flux consistently outweighs the combined incoming longwave fluxes from the atmosphere and surrounding debris, therefore maintaining a consistently negative net flux. The broken-down model results also show that shortwave radiation from the atmosphere

accounts for 89 % of the net shortwave flux, while shortwave radiation reflected by the debris onto ice-cliff surfaces contributes only the remaining 11 % (Figure 5.10c).

Figure 5.11 shows examples of the spatial distribution of the components of the shortwave and longwave radiative fluxes for the largest ice cliff on Llaca Glacier, while Supplementary Figures 5.S2 - 5.S9 shows further examples for other smaller ice cliffs. The south-facing cliffs generally receive the most longwave radiation from the atmosphere (Figure 5.11c), while north-facing cliffs receive the most longwave radiation emitted by the surrounding debris (Figure 5.11d). The tops of ice cliffs receive less longwave radiation from the atmosphere compared to nearer the bases of cliffs, while there is no obvious pattern in base-to-crest gradient in longwave radiation emitted from the debris onto ice-cliff faces (Figures 5.11c-d). Overall, the net longwave flux is generally slightly less negative at cliff bases compared to further up cliff faces, where the net longwave flux is even more negative (Figure 5.11b).

The model results also indicate that north-facing cliffs receive the most shortwave radiation from the atmosphere, while cliffs facing south receive the least (Figure 5.11f). South-facing cliffs receive less shortwave radiation from the atmosphere near their crests compared to near their bases, while north-facing cliffs tend to have a more even distribution of shortwave radiation (Figure 5.11g). North-facing cliffs receive the most shortwave radiation reflected from the surrounding debris, while south-facing cliffs receive the least (Figure 5.11h). The results do not indicate any strong base-to-crest gradients in shortwave radiation reflected by the debris onto ice-cliff faces. Overall, the net shortwave flux is greatest on north-facing cliff faces and lowest on south-facing cliff faces.

Overall, the net energy flux is greatest for north-facing cliffs and cliffs facing in all other directions receive relatively low net energy fluxes in comparison. The results also indicate that the majority of cliff faces, regardless of aspect, appear to receive greater net fluxes at their bases relative to their tops.

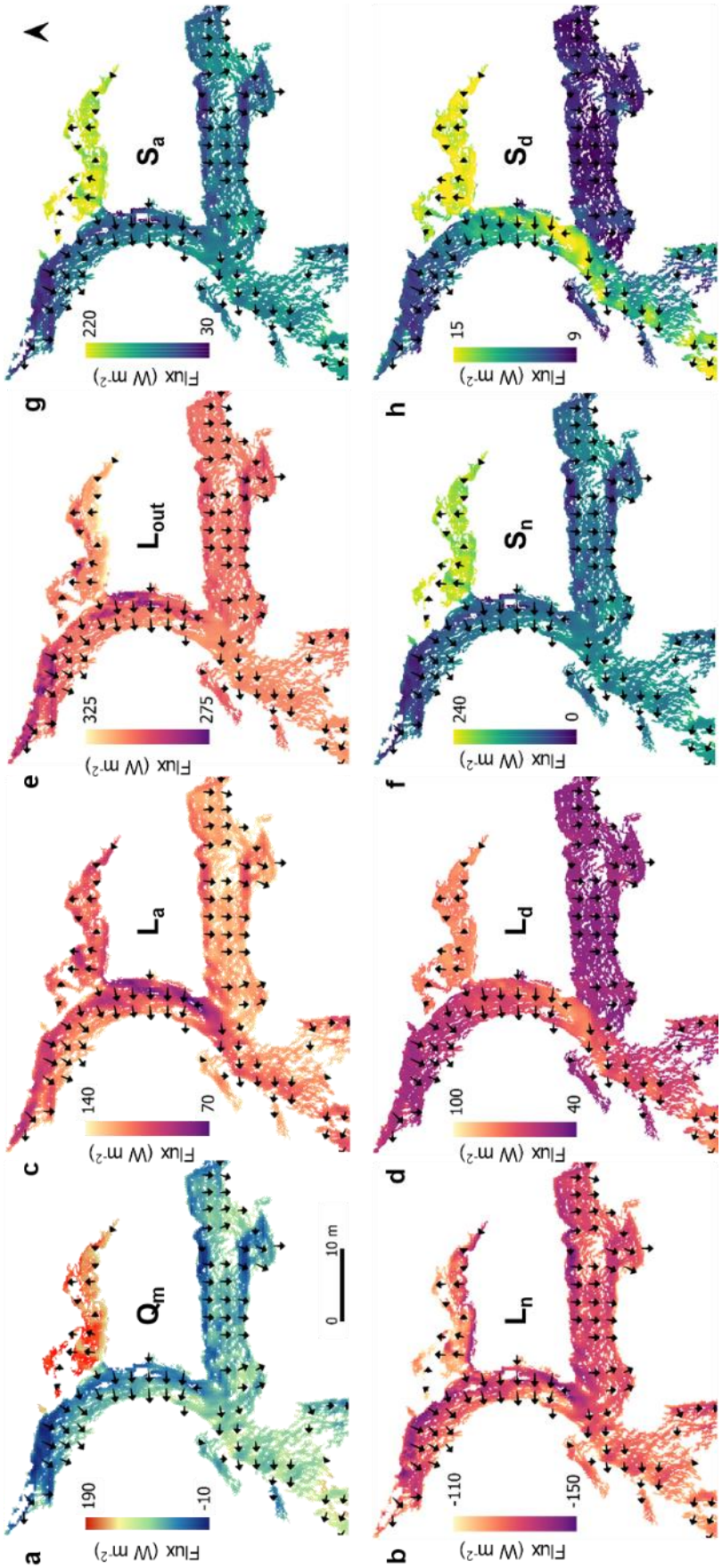

Figure 5.11. Mean simulated radiative fluxes on the largest supraglacial ice cliff on Llaca Glacier tongue for 12 to 26 August 2019. Black arrows show the directions in which different sections of the ice cliff face. (a) Total energy flux (Q_m); (b) Net longwave flux (L_n); (c) –(e) Individual components of the net longwave flux (L_a, L_d and L_{out}); (f) Net shortwave flux (S_n); (g)-(h) Individual components of the net shortwave flux (S_a and S_d).

5.5 Discussion

5.5.1 Evolution of Llaca Glacier tongue

The results show a clear pattern of ice-surface lowering between 2014 and 2019 (Figure 5.2). The mean annual surface lowering rate observed in this study is nearly double the rate observed by Wigmore et al. (2017) between 2014 and 2015, indicating that ice thinning may have accelerated over the past several years. However, further data from a greater range of years are required to confirm a speed-up in ice thinning. The mean annual ice surface lowering rate observed in this study was 37% greater than the mean surface lowering observed from satellite data by Seehaus et al. (2019) between 2013 and 2016. This difference could arise either from the differences in precision between the two studies, or differences in melt rates between the two periods, or a combination of both. Regardless, the results of this study and Wigmore et al. (2017) indicate high spatial variability in ice-surface-elevation change rates across Llaca Glacier tongue (Figure 5.2) that is not captured by present satellite observations. The higher resolution of the UAV observations allows us to capture the advection of surface features as the ice flows downhill, which appears predominantly responsible for the high variability in elevation change. Spatially-heterogeneous melt rates, also owing their detection to the higher resolution of UAV surveying, and caused by ice-cliff backwasting and supraglacial debris-thickness variability across the ice tongue, likely also drive the spatial variability in ice-surface lowering rates. Overall, we have found that with UAV surveying we detect potentially greater and more variable rates of ice loss from Llaca Glacier than inferred from satellite observations, suggesting that future regional satellite-derived mass balance observations would benefit from validation and calibration with further UAV-based data collection on several glaciers in the Cordillera Blanca.

The increase in ice flow velocity with distance upstream on the debris-covered tongue of Llaca Glacier (Figure 5.3) matches similar ice-flow behaviour on debris-covered glaciers in other mountain regions (e.g. Anderson and Anderson,

2016; Thompson et al., 2016; Loriaux and Ruiz, 2021). A similar up-glacier velocity increase was observed at Jatunraju Glacier (Emmer et al., 2015), which is located approximately 50 km northwest of Llaca Glacier, where it was also found that velocities in the lower portion of the glacier had decelerated significantly to less than a quarter of ice flow velocities previously-observed in the 1960s to 1980s (Lliboutry, 1977; Ames, 1984; Emmer et al., 2015). In comparison to the velocities observed by Wigmore et al. (2017) at Llaca Glacier tongue between 2014 and 2015, the mean annual velocities observed between 2014 and 2019 were approximately one third lower, indicating that a similar pattern of deceleration may be occurring in the lower portion of Llaca Glacier. This apparent deceleration could potentially have arisen from a reduction in gravitational driving stress due to ice thinning, a pattern which has been observed on many glaciers in High Mountain Asia (e.g. Neckel et al., 2017; Dehecq et al., 2019), although further evidence from additional years is required to confirm ice deceleration on Llaca Glacier tongue.

5.5.2 Contribution of ice-cliff backwasting towards overall mass loss

The results of this study indicate that, despite covering only 5 % of the survey surface area, the backwasting of ice cliffs is responsible for a fifth of ice loss across the survey area during the 15-day simulation period. This finding suggests that, similar to ice cliffs on debris-covered glaciers in higher-latitude regions such as High Mountain Asia (e.g. Sakai et al., 1998; Thompson et al., 2016) and Alaska (Anderson et al., 2021), supraglacial ice cliffs are likely to be contributing disproportionately towards the overall melt rates of debris-covered glaciers in the Cordillera Blanca. This underscores the importance of further studies of ice-cliff backwasting on debris-covered glaciers in low-latitude regions in order to improve the parameterisation of glacial melt rates and hydrological runoff in glaciological models.

In a study of Lirung Glacier, Nepal, Buri et al. (2021) showed an up-glacier reduction in melt enhancement caused by ice-cliff backwasting, from the glacier terminus to the upper portion of the debris-covered area, as debris thickness reduced

and sub-debris melt rates increased, therefore contributing towards a greater proportion of melt rates. It is therefore possible that in the lower part of Llaca Glacier tongue, which was not simulted in this study, ice-cliff backwasting had an even greater contribution towards overall rates of mass loss, since the sub-debris melt contribution may be further limited by a thicker debris layer. In future, high-resolution simulations over greater spatial and temporal scales and on a variety of glaciers across the region would be highly beneficial in order to establish the regional importance of ice-cliff backwasting in amplifying meltwater production rates in the Cordillera Blanca.

The results of this study also show that, during the 15-day simulation period, north-facing ice-cliff faces within the survey area had the greatest backwasting rates, as exemplified for the multidirectional ice cliff shown in Figure 5.9b, while south-facing cliff faces generally had the lowest backwasting rates (Figure 5.9b-d). This indicates that, relative to their surface area, north-facing cliffs are likely to contribute more towards the mass loss of the ice tongue. However, since north-facing cliff faces cover a much smaller proportion of the glacier surface than cliffs facing south/southwest (Figure 5.5b,d,f), they are likely to play a relatively small role in controlling overall rates of mass loss. Conversely, despite south/southwest-facing cliffs having slower backwasting rates (Figure 5.9b-d), these cliffs have considerably better rates of survival (Figure 5.5b,d,f). Therefore, the backwasting of south/southwest-facing cliffs is likely to provide a more significant contribution towards overall rates of mass loss on Llaca Glacier tongue.

5.5.3 Factors driving ice-cliff survival and evolution

The spatial distribution of radiative fluxes across ice-cliff faces is likely to play a key role in driving ice-cliff survival on Llaca Glacier. As previously discussed, southwest/south-facing cliff faces are most prevalent on Llaca Glacier tongue, while north-facing cliffs are relatively rare (Figure 5.5). These findings indicate that supraglacial ice cliffs on Llaca Glacier may be behaving similarly to ice cliffs on debris-covered glaciers in the northern hemisphere, where studies have shown that

north-facing cliffs survive preferentially over south-facing cliffs, which generally flatten and disappear over time (e.g. Kraaijenbrink et al., 2016; Watson et al., 2017; Buri and Pelliciotti, 2018; Steiner et al., 2019). This trend has previously been linked to the aspect-dependent distribution of radiation across cliff surfaces, with surviving ice cliffs receiving an equal or even greater net radiation flux near their bases compared to the radiation flux received towards their crests, allowing these ice cliffs to retain or steepen their surface slopes (e.g. Sakai et al., 1998; Buri and Pelliciotti, 2018; Sakai et al., 2018; Buri et al., 2021). It is therefore likely that radiative flux distributions at least partially determine the survival of supraglacial cliffs on the surface of Llaca Glacier.

Previous studies have indicated that longwave radiation emitted by the debris (L_d) is generally most concentrated near the bases of ice cliffs, therefore playing a role in the survival of supraglacial ice cliffs (e.g. Steiner et al., 2015; Buri et al., 2016). However, the results of this study do not show any identifiable base-to-crest gradients in L_d, as demonstrated for the largest cliff on Llaca glacier tongue (Figure 5.11d). Meanwhile, longwave radiation from the atmosphere (L_a) appears generally to be slightly lower near the crests of ice cliffs (Figure 5.11c), which could potentially result from a reduced sky view factor near the tops of ice-cliff faces due to the debris directly above cliff faces. North-facing cliffs appear to receive the most longwave radiation emitted by the debris (L_d), as well as the most shortwave radiation reflected by the debris (S_d) (Figure 5.11d,h). The most likely explanation for this pattern is that north-facing cliffs face up-glacier, therefore are likely to have the greatest debris view factor. Likewise, north-facing cliffs appear to receive the smallest flux of longwave radiation from the atmosphere (L_a) (Figure 5.11c), which is likely to result from these up-glacier-facing cliffs having a lower sky view factor. However, north-facing cliffs appear to receive the greatest flux of shortwave radiation from the atmosphere (S_a), indicating that, although the sky view factor is smaller, the higher incidence angle results in a higher overall shortwave flux (S_n) on north-facing cliffs (Figure 5.10f,g).

The finding that ice cliffs are most commonly orientated towards the southwest, as opposed to directly south, suggest that another factor beyond the radiative forcing discussed above is likely to be contributing towards ice-cliff survival at Llaca Glacier. Previous research on the Lirung Glacier, Nepal, indicated that northwest-facing cliffs have a greater survival rate than north/northeast-facing cliffs (in the Northern Hemisphere), since the solar input is greatest during the morning (when the sun is towards the east) as a result of monsoon-driven afternoon cloud cover (Buri and Pellicciotti, 2018). This study showed that for northeast-facing cliffs, as a consequence of these diurnal patterns in solar input, the positive base-crest gradient in incoming shortwave radiation outweighs the negative base-to-crest gradient in longwave radiation emitted by the debris, resulting in cliff flattening and reburial. Contrastingly, for northwest-facing cliffs, the positive base-to-crest incoming shortwave gradient is not sufficient to outweigh the negative base-to-crest longwave gradient, allowing cliffs to retain or even steepen their surface slopes (Buri and Pellicciotti, 2018). Therefore, if diurnal patterns in solar input were also responsible for the survival of southwest-facing cliffs on Llaca Glacier, the shortwave radiation would likely be greater in the morning, when the sun is towards the east. However, our results indicate that, during the three months preceding the UAV data collection in 2019, the total flux of incoming shortwave radiation recorded at Cuchillacocha weather station was lower in the morning compared to in the afternoon (Figure 5.8b), indicating that diurnal patterns in solar input are unlikely to be responsible for the abundance of southwest-facing cliffs.

The orientation of ice cliffs appears generally to correlate with the flow direction of the glacier in all three survey years (2014, 2015 and 2019), implicating a role for ice dynamics in the formation, development and/or preservation of supraglacial ice cliffs on Llaca Glacier. As shown in Figure 5.7d-f, mean ice-cliff aspect initially increases up-glacier, from a south/southeast-facing direction near the terminus towards a southwest-facing direction approximately 100 m elevation up-glacier from the terminus (Figure 5.7d-f). This shift in aspect could potentially be linked to changes in ice-flow direction, since the glacier flows in a roughly southward

direction near the terminus, in comparison to a roughly southwest-facing direction further up-glacier (Figure 5.3). However, in the uppermost portion of the survey area, this trend in ice-cliff aspect dissipates, if anything reversing (Figure 5.7d-e). This indicates the possibility that ice cliffs could evolve over time to face in a perpendicular direction to the direction of ice flow, since ice cliffs near the upper portion of the debris-covered zone may have formed more recently, while cliffs located further down-glacier may have had a longer time to adjust in orientation to match the ice flow direction. However, further evidence is required in order to investigate the causes of this apparent trend in ice-cliff aspect.

The surface slope of supraglacial ice cliff faces appears initially to decrease up-glacier from the terminus of Llaca Glacier (Figure 5.7a-c). A potential explanation for this is that the ice cliffs that survive over the melt season are steepening over time as they are advected down-glacier with ice flow. Another potential explanation could be that as debris thickness decreases up-glacier from the terminus, the longwave flux emitted from the debris may decrease as a result of the reducing debris surface temperature, resulting in reduced ablation at the base of ice cliffs which could prevent cliff steepening. Similar to the up-glacier trend in cliff aspect, the decreasing up-glacier trend in cliff surface slope appears to be interrupted or even reversed in the uppermost portion of the debris-covered tongue. A potential explanation for this could be that where debris is below the critical thickness, the mechanisms driving ice-cliff formation may be different. As shown in Figure 5.4a, ice cliffs in the uppermost portion of the survey area appear to be orientated around an area devoid of ice cliffs, which corresponds with a local bulge in glacier surface elevation (Figure 5.1a). In this area, the ice cliffs appear to run parallel to the edge of this surface bulge, towards a central localised depression down-glacier from this area (Figure 5.4a). This pattern indicates that ice cliffs in this area could potentially be forming along supraglacial streams as a result of channel incision, indicating that hydrology may act as a cliff-forming mechanism in the upper area of the ice tongue. This provides another potential explanation for the disruption of the general

correlation between distance up-glacier and cliff aspect in the upper area of the debris-covered zone (Figure 5.7a-c).

The spatial coverage of supraglacial ice cliffs across the survey area on Llaca Glacier in 2019 (8,700 m^2) was significantly lower than in 2014 (11,300 m^2) and 2015 (10,400 m^2) (Figure 5.4c). This apparent reduction in ice-cliff coverage over time indicates that the contribution of ice-cliff backwasting towards overall rates of mass loss could potentially be decreasing. However, seasonal ice-cliff evolution may also be contributing towards the observed differences in ice-cliff coverage between years, since the 2019 survey was conducted on 21 August while the 2014 and 2015 surveys were conducted on 23 and 28 July, respectively. Similar to patterns observed in High Mountain Asia (Watson et al., 2017; Miles et al., 2020), the results indicate that the largest ponds on the tongue of Llaca Glacier were connected to supraglacial ice cliffs in all 3 years (2014, 2015 and 2019). The results also indicate that, as observed by Watson et al. (2017) in the Himalaya, the most irregularly-shaped ponds on Llaca Glacier tongue were bordered by ice cliffs, while ponds independent from ice cliffs were generally more circular. Previous studies have shown that ablation of supraglacial ice cliffs sustains these larger, irregularly-shaped meltwater ponds (e.g. Röhl, 2008; Steiner et al., 2019; Miles et al., 2020). In 2019, supraglacial ponds covered approximately double the surface area covered in 2014 and 2015. Previous studies in regions such as High Mountain Asia and the Southern Alps have highlighted that surface lowering and glacier stagnation promote supraglacial pond formation and expansion (e.g. Watanabe et al., 1994; Richardson and Reynolds, 2000; Röhl, 2008; Watson et al., 2016), therefore it is possible that the observed increase in ponded area on Llaca Glacier tongue has been driven by the persistent ice-surface lowering observed.

5.5.4 Limitations and recommendations for future studies

One limitation of this study is that the sub-debris melt rates which were used in conjunction with the simulated ice-cliff backwasting rates to estimate the contribution of cliff backwasting towards overall rates of mass loss were simulated

using daily mean meteorological data. While Nicholson and Benn (2006) found that the use of daily mean values produces realistic sub-debris melt rates, it is possible that the accuracy of sub-debris melt rates simulated in this study is impacted by nonlinear relationships between meteorological parameters and sub-debris ablation.

A limitation of the model used to estimate cliff backwasting rates is that the estimation of longwave radiation emitted by the debris assumes a linear vertical debris temperature gradient through the debris layer. Consequently, debris surface temperatures may be underestimated during the middle of the night and overestimated during the middle of the day, when temperature gradients are likely to be nonlinear (Nicholson and Benn, 2006), leading to underestimation of the longwave radiation flux emitted by the debris during the night (L_d) and overestimation of L_d during the day. During the night, since net radiation fluxes at ice cliff surfaces are strongly negative, simulated melt rates are zero regardless of any underestimations of debris surface temperature, therefore the impact of our assumption is negligible. To test the impact of our assumption on simulated melt rates during the middle of the day, we calculated L_d using UAV-derived surface temperatures at midday on 19 August 2019 and compared the results to simulated L_d at midday on 19 August 2019. We found that overestimation of debris surface temperature led to a maximum overestimation of L_d of 14 %, with a maximum impact of 3 % on the simulated net radiation flux (Q_m). Consequently, our assumption will impact simulated cliff backwasting rates rates by 3 % or less, with impacts expected to be considerably lower towards early morning and late afternoon, when temperature gradients are less nonlinear. Nevertheless, in future, a more complex model of hourly debris surface temperature could be developed in order to account for nonlinear temperature gradients within the debris layer, based on vertically-profiled debris temperature time-series measurements.

Sensitivity analyses show that the ice-cliff backwasting model is particularly sensitive to wind speed and direction, as well as moderately sensitive to air temperature and ice-cliff surface slope (Table 5.S1), all of which impact the turbulent heat fluxes. Since wind speed and direction are often highly variable above

debris-covered glacier surfaces as a result of local topographic differences (Bonekamp et al., 2020), future studies which parameterise small-scale variations in these parameters will be beneficial for improving estimates of the overall energy fluxes which drive ice-cliff backwasting.

To determine whether it was possible to increase the computational efficiency of the model by using a daily model time step, as opposed to an hourly time step, we tested the use of daily mean meteorological data to simulate the backwasting rates of ice cliffs. Comparison of the daily model results to the hourly model results indicated that using daily mean meteorological data was likely to result in an underestimation of cliff melt rates, with daily melt rates calculated from the daily model being less than half of those estimated from the hourly model. This demonstrates the importance of using sub-daily model time steps in order to simulate the backwasting rates of supraglacial ice cliffs effectively.

Our study demonstrates that a low-cost multirotor drone can be used to collect high-resolution aerial imagery suitable for detailed analysis of the surface morphology of mountain glaciers. Using imagery collected using an off-the-shelf DJI Phantom 4 with a built-in visible camera, we were able to produce 10 cm-resolution maps of ice surface-elevation change and detailed ice flow maps of Llaca Glacier tongue. We found that, while the flight time that can be obtained from each drone battery is approximately halved due to the additional power required to lift the UAV in thin-air conditions, the DJI Phantom 4 (P4) was able to fly effectively at high altitudes of up to 4700 m a.s.l., demonstrating the potential for compact multirotor drones to be used to conduct detailed future studies of high-altitude debris-covered glaciers.

5.6 Conclusions

This study has investigated the characteristics, development and ablation contribution of supraglacial ice cliffs on the debris-covered tongue of Llaca Glacier, Cordillera Blanca, using high-resolution, multi-temporal UAV data. The results

indicate that, similarly to debris-covered glaciers in higher-latitude regions, the backwasting of supraglacial ice cliffs contributes disproportionately towards the overall melt rates of Llaca Glacier. More specifically, we found that while ice cliffs only covered 5 % of the survey area, they were responsible for 20 % of the ablation within this area during the 15-day simulation period in August 2019. The results also suggest that the survival of ice cliffs is predominantly controlled by aspect, with south/southwest-facing cliffs surviving preferentially over north-facing cliffs. We found that, while the distribution of radiative fluxes is likely to principally drive ice-cliff survival, other factors such as ice flow dynamics and supraglacial hydrology are also likely to be playing a role in regulating ice-cliff evolution. Overall, the results of this study highlight the need for increased research attention to be placed on the mechanisms controlling the mass losses of tropical debris-covered glaciers, in order to simulate more accurately the future meltwater contribution towards downstream water resources in low-latitude regions. Further detailed UAV-based studies of the dynamic behaviour of debris-covered glaciers are also needed in order to calibrate satellite-derived observations and glacier evolution models.

5.7 Supplement

Table 5.S1. Model sensitivity analysis results. Percentage changes in the mean simulated ice-cliff backwasting rate in response to changes in input parameter values are shown. Results are based on day 1 of the model run (12 August 2019).

	Input parameter change	Mean change in M (%)
S_{in}	+10 % -10 %	7.6 -7.6
L_{in}	+10 % -10 %	2.2 -2.1
T_{air}	+1 °C -1 °C	10.5 -10.1
H_R	+5 % -5 %	3.8 -7.4
u	+1 m s^{-1} -1 m s^{-1}	19.7 -26.9
W_D	+45 ° -45 °	0.5 -23.7
A	+10 ° -10 °	-2.7 2.1
B	+10 ° -10 °	10.2 -8.6
ε	+0.02 -0.02	-0.9 0.9
α	+0.1 -0.1	-8.4 8.4
h_c	+1 m -1 m	3.0 -2.9
T_S	+1 °C -1 °C	-0.8 0.9
T_d	+5 °C -5 °C	1.0 -1.0

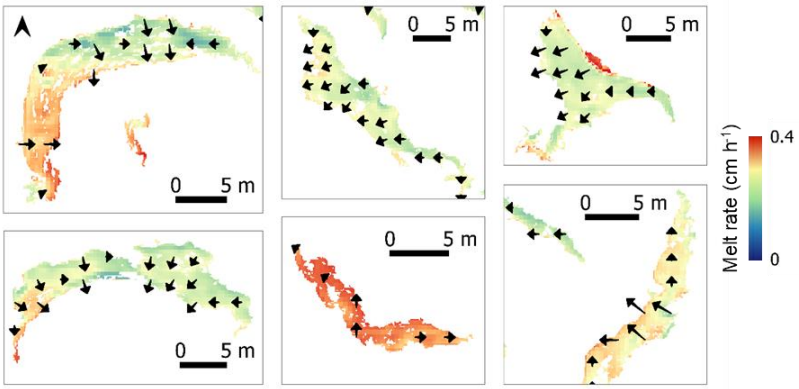

Figure 5.S1. Simulated ice-cliff backwasting rates. Additional examples of supraglacial ice cliffs, to supplement those shown in Figure 5.9. All examples are of supraglacial ice cliffs within the shaded grey area in Figure 9e.

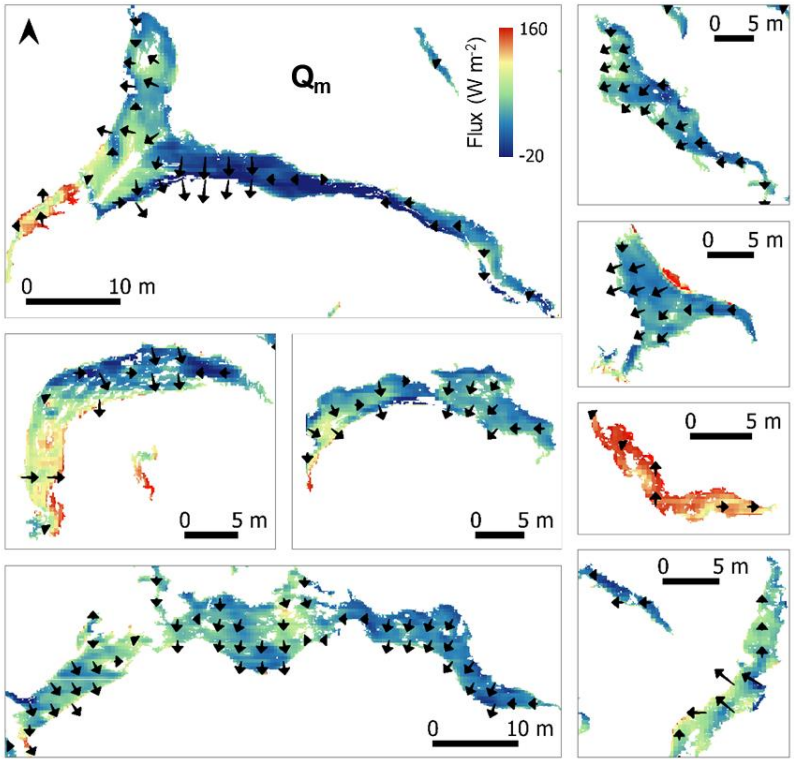

Figure 5.S2. Mean net radiative flux (Q_m) distribution between 12 and 26 August 2019. Additional examples of supraglacial ice cliffs (to supplement the largest cliff shown in Figure 5.11) are given here. Black arrows show the directions in which different sections of the ice cliff face. All examples are of supraglacial ice cliffs within the shaded grey area in Figure 9e.

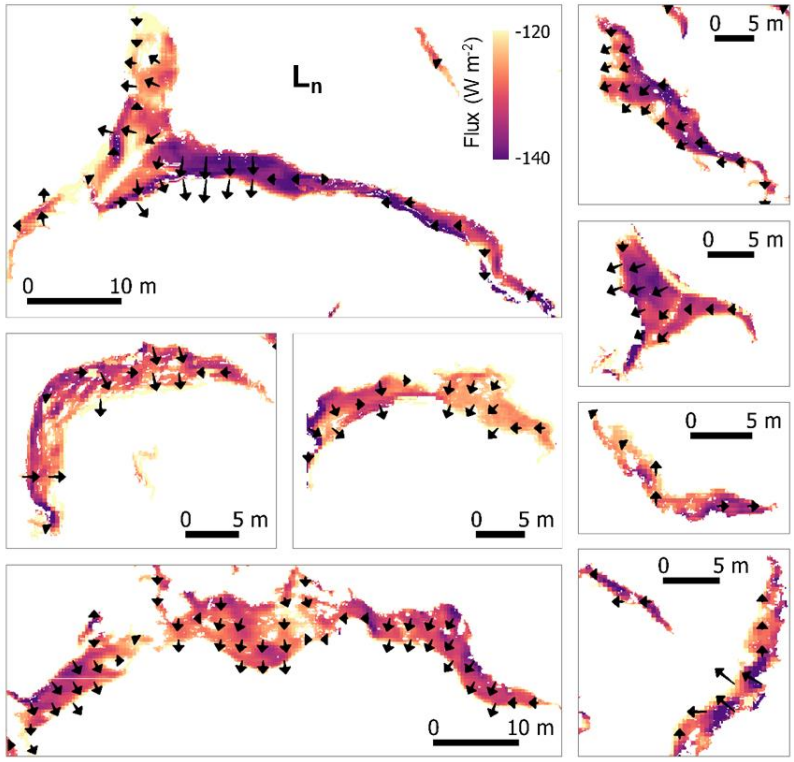

Figure 5.S3. Mean net longwave flux (L_n) distribution between 12 and 26 August 2019. Additional examples of supraglacial ice cliffs (to supplement the largest cliff shown in Figure 5.11) are given here. Black arrows show the directions in which different sections of the ice cliff face. All examples are of supraglacial ice cliffs within the shaded grey area in Figure 9e.

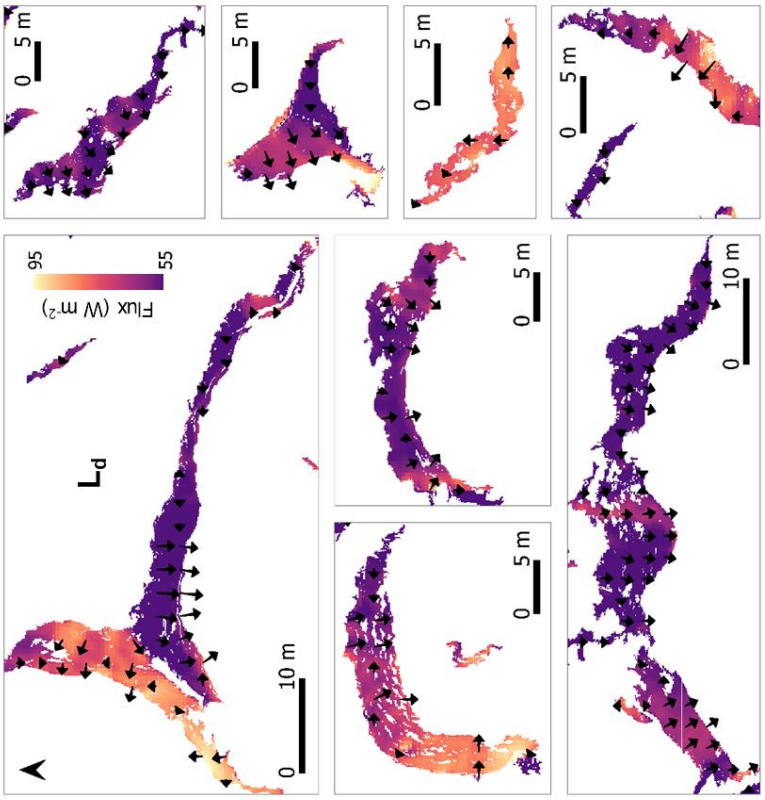

Figure 5.S5. Mean longwave flux from debris (L_d) distribution between 12 and 26 August 2019. Additional examples of supraglacial ice cliffs (to supplement the largest cliff shown in Figure 5.11) are given here. Black arrows show the directions in which different sections of the ice cliff face. All examples are of supraglacial ice cliffs within the shaded grey area in Figure 9e.

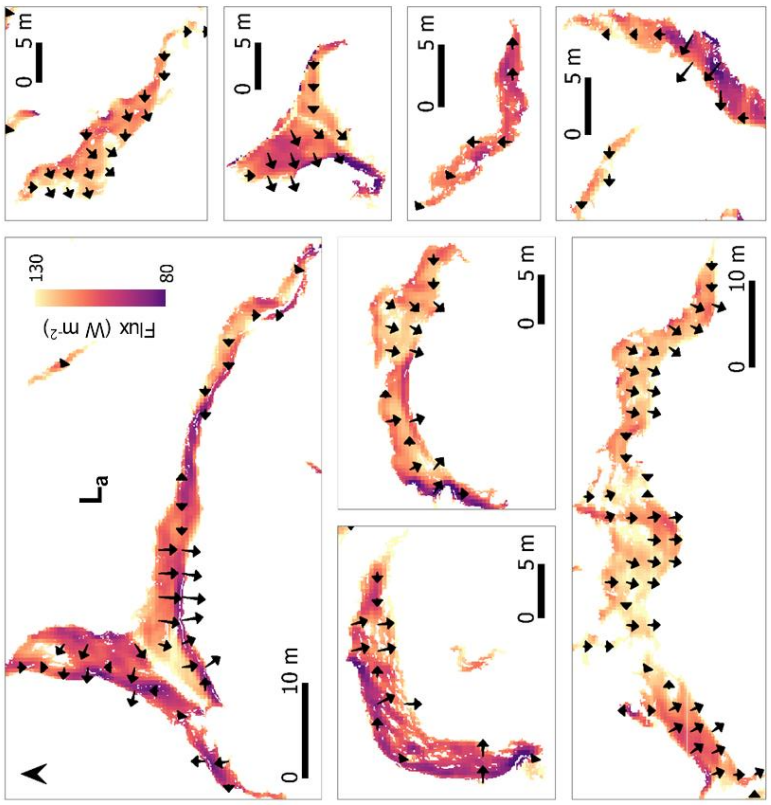

Figure 5.S4. Mean longwave flux from the atmosphere (L_a) distribution between 12 and 26 August 2019. Additional examples of supraglacial ice cliffs (to supplement the largest cliff shown in Figure 5.11) are given here. Black arrows show the directions in which different sections of the ice cliff face. All examples are of supraglacial ice cliffs within the shaded grey area in Figure 9e.

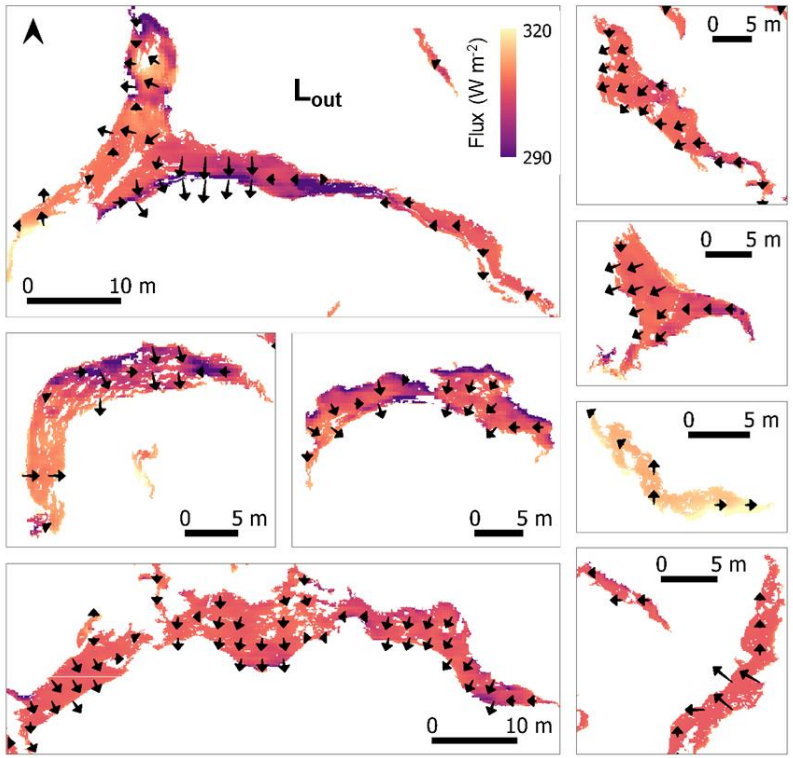

Figure 5.S6. Mean longwave outgoing flux (L_{out}) distribution between 12 and 26 August 2019. Additional examples of supraglacial ice cliffs (to supplement the largest cliff shown in Figure 5.11) are given here. Black arrows show the directions in which different sections of the ice cliff face. All examples are of supraglacial ice cliffs within the shaded grey area in Figure 9e.

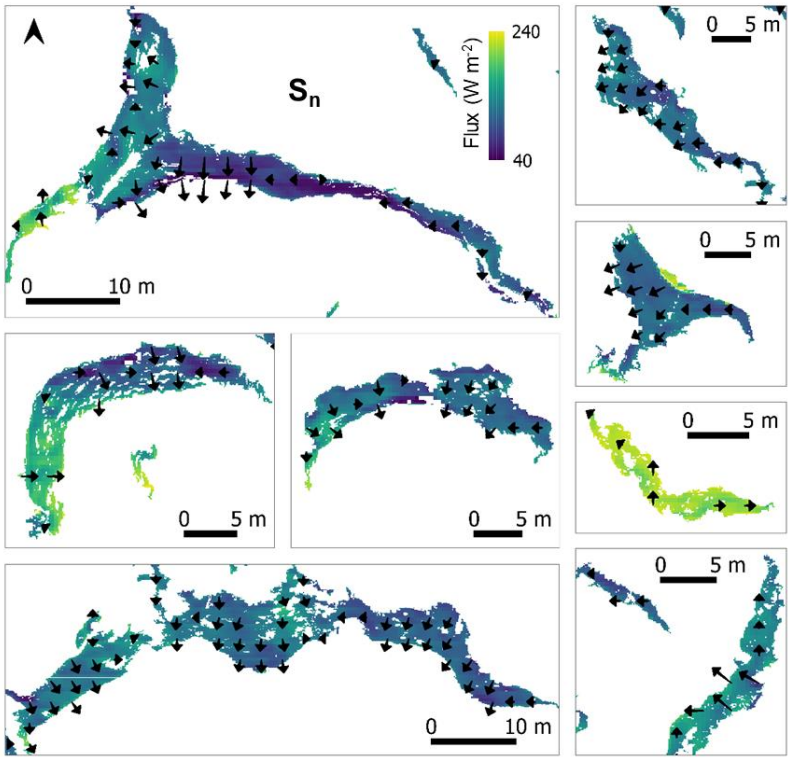

Figure 5.S7. Mean net shortwave flux (S_n) distribution between 12 and 26 August 2019. Additional examples of supraglacial ice cliffs (to supplement the largest cliff shown in Figure 5.11) are given here. Black arrows show the directions in which different sections of the ice cliff face. All examples are of supraglacial ice cliffs within the shaded grey area in Figure 9e.

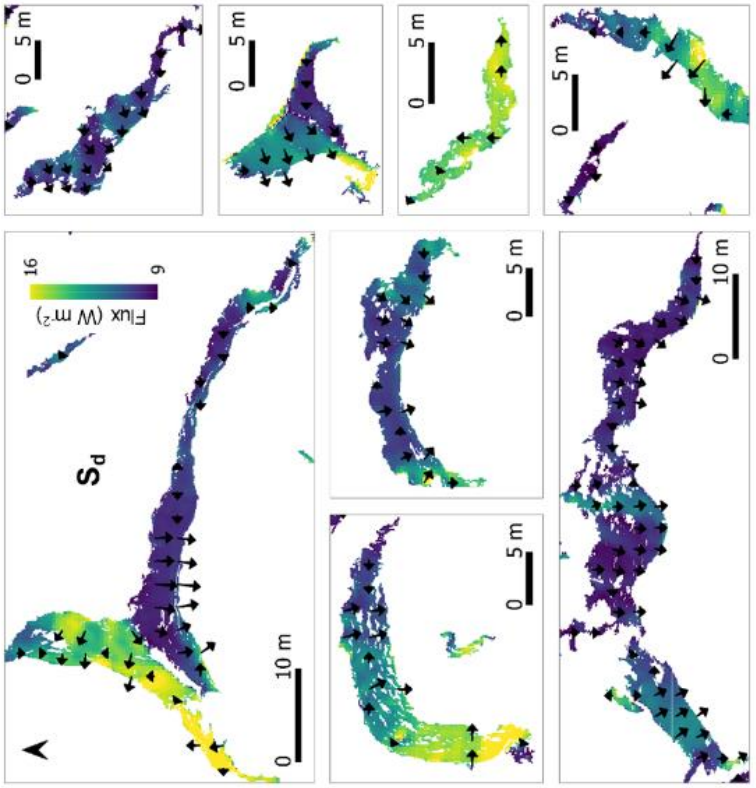

Figure 5.S9. Mean shortwave flux from the debris (S_d) distribution between 12 and 26 August 2019. Additional examples of supraglacial ice cliffs (to supplement the largest cliff shown in Figure 5.11) are given here. Black arrows show the directions in which different sections of the ice cliff face. All examples are of supraglacial ice cliffs within the shaded grey area in Figure 9e.

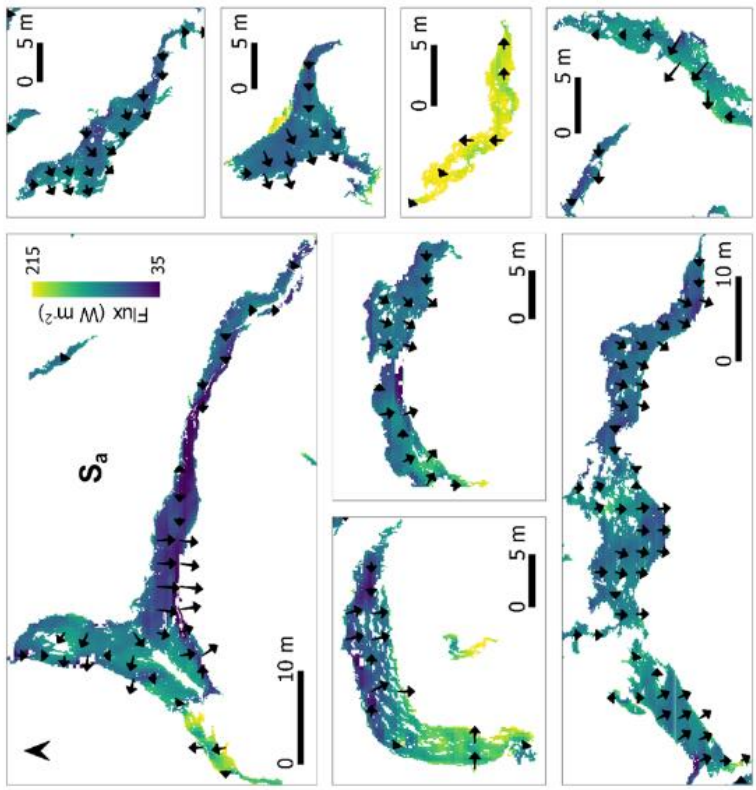

Figure 5.S8. Mean shortwave flux from the atmosphere (S_a) distribution between 12 and 26 August 2019. Additional examples of supraglacial ice cliffs (to supplement the largest cliff shown in Figure 5.11) are given here. Black arrows show the directions in which different sections of the ice cliff face. All examples are of supraglacial ice cliffs within the shaded grey area in Figure 9e.

Chapter 6

Discussion

6.1 Thesis overview

The overall aims of this thesis were to use satellite and UAV remote sensing to investigate the complex behaviour of debris-covered glaciers and to develop new techniques for monitoring these glaciers. This work has been motivated by the need to forecast better the future impacts of glacial retreat on water resources in some of the most socio-economically vulnerable regions on Earth. The specific research goals, established in Chapter 2 and recapped here, were:

- To quantify the surface mass balance (SMB) gradients of the largest debris-covered glaciers in High Mountain Asia using a remote-sensing-based mass continuity approach.
- To develop a method for simulating supraglacial debris thicknesses and sub-debris melt rates from high-resolution, UAV-acquired thermal infrared imagery.
- To investigate the characteristics and melt rates of supraglacial ice cliffs on a debris-covered glacier using high-precision UAV imagery.

These goals were addressed using freely-available datasets produced by previous remote sensing studies, as well as newly-generated high-resolution datasets derived from UAV surveys conducted in August 2019 at Llaca Glacier, Ancash, Peru.

Meeting these goals has brought about the development of new techniques that can be used to monitor debris-covered glaciers using satellite- and UAV-derived data. Additionally, applying these techniques to glaciers in High Mountain Asia and the Peruvian Andes has uncovered new information about the characteristics and evolution of debris-covered glaciers in the mid-latitudes and tropics.

Section 6.2 describes the key outcomes of this thesis while Section 6.3 highlights relevant studies that have been published since publication of the thesis findings of Chapter 3. Section 6.4 identifies the current limitations associated with the research within this thesis and highlights future opportunities to reduce these limitations and build upon the work conducted within this thesis.

6.2 Key outcomes

In Chapter 3, I tested the use of a novel mass-continuity approach, applied to recent remote sensing datasets, in order to compute the spatially-distributed SMB of the largest glaciers within five key regions in High Mountain Asia. The results of this work revealed key differences between the altitudinal ablation gradients of debris-covered and debris-free glaciers, which were not previously visible from available geodetic mass balance datasets. These findings indicated that altitudinal variations in ice-flow dynamics are likely to be obscuring the contrasting melt patterns of debris-covered glaciers from geodetic datasets, highlighting the importance of separating signals of SMB and ice dynamics. Overall, this work provided a proof of concept for a method to account effectively for the role of ice flow and quantify the spatially-distributed SMB of debris-covered glaciers.

In Chapter 4, I tested the utility of high-resolution thermal infrared imagery, acquired with a UAV, to calculate spatially-distributed supraglacial debris thickness over a portion of Llaca Glacier, a tropical debris-covered glacier in the Cordillera Blanca, Peru. Additionally, I tested the use of the calculated debris-thickness map produced here to simulate spatially-distributed daily melt rates for a three-month

period in 2019. This work demonstrated the benefits of using UAV-derived thermal imagery, rather than satellite imagery, to parameterise debris thicknesses with high spatial precision and accuracy, facilitating improved simulation of sub-debris melt rates. Additionally, the results of this work indicated a mean sub-debris melt rate nearly three times higher than the mean melt rate simulated from satellite-derived debris thicknesses, emphasising the importance of acquiring further high-precision debris thickness data for investigating glacier-scale ablation processes and calibrating regional melt models. In order to aid the production of such data in the future, this chapter also produced a set of recommendations for using thermal UAV imagery to simulate debris thicknesses, to ensure that the imagery is appropriately calibrated and that spatial and temporal variations in meteorological parameters are accounted for effectively.

In Chapter 5, I used high-resolution visible UAV data of Llaca Glacier tongue to examine the characteristics of supraglacial ice cliffs and simulate their contribution towards overall ablation. This work showed that, similarly to previous findings in mid/high latitude regions, the backwasting of supraglacial ice cliffs contributes disproportionately towards the overall glacier mass loss. The findings also demonstrated that, even in low-latitude regions, the survival of ice cliffs is strongly dependent on aspect, with southwest-facing cliffs surviving preferentially over cliffs facing in other directions. The results also indicated that while shortwave radiation receipt is the predominant control on ice-cliff evolution, other mechanisms such as ice-flow dynamics and supraglacial hydrology are also likely to regulate the development of supraglacial ice cliffs. Overall, this chapter emphasised the need for further high-precision UAV-based studies of the complex mechanisms through which tropical debris-covered glaciers are losing mass in response to climate change.

6.3 Recent progress

A number of relevant studies, which have recently been published, have further progressed the use of remote-sensing-based mass continuity approaches for obtaining

SMB estimates for debris-covered (and debris-free) glaciers. These studies, which have been published since publication of Chapter 3 (Bisset et al., 2020), further optimised the mass continuity approach and expanded their applications to other regions and larger spatial scales. This section will discuss the main advances in the approaches used by these studies and their contributions towards enabling future studies to gain higher-accuracy, regional-scale estimates of SMB using remote-sensing-based mass continuity approaches.

Miles et al. (2021) used a mass-continuity approach, similar to that tested in Chapter 3, in order to quantify SMB for 5527 glaciers in High Mountain Asia. By developing a fully-automated grid-based approach, as opposed to computing SMB for cross-sectional glacier segments (Chapter 3), Miles et al. (2021) were able expand their calculations to a larger regional scale. The results of this work demonstrated that, between 2000 and 2016, only 60 ± 10 % of yearly regional ablation was balanced by accumulation and that, even in a scenario without warming during the 21st century, 28 ± 1 % of the total ice volume within High Mountain Asia will disappear by the end of the century. Miles et al. (2021) compared their results to the results of Chapter 3 of this thesis (Bisset et al., 2020), finding that their results, as well as their uncertainty estimates, were highly consistent. Also consistent with Chapter 3 here, Miles et al. (2021) also observed reversed mass balance gradients in the lower portions of debris-covered glaciers in High Mountain Asia.

Van Tricht et al. (2021) used high-resolution UAV-derived ice velocities and surface-elevation-change measurements, in conjunction with GPR-derived ice-thickness maps, to estimate spatially-distributed SMB on two Swiss glaciers (Vadret da Morteratsch and Vadret Pers) using the mass continuity approach. Comparison of the results against ablation-stake measurements indicated that this approach could produce SMB estimates with a mean absolute error of < 0.5 m w.e. a^{-1}. This is an improvement on the uncertainties associated with individual point estimates of SMB in Chapter 3 (e.g. Figure 3.3), as well as in Miles et al. (2021), which can be up to several metres per year. This demonstrates that for detailed studies of SMB on

individual glaciers, it is optimal to use a UAV-based approach similar to that of Van Tricht et al. (2021) since this approach provides greater spatial coverage than ablation-stake measurements while retaining greater levels of certainty than satellite-based approaches.

Pelto and Menounos (2021) applied a mass-continuity approach to simulate the SMB gradients of five glaciers in the Columbia Mountains, British Columbia. This study used high-resolution (1 m) DEMs, derived from airborne laser-scanning surveys, to generate maps of ice-surface-elevation change and surface velocity with considerably greater precision than those used in Chapter 3. Pelto and Menounos (2021) also compared the use of ice thicknesses derived from ice-penetrating radar surveys to model-derived ice thicknesses, finding that these datasets yield comparable mass balance gradients. Overall, this study demonstrated that the mass-continuity approach could be used to obtain SMB gradients which approximate well those directly measured using ablation stakes, emphasising the potential for this approach to be upscaled in future. Pelto and Menounos (2021) warned against over-interpretation of SMB estimates associated with individual flux bins, due to large mass balance residuals, indicating that SMB gradients derived from the mass-continuity approach were considerably more reliable.

These recently-published studies further demonstrate the potential of remote-sensing-based mass-continuity methods for determining the SMB gradients of glaciers. Miles et al. (2021) demonstrated that, by fully automating the delineation of flux bins, the mass-continuity approach can be used to compute SMB at a regional scale. Meanwhile, Van Tricht et al. (2021) and Pelto and Menounos (2021) showed that, through the use of high-resolution airborne datasets, this approach can also be used to quantify SMB gradients more accurately and over greater spatial scales than is possible using in-situ measurement techniques.

6.4 Limitations and future developments

There are several limitations associated with the work within this thesis. As discussed in Chapter 3, the accuracy of SMB estimates derived from the mass-continuity approach is impacted by uncertainties associated with the ice-thickness inversion used to produce the simulated ice thickness input data (Farinotti et al., 2019). As discussed in Section 6.3, Pelto and Menounos (2021) found that, while considerable uncertainties are associated with SMB estimates associated with individual flux bins, the use of simulated ice-thickness datasets can be used to produce reliable SMB estimates. Additionally, with future improvements to the parameterisation of ice thickness in glaciological models, the potential of mass-continuity approaches to generate well-resolved regional estimates of spatially-distributed SMB will increase further.

The coverage of distributed SMB estimates in high-altitude accumulation areas (Chapter 3) was limited due to the lower accuracy of velocity data, which prevented the sampling of SMB in these areas. The poor accuracy of velocities in the upper accumulation areas of glaciers results from challenges associated with feature-tracking due to the homogenous appearance of the ice surface. Additionally, some glaciers with particularly steep surface slopes and/or large icefalls (e.g. Khumbu Glacier) could not be included in the analyses, as the accuracy of the velocities is also poor in these areas. Therefore, with future improvements to the resolution of optical satellite imagery, in conjunction with further optimisation of feature-tracking algorithms, it will likely be possible to increase the coverage and accuracy of mass-continuity-derived SMB estimates in the uppermost portions of glaciers in mountain regions.

Analysis of the role of supraglacial debris in controlling the SMB gradients (Chapter 3) was limited by the accuracy of simulated debris-thickness estimates derived from thermal satellite imagery. The low resolution of thermal satellite imagery (60 – 100 m) results in a 'mixed pixel' effect, where supraglacial ice cliffs or

ponds are present within many pixels, resulting in underestimation of debris thicknesses through reduction of the surface temperature by these features (Rounce et al., 2018). In future, as presented in Chapter 4, high-resolution UAV-derived thermal imagery could be used to produce distributed debris-thickness datasets with considerably greater spatial precision and accuracy. These datasets could be used not only to conduct detailed investigations of specific debris-covered glaciers, but also to calibrate the coarser-resolution satellite-derived regional and global models.

The main limitation associated with the simulated debris thicknesses produced in Chapter 4 was the scarcity of validation data, which resulted from a technical issue in the field. As a result, there is still some uncertainty in the reliability of debris thicknesses calculated from UAV-derived thermal imagery. In future, further thermal UAV surveys of debris-covered glaciers, coupled with a greater number of in-situ debris thickness measurements, would be highly beneficial for establishing this technique as a viable method for obtaining high-precision, more accurate estimates of supraglacial debris thickness. Furthermore, the collection of ablation-stake measurements at debris-thickness simulation sites would enable validation of simulated sub-debris melt rates derived from UAV-derived simulated debris thicknesses.

As discussed in Chapter 4, there are several significant challenges associated with the use of thermal UAV imagery for glaciological applications. While the methodology laid out in Chapter 4 demonstrated a viable workflow for minimising the effects of sensor biases, atmospheric signal attenuation and temporal variations in meteorological conditions, further studies conducting thermal UAV surveys on debris-covered glaciers would be advantageous for optimising this workflow. Additionally, technological advances to UAV-mountable thermal cameras will likely enable the production of higher-accuracy estimates of supraglacial debris thickness in the future.

The SMB estimates calculated in Chapter 3 could differ from SMB estimates derived from debris thicknesses and local Östrem curves (e.g. Rowan et al., 2021), due to key differences in the input datasets associated with these methods. While SMB estimates derived from the mass continuity method are impacted by uncertainties associated with the ice velocity and thickness, SMB estimates derived from local Östrem curves are unaffected by uncertainties associated with these parameters. Additionally, mass-continuity derived values are impacted by ablation processes such as ice-cliff backwasting, thermal erosion by supraglacial ponds, englacial melting and subglacial melting (in addition to surface ablation), while estimates derived from Östrem curves are not impacted by any melt processes other than surface ablation. Meanwhile, unlike SMB simulated using the mass continuity method, SMB simulated from the Östrem-based method is impacted by uncertainties associated with debris thickness. For example, remote sensing methods typically underestimate debris thickness (e.g. Rounce et al., 2018), which could result in an overestimation of sub-debris melt rates. In future, the mass continuity method could be used in conjunction with an Östrem-curve based method in order to produce more robust SMB estimates.

A disadvantage of the model used to estimate ice-cliff backwasting rates in Chapter 5 is that ice-cliff geometry is not updated through time in response to simulated ice-cliff backwasting rates. As a result, changes in radiative fluxes in response to changes in cliff slope angle, aspect and position are not accounted for. It is therefore important that future studies develop iterative models which calculate ice-cliff backwasting rates whilst continuously updating the surface topography data used within these calculations.

A further limitation of the work conducted in Chapter 5 is that in estimating the contribution of ice-cliff backwasting towards overall rates of ice mass loss, several factors were unaccounted for. The sub-debris melt rates which were used to calculate ice loss unlinked to cliff backwasting were derived from the surface energy balance model within Chapter 4, which was based on the model of Nicholson and

Benn (2006). The disadvantage of this model is that, although it accounts for the effects of surface topography on the incoming shortwave radiation flux, it does not account for the impacts of surface topography on longwave and turbulent heat fluxes. While this is less important for debris-covered areas on the glacier, which are generally flatter in comparison to the surfaces of supraglacial ice cliffs, the surfaces of debris-covered glacier tongues usually undulate considerably (e.g. Bartlett et al., 2021). An additional disadvantage of using this model is that it uses mean daily meteorological variables as input data, as opposed to hourly meteorological data which were used to simulate ice-cliff backwasting in Chapter 5. While Nicholson and Benn (2006) found that the daily model can still produce sub-debris melt estimates which compare well to those observed in the field, it is possible that nonlinear relationships between meteorological parameters and melt rates could result in underestimation of sub-debris ablation. It would therefore be beneficial for future studies to simulate both cliff backwasting and sub-debris melting using hourly input data, as well as accounting for the impacts of surface topography on all radiative fluxes, to ensure unbiased estimates of the contribution of ice-cliff backwasting towards overall rates of mass loss on debris-covered glaciers.

The estimated thermal conductivities used to simulate sub-debris melt rates and ice-cliff backwasting (Chapters 4 and 5) are limited by the relatively short period (64 hours) over which the thermistor measurements were collected, in comparison to the longer periods over which ablation was simulated (15 – 90 days), since the thermal conductivity of the debris layer is likely to vary over time. For example, Nicholson and Benn (2012) found that the thermal conductivity of the debris layer on Ngozumpa Glacier (Nepal) was 30 % greater during summer compared to during winter. It would therefore be beneficial for future studies performing melt simulations to acquire longer time-series of vertical debris temperature profiles, in order to ensure that temporal changes in thermal conductivity are accounted for.

In future, it would be valuable for further simulations of sub-debris melt and ice-cliff backwasting rates on debris-covered glaciers, similar to those conducted in Chapters 4 and 5, to be performed in conjunction with in-situ ablation stake measurements. These in-situ measurements would be beneficial both for the purposes of validating simulated melt rates and performing model calibration to improve the accuracy of future simulations.

In future, technological advances in the capability of UAVs will facilitate larger-scale aerial surveys of debris-covered glaciers. The increasing availability of Real Time Kinematic (RTK) drones will likely reduce the need for ground control surveys to be conducted, meaning that more hazardous and inaccessible areas of glaciers can likely be surveyed in the future. Additionally, potential changes to BVLOS regulations (associated with conducting UAV surveys beyond visual line of sight) will enable larger-scale studies of debris-covered glaciers and improved access to remote sites. Lastly, advances in UAV technology may increase the capability of drones to fly at high-altitude sites, while improvements to drone battery life will enable larger-scale studies of debris-covered glaciers to be conducted in the future.

6.5 Outlook

The research within this thesis has demonstrated the value of emerging satellite- and UAV-based remote sensing techniques for monitoring debris-covered glaciers in Earth's high-mountain regions.

In future, further development of satellite-based techniques, such as the remote-sensing-based mass continuity approach presented in Chapter 3, and further acquisition of high-precision UAV datasets, such as those presented in Chapters 4 and 5, will allow us to gain not only a better understanding of the complex melt processes occurring on debris-covered glaciers, but also provide valuable calibration data for glacio-hydrological models.

Further research attention also needs to be given to debris-covered glaciers within low-latitude regions such as the Cordillera Blanca, which are particularly sensitive to climatic changes (Seehaus et al., 2019). Global glacier runoff modelling indicates that peak water will be reached considerably earlier in these regions (Hock et al., 2020), with many watersheds having already passed this critical transition point (Baraer et al., 2012). However, while a large proportion of glaciers in low-latitude regions are debris-covered, regional hydrological modelling studies do not currently account for the impacts of debris cover on meltwater runoff (e.g. Baraer et al., 2010; Fyffe et al., 2021).

Current international research projects (PeruGROWS and PEGASUS) are conducting glacio-hydrological modelling for all glaciers within the Peruvian Andes, with the aim of incorporating the influence of debris cover within this work. However, a key missing data input for this work is accurate supraglacial debris thickness data that can be used for validation of satellite-derived estimates (personal communication with Catriona Fyffe, who is leading this modelling work). It is therefore critical that further efforts are made to acquire high-resolution debris thickness datasets, such as the one produced in Chapter 4, in order to effectively validate simulated debris thickness estimates and enable higher-accuracy hydrological modelling.

Finally, it is important that further high-precision studies of supraglacial ice cliffs, such as that of Chapter 5, are conducted in understudied regions such as the Cordillera Blanca, in order to effectively account for the future contribution of ice-cliff backwasting in glacio-hydrological models.

Chapter 7

Conclusions

This thesis sought to contribute towards the development of novel techniques for monitoring the characteristics and evolution of debris-covered glaciers, based on satellite- and UAV-acquired remote sensing data. By applying these techniques to debris-covered glaciers in High Mountain Asia and the Ancash region of Peru, this thesis has contributed towards improved understanding of the complex mechanisms through which debris-covered glaciers lose mass.

Chapter 3 aimed to quantify the surface mass balance (SMB) gradients of the largest debris-covered glaciers within five regions of High Mountain Asia using a remote-sensing-based mass continuity approach. The main research findings were as follows:

- Through the use of a remote-sensing-based mass-continuity method, it is possible to separate signals of climatic mass balance and ice flow dynamics in order to parameterise the ablation gradients of the largest debris-covered glaciers in High Mountain Asia.
- Applying this approach revealed reversed SMB gradients on the lower portions of debris-covered glaciers, which were not previously visible from geodetic studies.

- These reversed SMB gradients were likely offset by patterns in ice-flow dynamics, leading to similar patterns of thinning on debris-covered and debris-free glaciers being observed.
- In future, the approach presented within this study can be developed and applied at larger scales, providing the opportunity to uncover regional-scale SMB patterns.

Chapter 4 aimed to develop a method for simulating supraglacial debris thicknesses and sub-debris melt rates using UAV-acquired thermal data, in conjunction with local meteorological data, visible UAV data and thermally-profiled debris temperature time-series. The main research findings are as follows:

- By effectively calibrating the radiometric thermal imagery and accounting for temporal and spatial variations in meteorological parameters during UAV surveys, thermal UAV data can be used to better represent the highly heterogeneous patterns of debris thickness and sub-debris melt on debris-covered glaciers.
- Based on this approach, the mean debris thickness calculated across a portion of Llaca Glacier tongue was ~ 71 % lower than the satellite-derived estimate, indicating that the accuracy of satellite-derived debris thicknesses is likely to be poor in some places.
- Consequently, sub-debris melt rates across Llaca Glacier could be significantly underestimated using satellite-derived debris thicknesses, with simulated melt rates for the study area on Llaca Glacier tongue being 65 % less than those simulated from UAV-derived debris thicknesses.
- Further studies are now required in order to further establish the use of UAV-derived thermal data for simulating debris thickness and provide high-precision calibration data for glacio-hydrological models.

Chapter 5 aimed to investigate the characteristics and melt contribution of supraglacial ice cliffs on a tropical debris-covered glacier in the Cordillera Blanca, Peru. The main research findings were as follows:

- High-resolution UAV-derived datasets can be used to investigate the complex behaviour of supraglacial ice cliffs and generate estimates of their contribution towards overall rates of mass loss.
- Similarly to debris-covered glaciers in higher-latitude regions, the backwasting of supraglacial ice cliffs contributes disproportionately towards the overall mass loss of Llaca Glacier. More specifically, while covering only 5 % of the survey area, ice cliffs were responsible for 20 % of simulated ablation within this area during the 15-day simulation period in August 2019
- While the distribution of radiative fluxes is likely to principally drive ice-cliff survival, other factors such as ice flow dynamics and supraglacial hydrology are also likely to be playing a role in regulating ice-cliff evolution.
- Increased research attention needs to be focused on ice-cliff backwasting on tropical debris-covered glaciers, in order to simulate more accurately the future meltwater contribution towards downstream water resources in low-latitude regions.

Future research into the optimisation of satellite and UAV remote sensing techniques for monitoring debris-covered glaciers, such as those developed within this thesis, will facilitate improvements to the precision, accuracy and scale at which debris-covered glaciers can be monitored. Continued research into the complex ablation processes of debris-covered glaciers is critical for improving the calibration of glaciological models and effectively forecasting the impacts of glacial retreat on downstream water resources in some of the most socio-economically vulnerable regions in the world.

References

Abramowitz, M.; Stegun, I. A. (1965) *Handbook of Mathematical Functions.* Dover, New York.

Allen, S.K., Linsbauer, A., Randhawa, S.S., Huggel, C., Rana, P. and Kumari, A. (2016) Glacial lake outburst flood risk in Himachal Pradesh, India: an integrative and anticipatory approach considering current and future threats. *Natural Hazards*. 84(3), 1741-1763.

Ames, A.M. (1984) Informe sobre las mediciones de desplizamiento de balizas colocadas sobre la morrena y glaciar Hatunraju, Paron. *Electroperu S.A.*, Huaráz, Peru.

Anderson, L.S., Anderson, R.S. (2016) Modeling debris-covered glaciers: response to steady debris deposition. *The Cryosphere*. 10, 1105-1124.

Anderson, L.S., Armstrong, W.H., Anderson, R.S. and Buri, P. (2021) Debris cover and the thinning of Kennicott Glacier, Alaska: in situ measurements, automated ice cliff delineation and distributed melt estimates. *The Cryosphere*. 15(1), 265-282.

Azam, M. F.; Ramanathan, A. L.; Wagnon, P.; Vincent, C.; Linda, A.; Berthier, E.; Sharma, P.; Mandal, A.; Angchuk, T.; Singh, V. B.; Pottakkal, J.G. (2016) Meteorological Conditions, Seasonal and Annual Mass Balances of Chhota Shigri Glacier, Western Himalaya, India. *Annals in Glaciology.* 57 (71), 328–338.

Azam, M. F.; Wagnon, P.; Patrick, C.; Ramanathan, A.; Linda, A.; Singh, V. B. (2014) Reconstruction of the Annual Mass Balance of Chhota Shigri Glacier, Western Himalaya, India, since 1969. *Annals in Glaciology.* 55 (66), 69–80.

Banerjee, A., Shankar, R. (2013) On the response of Himalayan glaciers to climate change. *Journal of Glaciology*. 59(215), 480-490.

Banerjee, A. (2017) Brief communication: Thinning of debris-covered and debris-free glaciers in a warming climate. *The Cryosphere*. 11, 133-138.

Baraer, M., Mark, B.G., McKenzie, J.M., Condom, T., Bury, J., Huh, K.I., Portocarrero, C., Gómez, J. and Rathay, S. (2012) Glacier recession and water

resources in Peru's Cordillera Blanca. *Journal of Glaciology.* 58(207), 134-150.

Barandun, M.; Huss, M.; Sold, L.; Farinotti, D.; Azisov, E.; Salzmann, N.; Usubaliev, R.; Merkushkin, A.; Hoelzle, M. (2015) Re-Analysis of Seasonal Mass Balance at Abramov Glacier 1968-2014. *Journal of Glaciology.* 61 (230), 1103–1117.

Barnett, T.P., Adam, J.C. and Lettenmaier, D.P. (2005) Potential impacts of a warming climate on water availability in snow-dominated regions. *Nature.* 438(7066), 303-309.

Bartlett, O.T., Ng, F.S. and Rowan, A.V. (2021) Morphology and evolution of supraglacial hummocks on debris-covered Himalayan glaciers. *Earth Surface Processes and Landforms.* 46(3), 525-539.

Bell, S.A., 1996. A guide to the measurement of humidity (NPL Guide 103*).* *Teddington: National Physical Laboratory.*

Benn, D.I., Bolch, T., Hands, K., Gulley, J., Luckman, A., Nicholson, L.I., Quincey, D., Thompson, S., Toumi, R., Wiseman, S. (2012) Response of debris-covered glaciers in the Mount Everest region to recent warming, and implications for outburst flood hazards. *Earth Science Reviews.* 114(1-2), 156-174.

Benn, D.I., Lehmkuhl, F. (2000) Mass balance and equilibrium-line altitudes of glaciers in high mountain environments. *Quaternary International.* 65 (66), 15–29.

Berni, J.A.J., Zarco-Tejada, P.J., Suárez, L., González-Dugo, V. and Fereres, E. (2009) Remote sensing of vegetation from UAV platforms using lightweight multispectral and thermal imaging sensors. *The International Archives of the Photogrammetry, Remote Sensing and Spatial Information Sciences.* 38(6), 6.

Berthier, E.; Vincent, C. Relative Contribution of Surface Mass Balance and Ice Flux Changes to the Accelerated Thinning of the Mer de Glace (Alps) over 1979-2008 (2012). *Journal of Glaciology.* 58 (209), 1979–2008.

Bhushan, S., Syed, T.H., Arendt, A.A., Kulkarni, A.V. and Sinha, D. (2018) Assessing controls on mass budget and surface velocity variations of glaciers in Western Himalaya. *Scientific reports.* 8(1), 1-11.

Bisset, R.R., Dehecq, A., Goldberg, D.N., Huss, M., Bingham, R.G., Gourmelen, N. (2020) Reversed Surface-Mass-Balance Gradients on Himalayan Debris-Covered Glaciers Inferred from Remote Sensing. *Remote Sensing.* 12(10), 1563.

Bolch, T. (2017) Asian glaciers are a reliable water source. *Nature.* 545(7653), 161-162.

Bonekamp, P.N.J., van Heerwaarden, C.C., Steiner, J.F., Immerzeel, W.W. (2020) Using 3D turbulence-resolving simulations to understand the impact of

surface properties on the energy balance of a debris-covered glacier. *The Cryosphere*. 14, 1611-1632.

Bookhagen, B., Burbank, D.W. (2010) Toward a complete Himalayan hydrological budget: spatiotemporal distribution of snowmelt and rainfall and their impact on river discharge. *Journal of Geophysical Research*. 115(3), 1-25.

Brock, B.W., Mihalcea, C., Kirkbride, M.P., Diolaiuti, G., Cutler, M.E.J., Smiraglia, C. (2010) Meteorology and surface energy fluxes in the 2005–2007 ablation seasons at the Miage debris-covered glacier, Mont Blanc Massif, Italian Alps. *Journal of Geophysical Research*. 115(D9), D09106.

Brun, F., Buri, P., Miles, E.S., Wagnon, P., Steiner, J., Berthier, E., Ragettli, S., Kraaijenbrink, P., Immerzeel, W.W. and Pellicciotti, F. (2016) Quantifying volume loss from ice cliffs on debris-covered glaciers using high-resolution terrestrial and aerial photogrammetry. *Journal of Glaciology*. 62(234), 684-695.

Brun, F., Berthier, E., Wagnon, P., Kääb, A. and Treichler, D. (2017) A spatially resolved estimate of High Mountain Asia glacier mass balances from 2000 to 2016. *Nature Geoscience*. 10(9), 668-673.

Brun, F. (2018) Impact of the debris cover on High Mountain Asia glacier mass balances: a multiscale approach. Glaciology. Université Grenoble Alpes, 2018.

Brun, F., Wagnon, P., Berthier, E., Shea, J.M., Immerzeel, W.W., Kraaijenbrink, P.D., Vincent, C., Reverchon, C., Shrestha, D. and Arnaud, Y. (2018) Ice cliff contribution to the tongue-wide ablation of Changri Nup Glacier, Nepal, central Himalaya. *The Cryosphere*. 12(11), 3439-3457.

Brun, F.; Wagnon, P.; Berthier, E.; Jomelli, V.; Maharjan, S. B.; Shrestha, F.; Kraaijenbrink, P. D. A. (2019) Heterogeneous Influence of Glacier Morphology on the Mass Balance Variability in High Mountain Asia. *Journal of Geophysical Research: Earth Surface*. 124 (6), 1331–1345.

Budzier, H.; Gerlach, G. (2015) Calibration of uncooled thermal infrared cameras. *J. Sensors Sens. Syst.* 4, 187–197.

Buri, P., Pellicciotti, F., Steiner, J.F., Miles, E.S., Immerzeel, W.W. (2016) A grid-based model of backwasting of supraglacial ice cliffs on debris-covered glaciers. *Annals of Glaciology*. 57(71), 199-211.

Buri, P., Pellicciotti, F. (2018) Aspect controls the survival of ice cliffs on debris-covered glaciers. *PNAS*. 155(17), 4369-4374.

Buri, P., Miles, E.S., Steiner, J.F., Ragettli, S., Pelliciotti, F. (2021) Supraglacial Ice Cliffs Can Substantially Increase the Mass Loss of Debris-Covered Glaciers. *Geophysical Research Letters*. 48(6), 1-11.

Burns, P., Nolin, A. (2014) Using atmospherically-corrected Landsat imagery to measure glacier area change in the Cordillera Blanca, Peru from 1987 to 2010. *Remote Sensing of the Environment.* 140, 165-178.

Buytaert, W., Moulds, S., Acosta, L., De Bievre, B., Olmos, C., Villacis, M., Tovar, C. and Verbist, K.M. (2017) Glacial melt content of water use in the tropical Andes. *Environmental Research Letters.* 12(11), 114014.

Carey, M. (2005) Living and dying with glaciers: people's historical vulnerability to avalanches and outburst floods in Peru. *Global and Planetary Change.* 47(2–4), 122-134.

Carrivick, J.L., Tweed, S.T. (2016) A global assessment of the societal impacts of glacier outburst floods. *Global and Planetary Change.* 144, 1-16.

Charturvedi, R., Kulkarni, A., Karyakarte, Y., Joshi, J., Bala, G. (2014) Glacial mass balance changes in the Karakoram and Himalaya based on CMIP5 multi-model climate projections. *Climatic Change.* 123(2), 315-328.

Chevallier, P., Pouyaud, B., Suarez, W. and Condom, T. (2011) Climate change threats to environment in the tropical Andes: glaciers and water resources. *Regional Environmental Change.* 11(1), 179-187.

Clark, S.P. (1966) *Handbook of physical constants* (Vol. 97). Geological Society of America.

Conway, H., Rasmussen, L.A. (2000) Summer temperature profiles within supraglacial debris on Khumbu Glacier, Nepal. *Proceedings of a workshop held at Seattle, Washington, USA, September 2000.*

Cuffey, K.M., Paterson, W.S.B. (2010) *The Physics of Glaciers: Fourth Edition*, Burlington/Oxford: Elsevier.

Dehecq, A.; Gourmelen, N.; Trouve, E. (2018) Deriving Large-Scale Glacier Velocities from a Complete Satellite Archive: Application to the Pamir–Karakoram–Himalaya. *Remote Sensing of Environment.* 162, 55–66.

Dehecq, A., Gourmelen, N., Gardner, A.S., Brun, F., Goldberg, D., Nienow, P., Berthier, E., Vincent, C., Wagnon, P., Trouvé, E. (2018) Twenty-first century glacier slowdown driven by mass loss in High Mountain Asia. *Nature Geoscience.* 12, 22-27.

Dilley, A.C., O'Brien, D.M. (1998) Estimating downward clear sky long-wave irradiance at the surface from screen temperature and precipitable water. *Quarterly Journal of the Royal Meteorological Society.* 124(549), 1391-1401.

Emmer, A., Loarte, E.C., Klimes, J., Vilímeka, V. (2015) Recent evolution and degradation of the bent Jatunraju glacier (Cordillera Blanca, Peru). *Geomorphology.* 228, 345-355.

Farinotti, D.; Huss, M.; Fürst, J. J.; Landmann, J.; Machguth, H.; Maussion, F.; Pandit, A. (2019) A Consensus Estimate for the Ice Thickness Distribution of All Glaciers on Earth. *Nature Geoscience*. 12(3), 168–173.

Farinotti, D., Immerzeel, W.W., de Kok, R.J., Quincey, D.J., Dehecq, A. (2020) Manifestations and mechanisms of the Karakoram glacier Anomaly. *Nature Geoscience*. 13, 8-16.

Farr, T. G.; Rosen, P. A.; Caro, E.; Crippen, R.; Duren, R.; Hensley, S.; Kobrick, M.; Paller, M.; Rodriguez, E.; Roth, L.; Seal, D.; Shaffer, S.; Shimada, J.; Umland, J.; Werner, M.; Oskin, M.; Burbank, D.; Alsdorf, D. (2007) The Shuttle Radar Topography Mission. *Reviews of Geophysics.* 45 (2), RG2004.

Foresta, L.; Gourmelen, N.; Pálsson, F.; Nienow, P.; Björnsson, H.; Shepherd, A. (2016) Surface Elevation Change and Mass Balance of Icelandic Ice Caps Derived from Swath Mode CryoSat-2 Altimetry. *Geophysical Research Letters.* 43 (23), 12,138-12,145.

Fortner, S.K., Mark, B.G., McKenzie, J.M., Bury, J., Trierweiler, A., Baraer, M., Burns, P.J. and Munk, L. (2011) Elevated stream trace and minor element concentrations in the foreland of receding tropical glaciers. *Applied Geochemistry*. 26(11), 1792-1801.

Foster, L.A., Brock, B.W., Cutler, M.E.J., Diotri, F. (2012) A physically based method for estimating supraglacial debris thickness from thermal band remote-sensing data. *Journal of Glaciology*. 58(210), 677-691.

Frey, H., Huggel, C., Chisholm, R.E., Baer, P., McArdell, B., Cochachin, A., Portocarrero. (2018) Multi-Source Glacial Lake Outburst Flood Hazard Assessment and Mapping for Huaraz, Cordillera Blanca, Peru. *Frontiers in Earth Science*. 6(210), 1-16.

Fyffe, C.L., Potter, E., Fugger, S., Orr, A., Fatichi, S., Loarte, E., Medina, K., Hellström, R.Å., Bernat, M., Aubry-Wake, C. and Gurgiser, W. (2021) The energy and mass balance of Peruvian glaciers. *Journal of Geophysical Research: Atmospheres*. JD034911.

Gardelle, J.; Berthier, E.; Arnaud, Y. (2013) Region-Wide Glacier Mass Balances over the Pamir-Karakoram-Himalaya during 1999--2011. *Cryosphere.* 7 (4), 1263–1263.

Gibson, M.J., Glasser, N.F., Quincey, D.J., Mayer, C., Rowan, A.W., Invine-Fynn, T.D.L. (2017) Temporal variations in supraglacial debris distribution on Baltoro Glacier, Karakoram between 2001 and 2012. *Geomorphology*. 295, 572-585.

Giese, A., Boone, A., Wagnon, P., Hawley, R. (2020) Incorporating moisture content in surface energy balance modeling of a debris-covered glacier. *The Cryosphere*. 14, 1555-1577.

Gudmundsson, G.H. and Bauder, A. (1999) Towards an indirect determination of the mass-balance distribution of glaciers using the kinematic boundary condition. *Geografiska Annaler: Series A, Physical Geography.* 81(4), 575-583.

Guittard, A., Baraer, M., McKenzie, J.M., Mark, B.G., Wigmore, O., Fernandez, A., Rapre, A.C., Walsh, E., Bury, J., Carey, M. and French, A. (2017) Trace-metal contamination in the glacierized Rio Santa watershed, Peru. *Environmental monitoring and assessment.* 189(12), 1-16.

Hammerle, A.; Meier, F.; Heinl, M.; Egger, A.; Leitinger, G. (2017) Implications of atmospheric conditions foranalysis of surface temperature variability derived from landscape-scale thermography. *International Journal of Biometeorology.* 61, 575–588

Han, H., Wang, J., Wei, J. and Liu, S. (2010) Backwasting rate on debris-covered Koxkar glacier, Tuomuer mountain, China. *Journal of Glaciology.* 56(196), 287-296.

Harris, S.A., Pederson, D.E. (1998) Thermal regimes beneath coarse blocky debris. *Permafrost and Periglacial Processes.* 9, 107-120.

Heid, T and Kääb, A (2012) Repeat optical satellite images reveal widespread and long term decrease in land-terminating glacier speeds. *Cryosphere.* 6, 467–478.

Herreid, S. and Pellicciotti, F. (2018) Automated detection of ice cliffs within supraglacial debris cover. *The Cryosphere.* 12(5), 1811-1829.

Herreid, S. and Pellicciotti, F. (2020) The state of rock debris covering Earth's glaciers. *Nature Geoscience.* 13(9), 621-627.

Hock, R., G. Rasul, C. Adler, B. Cáceres, S. Gruber, Y. Hirabayashi, M. Jackson, A. Kääb, S. Kang, S. Kutuzov, Al. Milner, U. Molau, S. Morin, B. Orlove, and H. Steltzer (2019) High Mountain Areas. In: *IPCC Special Report on the Ocean and Cryosphere in a Changing Climate* [H.-O. Pörtner, D.C. Roberts, V. Masson-Delmotte, P. Zhai, M. Tignor, E. Poloczanska, K. Mintenbeck, A. Alegría, M. Nicolai, A. Okem, J. Petzold, B. Rama, N.M. Weyer (eds.)]. In press.

Huo, D., Bishop, M.P. and Bush, A.B. (2021) Understanding Complex Debris-Covered Glaciers: Concepts, Issues, and Research Directions. *Frontiers in Earth Science.*

Huss, M., Bookhagen, B., Huggel, C., Jacobsen, D., Bradley, R.S., Clague, J.J., Vuille, M., Buytaert, W., Cayan, D.R., Greenwood, G. and Mark, B.G. (2017) Toward mountains without permanent snow and ice. *Earth's Future.* 5(5), 418-435.

Huss, M. and Hock, R. (2018) Global-scale hydrological response to future glacier mass loss. *Nature Climate Change*. 8(2), 135-140.

Immerzeel, W.W., Van Beek, L.P. and Bierkens, M.F. (2010) Climate change will affect the Asian water towers. *Science*. 328(5984), 1382-1385.

Immerzeel, W.W., Kraaijenbrink, P.D.A., Shea, J.M., Shrestha, A.B., Pelliciotti, F., Bierkens, M.F.P., de Jong, S.M. (2014) High-resolution monitoring of Himalayan glacier dynamics using unmanned aerial vehicles. *Remote Sensing of Environment*. 150, 93-103.

Immerzeel, W.W., Lutz, A.F., Andrade, M., Bahl, A., Biemans, H., Bolch, T., Hyde, S., Brumby, S., Davies, B.J., Elmore, A.C. and Emmer, A. (2020) Importance and vulnerability of the world's water towers. *Nature*. 577(7790), 364-369.

Irvine-Fynn, T.D.L., Porter, P.R., Rowan, A.V., Quincey, D.J., Gibson, M.J., Bridge, J.W., Watson, C.S., Hubbard, A., Glasser, N. (2017) Supraglacial Ponds Regulate Runoff From Himalayan Debris-Covered Glaciers. *Geophysical Research Letters*. 44(23), 11894-11904.

James, M.R., Robson, S., d'Oleire-Oltmanns, S. and Niethammer, U. (2017) Optimising UAV topographic surveys processed with structure-from-motion: Ground control quality, quantity and bundle adjustment. *Geomorphology*. 280, 51-66.

Jansson, P., Hock, R. and Schneider, T. (2003) The concept of glacier storage: a review. *Journal of Hydrology*. 282(1-4), 116-129.

Juen, M., Mayer, C., Lambrecht, A., Wirbel, A., Kueppers, U. (2012) Thermal properties of a supraglacial debris layer with respect to lithology and grain size. *Geografiska Annaler: Series A, Physical Geography*. 95(3), 197-209.

Juszak, I., Pellicciotti, F. (2013) A comparison of parameterizations of incoming longwave radiation over melting glaciers: Model robustness and seasonal variability. *Journal of Geophysical Research: Atmospheres*. 118, 3066-3084.

Kääb, A., Berthier, E., Nuth, C., Gardelle, J. and Arnaud, Y. (2012) Contrasting patterns of early twenty-first-century glacier mass change in the Himalayas. *Nature*. 488(7412), 495-498.

Kapnick, S.B., Delworth, T.L., Ashfaq, M., Malyshev, S., Milly, P.C.D. (2014) Snowfall less sensitive to warming in Karakoram than in Himalayas due to a unique seasonal cycle. *Nature Geoscience*. 7(11), 834-840.

Kaser, G., Ames, A., Zamora, M. (2017) Glacier Fluctuations and Climate in the Cordillera Blanca, Peru. *Annals of Glaciology*. 14, 136-140.

Kattelmann, R. (2003) Glacial Lake Outburst Floods in the Nepal Himalaya: A Manageable Hazard? *Natural Hazards*. 28, 145-154.

Kayastha, R. B.; Takeuchi, Y.; Nakawo, M.; Ageta, Y. (2000) Practical Prediction of Ice Melting beneath Various Thickness of Debris Cover on Khumbu Glacier, Nepal, Using a Positive Degree-Day Factor. *IAHS Publication*. 264, 71–81.

Kelly, J., Kljun, N., Olsson, P.O., Mihai, L., Liljeblad, B., Weslien, P., Klemedtsson, L. and Eklundh, L. (2019) Challenges and best practices for deriving temperature data from an uncalibrated UAV thermal infrared camera. *Remote Sensing*. 11(5), 567.

Kirkbride, M.P. (1993) The temporal significance of transitions from melting to calving termini at glaciers in the central Southern Alps of New Zealand. *The Holocene*. 3(3), 232-240.

Kirkbride, M.P. and Dugmore, A.J. (2003) Glaciological response to distal tephra fallout from the 1947 eruption of Hekla, south Iceland. *Journal of Glaciology*. 49(166), 420-428.

Kirkbride, M.P., Deline, P. (2013) The formation of supraglacial debris covers by primary dispersal from transverse englacial debris bands. *Earth Surface Processes and Landforms*. 38, 1779-1792.

Kneib, M., Miles, E.S., Jola, S., Buri, P., Herreid, S., Bhattacharya, A., Watson, C.S., Bolch, T., Quincey, D. and Pellicciotti, F. (2021) Mapping ice cliffs on debris-covered glaciers using multispectral satellite images. *Remote Sensing of Environment*. 253, 112201.

Kraaijenbrink, P.D.A., Shea, J.M., Pelliciotti, F., de Jong, S.M., Immerzeel, W.W. (2016) Object-based analysis of unmanned aerial vehicle imagery to map and characterise surface features on a debris-covered glacier. *Remote Sensing of Environment*. 186, 581-595.

Kraaijenbrink, P. D. A.; Bierkens, M. F. P.; Lutz, A. F.; Immerzeel, W. W. (2017) Impact of a Global Temperature Rise of 1.5 Degrees Celsius on Asia's Glaciers. *Nature*. 549 (7671), 257–260.

Kraaijenbrink, P.D., Shea, J.M., Litt, M., Steiner, J.F., Treichler, D., Koch, I. and Immerzeel, W.W. (2018) Mapping surface temperatures on a debris-covered glacier with an unmanned aerial vehicle. *Frontiers in Earth Science*. 6, 64.

Lambrecht, A.; Mayer, C.; Hagg, W.; Popovnin, V.; Rezepkin, A.; Lomidze, N.; Svanadze, D. (2011) A Comparison of Glacier Melt on Debris-Covered Glaciers in the Northern and Southern Caucasus. *Cryosphere*. 5, 525–538.

Lejeune, Y.; Bertrand, J.-M.; Wagnon, P.; Morin, S. A. (2013) A Physically Based Model of the Year-Round Surface Energy and Mass Balance of Debris-Covered Glaciers. *Journal of Glaciology*. 59 (214), 327–344.

Lliboutry, L. (1977) Glaciological problems set by the control of dangerous lakes in Cordillera Blanca, Peru. II. Movement of a covered glacier embedded within a rock glacier. *Journal of Glaciology*. 18, 255-273.

Lloyd, J.M. (2013) *Thermal imaging systems*. Springer Science & Business Media.

Ludwig, M., M Runge, C., Friess, N., Koch, T.L., Richter, S., Seyfried, S., Wraase, L., Lobo, A., Sebastià, M., Reudenbach, C. and Nauss, T. (2020) Quality assessment of photogrammetric methods—A workflow for reproducible UAS orthomosaics. *Remote Sensing*. 12(22), 3831.

Maes, W.H.; Huete, A.R.; Steppe, K. (2017) Optimizing the processing of UAV-based thermal imagery. *Remote Sensing*. 9, 476.

Mark, B.G., Bury, J., McKenzie, J.M., French, A. and Baraer, M. (2010) Climate change and tropical Andean glacier recession: Evaluating hydrologic changes and livelihood vulnerability in the Cordillera Blanca, Peru. *Annals of the Association of American geographers*. 100(4), 794-805.

Mark, B.G., French, A., Baraer, M., Carey, M., Bury, J., Young, K.R., Polk, M.H., Wigmore, O., Lagos, P., Crumley, R., McKenzie, J.M. Lautz, L. (2017) Glacier loss and hydro-social risks in the Peruvian Andes. *Global and Planetary Change*. 159, 61-76.

Mark, B.G., Seltzer, G.O. (2017) Tropical glacier meltwater contribution to stream discharge: a case study in the Cordillera Blanca, Peru. *Journal of Glaciology*. 49(165), 271-281.

Mattson, L.E. (1993) Ablation on debris covered glaciers: an example from the Rakhiot Glacier, Punjab, Himalaya. *International Association of Hydrological Sciences.* 218, pp.289-296.

Maussion, F., Butenko, A., Champollion, N., Dusch, M., Eis, J., Fourteau, K., Gregor, P., Jarosch, A.H., Landmann, J., Oesterle, F., Recinos, B., Rothenpieler, T., Vlug, A., Wild, C.T., Marzeion, B. (2019) The Open Global Glacier Model (OGGM) v1.1. *Geoscientific Model Development*. 12, 909-931.

McDowell, G., Koppes, M., Harris, L., Chan, K.M., Price, M.F., Lama, D.G. and Jiménez, G. (2021) Lived experiences of 'peak water' in the high mountains of Nepal and Peru. *Climate and Development*. 1-14.

Meier, M. F.; Post, A. (1969) What Are Glacier Surges? *Canadian Journal of Earth Sciences.* 6 (4), 807–817.

Meier, F., Scherer, D., Richters, J. and Christen, A. (2011) Atmospheric correction of thermal-infrared imagery of the 3-D urban environment acquired in oblique viewing geometry. *Atmospheric Measurement Techniques*. 4(5), 909-922.

Mihalcea, C., Mayer, C., Diolaiuti, G., Lambrecht, A., Smiraglia, C. and Tartari, G. (2006) Ice ablation and meteorological conditions on the debris-covered area of Baltoro glacier, Karakoram, Pakistan. *Annals of Glaciology*. 43, 292-300.

Mihalcea, C., Brock, B.W., Diolaiuti, G., D'Agata, C., Citterio, M., Kirkbride, M.P., Cutler, M.E.J., Smiraglia, C. (2008) Using ASTER satellite and ground-based surface temperature measurements to derive supraglacial debris cover and thickness patterns on Miage Glacier (Mont Blanc Massif, Italy). *Cold Regions Science and Technology*. 52(3), 341-354.

Miles, E.S., Pellicciotti, F., Willis, I.C., Steiner, J.F., Buri, P., Arnold, N.S. (2016) Refined energy-balance modelling of a supraglacial pond, Langtang Khola, Nepal. *Annals of Glaciology*. 57(71), 29-40.

Miles, E. S.; Watson, C. S.; Brun, F.; Berthier, E.; Esteves, M.; Quincey, D. J.; Miles, K. E.; Hubbard, B.; Wagnon, P. (2018) Glacial and Geomorphic Effects of a Supraglacial Lake Drainage and Outburst Event, Everest Region, Nepal Himalaya. *Cryosphere*. 12 (12), 3891–3905.

Miles, K.E., Hubbard, B., Irvine-Fynne, T.D.L., Miles, E.S., Quincey, D., Rowan, A.V. (2020) Hydrology of debris-covered glaciers in High Mountain Asia. *Earth-Science Reviews*. 207(103212).

Miles, E., McCarthy, M., Dehecq, A., Kneib, M., Fugger, S., Pellicciotti, F. (2021) Health and sustainability of glaciers in High Mountain Asia. *Nature Communications*. 12(2868).

Millan, R.; Mouginot, J.; Rabatel, A.; Jeong, S.; Cusicanqui, D.; Derkacheva, A.; Chekki, M. (2019) Mapping Surface Flow Velocity of Glaciers at Regional Scale Using a Multiple Sensors Approach. *Remote Sensing*. 11 (21), 2498.

Mlambo, R., Woodhouse, I.H., Gerard, F. and Anderson, K. (2017) Structure from motion (SfM) photogrammetry with drone data: A low cost method for monitoring greenhouse gas emissions from forests in developing countries. *Forests*. 8(3), 68.

Möller, R., Möller, M., Kukla, P.A. and Schneider, C. (2016) Impact of supraglacial deposits of tephra from Grímsvötn volcano, Iceland, on glacier ablation. *Journal of Glaciology*. 62(235), 933-943.

Mulakala, J. (2019) Measurement Accuracy of the DJI Phantom 4 RTK & Photogrammetry. *DroneDeploy, Technical Report.*

Nakawo, M.; Young, G. (1981) Field Experiments to determine the Effect of a Debris

Layer on ablation of Glacier Ice, *Annals of Glaciology.* 2, 85–91.

Nakawo, M., Rana, B. (1999) Estimate of Ablation Rate of Glacier Ice Under a Supraglacial Debris Layer. *Geografiska Annaler: Series A, Physical Geography.* 81(4), 695-701.

Neckel, N., Loibl, D. and Rankl, M. (2017) Recent slowdown and thinning of debris-covered glaciers in south-eastern Tibet. *Earth and Planetary Science Letters.* 464, 95-102.

Nicholson, L., Benn, D.I. (2006) Calculating ice melt beneath a debris layer using meteorological data. *Journal of Glaciology.* 52(178), 463-470.

Nicholson, L., Benn, D.I. (2012) Properties of natural supraglacial debris in relation to modelling sub-debris ice ablation. *Earth Surface Processes and Landforms.* 38(5), 490-501.

Nicholson, L., Mertes, J. (2017) Thickness estimation of supraglacial debris above ice cliff exposures using a high-resolution digital surface model derived from terrestrial photography. *Journal of Glaciology.* 63(242), 989-998.

Nicholson, L.I., McCarthy, M., Pritchard, H.D., Willis, I. (2018) Supraglacial debris thickness variability: impact on ablation and relation to terrain properties. *The Cryosphere.* 12(12), 3719-3734.

Nuimura, T.; Fujita, K.; Fukui, K.; Asahi, K.; Aryal, R.; Ageta, Y. Temporal Changes in Elevation of the Debris-Covered Ablation Area of Khumbu Glacier in the Nepal Himalaya since 1978. (2011) *Arctic, Antarctic and Alpine Research.* 43 (2), 246–255.

Nuimura, T.; Fujita, K.; Sakai, A. (2017) Downwasting of the Debris-Covered Area of Lirung Glacier in Langtang Valley, Nepal Himalaya, from 1974 to 2010. *Quaternary International.* 455, 93–101.

Östrem, G. (1959) Ice Melting under a Thin Layer of Moraine, and the Existence of Ice Cores in Moraine Ridges. *Geografiska Annaler.* 41(4), pp 228–230.

Paul, F. (2020) A 60-Year Chronology of Glacier Surges in the Central Karakoram from the Analysis of Satellite Image Time-Series. *Geomorphology.* 352, 106993.

Pelto, B.M., Menounos, B. (2021) Surface Mass-Balance Gradients From Elevation and Ice Flux Data in the Columbia Basin, Canada. *Frontiers in Earth Science.* 587.

Pratap, B.; Dobhal, D. P.; Mehta, M.; Bhambri, R. (2015) Influence of Debris Cover and Altitude on Glacier Surface Melting: A Case Study on Dokriani Glacier, Central Himalaya, India. *Annals of Glaciology.* 56 (70), 9–16.

Pritchard, H.D. (2019) Asia's shrinking glaciers protect large populations from drought stress. *Nature.* 569, 649-654.

Quincey, D.J., Luckman, A. and Benn, D. (2009) Quantification of Everest region glacier velocities between 1992 and 2002, using satellite radar interferometry and feature tracking. *Journal of Glaciology*. 55(192), 596-606.

Rabatel, A., Francou, B., Soruco, A., Gomez, J., Cáceres, B., Ceballos, J.L., Basantes, R., Vuille, M., Sicart, J.E., Huggel, C., Scheel, M., Lejeune, Y., Arnaud, Y., Collet, M., Condom, T., Consoli, G., Favier, V., Jomelli, V., Galarraga, R., Ginot, P., Maisincho, L., Mendoza, J., Ménégoz, M., Ramarez, E., Ribtein, P., Suarez, W., Villacis, M., Wagnon, P. (2012) Current state of glaciers in the tropical Andes: a multi-century perspective on glacier evolution and climate change. *The Cryosphere*. 7 (1), 81-102.

Radić, V., Bliss, A., Beedlow, A.C., Hock, R., Miles, E. and Cogley, J.G. (2014) Regional and global projections of twenty-first century glacier mass changes in response to climate scenarios from global climate models. *Climate Dynamics*. 42(1-2), 37-58.

RGI Consortium (2017) Randolph Glacier Inventory – A Dataset of Global Glacier Outlines: Version 6.0.

Reid, T.D., Carenzo, M., Pellicciotti, F. and Brock, B.W. (2012) Including debris cover effects in a distributed model of glacier ablation. *Journal of Geophysical Research: Atmospheres*. 117 (D18).

Reid, T.D. and Brock, B.W. (2014) An energy-balance model for debris-covered glaciers including heat conduction through the debris layer. *Journal of Glaciology*. 56(199), 903-916.

Reynolds, J.M. (2000) On the formation of supraglacial lakes on debris-covered glaciers. *Proceedings of a workshop held at Seattle, Washington, USA, September 2000*. IAHS Publ. no. 264, 153-161.

Ribeiro-Gomes, K., Hernández-López, D., Ortega, J.F., Ballesteros, R.., Poblete, T., Moreno, M.A. (2017) Uncooled thermal camera calibration and optimization of the photogrammetry process for UAV applications in agriculture. *Sensors*. 17, 2173.

Richardson, S.D., Reynolds, J.M. (2000). An overview of glacial hazards in the Himalayas. *Quaternary International*. 65–66, 31-47.

Röhl, K. (2008) Characteristics and evolution of supraglacial ponds on debris-covered Tasman Glacier, New Zealand. *Journal of Glaciology*. 54(188), 867-880.

Rounce, D.R., McKinney, D.C. (2014) Debris thickness of glaciers in the Everest area (Nepal Himalaya) derived from satellite imagery using a nonlinear energy balance model. *The Cryosphere*. 8(4), 1317-1329.

Rounce, D.R., Quincey, D.J. and McKinney, D.C. (2015) Debris-covered glacier energy balance model for Imja–Lhotse Shar Glacier in the Everest region of Nepal. *The Cryosphere*. 9(6), 2295-2310.

Rounce, D.R., McKinney, D.C., Lala, J.M., Byers, A.C., Watson, S.W. (2016) A new remote hazard and risk assessment framework for glacial lakes in the Nepal Himalaya. *Hydrology and Earth Systems Science*. 20, 3455-3475.

Rounce, D. R.; King, O.; McCarthy, M.; Shean, D. E.; Salerno, F. (2018) Quantifying Debris Thickness of Debris-Covered Glaciers in the Everest Region of Nepal Through Inversion of a Subdebris Melt Model. *Journal of Geophysical Research: Earth Surface*. 123 (5), 1094–1115.

Rounce, D.R., Hock, R. and Shean, D.E. (2020) Glacier mass change in High Mountain Asia through 2100 using the open-source python glacier evolution model (PyGEM). *Frontiers in Earth Science*. 7, 331.

Rounce, D.R., Hock, R., McNabb, R.W., Millan, R., Sommer, C., Braun, M.H., Malz, P., Maussion, F., Mouginot, J., Seehaus, T.C., Shean, D.E. (2021) Distributed Global Debris Thickness Estimates Reveal Debris Significantly Impacts Glacier Mass Balance. *Geophysical Research Letters*. 48(8), e2020GL091311.

Rowan, A. V.; Egholm, D. L.; Quincey, D. J.; Glasser, N. F. (2015) Modelling the Feedbacks between Mass Balance, Ice Flow and Debris Transport to Predict the Response to Climate Change of Debris-Covered Glaciers in the Himalaya. *Earth and Planetary Science Letters*. 430, 427–438.

Rowan, A.V., Quincey, D.J., Gibson, M.J., Glasser, N.F., Westoby, M.J., Irvine-Fynn, T.D., Porter, P.R. and Hambrey, M.J. (2018) The sustainability of water resources in High Mountain Asia in the context of recent and future glacier change. *Geological Society, London, Special Publications*. 462(1), 189-204.

Rowan, A.V., Egholm, D.L., Quincey, D.J., Hubbard, B., King, O., Miles, E.S., Miles, K.E. and Hornsey, J. (2021) The Role of Differential Ablation and Dynamic Detachment in Driving Accelerating Mass Loss From a Debris-Covered Himalayan Glacier. *Journal of Geophysical Research: Earth Surface*. 126(9), 2020JF005761.

Sakai, A., Nakawo, M., and Fujita, K. (1998). Melt Rate of Ice Cliffs on the Lirung Glacier, Nepal Himalayas, 1996. *Bulletin of Glacier Research*. 16, 57–66.

Sakai, A., Takeuchi, N., Fujita, K., Nakawo, M. (2000) Role of supraglacial ponds in the ablation process of a debris-covered glacier in the Nepal Himalayas. *IAHS Publication*. 119-132.

Sakai, A., Nakawo, M., Fujita, K. (2018) Distribution Characteristics and Energy Balance of Ice Cliffs on Debris-covered Glaciers, Nepal Himalaya. *Arctic, Antarctic and Alpine Research*. 34(1), 12-19.

Salby, M.L. (1996) *Fundamentals of atmospheric physics*. Elsevier.

Salisbury, J.W. and D'Aria, D.M. (1992) Emissivity of terrestrial materials in the 8–14 μm atmospheric window. *Remote sensing of Environment*. 42(2), 83-106.

Sato, Y., Fujita, K., Inoue, H., Sunako, S., Sakai, A., Tsushima, A., Podolskiy, E.A., Kayastha, R. Kayastha, R.B. (2021) Ice cliff dynamics of debris-covered Trakarding Glacier in the Rolwaling region, Nepal Himalaya. *Frontiers in Earth Science*. 9, 398.

Schauwecker, S., Rohrer, M., Acuña, D., Cochachin, A., Dávila, L., Frey, H., Giráldez, C., J.Gómez, J., Huggel, C., Jacques-Coper, M., Loarte, E., Salzmann, N., Vuille, M. (2014) Climate trends and glacier retreat in the Cordillera Blanca, Peru, revisited. *Global and Planetary Change*. 119, 85-97.

Scherler, D., Bookhagen, B., Strecker, M.R. (2011) Spatially variable response of Himalayan glaciers to climate change affected by debris cover. *Nature Geoscience*. 4, 156-159.

Scherler, D.; Wulf, H.; Gorelick, N. (2018) Global Assessment of Supraglacial Debris-Cover Extents. *Geophysical Research Letters.* 45 (21), 11,798-11,805.

Seehaus, T., Malz, P., Sommer, C., Lippl, S. Cochachin, A., Braun, M. (2019) Changes of the tropical glaciers throughout Peru between 2000 and 2016 – mass balance and area fluctuations. *The Cryosphere*. 13, 2537-2556.

Sevestre, H.; Benn, D. I. (2015) Climatic and Geometric Controls on the Global Distribution of Surge-Type Glaciers: Implications for a Unifying Model of Surging. *Journal of Glaciology.* 61 (228), 646–662.

Shah, S.S., Banerjee, A., Nainwal, H.C. and Shankar, R. (2019) Estimation of the total sub-debris ablation from point-scale ablation data on a debris-covered glacier. *Journal of Glaciology*. 65(253), 759-769.

Shannon, S., Smith, R., Wiltshire, A., Payne, T., Huss, M., Betts, R., Caesar, J., Koutroulis, A., Jones, D. and Harrison, S. (2019) Global glacier volume projections under high-end climate change scenarios. *The Cryosphere*. 13(1), 325-350.

Shea, J. M.; Immerzeel, W. W.; Wagnon, P.; Vincent, C. (2015) Bajracharya, S. Modelling Glacier Change in the Everest Region, Nepal Himalaya. *Cryosphere. 9*, 1105–1128.

Shean, D.E., Bhushan, S., Montesano, P., Rounce, D.R., Arendt, A. and Osmanoglu, B. (2020) A systematic, regional assessment of high mountain Asia glacier mass balance. *Frontiers in Earth Science*. 7, 363.

Sherpa, S. F.; Wagnon, P.; Brun, F.; Berthier, E.; Vincent, C.; Lejeune, Y.; Arnaud, Y.; Kayastha, R. B.; Sinisalo, A. (2017) Contrasted Surface Mass Balances of Debris-Free Glaciers Observed between the Southern and the Inner Parts of the Everest Region (2007-15). *Journal of Glaciology*. 63 (240), 637–651.

Shugar, D.H., Burr, A., Haritashya, U.K., Kargel, J.S., Watson, C.S., Kennedy, M.C., Bevington, A.R., Betts, R.A., Harrison, S. and Strattman, K. (2020) Rapid worldwide growth of glacial lakes since 1990. *Nature Climate Change*. 10(10), 939-945.

Silverio, W., Jaquet, J.M. (2017) Evaluating glacier fluctuations in Cordillera Blanca (Peru). *Archives des Sciences*. 69, 145–62.

Steiner, J.F., Pellicciotti, F., Buri, P., Miles, E.S., Immerzeel, W.W. and Reid, T.D. (2015) Modelling ice-cliff backwasting on a debris-covered glacier in the Nepalese Himalaya. *Journal of Glaciology*. 61(229), 889-907.

Steiner, J.F., Buri, P., Miles, E., Ragettli, S., Pellicciotti, F. (2019) Supraglacial ice cliffs and ponds on debris-covered glaciers: spatio-temporal distribution and characteristics. *Journal of Glaciology*. 65(252), 617-632.

The Global Runoff Data Centre - Major River Basins of the World. Available online: https://www.bafg.de/GRDC/EN/02_srvcs/22_gslrs/221_MRB/riverbasins_node.html (accessed 9/3/2020).

Thompson, S., Benn, D.I., Mertes, J. and Luckman, A. (2016) Stagnation and mass loss on a Himalayan debris-covered glacier: processes, patterns and rates. *Journal of Glaciology*. 62(233), 467-485.

Tomaštík, J., Mokroš, M., Surový, P., Grznárová, A. and Merganič, J. (2019) UAV RTK/PPK method—an optimal solution for mapping inaccessible forested areas? *Remote sensing*. 11(6), 721.

USGS (1999) *Peruvian Cordilleras* [online]. Available at: https://pubs.usgs.gov/pp/p1386i/peru/occident.html [Accessed 13/9/2021].

Van Tricht, L., Huybrechts, P., Van Breedam, J., Vanhulle, A., Van Oost, K. and Zekollari, H. (2021) Estimating surface mass balance patterns from unoccupied aerial vehicle measurements in the ablation area of the Morteratsch–Pers glacier complex (Switzerland). *The Cryosphere*. 15(9), 4445-4464.

Veettil, B.K. (2018) Glacier mapping in the Cordillera Blanca, Peru, tropical Andes, using Sentinel-2 and Landsat data. *Singapore Journal of Tropical Geography*. 39(3), 351-363.

Veh, G.; Korup, O.; von Specht, S.; Roessner, S.; Walz, A. (2019) Unchanged Frequency of Moraine-Dammed Glacial Lake Outburst Floods in the Himalaya. *Nature Climate Change*. 9, 379–383.

Veh, G., Korup, O., Walz, A. (2020) Hazard from Himalayan glacier lake outburst floods. *Proceedings of the National Academy of Sciences of the United States of America*. 117(2), 907-912.

Vincent, C., Soruco, A., Six, D. and Le Meur, E. (2009) Glacier thickening and decay analysis from 50 years of glaciological observations performed on Glacier d'Argentière, Mont Blanc area, France. *Annals of glaciology*. 50(50), 73-79.

Vincent, C., Wagnon, P., Shea, J.M., Immerzeel, W.W., Kraaijenbrink, P., Shrestha, D., Soruco, A., Arnaud, Y., Brun, F., Berthier, E., Sherpa, S.F. (2016) Reduced melt on debris-covered glaciers: Investigations from Changri Nup Glacier, Nepal. *The Cryosphere*. 10(4), 1845-1858.

Viviroli, D., Dürr, H.H., Messerli, B., Meybeck, M. and Weingartner, R. (2007) Mountains of the world, water towers for humanity: Typology, mapping, and global significance. *Water resources research*. 43(7).

Vollmer, M. and Möllmann, K.P. (2017) *Infrared thermal imaging: fundamentals, research and applications*. John Wiley & Sons.

Wagnon, P.; Linda, A.; Arnaud, Y.; Kumar, R.; Sharma, P.; Vincent, C.; Pottakkal, J. G.; Berthier, E.; Ramanathan, A.; Hasnain, S. I., Chevallier, P. (2007) Four Years of Mass Balance on Chhota Shigri Glacier, Himachal Pradesh, India, a New Benchmark Glacier in the Western Himalaya. *Journal of Glaciology*. 53 (183), 603–611.

Wagnon, P.; Vincent, C.; Arnaud, Y.; Berthier, E.; Vuillermoz, E.; Gruber, S.; Gilbert, A.; Dumont, M.; Shea, J. M.; Stumm, D.; Pokhrel, B. K. (2013) Seasonal and Annual Mass Balances of Mera and Pokalde Glaciers (Nepal Himalaya) since 2007. *Cryosphere*. 7 (6), 1769–1769.

Wallace, L., Lucieer, A., Watson, C. and Turner, D. (2012) Development of a UAV-LiDAR system with application to forest inventory. *Remote sensing*. 4(6), 1519-1543.

Wang, C. and Myint, S.W. (2015) A simplified empirical line method of radiometric calibration for small unmanned aircraft systems-based remote sensing. *IEEE Journal of selected topics in applied earth observations and remote sensing*. 8(5), 1876-1885.

Watanabe, T., Ives, J.D., Hammond. J.E. (1994) Rapid growth of a glacial lake in Khumbu Himal, Himalaya: prospects for a catastrophic flood. *Mountain Research and Development*. 14 (4), 329-340.

Watson, C.S., Quincey, D.J., Carrivick, J.L. and Smith, M.W. (2016) The dynamics of supraglacial ponds in the Everest region, central Himalaya. *Global and Planetary Change*. 142, 14-27.

Watson, C.S., Quincey, D.J., Carrivick, J.L., Smith, M.W. (2017) Ice cliff dynamics in the Everest region of the Central Himalaya. *Geomorphology*. 278, 238-251.

Wigmore, O. and Mark, B. (2017) Monitoring tropical debris-covered glacier dynamics from high-resolution unmanned aerial vehicle photogrammetry, Cordillera Blanca, Peru. *The Cryosphere*. 11(6), 2463-2480.

Yang, W., Zhao, C., Westoby, M., Yao, T., Wang, Y., Pellicciotti, F., Zhou, J., He, Z., Miles, E. (2020) Seasonal Dynamics of a Temperate Tibetan Glacier Revealed by High-Resolution UAV Photogrammetry and In Situ Measurements. *Remote Sensing*. 12(15), 2389.

Zhang, Z., Chan, J.C.L., Ding, Y. (2004) Characteristics, evolution and mechanisms of the summer monsoon onset over Southeast Asia. *International Journal of Climatology*. 24(12), 1461-1482.

Zhang, Y, Fujita, K, Liu, S, Liu, Q and Nuimura, T (2011) Distribution of debris thickness and its effect on ice melt at Hailuogou glacier, southeastern Tibetan Plateau, using in situ surveys and ASTER imagery. *Journal of Glaciology*. 57(206), 1147–1157.

Zhang, Y., Hirabayashi, Y., Fujita, K., Liu, S.Y. (2016) Heterogeneity in supraglacial debris thickness and its role in glacier mass changes of the Mount Gongga. *Science China Earth Sciences*. 59(1), 170-184.

Appendix A

Published *Remote Sensing* article

remote sensing

MDPI

Article

Reversed Surface-Mass-Balance Gradients on Himalayan Debris-Covered Glaciers Inferred from Remote Sensing

Rosie R. Bisset [1,*], Amaury Dehecq [2,3], Daniel N. Goldberg [1], Matthias Huss [2,3,4], Robert G. Bingham [1] and Noel Gourmelen [1]

1 School of GeoSciences, University of Edinburgh, Edinburgh EH8 9XP, UK; Dan.Goldberg@ed.ac.uk (D.N.G.); r.bingham@ed.ac.uk (R.G.B.); Noel.Gourmelen@ed.ac.uk (N.G.)
2 Laboratory of Hydraulics, Hydrology and Glaciology, ETH Zurich, 8093 Zurich, Switzerland; adehecq@vaw.baug.ethz.ch (A.D.); matthias.huss@unifr.ch (M.H.)
3 Swiss Federal Institute for Forest, Snow and Landscape Research (WSL), CH-8903 Birmensdorf, Switzerland
4 Department of Geosciences, University of Fribourg, 1700 Fribourg, Switzerland
* Correspondence: rosie.bisset@ed.ac.uk

Received: 27 March 2020; Accepted: 7 May 2020; Published: 14 May 2020

Abstract: Meltwater from the glaciers in High Mountain Asia plays a critical role in water availability and food security in central and southern Asia. However, observations of glacier ablation and accumulation rates are limited in spatial and temporal scale due to the challenges that are associated with fieldwork at the remote, high-altitude settings of these glaciers. Here, using a remote-sensing-based mass-continuity approach, we compute regional-scale surface mass balance of glaciers in five key regions across High Mountain Asia. After accounting for the role of ice flow, we find distinctively different altitudinal surface-mass-balance gradients between heavily debris-covered and relatively debris-free areas. In the region surrounding Mount Everest, where debris coverage is the most extensive, our results show a reversed mean surface-mass-balance gradient of −0.21 ± 0.18 m w.e. a^{-1} $(100\ m)^{-1}$ on the low-elevation portions of glaciers, switching to a positive mean gradient of 1.21 ± 0.41 m w.e. a^{-1} $(100\ m)^{-1}$ above an average elevation of 5520 ± 50 m. Meanwhile, in West Nepal, where the debris coverage is minimal, we find a continuously positive mean gradient of 1.18 ± 0.40 m w.e. a^{-1} $(100\ m)^{-1}$. Equilibrium line altitude estimates, which are derived from our surface-mass-balance gradients, display a strong regional gradient, increasing from northwest (4490 ± 140 m) to southeast (5690 ± 130 m). Overall, our findings emphasise the importance of separating signals of surface mass balance and ice dynamics, in order to constrain better their contribution towards the ice thinning that is being observed across High Mountain Asia.

Keywords: glaciers; surface mass balance; mass continuity; remote sensing; debris cover

1. Introduction

The glaciers in High Mountain Asia collectively form the largest glaciated area outside the polar regions, covering an estimated ~118,264 km^2 [1]. Meltwater from these glaciers feeds into major river basins, including the Indus, Ganges, Brahmaputra, Yellow, and Yangtze, providing water resources to 221 ± 59 million people living in central and southern Asia [2]. Furthermore, the melt rates of the glaciers in High Mountain Asia modify the frequency and magnitude of glacial-lake outburst floods, posing significant threats to downstream communities [3–5]. Quantifying and improving our understanding of glacier surface-mass-balance distribution across High Mountain Asia is critical in the effective prediction and mitigation of these impacts.

Glacier surface mass balance (hereafter SMB) is defined as the difference between accumulation and ablation, being negative where there is net melt. Many of the glaciers in High Mountain Asia are characterised by supraglacial debris cover of varying thickness and extent, which plays an important role in modifying SMB through its impact on glacier ablation rates. Field-based studies have shown that a thin layer of supraglacial debris, less than a critical thickness of ~3–8 cm, enhances glacier melt rates (e.g., [6]) through a reduction in the ice-surface albedo, as first demonstrated experimentally [7], and more recently constrained from surface energy balance modelling (e.g., [8,9]). In contrast, debris cover exceeding the critical thickness has the opposite effect, reducing ablation by insulating the ice surface (e.g., [6,10–14]). Other properties of supraglacial debris, such as moisture content, rock type, and grain size, can alter the thermal conductivity of the debris layer, consequently modifying the relationship between debris thickness and surface melt rates (e.g., [15–17]). The ablation rates on heavily debris-covered glaciers are extremely difficult to measure, due to the challenges that are associated with drilling stakes through the debris layer, as well as the large heterogeneity of local ablation rates (e.g., [13,18]).

Previous geodetic studies of ice-surface-elevation change have shown that, collectively, the glaciers in High Mountain Asia are rapidly losing mass [19–22], with a total annual mass change of $-19.0 \pm 2.5\,\mathrm{Gt\,a^{-1}}$ between 2000 and 2018 [22]. However, despite the well-known importance of debris cover, geodetic studies have identified no clear relationship between supraglacial debris cover and rates of ice thinning in High Mountain Asia [19,20,23]. The presence of supraglacial features on debris-covered ice, such as ice cliffs and meltwater ponds, is one factor that is likely to be contributing to this anomaly. These features enhance localised melt rates and therefore partially offset the effects of reduced surface melting on ice thinning rates in debris-covered areas [24–26]. The reduced emergence velocity of debris-covered glaciers [27,28], leading to greater rates of ice-surface lowering compared to clean-ice glaciers, is another factor that is hypothesised to play a role in the debris anomaly. This surface lowering counteracts against the reduced ice-thinning rate in debris-covered areas, therefore potentially contributing towards the similar rates of thinning that have been observed on both debris-free and debris-covered glaciers [27–29].

The previously observed ice-surface-elevation changes are a result of a combination of both SMB and ice dynamics, as well as other processes, such as basal melting, internal accumulation, and calving (for lake-terminating glaciers) [30]. Therefore, producing regional distributed SMB observations is critical for separating signals of climate and ice flow dynamics and better constraining the region-wide influence of debris cover in glaciological models. Several studies have shown that it is possible to disentangle these contributions towards ice-surface-elevation changes using the principle of mass conservation [25,28,29,31,32]. Here, we present a methodology employing this principle in order to calculate SMB for a larger sample of glaciers across multiple regions, using recently produced spatially extensive remote sensing datasets. All of the mass-conservation terms are estimated from remote-sensing datasets [21,33] and modelled ice-thickness data [34]. After isolating the contribution of SMB towards ice thinning, we investigate the contrasting altitudinal patterns of SMB on debris-covered and clean-ice glaciers at a regional level.

2. Materials and Methods

2.1. Overview

Using a mass-continuity approach, we combined existing remote-sensing observations and modelled datasets to derive spatially-distributed estimates of mean SMB over a total glaciated area of ~2000 $\mathrm{km^2}$ within the Pamir-Karakoram-Himalaya. Our computations were performed for 25 glaciers within these regions. We divided each glacier into sections of ~2 km in length (Figure A1). For each section, we computed the ingoing and outgoing ice fluxes from existing feature-tracking-derived ice velocities [33] and modelled ice thickness [34] (see Section 2.2). We calculated the mean elevation change for each section from previously derived geodetic measurements [18] and, based on mass

continuity, constrained the contribution of SMB. Using surface digital elevation models [35] and existing modelled debris-thickness maps [36], we analysed the dependence of SMB on elevation and debris thickness. We used breakpoint analyses in order to determine the elevations of transition points between different altitudinal SMB gradients for each glacier, and applied weighted regression models to determine the altitudinal SMB gradients below and above these elevations.

Our mean SMB estimates were generated for the period 2000–2015, which aligns with the periods of the input datasets (see Section 2.2). We carried out our analyses for five regions within High Mountain Asia (Figure 1), which were chosen based on the mutual availability of ice-surface velocity and elevation-change data, and to cover a range of meteorological and environmental conditions. Figure 1 shows the mean percentage debris cover for each region, as computed from an existing global debris-cover-extent dataset [37]. The largest glaciers within each region were included in our analyses (Figure A1), as smaller glaciers (<~10 km in length) do not provide a sufficient number of measurements to compute SMB gradients. The glacier-wide coverage of our SMB calculations was dependent on the availability of ice velocity data, which was often limited in coverage in high-altitude accumulation areas. We used our final SMB results to investigate the influence of supraglacial debris cover on altitudinal SMB gradients at a regional scale.

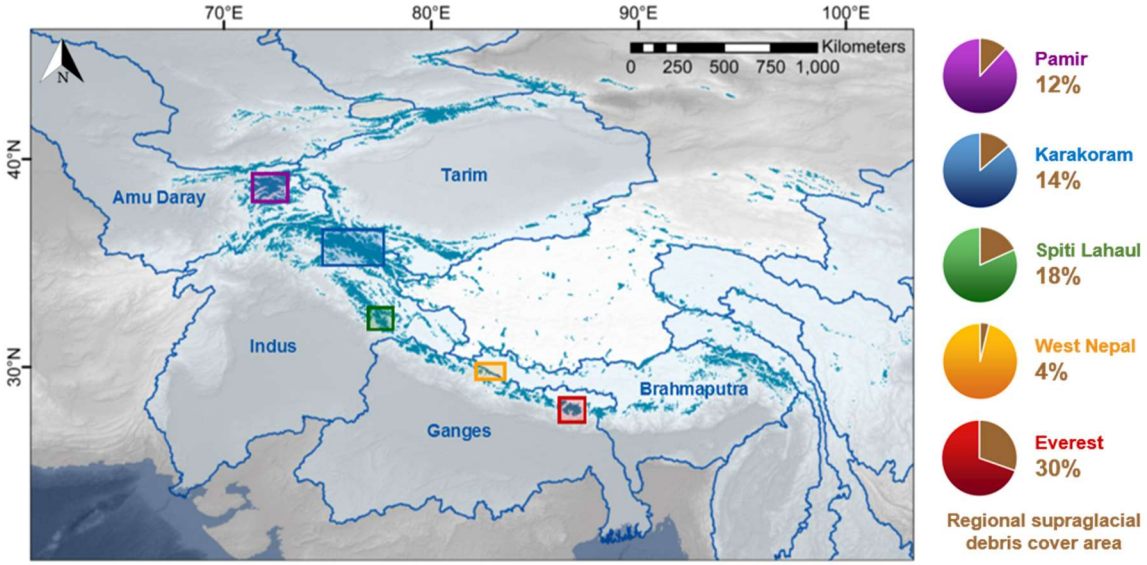

Figure 1. Regions of study across High Mountain Asia. Coloured boxes show the five regions for which surface mass balance is computed: Pamir (purple), Karakoram (blue), Spiti Lahaul (green), West Nepal (orange), and Everest (red). Pie charts on right show the mean percentage of ice covered by debris (computed from an existing debris cover distribution dataset for 2013–2017 [37]) for the glaciers analysed within each of the five study regions. Turquoise shaded areas show the glaciers from the Randolph Glacier Inventory v6.0 [1]. Blue outlined areas show the major river basins [38], which drain meltwater from the glaciers in High Mountain Asia.

2.2. Data

The ice velocities used in this study cover the period 1999–2015 at 120 m resolution and they were produced using semi-automated feature tracking, applied to Landsat multispectral satellite imagery [see 33 for full derivation]. The ice-surface-elevation change dataset used in this study was derived by [21] from differencing of digital elevation models that were produced from ASTER optical satellite stereo imagery, and provides coverage for 2000–2016 at a 30 m resolution. We used this ice-surface-elevation dataset rather than the more recent compilation that was published in [22], because the former aligns more closely with the temporal coverage of the ice-velocity dataset. As a consequence, the SMB dataset that we produced in this study is representative of the mean SMB for the period 2000–2015, which is covered by both the ice-velocity and ice-surface-elevation-change datasets.

The modelled ice thicknesses used in this study are part of a global dataset, which was produced by [34] using an ensemble of models based on ice-thickness inversion from surface characteristics. The surface-elevation data used in this study are from SRTM 1 Arc-Second Global digital elevation data, which were collected in 2000 [35]. The debris-thickness dataset used in this study has a 30 m resolution and was modelled by [36] from thermal infrared Landsat 8 satellite imagery (2013–present). This dataset was selected for use as it is the only regional dataset providing consistent coverage of debris thickness across all five study regions.

2.3. Computing Cross-Sectional Ice Fluxes

Cross-sectional ice fluxes were computed from ice velocities [33] and ice thicknesses [34]. Cross-sectional transects between each glacier section were demarcated with two points at the lateral edges of the glacier, with transects being distributed at intervals of approximately 2 km along the length of each glacier. A spacing of approximately 2 km was chosen as a compromise between providing a sufficient number of data points to establish trends, and averaging over a sufficiently long along-flow distance to prevent large correlations and potentially strong correlation of velocity errors. Each transect was divided into 20 segments of equal length. The normal velocity and ice thickness were interpolated to the midpoint of each segment and then multiplied to compute flux. The resulting values were summed to compute the total ice flux perpendicular to each transect. These calculations were carried out twice for every transect, using median velocities for two periods (1999–2003 and 2013–2015), and the results averaged. These periods align with the temporal coverage of Landsat 7 (before the Scan Line Corrector failure) and Landsat 8 [33]. The formula for ice flux Q_t, where t is 1999–2003 or 2013–2015, is thus

$$Q_t = \sum_{i=1}^{n=20} u_i h_i l_i \quad (1)$$

where i is the index of the segment, u_i is the normal velocity interpolated to segment i, h_i is the thickness interpolated to the segment, and l_i is the length of the segment. The calculated mean values of Q_t for each transect were used to quantify the ingoing and outgoing ice fluxes (Q_{in} and Q_{out}) for each section between every adjacent pair of transects (or group of 3+ transects, where tributaries are present). The depth-averaged velocity depends on the fraction of basal sliding, which is unknown. Since the surface velocities are high for the observed glaciers, we assume that internal deformation makes a negligible contribution and, hence, that ice-surface velocity approximates to depth-averaged velocity. In order to test the impact of this assumption, we produced an additional set of surface-mass-balance estimates for the Gechongkang Glacier, based on a depth-averaged velocity equal to 90% of the surface velocity.

2.4. Producing Sectional Surface-Mass-Balance Estimates

The ice-surface area between each pair of transects was digitised and quantified using glacier outlines from the Randolph Glacier Inventory v6.0 [1]. The mean annual ice-surface-elevation change was calculated for each glacier section using glacier-wide elevation-change maps that were derived from digital elevation-model differencing [21]. The mean annual SMB between each pair/group of transects was computed using the mass-continuity method, as used by previous studies [25,28,29,31,32]:

$$b_j = \left(\frac{dh_j}{dt} - \frac{Q_{in\,j} - Q_{out\,j}}{A_j} \right) \times \frac{\rho_{ice}}{\rho_{water}} \quad (2)$$

where b is the mean SMB in glacier section j, $\frac{dh}{dt}$ is the mean ice-surface-elevation change, A is the surface area of the section, ρ_{ice} is the density of ice (920 kg m^{-3}), and ρ_{water} is the density of water (1000 kg m^{-3}).

2.5. Statistically Approximating Altitudinal Gradients

For each glacier, we used breakpoint analysis to detect the transition points between contrasting altitudinal SMB gradients and to determine the elevation at which the transition point occurs. We used regression models, weighted by SMB uncertainties (discussed in Section 2.7), to estimate the altitudinal SMB gradients below and above computed breakpoint elevations. These gradients were compared to previously modelled SMB gradients from a regionally calibrated global glacier model used to estimate global glacier runoff changes [39]. We computed mean regional breakpoint elevations as the arithmetic average of breakpoint elevations for each individual glacier within the region. Similarly, we computed the mean regional altitudinal gradients above and below the breakpoint elevation using the arithmetic averages of the gradients for each glacier within each region. Using our collective dataset of sectional SMB values for each region, we used arithmetic averages to approximate the mean regional SMB, which was partitioned by elevation bands. For each glacier section, mean surface elevation and mean debris thickness were computed from digital elevation models [35] and a modelled debris-thickness dataset [36], respectively.

2.6. Estimating Equilibrium Line Altitudes

From our generated SMB results, we calculated the equilibrium line altitude (ELA) for each region, which describes the mean elevation at which accumulation and ablation are in balance [30]. Using our elevation-dependent SMB gradients, for each glacier we calculated the ELA value as the elevation at which SMB is equal to zero. We took the arithmetic average of the ELA values for all the glaciers analysed within each region to estimate the mean regional ELAs. We compared our regional ELA values to previous estimates [19,20,40].

2.7. Assessing Uncertainties

We assessed uncertainty in SMB through linear error propagation from errors in input data sets, as described by [41]. The error propagation involved an assessment of errors for all flux estimates via Equation (1). The uncertainties associated with the thickness and velocity components are 25% and 5–10 m a^{-1}, respectively. To estimate the error of flux, ε_{Q_t}, we assumed that both velocity and thickness uncertainty have multivariate Gaussian distributions, and that each have exponentially decaying autocorrelations with a length scale of L = 2 km. This was based on the autocorrelation of elevation differences from a previous geodetic study [20]; but overall, uncertainties were not found to depend strongly on L. Furthermore, thickness and velocity uncertainties were assumed to be independent. Thus, error in Q_t is given by

$$Q = \sum_{i=1}^{n} (u_i \Delta h_i) l_i + (h_i + \Delta h_i) \Delta u_i l_i \tag{3}$$

where Δh_i and Δu_i are error in the interpolated velocity and thickness at a given segment i in the calculation of Q_t. As this is a nonlinear expression of Δh_i and Δu_i, linear propagation cannot be applied. Therefore, we approximated this expression as

$$\varepsilon_{Q_t} = \sum_{i=1}^{n} (u_i \Delta h_i) l_i + (h_i + 3\sigma_{h_i}) \Delta u_i l_i \tag{4}$$

where σ_{h_i} is the standard deviation of the error. Although this replaces a random error (Δh_i) by a nonrandom term $\left(3\sigma_{h_i}\right)$, there is a 99.8% probability that the error term lies within the ±3σ interval [42].

Error was then propagated from the flux and elevation change estimates to SMB errors. The uncertainties in the computed breakpoint elevations were approximated as the standard errors that were computed from the weighted breakpoint analyses. The uncertainties in the computed altitudinal SMB gradients were approximated as the standard errors associated with the coefficients of the weighted regression models.

2.8. Validating Against Previous Findings

In order to validate our results, we firstly compared our computed SMB gradients directly to gradients previously calculated from in-situ measurements for the benchmark Chhota Shigri Glacier, in the Spiti Lahaul region. This glacier was selected for validation purposes due to data availability, meeting the minimum size requirements for inclusion in our analyses, and the existence of a record of altitudinally-varying ablation stake measurements covering a similar period to that of our study [10,43]. We are not aware of additional field-based altitudinal SMB gradients for any of the other glaciers included in our analyses and we were unable to compare directly to smaller glaciers for which previous gradients have been estimated from in-situ measurements since small glaciers provide an insufficient number of data points to compute reliable SMB gradients from our approach. Therefore, we made additional comparisons to previously computed gradients for glaciers within the vicinity of the glaciers in our analyses. These gradients were based on in-situ measurements at Abramov Glacier in the Pamir [44], as well as Pokalde Glacier [45,46] and Changri Nup Glacier [45] in the Everest region. For further validation, we compared our computed regional ELA values to previous values [19,20,40], which were estimated from different approaches, e.g., from snowline altitudes [20].

3. Results

3.1. Regional Surface-Mass-Balance Results

The mean regional SMB results, as partitioned by elevation band, indicate distinctly different elevation-dependent SMB patterns in West Nepal, in comparison to those that were observed in the other four regions (Figure 2). In West Nepal, the lowest mean SMB values (i.e., greatest average melt rates) occur at the lowest elevations (Figure 2d). In this region, the debris cover distribution is very low (Figure 1) and the mean modelled debris thickness is <3.5 cm in all elevation bands (Figure 2i).

In contrast, our results indicate that, in the Pamir, Karakoram, Spiti Lahaul, and Everest regions, the lowest mean SMB values do not occur at the lowest elevations. Instead, the lowest mean SMB values occur at mid-elevations (Figure 2). Within all four of these regions, there is a considerably higher debris-cover distribution when compared to West Nepal (see Figure 1). In addition, the mean debris thickness is the greatest in the lowest elevation band (modelled by [36] as > 30 cm) and decreases consistently with elevation.

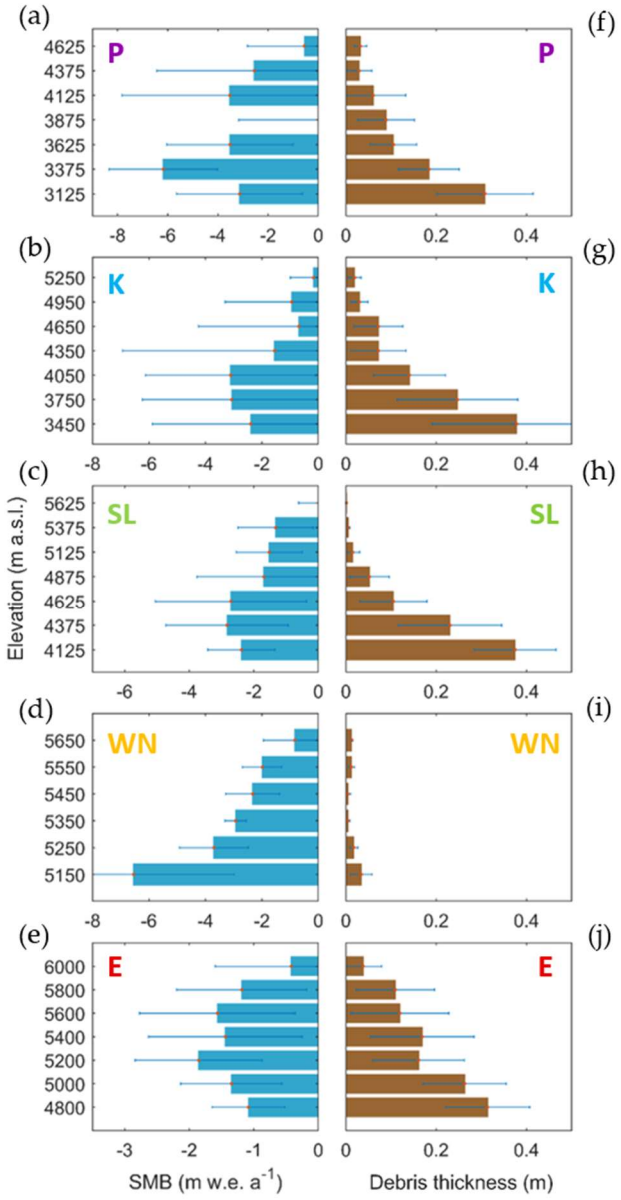

Figure 2. Regional elevation-dependent trends in surface mass balance (SMB) and debris thickness. (**a**–**e**) Regional mean surface mass balance, binned by elevation, for Pamir (P), Karakoram (K), Spiti Lahaul (SL), West Nepal (WN), and Everest (E). Horizontal bars represent standard error values. (**f**–**j**) Corresponding mean debris-thickness values [36].

3.2. Altitudinal Surface-Mass-Balance Gradients

We present the individual SMB estimates for every region in Figure A2. At a regional level, West Nepal shows a strong (R^2 = 0.65), linear altitudinal SMB gradient (Figure A2a). Meanwhile, in the Everest, Spiti Lahaul, Karakoram, and Pamir regions, no clear linear altitudinal gradients were detected at a regional scale (R^2 = 0.14 or less). However, breakpoint analysis of SMB gradients at a glacier-specific scale revealed that breakpoints in altitudinal SMB profiles commonly occur within the Everest, Spiti Lahaul, Karakoram, and Pamir regions (Table A1). Below the elevations where these breakpoints occur, reversed altitudinal SMB gradients (where SMB decreases with increasing elevation) were commonly found. More specifically, convex breakpoints in altitudinal SMB gradients were detected for 15 out of 18 of the analysed glaciers within these four regions. Of the 15 glaciers where breakpoints were detected, 13 show negative altitudinal SMB gradients below their breakpoint elevation. Conversely, in the West Nepal region, where debris cover is very minimal (Figure 1), breakpoints were not detected

for six of the seven analysed glaciers. Positive altitudinal gradients were found for all seven glaciers within this region (Table A1).

Figure 3 shows examples of the segmented altitudinal SMB gradients for the glaciers we analysed in the Everest region, with the corresponding debris-thickness values shown for each SMB data point. All five glaciers transition from negative altitudinal-SMB gradients of between −0.54 ± 0.19 and −0.06 ± 0.10 m w.e. a^{-1} $(100m)^{-1}$ at low elevations to positive altitudinal-SMB gradients of between 1.01 ± 0.39 and 1.56 ± 0.49 m w.e. a^{-1} $(100m)^{-1}$ at high elevations. The elevations at which convex breakpoints were detected range from 5180 ± 40 m a.s.l. (Ngozumpa Glacier) to 5920 ± 40 m a.s.l. (Gechongkang Glacier). The debris thickness decreases from low elevations to high elevations for every glacier within this region, as shown in Figure 3.

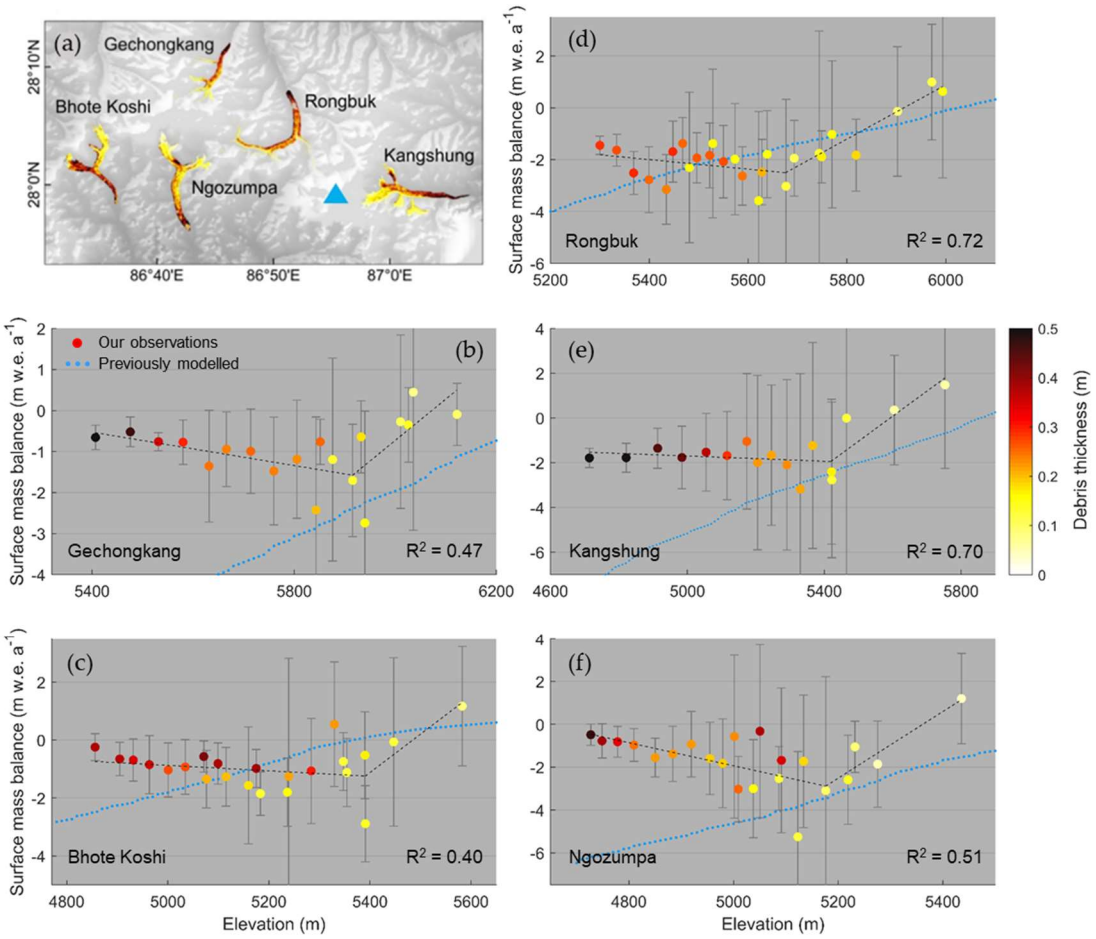

Figure 3. Elevation-dependent trends in SMB and debris thickness in the Everest region. Locations of the five largest glaciers surrounding Mount Everest (blue triangle). (**b**–**f**) Altitudinal surface-mass-balance trends for these glaciers. Vertical bars represent (1σ) uncertainties in the computed SMB values, estimated using a linear propagation of errors. Corresponding debris-thickness values [36] are represented on all panels with the colour scale on right. Dotted black lines represent our computed altitudinal SMB gradients, with corresponding R^2 values of the combined linear trends shown. The values of these gradients and their uncertainties are shown in Table A1. Blue dotted lines represent previously modelled SMB gradients from a regionally-calibrated global glacier model ignoring the effect of supraglacial debris [39].

Table 1 shows the mean regional breakpoint elevations and SMB gradients, which were computed from the glacier-specific results for each region. In the Pamir, Karakoram, Spiti Lahaul, and Everest regions, we found regional mean SMB gradients of between −1.87 ± 2.57 and −0.17 ± 0.30 m w.e. a^{-1} $(100m)^{-1}$ below breakpoint elevations, with a transition to mean gradients of between 0.94 ± 0.40

and 1.21 ± 0.41 m w.e. a^{-1} $(100m)^{-1}$ above breakpoint elevations (Table 1). The results show that the regional breakpoint elevation varies considerably between regions. The lowest mean regional breakpoint elevation of 3680 ± 280 m a.s.l. is found in the Pamir, while the highest breakpoint elevation of 5520 ± 50 m a.s.l. is found in the Everest region.

Table 1. Regional mean altitudinal SMB gradients and breakpoint elevations.

Region	Mean Breakpoint Elevation (m)	Mean Elevation-Dependent SMB Gradient (m w.e. a^{-1} $(100m)^{-1}$)		
		Below Breakpoint Elevation	Above Breakpoint Elevation	R^2 Value
Pamir	3680 ± 280	−1.87 ± 2.57	1.01 ± 0.88	0.47
Karakoram	3860 ± 220	−1.04 ± 2.08	1.05 ± 0.59	0.22
Spiti Lahaul	4890 ± 100	−0.17 ± 0.30	0.94 ± 0.40	0.63
West Nepal	Not found	1.18 ± 0.40		0.74
Everest	5520 ± 50	−0.21 ± 0.18	1.21 ± 0.41	0.56

For the Pamir, Karakoram, Spiti Lahaul, and Everest regions, where breakpoints were detected for the majority of glaciers (Table A1), we display the mean altitudinal SMB gradients below and above the breakpoint elevation. These gradients represent the arithemetic average of glacier-specific gradients computed from breakpoint analyses (Table A1) within each region, and exclude glaciers where breakpoints were not detected. We also report the mean of the R^2 values, arising from the breakpoint analyses, from the same glaciers. For West Nepal, where breakpoints were not detected for the majority of glaciers, we report the mean altitudinal gradient (and its associated R^2 value), computed from the glacier-specific gradients, excluding the single glacier for which a breakpoint was detected. Error values reported are the mean standard error values associated with the gradients computed from linear regression (for West Nepal) and breakpoint analyses (for all other regions).

Our results also indicate considerable intra-regional variability in both the breakpoint elevation and the magnitude of the reversed gradients within each of the Everest, Spiti Lahaul, Karakoram, and Pamir regions, with the latter ranging over as much as two orders of magnitude (Table A1). This variability precludes any clear region-wide elevation-SMB relationships in these regions (as opposed to in West Nepal, Figure A2). However, there is more conformity in above-breakpoint mass-balance gradients (Table A1).

3.3. Equilibrium Line Altitudes

From our altitudinal SMB gradients, we estimate regional ELA values of between 4490 ± 140 m (Pamir) and 5700 ± 60 m (West Nepal), as shown in Figure 4. Our ELA values generally increase from the northwest to the southeast of the mountain belt. The exception to this trend is that we observe a slightly higher ELA in West Nepal than in Everest to its southeast. Figure 4 shows a comparison of our ELA values against previous estimates [19,20,40]. The uncertainty ranges of all of our estimated ELA values fall within the error bounds of the ELA values previous estimated from snow line altitudes [20] (Table A2).

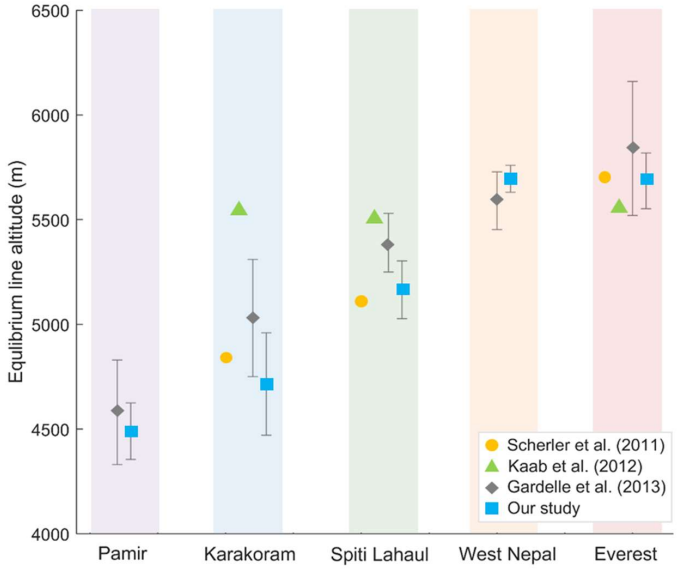

Figure 4. Regional equilibrium line altitudes in Pamir-Karakoram-Himalaya. Coloured symbols show regional mean equilibrium line altitudes (ELAs) calculated by previous studies [19,20,40] and our study. Coloured shaded areas enclose the ELA values for each of the five study regions, from northwest (left) to southeast (right).

4. Discussion

4.1. Influence of Supraglacial Debris Cover

The reversed altitudinal SMB gradients observed at low elevations in the Pamir, Karakoram, Spiti Lahaul, and Everest regions (Table 1; Figure 3) are likely to be attributable to the effects of supraglacial debris cover. Numerous previous studies have shown that supraglacial debris cover significantly influences glacier melt rates, as discussed in Section 1: a thin layer of debris enhances melt rates while a thicker layer of debris (exceeding a critical thickness of ~ 3–8 cm) reduces melt rates (e.g., [6–9]). Near the snouts of the glaciers in our analyses, where debris cover is thickest, the ice surface is likely to be insulated the most. As a result, the ablation rate is reduced and the SMB is raised (Figure 3). As elevation increases up-glacier from the snout, debris thickness decreases, therefore reducing the insulation effect. As a result, melt rates are enhanced up-glacier from the terminus, therefore contributing towards the reversed SMB gradients observed (Figure 3), which have also been reproduced in models (e.g., [47]). Furthermore, as the debris thins to below the critical thickness, the albedo effect is likely to dominate, therefore further enhancing melt rates and contributing towards the lowest mean SMB values being observed at mid-elevations (Figure 2).

The strong region-wide linear correlation between elevation and SMB for the relatively debris-free glaciers in West Nepal (Table 1; Figure A2) suggests that, where debris cover is largely absent, SMB is dominated by altitudinal climatic gradients. This pattern is also observed on other debris-free glaciers in the Himalayas (e.g., [43,45,46]). As a result, the lowest mean SMB values (i.e., greatest melt rates) occur at the lowest elevations in this region (Figure 2). The absence of negative altitudinal-SMB gradients in West Nepal also provides further evidence that the negative gradients observed in the Pamir, Karakoram, Spiti Lahaul, and Everest regions could be attributed to supraglacial debris cover.

The intra-regional variations in breakpoint elevations and altitudinal gradients observed within the Pamir, Karakoram, Spiti Lahaul, and Everest regions (Figure 3; Table A1) seem to preclude any clear region-wide relationships between elevation and SMB (Figure A2), despite strong correlation at the scale of individual glaciers. This variation could potentially arise from variations in supraglacial debris coverage. Differences in debris-thickness distribution, as well as local debris properties, such as lithology, grain size, and moisture content, may contribute towards the contrasting breakpoint

elevations and magnitudes of reversed altitudinal SMB gradients that were observed within these regions (e.g., [15–17]. Supraglacial ice cliffs and ponds can also influence the SMB of debris-covered glaciers by creating localised areas of enhanced melting [24–27]. Therefore, it is possible that these features could also partially explain the heterogeneity that was observed between debris-covered glaciers. Further detailed investigations of relationships between debris characteristics and altitudinal SMB gradients are required to gain a better understanding of these variations in reversed gradients.

4.2. Contribution of Glacier Dynamics

Our results enabled us to separate the relative contributions of SMB and ice dynamics towards ice-surface thinning. There is a considerable difference between our SMB estimates (black dotted line, Figure 5) and the previously observed ice-surface-elevation change (white dotted line). This difference represents the ice emergence velocity that was calculated from the mass convergence/divergence. At low elevations, where we observe a low ablation rate, the emergence velocity is also low (Figure 5), as also indicated by previous studies (e.g., [25,27,48,49]). This can be explained by the low slope and velocity gradient that are characteristic of the stagnant tongues of debris-covered glaciers. Further up-glacier near the breakpoint elevation, where melt rates are high, the emergence velocity is also high (see Figure 5). This is a consequence of the mass convergence at the transition between the stagnant tongue and the steeper debris-free part of the glacier. The reversed SMB gradient in the lower part of the glacier likely helps to maintain this mass convergence, by causing an inflexion of the glacier surface at its middle elevation. Consequently, the surface-elevation change, which is the sum of these two opposite processes of melt and emergence, shows a smooth trend along the length of the glacier, as observed by geodetic studies. Our results demonstrate the importance of ice dynamics in explaining the apparent contradiction between the reversed altitudinal SMB gradients expected on debris-covered ice and the relatively stable or positive altitudinal ice-surface-elevation-change gradients that were observed by geodetic studies.

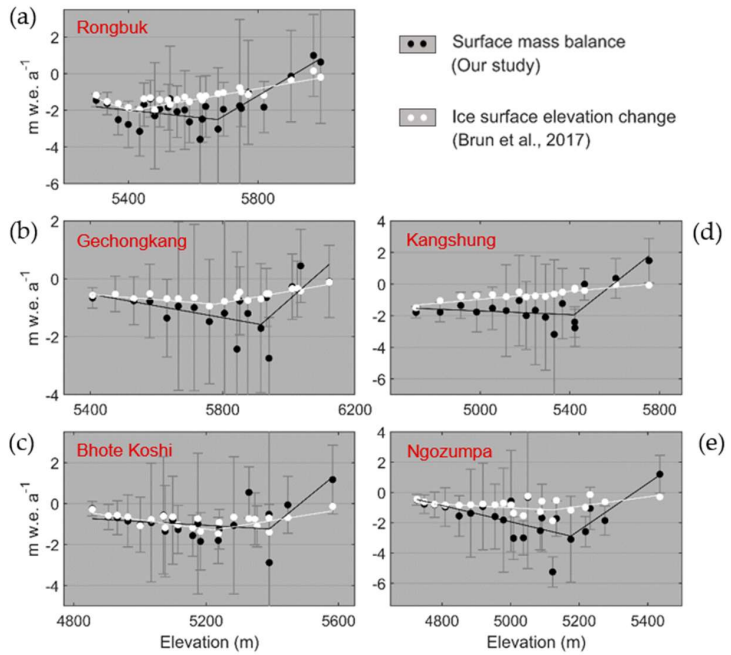

Figure 5. Comparison of surface mass balance and ice-surface-elevation change. (**a**–**e**) show the contrasting altitudinal patterns of SMB (black) and ice-surface-elevation change (white) for the five largest glaciers surrounding Mount Everest. Each point represents the mean SMB / ice-surface-elevation change value computed for each ~2 km sub-section of each glacier. Vertical bars represent (1σ) uncertainties in the computed SMB values, estimated using a linear propagation of errors.

4.3. Role of Glacier Surging

Referring to a recent inventory of surging glaciers [50], all of the glaciers that we have analysed in the Pamir and Karakoram are surge-type glaciers or have been exhibiting large velocity change during the study period. Surging behaviour can result in temporal variability in ice thickness and velocity (e.g., [51,52]); therefore, it is likely that this behaviour might be complicating the SMB trends and contributing towards the generally weaker R^2 values in the Pamir and Karakoram. An implicit assumption of our study is that the ice fluxes are in balance with the SMB gradient, but this is not the case for surging glaciers. Further investigation is required in the future in order to isolate signals of glacier surging, allowing for us to gain more accurate representations of altitudinal SMB gradients in regions where surge-type behaviour is occurring.

4.4. Validation of SMB Gradients With Previous In-Situ Measurements

For the benchmark Chhota Shigri Glacier in Spiti Lahaul, we computed an above-breakpoint altitudinal SMB gradient within 7–12% of the gradients previously measured in the field on the debris-free portion of this glacier (see Table 2). For Kangshung and Ngozumpa Glaciers in the Everest region, we computed above-breakpoint altitudinal gradients with differences of between 3% and 26% as compared to previously derived gradients for clean ice on West Changri Nup and Pokalde Glaciers, which are both located in between Kangshung and Ngozumpa Glaciers. For Fortambek Glacier in the Pamir, we computed an above-breakpoint gradient that was 27% lower than the field-based gradient for Abramov Glacier, located approximately 70 km northwest of Fortambek Glacier. The ELA values estimated from our SMB gradients are comparable to those calculated by previous studies [19,20,40], and follow a similar northwest-southeast increasing trend, as shown in Figure 4.

Table 2. Comparison of altitudinal SMB gradients with previous field-based findings.

	Measurement Period	Elevation Range (m)	Altitudinal Surface-Mass-Balance Gradient (m w.e. a^{-1} $(100m)^{-1}$)		
			Spiti Lahaul	Everest	Pamir
Our study	2000–2015	4570–5180	0.74 ± 0.14 (CS)	-	-
		5420–5750		1.12 ± 0.24 (K)	-
		5180–5230	-	1.56 ± 0.49 (N)	-
		3400–4020	-	-	0.74 ± 0.90 (F)
Azam et al. (2016) [43]	2002–2014	4400–5200	0.66 ± 0.09 (CS)	-	-
Wagnon et al. (2007) [10]	2002–2006	4400–4900	0.69 (CS)	-	-
Sherpa et al. (2017) [45]	2010–2015	5330–5690	-	1.47 (WCN)	-
	2009–2015	5430–5690		1.37 (P)	
Wagnon et al. (2013) [46]	2009–2012	5500–5600	-	1.51 (P)	-
Barandun et al. (2015) [44]	2011–2015	3720–4400	-	-	1.02 ± 0.05 (A)

The altitudinal SMB gradients computed above the breakpoint elevation for selected glaciers within the Spiti Lahaul, Everest and Pamir regions are shown. Gradients previously estimated by field-based studies [10,43–46] for debris-free ice in the ablation area are also shown for glaciers within these regions. The measurement periods and elevation ranges associated with each gradient are indicated. The initials provided after each SMB gradient represent Chhota Shigri (CS), Kangshung (K), Ngozumpa (N), West Changri Nup (WCN), Pokalde (P), Fortambek (F), and Abramov (A). WCN is located ~10 km east of N and ~15 km west of K. P is located ~15 km southeast of N and ~15 km southwest of K. A is located ~70 km northwest of F.

4.5. Limitations and Future Directions

While the ensemble approach used by [34] to model ice thickness minimises errors in the input ice-thickness dataset, there are still considerable uncertainties that are associated with ice thickness inversion [34]. These uncertainties are likely to have an impact on the accuracy of our results and we have accounted for these errors where possible. However, the improvement of ice thickness estimations in the future will increase the potential of this approach to produce better-resolved estimates of distributed SMB.

Our approach is also partly limited by the inability to sample SMB in high-altitude accumulation areas, due to larger uncertainties in ice velocities that are associated with feature-tracking in snow-covered areas [33]. Additionally, it is difficult to resolve accurately the SMB gradients of small glaciers < ~10 km in length, due to poorer signal-noise relationships and a lack of sufficient data points to accurately predict SMB gradients. The coverage of high-altitude areas and smaller glaciers can be improved in the future with the improvement of optical-satellite-imagery resolution [53] and the enhancement of feature-tracking algorithms.

There are also some uncertainties that are associated with the depth-dependence of ice velocities used to compute SMB, which can vary in space over a single glacier. Testing our depth-averaged velocity assumption for Gechongkang Glacier indicated that changing the depth-averaged velocity from 100% to 90% of the surface velocity resulted in an average change of 0.05 m w.e. a^{-1} in our absolute SMB values (equivalent to an average change of 5%). While the effects of this assumption are relatively small, the associated uncertainties can be reduced in the future with better knowledge of spatially-distributed depth-dependences of mountain glacier velocities.

We recognise that there are some significant uncertainties that are associated with the debris-thickness model used in this study, associated with the coarse resolution of thermal infrared satellite imagery, as well as high temporal and spatial variabilities in surface temperatures and vertical debris-temperature profiles [32,54]. A further limitation is that since we compute the mean debris thickness for each glacier section, we do not account for small-scale variations in debris thickness, which have been demonstrated to often be highly heterogeneous (e.g., [55]). These local-scale variations lead to the formation of supraglacial features, which result in significant variations in melt rates over small spatial scales [25,26]. As previously discussed, it is likely that these localised melt variations may be contributing towards the heterogeneity in our SMB gradients. It is also possible that the debris-cover distribution and thickness may have evolved over the course of our study period [49,56]. However, significant changes generally occur over multi-decadal timescales [49] and, therefore, we consider it to be unlikely that the position of the transition zone between thin debris (below the critical thickness) and thicker debris significantly shifted during our study period.

A significant challenge that is associated with our approach is the highly branching nature of the glaciers that we analysed. Due to the presence of many glacier tributaries, only a semi-automated approach was possible, involving manual matching of ingoing/outgoing ice fluxes with corresponding glacier tributary sections. The development of a fully-automated approach, for example using flow lines to assign fluxes to corresponding tributary sections, would allow for a greater spatial coverage of distributed SMB and an expansion of our approach to further regions across High Mountain Asia.

Due to the uncertainties associated with the datasets produced in this study, we advocate that further field-based data acquisition is critical in order to validate remote-sensing-based observations thoroughly, and to facilitate accurate upscaling of SMB estimates over wider spatial scales.

5. Conclusions

In this paper, we have presented an approach for producing spatially distributed estimates of glacial surface mass balance from remote-sensing observations, based on the principle of mass continuity. We applied our approach to the largest glaciers within five key regions of the Pamir-Karakoram-Himalaya. Each glacier was divided into sections of approximately 2 km in length and we computed the ingoing and outgoing ice fluxes for each of these sections using satellite-derived ice velocities and modelled ice thicknesses.. Using geodetic measurements, we calculated mean sectional ice-surface-elevation changes and subsequently isolated the contribution of surface mass balance towards the ice thinning rates using mass continuity. Using breakpoint analyses and regression models, we produced estimates of altitudinal surface-mass-balance gradients and equilibrium line altitudes for each of the five study regions. Our results show reversed altitudinal surface-mass-balance gradients in the lower-elevation portions of debris-covered glaciers, with a transition to positive surface-mass-balance gradients at higher elevations. In contrast, our results show continuously

positive altitudinal surface-mass-balance gradients on debris-free glaciers. This demonstrates that there are important differences in altitudinal ablation trends between debris-covered and debris-free glaciers, which were not previously visible from geodetic mass balance datasets. These differences in surface mass balance are likely offset by differences in ice dynamics, leading to similar thinning rates for debris-covered and clean-ice glaciers being observed by remote sensing. Our results show a regional equilibrium-line-altitude spatial gradient, with the values increasing from the northwest to the southeast. In future, with the generalisation and refinement of ice-velocity measurements and glacier thickness datasets, our operational approach can be developed and applied to glacierised mountain regions worldwide, providing the opportunity to uncover regional-scale surface-mass-balance patterns in areas where scale and location create challenges in field-based data acquisition.

Supplementary Materials: Supplementary materials are available online at http://www.mdpi.com/2072-4292/12/10/1563/s1.

Author Contributions: R.R.B., A.D., N.G. and D.N.G. designed the study. R.R.B. performed the processing, analyses and interpretation, with inputs from A.D., N.G., D.N.G., R.G.B. and M.H. The paper was written by R.R.B., with inputs from all co-authors. All authors have read and agreed to the published version of the manuscript.

Funding: This research funded by the U.K. Natural Environment Research Council, under a studentship hosted by the Edinburgh U.K. Natural Environment Research Council E^3 Doctoral Training Partnership (NE/L002558/1).

Acknowledgments: We thank Fanny Brun for her insights on debris-covered-glacier processes. We thank Philip Kraaijenbrink, Dirk Scherler, Daniel Farinotti, Fanny Brun and Heidi Sevestre for sharing their datasets. We thank the editor and three anonymous reviewers for their detailed comments that helped to improve this manuscript.

Conflicts of Interest: The authors declare no conflict of interest.

Data availability: The data produced in this study are available in the Supplementary Materials.

Appendix A

Table A1. Glacier-specific altitudinal SMB gradients and breakpoint elevations for all glaciers analysed.

Glacier	RGI 6.0 ID	Area (km^2)	Elevation Range (m)	Breakpoint Elevation (m)	Elevation-Dependent SMB Gradient (m w.e. a^{-1} (100m)$^{-1}$)		
					Below Breakpoint Elevation	Above Breakpoint Elevation	R^2 Value
Pamir							
Fortambek	13.19750	40.2	2930–6283	3400 ± 210	−2.04 ± 2.28	0.74 ± 0.90	0.27
Grumm-Grzhimaylo	13.13574	152.1	3615–6814	4020 ± 400	−1.77 ± 4.85	1.17 ± 1.12	0.24
Fedchenko	13.54431	663.7	2908–7392	3620 ± 240	−1.80 ± 0.58	1.13 ± 0.61	0.90
Garmo	13.19758	129.4	2976–6712	Not found	0.32 ± 0.13		0.34
Karakoram							
Hispar	14.04477	495.6	3110–7794	4230 ± 120	−0.62 ± 0.34	1.34 ± 0.72	0.23
Biafo	14.00005	559.8	3045–7148	3560 ± 310	−1.65 ± 4.00	1.50 ± 0.91	0.29
Baltoro	14.06794	809.1	3385–8569	3790 ± 230	−0.84 ± 1.89	0.30 ± 0.14	0.15
Siachen	14.07524	1078.0	3596–7579	Not found	−0.48 ± 0.06		0.75
Spiti Lahaul							
Samudra Tapu	14.15613	80.0	4237–6098	4750 ± 220	0.27 ± 0.48	0.97 ± 0.32	0.48
Bara Shigri	14.15447	112.4	3931–6309	5460 ± 90	0.02 ± 0.03	1.26 ± 0.75	0.58
Tichu Glacier	14.16068	24.8	4154–5875	4770 ± 50	−0.02 ± 0.08	0.78 ± 0.37	0.49
Sara Umga	14.16065	33.2	3835–5994	Not found	0.31 ± 0.10		0.39
Chhota Shigri	14.15990	16.8	4280–5764	4570 ± 50	−0.93 ± 0.59	0.74 ± 0.14	0.96
West Nepal							
CN5O257E0002	15.11019	20.8	5032–6333	Not found	0.59 ± 0.17		0.75
CN5O257D0011	15.11003	28.6	5185–6635	Not found	1.41 ± 0.53		0.59
CN5O257D0018	15.10994	29.9	5107–6501	Not found	2.36 ± 0.86		0.78
CN5O257D0003	13.26906	6.5	5355–6466	Not found	0.71 ± 0.25		0.74
CN5O257D0006	15.11011	7.2	5285–6399	Not found	0.47 ± 0.17		0.80
CN5O257D0001	13.26909	3.6	5387–6222	Not found	1.54 ± 0.45		0.75
CN5O257D0005	13.26904	7.2	5308–6252	5590 ± 20	0.03 ± 0.41	4.73 ± 1.02	0.98

Table A1. *Cont.*

Glacier	RGI 6.0 ID	Area (km^2)	Elevation Range (m)	Breakpoint Elevation (m)	Elevation-Dependent SMB Gradient (m w.e. a^{-1} $(100m)^{-1}$)		
					Below Breakpoint Elevation	Above Breakpoint Elevation	R^2 Value
Everest							
Rongbuk	15.09991	73.2	5155–7947	5680 ± 40	−0.18 ± 0.13	1.05 ± 0.20	0.72
Ngozumpa	15.03473	61.1	4702–8181	5180 ± 40	−0.54 ± 0.19	1.56 ± 0.49	0.51
Kangshung	15.09803	64.4	4587–8799	5420 ± 50	−0.06 ± 0.10	1.12 ± 0.24	0.70
Bhote Koshi	15.03422	27.2	4787–6550	5390 ± 70	−0.09 ± 0.09	1.33 ± 0.71	0.40
Gechongkang	15.09921	47.1	5328–7927	5920 ± 40	−0.20 ± 0.39	1.01 ± 0.39	0.47

Table A2. Regional ELA estimates.

	ELA Estimates (m)			
	Our Study	**Gardelle et al. (2013)**	**Kääb et al. (2012)**	**Scherler et al. (2011)**
Pamir	4490 ± 140	4580 ± 250	-	-
Karakoram	4720 ± 240	5030 ± 280	5540	4845
Spiti Lahaul	5170 ± 140	5390 ± 140	5500	5103
West Nepal	5700 ± 60	5590 ± 138	-	-
Everest	5690 ± 130	5840 ± 320	5550	5700

Estimated ELAs (and standard errors) computed in this study are shown for each of the five study regions. Other previous estimates for these regions [19,20,40] are also shown.

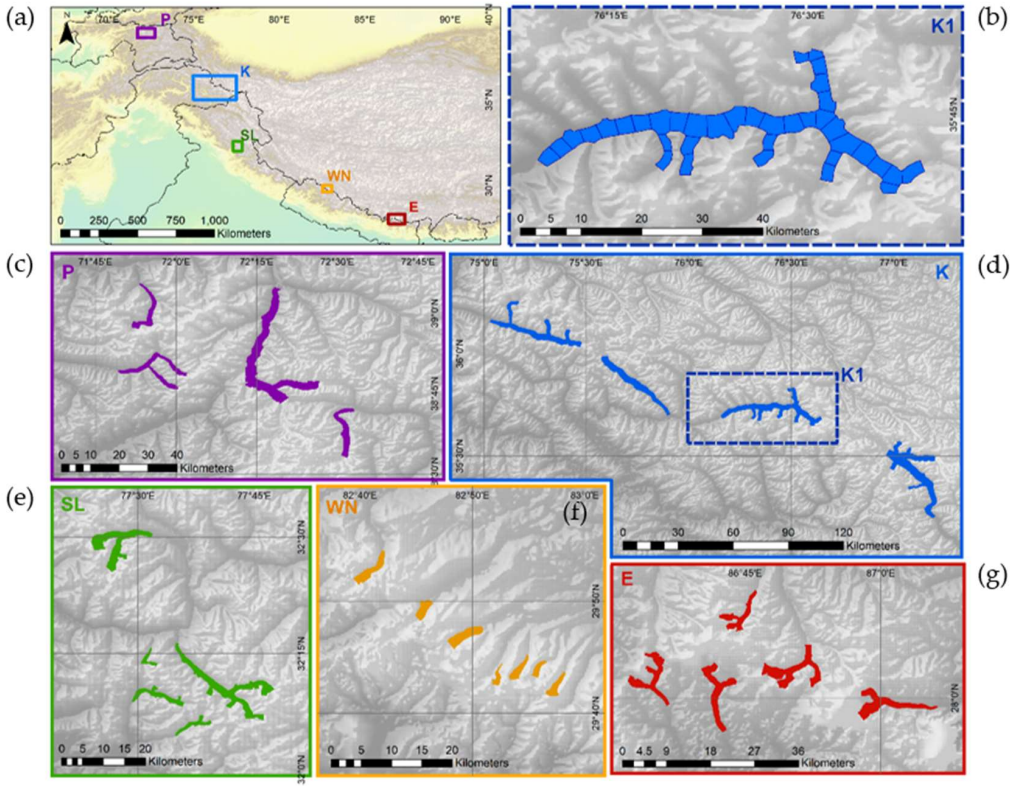

Figure A1. Detailed breakdown of study sites and glacier sampling method. The coloured areas in (**c**–**g**) show the glacier areas which were monitored in each of the five study regions shown in (**a**). Labels P, K, SL, WN and E denote Pamir, Karakoram, Spiti Lahaul, West Nepal and Everest. (**b**) shows an example of the flux gates (black cross-sectional lines) used for Baltoro Glacier, shown in subset K1 in d. For the area between each set of two or more flux gates (depending on the presence of tributaries), SMB is computed using the mass continuity method. Background DEMs are from Shuttle Radar Topography Mission [35].

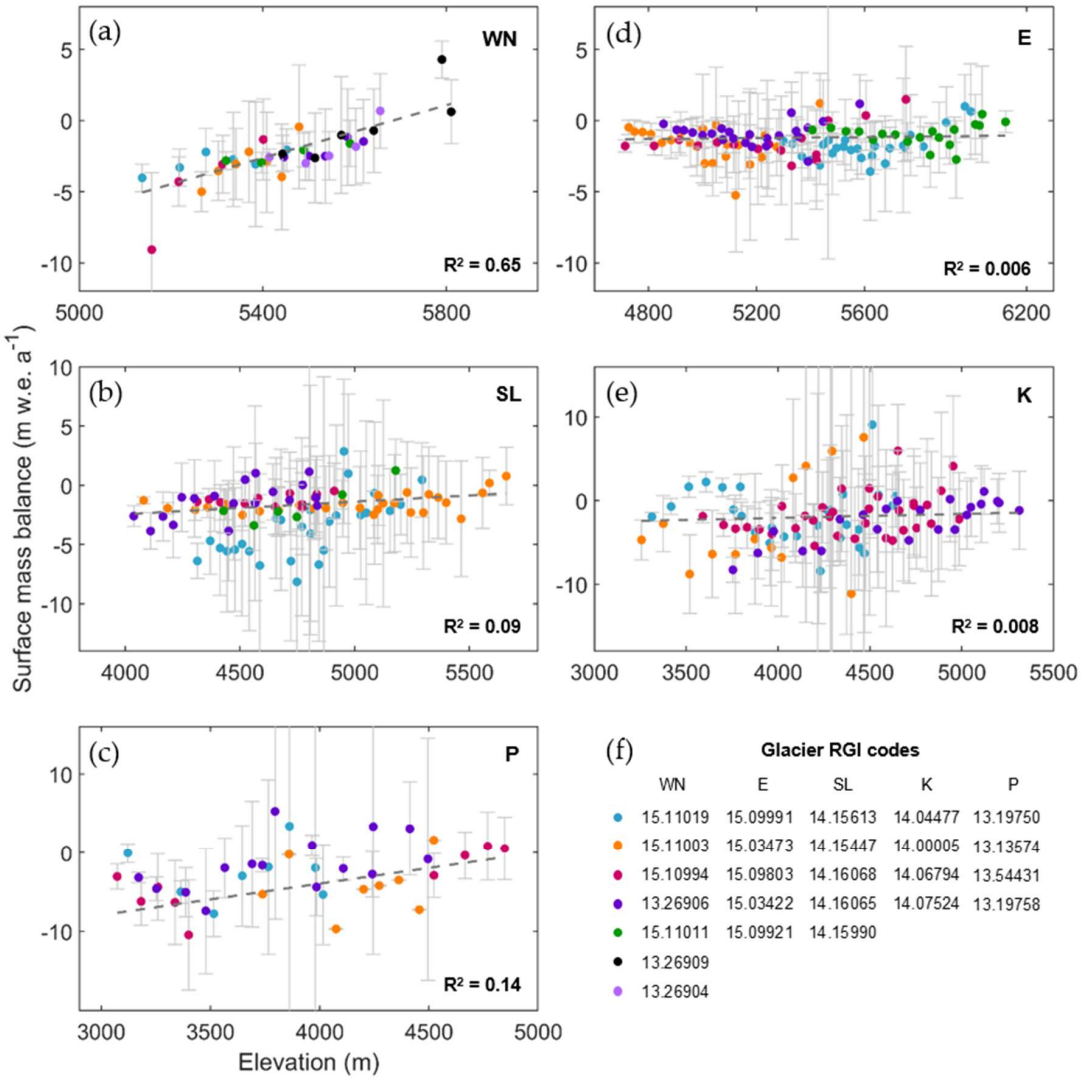

Figure A2. Detailed breakdown of glacier-specific SMB observations within each region. Elevation-dependent SMB observations for every glacier analysed within West Nepal (WN), Everest (E), Spiti Lahaul (SL), Karakoram (K) and Pamir (P) are shown in (**a**–**e**). Each glacier within each region is shown in a different colour. RGI codes for each glacier and its corresponding colour are shown within the legend in (**f**). Error bars show uncertainties associated with SMB estimates. Dashed grey lines show regional simple linear regression trends, which were calculated from all points combined within each region and weighted by SMB uncertainties. The R^2 values associated with each linear regression trend are also shown.

References

1. RGI Consortium. Randolph Glacier Inventory—A Dataset of Global Glacier Outlines: Version 6.0. Available online: https://doi.org/10.7265/N5-RGI-60 (accessed on 3 March 2020).
2. Pritchard, H.D.; Arthern, R.J.; Vaughan, D.G.; Edwards, L.A. Extensive dynamic thinning on the margins of the Greenland and Antarctic ice sheets. *Nature* **2009**, *461*, 971–975. [CrossRef]
3. Richardson, S.D.; Reynolds, J.M. An overview of glacial hazards in the Himalayas. *Quat. Int.* **2000**, *65–66*, 31–47. [CrossRef]
4. Veh, G.; Korup, O.; von Specht, S.; Roessner, S.; Walz, A. Unchanged frequency of moraine-dammed glacial lake outburst floods in the Himalaya. *Nat. Clim. Change* **2019**, *9*, 379–383. [CrossRef]
5. Veh, G.; Korup, O.; Walz, A. Hazard from Himalayan glacier lake outburst floods. *Proc. Natl. Acad. Sci. USA* **2020**, *117*, 907–912. [CrossRef] [PubMed]

6. Kayastha, R.B.; Takeuchi, Y.; Nakawo, M.; Ageta, Y. Practical prediction of ice melting beneath various thickness of debris cover on Khumbu Glacier, Nepal, using a positive degree-day factor. *IAHS Publ.* **2000**, *264*, 71–81.
7. Östrem, G. Ice melting under a thin layer of moraine, and the existence of ice cores in moraine ridges. *Geogr. Ann.* **1959**, *41*, 228–230. [CrossRef]
8. Lejeune, Y.; Bertrand, J.-M.; Wagnon, P.; Morin, S. A physically based model of the year-round surface energy and mass balance of debris-covered glaciers. *J. Glaciol.* **2013**, *59*, 327–344. [CrossRef]
9. Rounce, D.R.; Quincey, D.J.; McKinney, D.C. Debris-covered glacier energy balance model for Imja–Lhotse Shar Glacier in the Everest region of Nepal. *Cryosphere* **2015**, *9*, 2295–2310. [CrossRef]
10. Wagnon, P.; Linda, A.; Arnaud, Y.; Kumar, R.; Sharma, P.; Vincent, C.; Pottakkal, J.G.; Berthier, E.; Ramanathan, A.; Hasnain, S.I.; et al. Four years of mass balance on Chhota Shigri Glacier, Himachal Pradesh, India, a new benchmark glacier in the Western Himalaya. *J. Glaciol.* **2007**, *53*, 603–611. [CrossRef]
11. Pratap, B.; Dobhal, D.P.; Mehta, M.; Bhambri, R. Influence of debris cover and altitude on glacier surface melting: A case study on Dokriani Glacier, Central Himalaya, India. *Ann. Glaciol.* **2015**, *56*, 9–16. [CrossRef]
12. Nicholson, L.; Benn, D.I. Calculating ice melt beneath a debris layer using meteorological data. *J. Glaciol.* **2006**, *52*, 463–470. [CrossRef]
13. Vincent, C.; Wagnon, P.; Shea, J.M.; Immerzeel, W.W.; Kraaijenbrink, P.; Shrestha, D.; Soruco, A.; Arnaud, Y.; Brun, F.; Berthier, E.; et al. Reduced melt on debris-covered glaciers: Investigations from Changri Nup Glacier, Nepal. *Cryosphere* **2016**, *10*, 1845–1858. [CrossRef]
14. Azam, M.F.; Wagnon, P.; Patrick, C.; Ramanathan, A.; Linda, A.; Singh, V.B. Reconstruction of the annual mass balance of Chhota Shigri Glacier, Western Himalaya, India, since 1969. *Ann. Glaciol.* **2014**, *55*, 69–80. [CrossRef]
15. Nakawo, M.; Young, G. Field experiments to determine the effect of a debris layer on ablation of glacier ice. *Ann. Glaciol.* **1981**, *2*, 85–91. [CrossRef]
16. Lambrecht, A.; Mayer, C.; Hagg, W.; Popovnin, V.; Rezepkin, A.; Lomidze, N.; Svanadze, D. A comparison of glacier melt on debris-covered glaciers in the northern and southern Caucasus. *Cryosphere* **2011**, *5*, 525–538. [CrossRef]
17. Nicholson, L.I.; Benn, D.I. Properties of natural supraglacial debris in relation to modelling sub-debris ice ablation. *Earth Surf. Processes Landforms* **2012**, *38*, 409–501. [CrossRef]
18. Mihalcea, C.; Mayer, C.; Diolaiuti, G.; Lambrecht, A.; Smiraglia, C.; Tartari, G. Ice ablation and meteorological conditions on the debris-covered area of Baltoro Glacier, Karakoram, Pakistan. *Ann. Glaciol.* **2006**, *43*, 292–300. [CrossRef]
19. Kääb, A.; Berthier, E.; Nuth, C.; Gardelle, J.; Arnaud, Y. Contrasting patterns of early twenty-first-century glacier mass change in the Himalayas. *Nature* **2012**, *488*, 495–498. [CrossRef]
20. Gardelle, J.; Berthier, E.; Arnaud, Y. Region-wide glacier mass balances over the Pamir-Karakoram-Himalaya during 1999–2011. *Cryosphere* **2013**, *7*, 1263. [CrossRef]
21. Brun, F.; Berthier, E.; Wagnon, P.; Kääb, A.; Treichler, D. A Spatially resolved estimate of high mountain asia glacier mass balances from 2000 to 2016. *Nat. Geosci.* **2017**, *10*, 668–673. [CrossRef]
22. Shean, D.E.; Bhushan, S.; Montesano, P.; Rounce, D.R.; Arendt, A.; Osmanoglu, B. A systematic, regional assessment of High Mountain Asia Glacier mass balance. *Front. Earth Sci.* **2020**, *7*, 363. [CrossRef]
23. Brun, F.; Wagnon, P.; Berthier, E.; Jomelli, V.; Maharjan, S.B.; Shrestha, F.; Kraaijenbrink, P.D.A. Heterogeneous influence of glacier morphology on the mass balance variability in High Mountain Asia. *J. Geophys. Res. Earth Surf.* **2019**, *124*, 1331–1345. [CrossRef]
24. Sakai, A.; Nakawo, M.; Fujita, K. Melt rate of ice cliffs on the Lirung Glacier, Nepal Himalayas, 1996. *Bull. Glaciol. Res.* **1998**, *16*, 57–66.
25. Brun, F.; Wagnon, P.; Berthier, E.; Shea, J.M.; Immerzeel, W.W.; Kraaijenbrink, P.D.A.; Vincent, C.; Reverchon, C.; Shrestha, D.; Arnaud, Y. Ice cliff contribution to the tongue-wide ablation of Changri Nup Glacier, Nepal, Central Himalaya. *Cryosphere* **2018**, *12*, 3439–3457. [CrossRef]
26. Miles, E.S.; Watson, C.S.; Brun, F.; Berthier, E.; Esteves, M.; Quincey, D.J.; Miles, K.E.; Hubbard, B.; Wagnon, P. Glacial and geomorphic effects of a supraglacial lake drainage and outburst event, Everest Region, Nepal Himalaya. *Cryosphere* **2018**, *12*, 3891–3905. [CrossRef]
27. Banerjee, A. Brief communication: Thinning of debris-covered and debris-free glaciers in a warming climate. *Cryosphere* **2017**, *11*, 133–138. [CrossRef]

28. Nuimura, T.; Fujita, K.; Fukui, K.; Asahi, K.; Aryal, R.; Ageta, Y. Temporal changes in elevation of the debris-covered ablation area of Khumbu Glacier in the Nepal Himalaya since 1978. *Arct. Antarct. Alp. Res.* **2011**, *43*, 246–255. [CrossRef]
29. Nuimura, T.; Fujita, K.; Sakai, A. Downwasting of the debris-covered area of Lirung Glacier in Langtang Valley, Nepal Himalaya, from 1974 to 2010. *Quat. Int.* **2017**, *455*, 93–101. [CrossRef]
30. Cuffey, K.M.; Paterson, W.S.B. *The Physics of Glaciers*, 4th ed.; Academic Press: Amsterdam, The Netherlands, 2010.
31. Berthier, E.; Vincent, C. Relative contribution of surface mass balance and ice flux changes to the accelerated thinning of the Mer de Glace (Alps) over 1979–2008. *J. Glaciol.* **2012**, *58*, 1979–2008. [CrossRef]
32. Rounce, D.R.; King, O.; McCarthy, M.; Shean, D.E.; Salerno, F. Quantifying debris thickness of debris-covered glaciers in the Everest Region of Nepal through inversion of a subdebris melt model. *J. Geophys. Res. Earth Surf.* **2018**, *123*, 1094–1115. [CrossRef]
33. Dehecq, A.; Gourmelen, N.; Trouve, E. Deriving large-scale glacier velocities from a complete satellite archive: Application to the Pamir–Karakoram–Himalaya. *Remote Sens. Environ.* **2015**, *162*, 55–66. [CrossRef]
34. Farinotti, D.; Huss, M.; Fürst, J.J.; Landmann, J.; Machguth, H.; Maussion, F.; Pandit, A. A consensus estimate for the ice thickness distribution of all glaciers on earth. *Nat. Geosci.* **2019**, *12*, 168–173. [CrossRef]
35. Farr, T.G.; Rosen, P.A.; Caro, E.; Crippen, R.; Duren, R.; Hensley, S.; Kobrick, M.; Paller, M.; Rodriguez, E.; Roth, L.; et al. The shuttle radar topography mission. *Rev. Geophys.* **2007**, *45*, RG2004. [CrossRef]
36. Kraaijenbrink, P.D.A.; Bierkens, M.F.P.; Lutz, A.F.; Immerzeel, W.W. Impact of a global temperature rise of 1.5 degrees celsius on Asia's glaciers. *Nature* **2017**, *549*, 257–260. [CrossRef]
37. Scherler, D.; Wulf, H.; Gorelick, N. Global assessment of supraglacial debris-cover extents. *Geophys. Res. Lett.* **2018**, *45*, 11798–11805. [CrossRef]
38. The Global Runoff Data Centre. Major River Basins of the World. Available online: https://www.bafg.de/GRDC/EN/02_srvcs/22_gslrs/221_MRB/riverbasins_node.html (accessed on 9 March 2020).
39. Huss, M.; Hock, R. Global-scale hydrological response to future glacier mass loss. *Nat. Clim. Change* **2018**, *8*, 135–140. [CrossRef]
40. Scherler, D.; Bookhagen, B.; Strecker, M.R. Spatially variable response of Himalayan glaciers to climate change affected by debris cover. *Nat. Geosci.* **2011**, *4*, 156–159. [CrossRef]
41. Foresta, L.; Gourmelen, N.; Pálsson, F.; Nienow, P.; Björnsson, H.; Shepherd, A. Surface elevation change and mass balance of icelandic ice caps derived from swath mode CryoSat-2 altimetry. *Geophys. Res. Lett.* **2016**, *43*, 12138–12145. [CrossRef]
42. Abramowitz, M.; Stegun, I.A. *Handbook of Mathematical Functions*; Dover: New York, NY, USA, 1965.
43. Azam, M.F.; Ramanathan, A.L.; Wagnon, P.; Vincent, C.; Linda, A.; Berthier, E.; Sharma, P.; Mandal, A.; Angchuk, T.; Singh, V.B.; et al. Meteorological conditions, seasonal and annual mass balances of Chhota Shigri Glacier, Western Himalaya, India. *Ann. Glaciol.* **2016**, *57*, 328–338. [CrossRef]
44. Barandun, M.; Huss, M.; Sold, L.; Farinotti, D.; Azisov, E.; Salzmann, N.; Usubaliev, R.; Merkushkin, A.; Hoelzle, M. Re-analysis of seasonal mass balance at Abramov Glacier 1968–2014. *J. Glaciol.* **2015**, *61*, 1103–1117. [CrossRef]
45. Sherpa, S.F.; Wagnon, P.; Brun, F.; Berthier, E.; Vincent, C.; Lejeune, Y.; Arnaud, Y.; Kayastha, R.B.; Sinisalo, A. Contrasted surface mass balances of debris-free glaciers observed between the southern and the inner parts of the Everest Region (2007–2015). *J. Glaciol.* **2017**, *63*, 637–651. [CrossRef]
46. Wagnon, P.; Vincent, C.; Arnaud, Y.; Berthier, E.; Vuillermoz, E.; Gruber, S.; Ménégoz, M.; Gilbert, A.; Dumont, M.; Shea, J.M.; et al. The cryosphere seasonal and annual mass balances of Mera and Pokalde Glaciers (Nepal Himalaya) since 2007. *Cryosphere* **2013**, *7*, 1769–1786. [CrossRef]
47. Shea, J.M.; Immerzeel, W.W.; Wagnon, P.; Vincent, C.; Bajracharya, S. Modelling glacier change in the Everest Region, Nepal Himalaya. *Cryosphere* **2015**, *9*, 1105–1128. [CrossRef]
48. Anderson, L.S.; Anderson, R.S. Modeling debris-covered glaciers: Response to steady debris deposition. *Cryosphere* **2016**, *10*, 1105–1124. [CrossRef]
49. Rowan, A.V.; Egholm, D.L.; Quincey, D.J.; Glasser, N.F. Modelling the feedbacks between mass balance, ice flow and debris transport to predict the response to climate change of debris-covered glaciers in the Himalaya. *Earth Planet. Sci. Lett.* **2015**, *430*, 427–438. [CrossRef]
50. Sevestre, H.; Benn, D.I. Climatic and geometric controls on the global distribution of surge-type glaciers: Implications for a unifying model of surging. *J. Glaciol.* **2015**, *61*, 646–662. [CrossRef]

51. Meier, M.F.; Post, A. What are glacier surges? *Can. J. Earth Sci.* **1969**, *6*, 807–817. [CrossRef]
52. Paul, F. A 60-year chronology of glacier surges in the Central Karakoram from the analysis of satellite image time-series. *Geomorphology* **2020**, *352*, 106993. [CrossRef]
53. Millan, R.; Mouginot, J.; Rabatel, A.; Jeong, S.; Cusicanqui, D.; Derkacheva, A.; Chekki, M. Mapping surface flow velocity of glaciers at regional scale using a multiple sensors approach. *Remote Sens.* **2019**, *11*, 2498. [CrossRef]
54. Foster, L.A.; Brock, B.W.; Cutler, M.E.J.; Diotri, F. A physically based method for estimating supraglacial debris thickness from thermal band remote-sensing data. *J. Glaciol.* **2012**, *58*, 677–691. [CrossRef]
55. Nicholson, L.I.; McCarthy, M.; Pritchard, H.D.; Willis, I. Supraglacial debris thickness variability: Impact on ablation and relation to terrain properties. *Cryosphere* **2018**, *12*, 3719–3734. [CrossRef]
56. Kirkbride, M.P.; Deline, P. The formation of supraglacial debris covers by primary dispersal from transverse englacial debris bands. *Earth Surf. Process. Landf.* **2013**, *38*, 1779–1792. [CrossRef]

© 2020 by the authors. Licensee MDPI, Basel, Switzerland. This article is an open access article distributed under the terms and conditions of the Creative Commons Attribution (CC BY) license (http://creativecommons.org/licenses/by/4.0/).

Appendix B

Submitted *Journal of Glaciology* article (in review)

JOURNAL OF GLACIOLOGY

CAMBRIDGE UNIVERSITY PRESS

THIS MANUSCRIPT HAS BEEN SUBMITTED TO THE JOURNAL OF GLACIOLOGY AND HAS NOT BEEN PEER-REVIEWED.

Using thermal UAV imagery to model distributed debris thicknesses and sub-debris melt rates on debris-covered glaciers

Journal:	*Journal of Glaciology*
Manuscript ID	Draft
Manuscript Type:	Article
Date Submitted by the Author:	n/a
Complete List of Authors:	Bisset, Rosie; The University of Edinburgh, School of GeoSciences Nienow, Peter; University of Edinburgh, Scotland, GeoSciences Goldberg, Daniel; The University of Edinburgh Wigmore, Oliver; Victoria University of Wellington, Antarctic Research Centre Loayza-Muro, Raúl; Universidad Peruana Cayetano Heredia Wadham, Jemma; University of Bristol, School of Geographical Sciences; UiT The Arctic University of Norway Macdonald, Moya; University of Bristol Bingham, Robert; University of Edinburgh, School of GeoSciences
Keywords:	Debris-covered glaciers, Remote sensing, Melt - surface
Abstract:	Supraglacial debris cover regulates the melt rates of many glaciers in mountainous regions around the world, thereby modifying the availability and quality of downstream water resources. However, the influence of supraglacial debris is often poorly parameterised within glaciological

	models, due to the absence of a technique to provide high-precision, spatially-continuous measurements of debris thickness. Here, we use high-resolution UAV-derived thermal imagery, in conjunction with local meteorological data, visible UAV imagery and vertically-profiled debris temperature time-series, to model the spatially-distributed debris thickness across a portion of Llaca Glacier in the Cordillera Blanca of Peru. Based on our results, we model daily sub-debris melt rates over a 3-month period during 2019. We demonstrate that, by effectively calibrating the radiometric thermal imagery and accounting for temporal and spatial variations in meteorological parameters during UAV surveys, thermal UAV data can be used to better represent the highly heterogeneous patterns of debris thickness and sub-debris melt on debris-covered glaciers. Additionally, our results indicate a mean sub-debris melt rate 71 % higher than the mean melt rate modelled from satellite-derived debris thicknesses, emphasising the importance of acquiring further high-precision debris thickness data for the purposes of investigating glacier-scale melt processes and calibrating regional melt models.

SCHOLARONE™
Manuscripts

Using thermal UAV imagery to model distributed debris thicknesses and sub-debris melt rates on debris-covered glaciers

Rosie R. Bisset[1], Peter W. Nienow[1], Daniel N. Goldberg[1], Oliver Wigmore[2], Raúl A. Loayza-Muro[3], Jemma L. Wadham[4,5], Moya L. Macdonald[5], Robert G. Bingham[1]

[1]*School of GeoSciences, University of Edinburgh, Edinburgh, UK*
[2]*Antarctic Research Centre, Victoria University of Wellington, Wellington, New Zealand*
[3]*Laboratory of Ecotoxicology, Faculty of Sciences and Philosophy, Universidad Peruana Cayetano Heredia, Lima, Peru*
[4]*UiT The Arctic University of Norway and The Norwegian Polar Institute, Norway*
[5]*School of Geographical Sciences, University of Bristol, Bristol, UK*

Abstract

Supraglacial debris cover regulates the melt rates of many glaciers in mountainous regions around the world, thereby modifying the availability and quality of downstream water resources. However, the influence of supraglacial debris is often poorly parameterised within glaciological models, due to the absence of a technique to provide high-precision, spatially-continuous measurements of debris thickness. Here, we use high-resolution UAV-derived thermal imagery, in conjunction with local meteorological data, visible UAV imagery and vertically-profiled debris temperature time-series, to model the spatially-distributed debris thickness across a portion of Llaca Glacier in the Cordillera Blanca of Peru. Based on our results, we model daily sub-debris melt rates over a 3-month period during 2019. We demonstrate that, by effectively calibrating the radiometric thermal imagery and accounting for temporal and spatial variations in meteorological parameters during UAV surveys, thermal UAV data can be used to better represent the highly heterogeneous patterns of debris thickness and sub-debris melt on debris-covered glaciers. Additionally, our results indicate a mean sub-debris melt rate 71 % higher than the mean melt rate modelled from satellite-derived debris thicknesses, emphasising the importance of acquiring further high-precision debris thickness data for the purposes of investigating glacier-scale melt processes and calibrating regional melt models.

1. Introduction

More than a quarter of the Earth's tropical glaciers are located in the Cordillera Blanca mountain range of Peru (RGI 6.0, 2017; Figure 1). The meltwater from these Peruvian glaciers feeds into the Rio Santa river basin, providing water resources to ~250,000 people living in the Ancash region of Peru (Mark et al., 2010). The glaciers of the Cordillera Blanca have shown consistently negative mass balances and significant reductions in spatial coverage over the past decades. For example, Silverio and Jaquet (2017) reported that the total area covered by these glaciers shrunk by 46% between 1930 and 2017, while Veettil (2018) indicated an area loss of 33.5% between 1975 and 2016. Rabatel et al. (2012) found an average mass balance of -0.76 m w.e. a^{-1} between 1976 and 2010, while Seehaus et al. (2019) reported a mass balance of -0.236 ± 0.042 m w.e. a^{-1} between 2000 and 2016. Glacial retreat in the Cordillera Blanca is impacting agriculture and drinking water supplies in the region not only by modifying the quantity of water available, but also negatively impacting the water quality via acid rock drainage due to enhanced weathering of metal- and sulphide-rich bedrock (Fortner et al., 2011; Guittard et al., 2017; Mark et al., 2017). Many of the glaciers within this region are mantled with a layer of supraglacial debris (Seehaus et al., 2019), which is likely to be impacting both the retreat rate and the melt rate of these glaciers, thereby influencing downstream water toxification and long-term water resource depletion.

A key factor controlling the melt rate of debris-mantled glaciers is the supraglacial debris thickness. Previous studies have shown that if the debris layer is thinner than a critical thickness, sub-debris melt rates are enhanced while, if the debris layer is thicker than the critical thickness, sub-debris melt rates

For Peer Review

are reduced through ice-surface insulation (e.g. Östrem, 1959; Nicholson and Benn, 2006; Vincent et al., 2016; Anderson et al., 2021). Furthermore, supraglacial ice cliffs and meltwater ponds, which are often abundant on debris-covered glaciers, create localised areas of enhanced ablation, further complicating the melt patterns on debris-covered glaciers (e.g. Sakai et al., 2000; Buri et al., 2016; Steiner at al., 2018). As the thickness of the debris layer and the presence of supraglacial features can change significantly over small spatial scales (e.g. Zhang et al., 2016; McCarthy et al., 2017; Nicholson et al., 2018), precisely mapping the debris thickness distribution is critical for effectively modelling their melt rates and meltwater contribution. Other debris characteristics, including moisture content, grain size and lithology can affect the relationship between debris thickness and sub-debris melt rate, by altering the thermal conductivity of the supraglacial debris (e.g. Nakawo and Young, 1981; Nicholson and Benn, 2012). Therefore, it is also important to quantify the thermal conductivity of the debris layer in order to effectively model sub-debris glacial melt rates with a high degree of accuracy.

Debris thickness can been measured *in situ* by manual excavation through the debris layer to the debris-ice interface (e.g. Reid et al., 2012). However, such measurements are limited in scale, due to the challenges associated with accessing and navigating the surface of debris-covered glaciers. More recently, structure-from-motion via terrestrial photogrammetry has been used to quantify the debris thickness exposed above ice cliffs (Nicholson and Mertes, 2017), while ground-penetrating radar (GPR) has been used to quantify debris thicknesses over glacier surface transects (McCarthy et al., 2017). While these techniques have yielded greater spatial coverage compared to manual excavations, neither provide spatially-complete, three-dimensional debris thickness observations. Additionally, since cliff-top debris thicknesses can differ considerably from surrounding debris thicknesses, the accuracy of debris thicknesses interpolated between observation sites is sometimes poor (McCarthy et al., 2017).

In order to provide spatially-distributed estimates of debris thickness, several previous studies have used surface energy balance modelling, combined with thermal satellite data, to derive the thermal resistance of the debris (e.g. Nakawo and Rana, 1999; Zhang et al., 2011). Since the thermal resistance is equal to the thermal conductivity divided by the debris thickness, in-situ measurements of debris thermal conductivity can then been used, in conjunction with meteorological data, to model the thickness of the debris layer (e.g. Foster et al., 2012; Rounce and McKinney, 2014). Mihalcea et al. (2008a) used a different approach to model debris thickness from thermal satellite imagery, which involved finding the correlation between field-derived debris thickness and satellite-derived surface temperature and subsequently using this relationship to model glacier-wide debris thicknesses. While this method offers reduced model complexity, it does not account for spatial variations in meteorological conditions such as incoming shortwave radiation, which can significantly modify the relationship between surface temperature and debris thickness. Additionally, while the use of thermal satellite imagery enables debris thicknesses to be modelled across entire glaciers or regions, the resolution of satellite-derived thermal imagery is relatively coarse (> 60 m). As a result, sub-pixel variations in debris thickness cannot be detected, while the presence of supraglacial ice ponds and ice cliffs can lead to underestimation of debris thickness values (Rounce and McKinney, 2014).

Imagery collected by uncrewed aerial vehicles (UAVs) offers significantly greater spatial precision compared to satellite imagery. In recent years, a number of studies have used UAVs to collect high-resolution visible imagery of debris-covered glaciers in the Himalaya, in order to investigate their surface characteristics (e.g. Immerzeel et al., 2014; Kraaijenbrink et al., 2016). In the Cordillera Blanca, visible UAV surveys of Llaca Glacier were conducted in 2014 and 2015 (Wigmore and Mark, 2017). Comparison of the data collected from these surveys showed spatially-variable rates of ice loss, with the highest rates occurring where supraglacial ice cliffs and meltwater ponds were present (Wigmore and Mark, 2017). The use of UAVs to collect thermal imagery of a debris-covered glacier was demonstrated for the first time at Lirung Glacier in the Central Himalaya (Kraaijenbrink et al.,

For Peer Review

2018). The results showed high levels of spatial and temporal heterogeneity in the glacier's surface temperature, highlighting the potential drawbacks of using coarser-resolution thermal satellite data to model supraglacial debris thickness. The study also demonstrated that while UAVs facilitate the collection of high-resolution thermal imagery, it is important to account for factors such as surface emissivity variations and sensor bias to derive reliable absolute surface temperatures (Kraaijenbrink et al., 2018).

Here, we test the use of UAV-derived radiometrically-calibrated thermal imagery, combined with local meteorological data, visible UAV imagery and thermal measurements taken within the debris layer, to produce centimetre-scale maps of distributed debris thickness for a portion of Llaca Glacier tongue (Figure 1). Following calibration of the thermal imagery, we model the thermal conductivity of the debris layer using a time-series of debris temperature measurements collected at varying depths within the debris layer. Spatially-distributed debris thicknesses are estimated using a surface energy balance modelling approach which accounts for the changes in meteorological conditions over the duration of the thermal UAV surveys. Additionally, a simpler method for modelling debris thickness from UAV-derived surface temperatures, using a field-derived polynomial relation between debris thickness and surface temperature, is tested. Using the high-resolution debris thickness maps produced in this study, daily spatially-distributed melt rates are modelled over the duration of a 3-month period in 2019. The results are compared to melt rates modelled based on satellite-derived debris thicknesses in order to investigate the impact of debris thickness parameterisation accuracy on the modelled melt rates of debris-covered glaciers.

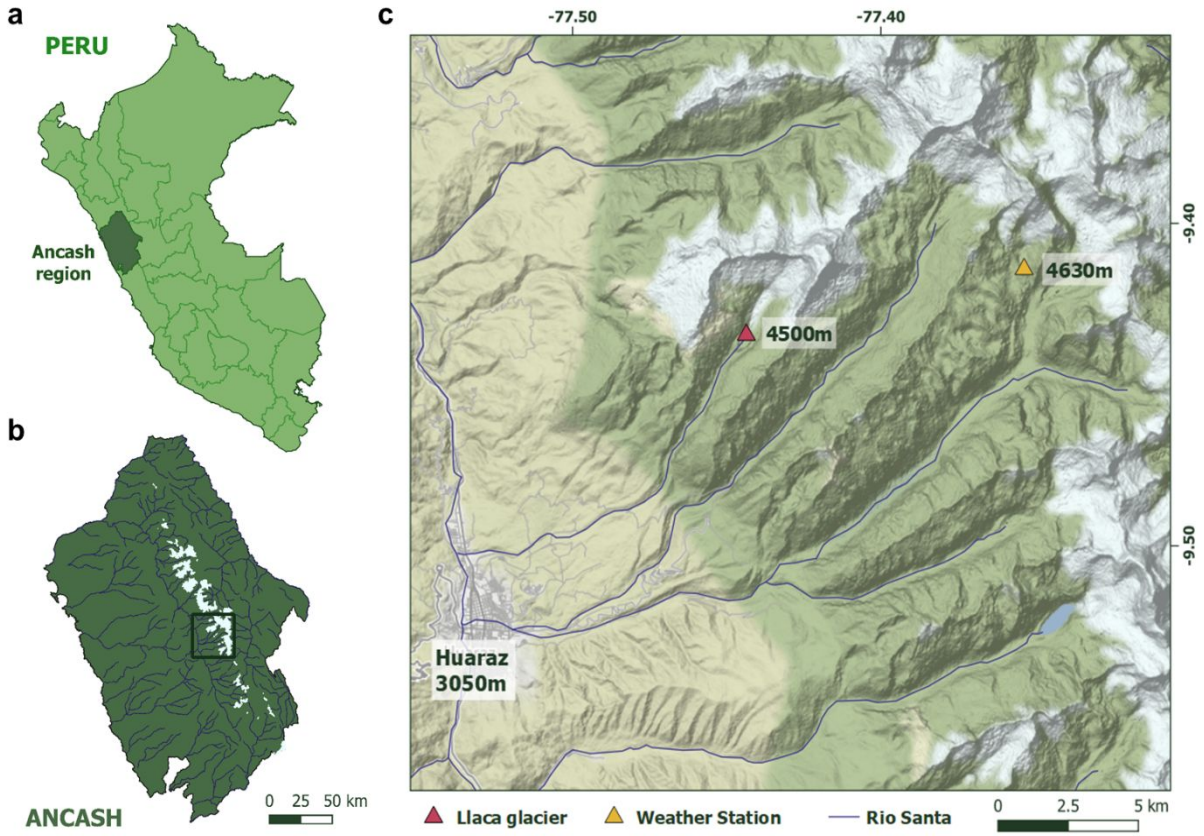

Figure 1. Map of the study site location. (a) Location of the Ancash region within Peru (dark green shading). (b) Location of panel (c) within Ancash. The ice-covered areas within the Ancash region are shown by the white shaded areas in (b) and (c), while the rivers are shown by the dark blue lines. The coloured triangles in (c) show the locations of Llaca Glacier (red) and the Cuchillacocha weather station (installed by Bridgewater State University) where the meteorological data used within this study were collected (yellow).

2. Methods

Figure 2 shows the workflow developed for this study, demonstrating schematically the links between the data acquisition, data processing and modelling steps of the methods, as described below.

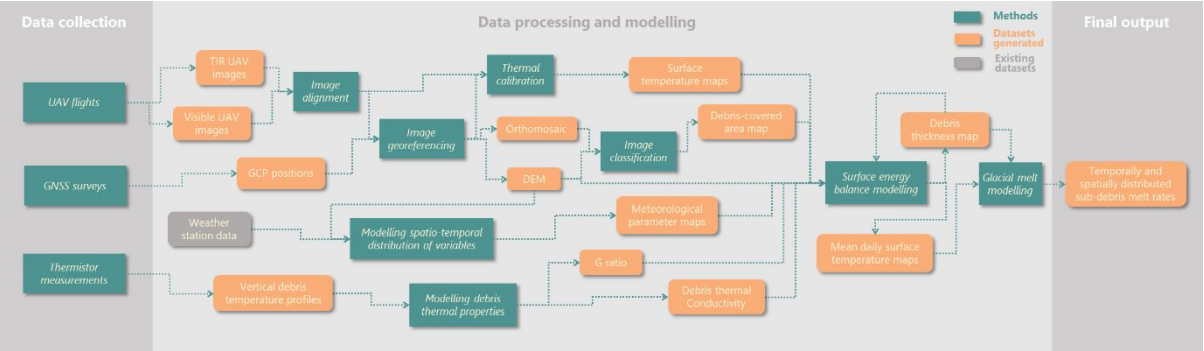

Figure 2. Workflow used in this study for modelling spatially-distributed, temporally-varying sub-debris melt rates.

2.1 Study site

Llaca Glacier is located in the central Cordillera Blanca, a 200-km-long mountain chain situated within the wider Peruvian Andes range (Figure 1). Covering an area of ~ 5.1 km^2, the glacier extends from ~ 4460 to ~ 6090 m a.s.l (RGI 6.0, 2017). The debris-covered tongue of the glacier has an area of ~ 0.22 km^2 and ranges in elevation from ~ 4460 m to ~ 4620 m a.s.l.. The meltwater from Llaca Glacier contributes to the supply of water for the Ancash region, which is inhabited by approximately 250,000 people. Llaca Glacier was selected as the site for this study due to its relative accessibility in comparison to other glaciers in the region and has previously been surveyed in 2014 and 2015 (Wigmore et al., 2017).

2.2 UAV-based data collection

2.2.1 Thermal imagery acquisition

A standard DJI Phantom 4 UAV was fitted with a custom-built thermal camera system, comprising a a FLIR Vue Pro R 640 (13 mm FOV) thermal camera and a U-BLOX GNSS GPS chip. This was used to collect ~15,000 radiometric thermal images across a total survey area of approximately 0.25 km^2 (Figure 3a). The Phantom 4 was chosen because, unlike most commercially-available drones, it is capable of flying at high altitudes of up to 6,000 m a.s.l. Standard Phantom 4 propellers were used. The Vue Pro R camera was selected due to its ability to collect radiometrically-calibrated thermal images at high thermal precision (30 mK / 0.03 °C). The built-in visible camera was removed from the Phantom 4 in order to reduce weight and allow greater flight times.

The UAV-based thermal imagery collection was conducted within two survey zones (Z_{T1} and Z_{T2}) with differing launch point altitudes (LP_1: 4537 m a.s.l. and LP_2: 4576 m a.s.l.)(Figure 3a), in order to ensure that the UAV maintained a safe altitude above the sloping glacier surface, since terrain correction was not used for the UAV flights. In total, four thermal UAV surveys (S_{T1} - S_{T4}) were conducted, each at different times of day on 18-19 August 2019 (Table 1). S_{T1}, S_{T2} and S_{T4} were launched LP_1 and conducted within the bounds of Z_{T1}, while S_{T3} was launched from LP_2 and conducted over the entire extent of Z_{T2}. S_{T1}, which covered an area of 94,000 m^2, was conducted between 16.25 and 17.20 on 18 August 2019. S_{T2} was conducted between 9.30 and 10.00 on 19 August and covered an area of 87,000 m^2. The largest of the four surveys, S_{T3}, was conducted between 10.55 and 12.50 on 19 August and covered an area of 137,000 m^2. The final survey, S_{T4}, was conducted between 14.25 and 15.45 on 19 August and covered an area of 72,000 m^2.

For Peer Review

The UAV was flown using an automated gridded flight plan, created using DroneDeploy flight planning software. As the option for terrain correction was not currently available with open-source flight planning software, the flight paths were along horizontal planes with a consistent altitude of 70 m relative to the launch point altitude. This flight altitude was chosen in order to provide a balance between obtaining high-resolution imagery (~ 5 cm) and providing coverage of a sufficiently large area (250,000 m^2 in total). The use of a consistent altitude relative to the launch altitude resulted in variations in the exact pixel spatial resolution and image overlap since the altitude above ground level (AGL) varied with surface topography. Since the surface elevation range of the complete survey area (~ 120 m) exceeded the average above-surface flight altitude (70 m), two separate launch points were used (Figure 3a).

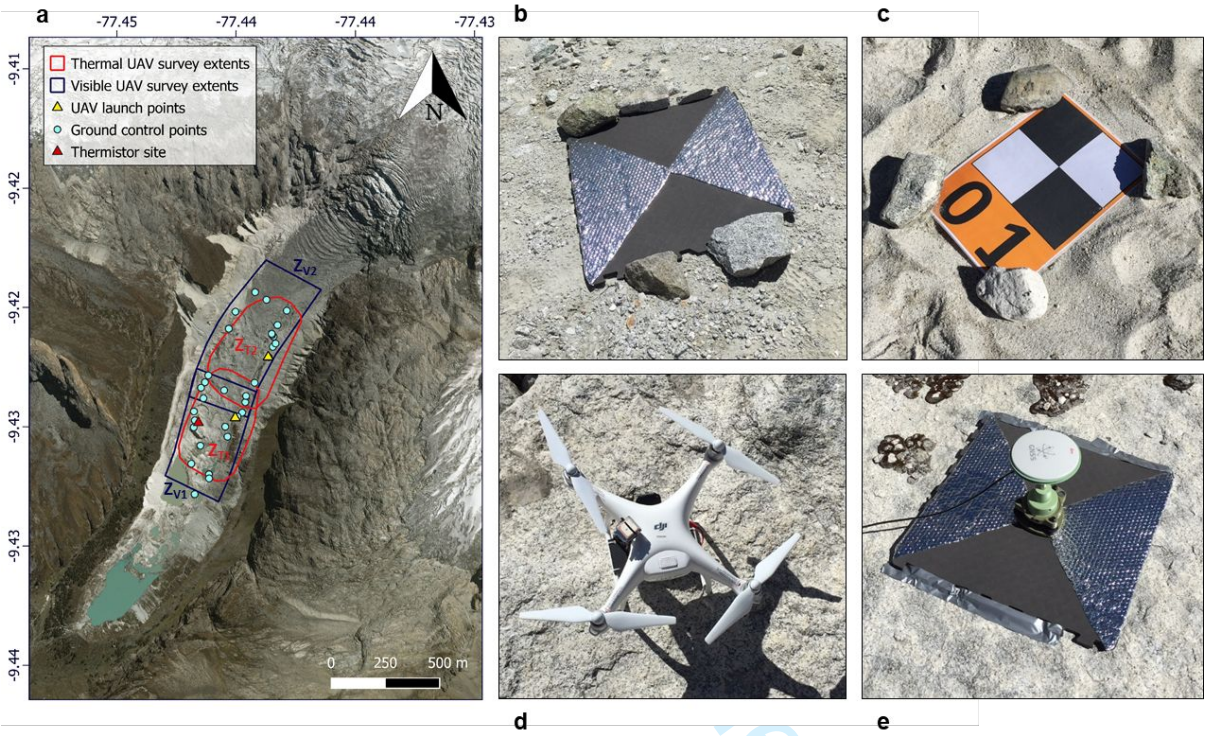

Figure 3. UAV survey setup at Llaca Glacier. (a) Extents of the thermal and visible UAV surveys, and locations of the two UAV launch points ground control points where GNSS data were collected and site where thermistors were installed within the debris layer. (b) and (c) Photographs of the materials used as ground control points for the thermal and visible UAV surveys respectively. (d) The custom-built UAV that was used to collect thermal imagery. (e) GNSS antenna setup for measuring the GPS position of each ground control point.

A flight speed of 7 m s^{-1} and an image capture interval of 1 second were used, in order to provide a forward image overlap of 90 %. The flight lines, which ran perpendicular to the glacier flow direction, were spaced 7 m apart in order to provide an 80 % lateral image overlap. During each of the four thermal surveys, the UAV was returned to its launch point multiple times to conduct battery changes. At an altitude close to sea level, the DJI Phantom 4 can fly for ~ 25 minutes between battery changes. However, due to the high altitude of Llaca Glacier (approximately 4500 m a.s.l.), the air is considerably thinner and a significantly greater amount of power is required to create lift. Consequently, the average flight time between battery changes was roughly halved to ~ 12 minutes.

Many UAV-mountable thermal cameras, including the Vue Pro R 640 used in this study, use uncooled microbolometers, which are sensitive to changes in the temperature of the sensor, body and lens. While radiometric cameras apply corrections to account for these effects, Kelly et al. (2019) highlight the need to allow time for the camera to stabilise after activation. For this reason, the camera was turned on ~20 minutes prior to the start of each survey, while a couple of extra flight lines were

added to the start of each survey to allow the camera to adjust to meteorological conditions experienced during flight.

For calibration purposes, images of 40 x 40 cm anodised aluminium calibration targets (Figure 3b) were collected with the Vue Pro R camera from an altitude of 10 m, at the beginning and end of every flight. Meanwhile, the temperatures of these panels were also recorded using an Apogee thermal infrared (TIR) radiometer for subsequent comparison against the UAV-acquired temperatures.

2.2.2 Visible imagery acquisition

Using a second DJI Phantom 4 UAV, with a built-in visible camera, 950 visible images of the glacier tongue were collected, covering a total survey area of ~325,000 m^2. Visible UAV data collection was also conducted using an automated gridded flight plan created using DroneDeploy flight planning software. An average flight altitude of 85 m was chosen, to allow the collection of high spatial resolution (2.5 cm) imagery, whilst providing coverage of a relatively large survey area. A flight speed of 5 ms^{-1} and an image capture interval of 1 second were used in order to provide 90% forward overlap between images, while flight lines were spaced 45 m apart to allow 80% lateral image overlap.

Table 1. UAV survey information.

Survey name	Survey date	Survey time	Survey area (m^2)	Survey zone	Launch point
S_{T1}	18 August 2019	16:25 - 17:20	94,000	Z_{T1}	LP1
S_{T2}	19 August 2019	09:30 - 10:00	87,000	Z_{T1}	LP1
S_{T3}	19 August 2019	10:55 - 12:50	137,000	Z_{T2}	LP2
S_{T4}	19 August 2019	14:25 - 15:45	72,000	Z_{T1}	LP1
S_{V1}	21 August 2019	09:20 - 10:10	150,000	Z_{V1}	LP1
S_{V2}	21 August 2019	10:50 - 12:20	211,000	Z_{V2}	LP2

Similar to the thermal UAV surveys, the UAV-based visible imagery collection was divided into two survey zones (Z_{V1} and Z_{V2}), with corresponding launch points LP_1 and LP_2 respectively (Figure 3a). In total, two visible UAV surveys (S_{V1} and S_{V2}) were conducted (one for each of the two visible survey zones). S_{V1} was conducted between 9.20 and 10.10 on 21 August 2019 and S_{V2} was conducted 10.50 and 12.20 on the same day (Table 1). Due to the slightly lighter weight of the visible camera, in comparison to the thermal camera, a slightly longer flight time of ~15 minutes could be achieved between battery changes. At the beginning of S_{V2}, there was a technical camera error, which resulted in the camera changing from a nadir 0° angle to an oblique 90° angle, resulting in a small data gap within the visible imagery.

2.3 Ground-based data collection

2.3.1 Ground control data acquisition for UAV surveys

In order to georeference the thermal and visible UAV imagery, two corresponding ground control surveys were conducted. The thermal ground control survey was carried out on 17 August 2019 (one day before the first thermal UAV survey) and the visible ground control survey was carried out on 20 August 2019 (one day before the visible UAV surveys). For each of the two ground control surveys, ground control point (GCP) targets were distributed across the UAV survey areas, with the greatest concentration of points around the perimeters of the UAV survey areas (Figure 3a). The GCP targets were fixed to flat surfaces using tape and rocks (Figure 3b-c).

For the thermal ground control survey, 20 ground control point (GCP) targets were assembled, each consisting of a 60 cm foam square with two triangles of insulated aluminium foil attached to the surface (Figure 3b). Foam and aluminium were chosen due to their contrasting emissivity values of ~0.6 and ~0.1 respectively, making their central point clearly distinguishable from the UAV-mounted thermal camera. For the visible ground control survey, 22 ground control point (GCP) targets, each consisting of a 30 cm x 30 cm checkboard square (Figure 3c), were set out across the glacier surface.

For each of the two ground control surveys, a Leica GNSS system was used to measure the GPS position of each GCP target with high (sub-cm) spatial accuracy. A fixed-location GNSS reference station was set up in a flat area ~20 m in front of the glacier terminus, in order to collect continuous GPS measurements over the complete ~8-hour duration of each ground control survey. Meanwhile, using a GNSS rover, the precise location of the centre of each GCP target was measured over a period of 5-10 minutes per target (Figure 3e).

2.3.2 Vertical debris temperature profile measurements

In order to measure vertical changes in debris temperature within the debris layer, a vertical profile of 5 thermistors, each connected to a DataHog2 data logger, was installed within the debris layer near the western margin of the glacier (Figure 3a). The thermistor probes were placed at depths of 5, 10, 20, 30 and 40 cm, with the 40 cm probe at the debris-ice interface. Once adjusted to local environmental conditions, the thermistors recorded temperatures at repeat intervals of 10 minutes between 17 August 2019 00:00 and 19 August 2019 16:00. These measurements were used to model the thermal properties of the debris layer for integration within the surface energy balance model (Figure 2).

2.3.3 In-situ surface temperature and debris thickness measurements

An Apogee TIR radiometer was used to collect a sequence of ground-based TIR measurements at 22 points across the glacier surface, with varying supraglacial debris thicknesses. At each measurement point, three emitted TIR measurements of the debris surface were taken. Subsequently, a pit was dug through the debris layer to the debris-ice interface and the depth of the debris layer was measured. These 22 measurements were taken in close succession over a total duration of 1 hour 40 minutes (13.25 – 15.05) on 21 August, in order to minimise biases associated with temporal changes in meteorological conditions.

In order to validate the debris thickness model, an additional set of debris thickness measurements were taken, in conjunction with high-precision GPS positions measured with the Leica GNSS System. Unfortunately, due to a technical glitch with the pre-programmed UAV flights, several of these measurements were just outside the bounds of the thermal UAV survey. As a result, only three of the coupled GPS-debris thickness measurements could be used for validation of the debris thickness model.

2.4 UAV data processing

2.4.1 Producing surface temperature maps, DEMs and orthomosaics

To produce maps of surface temperature, the radiometric TIR images were processed using Pix4Dmapper software, which was selected due to its compatibility with the radiometric jpeg files collected by the Vue Pro R camera. To produce DEMs and orthomosaics, the visible images were processed using Agisoft Metashape Software. This software contains proprietary implementations of common structure-from-motion (SfM) photogrammetric workflows, and includes feature recognition, image matching, bundle block adjustment, point cloud densification and ultimately the generation of high resolution digital surface models (DSMs) and orthomosaics. To provide accurate georeferencing, the thermal and visible GCP targets were identified within the thermal and visible UAV images and linked to the known coordinates recorded during the thermal and visible ground control surveys. To account for the effects of emissivity on the amount of TIR energy emitted by the debris surface, an emissivity value of 0.94 was assumed when converting emitted TIR values measured by the Vue Pro R to surface temperatures (Salisbury and D'Aria, 1992).

2.4.2 Calibrating UAV-derived surface temperature maps

For Peer Review

Images of a blackbody calibrator (a target object with an emissivity close to 1), captured in the lab using the same Vue Pro R camera that was used in the field, were used to calibrate the surface temperature maps to account for sensor bias (Figure S4). These thermal images were captured for blackbody temperatures between 5 °C and 60 °C, at 5 °C intervals. The equation of the best-fit line between measured temperature and actual temperature was used to calibrate the surface temperature values collected by the thermal camera.

The surface temperatures derived from UAV-mounted TIR cameras can be influenced by atmospheric attenuation of thermal radiance (Maes et al., 2017). Since the UAV flights were conducted across horizontal planes with constant flight heights of 4607 m a.s.l. (S_{T1}, S_{T2} and S_{T4}) and 4646 m a.s.l. (S_{T3}), the flight height above ground level (AGL) varied with surface topography. Consequently, the effect of atmospheric attenuation on measured surface temperatures is likely to have changed over the duration of the thermal UAV surveys. Since the flight height AGL is a function of elevation, a surface-altitude-dependent correction factor was applied to the thermal imagery in order to account for the effects of differential atmospheric attenuation on recorded surface temperatures. The surface-altitude-dependent correction factor was calculated based on differences between actual and recorded surface temperatures of exposed ice cliff surfaces, similar to the calibration approach used by Kraaijenbrink et al. (2018). It was assumed that exposed areas of ice cliffs have a surface temperature of 0°C. This assumption was validated using spot measurements of surface temperature collected in the field with an Apogee TIR radiometer. Using a series of ice cliffs distributed from the lowermost to the uppermost part of each thermal UAV survey, the linear relation between the glacier surface elevation and the measured-actual ice cliff temperature difference was computed and subsequently used to correct the surface temperatures within the thermal orthomosaics (Figure S4). Since the flight altitude AGL decreased continuously over the duration of each UAV survey (as the UAV gradually travelled up-glacier between sequential cross-sectional flight lines), it was assumed that this correction would also (at least partially) account for time-dependent sensor-related biases.

The accuracy of surface temperatures recorded by thermal cameras can be impacted by distortion caused by the lens optics, known as 'vignetting', where surface temperatures are slightly enhanced in the central region of each image and reduced in the outer portions of each image. It was assumed that, due to the continuously high overlap between subsequent images collected by the Vue Pro R camera, camera vignetting effects would be minimised by the averaging of temperature values during the image-stitching process and that any remaining vignetting effects, which may lower temperature values, were removed by the sensor bias correction.

2.5 Generating debris thickness maps

2.5.1 Modelling debris thermal properties

The effective conductivity of the debris was estimated at depths of 5, 10, 20, 30 and 40 cm within the debris layer, using the thermistor time-series (Section 2.3.2). Following the methods of Conway and Rasmussen (2000), debris thermal diffusivity K was approximated as the gradient between the first derivative of debris temperature T (K) with respect to time t (hr) and the second derivative of debris temperature with respect to depth z (m):

$$K = \frac{\dot{T}}{T''} = \frac{\left(\frac{\partial T}{\partial t}\right)}{\left(\frac{\partial^2 T}{\partial z^2}\right)} \quad (1)$$

Using the approximated thermal diffusivity values, the effective thermal conductivity k_{eff} was computed at each depth within the debris layer, assuming a rock density ρ_{rock} of 2700 kg m^{-3} and a heat capacity c_{rock} of 750 J kg^{-1} K^{-1} (Clark, 1966):

$$k_{eff} = K\rho_{rock}c_{rock} \quad (2)$$

For Peer Review

The overall k_{eff}, which was used in the SEB model (discussed in Section 2.5.3), was calculated by treating the debris layer as a series of conductors corresponding to specific layers within the overall debris layer, each with different conductivities. These specific layers were: 0 – 5 cm depth (assigned the 5 cm modelled k_{eff}), 5 – 10 cm (assigned an average of the 5 and 10 cm k_{eff} values), 10 – 15 (assigned the 10 cm k_{eff}), 15 – 25 cm (assigned the 20 cm k_{eff}), 25 – 35 cm (assigned the 30 cm k_{eff}) and 35 – 40 cm (assigned the 40 cm k_{eff}). The overall k_{eff} was calculated as the arithmetic average of the k_{eff} values assigned to these layers, accounting for the relative depth of each layer. The arithmetic average was used in order to minimise skewing of the results due to a single layer with a very small or large k_{eff}.

In order to account for the nonlinearity of the vertical temperature gradient, we estimated a nonlinearity factor G_{ratio}, after Rounce and McKinney (2014). Due to the lower reliability of the thermistor measurements closest to the surface, the equation for G_{ratio} was adjusted slightly to incorporate the vertical temperature gradients for 10-20 cm and 10-40 cm depth, instead of the gradients for 0-10 cm and 0-40 cm depth used by Rounce and McKinney (2014).

$$G_{ratio} = \frac{T_{0.1m} - T_{0.2m}}{T_{0.1m} - T_d} \cdot \frac{z_d - 0.1}{0.1} \quad (3)$$

where $T_{0.1m}$ and $T_{0.2m}$ are the temperatures 10 cm and 20 cm below the surface, T_d is the temperature at the debris-ice interface and d is the depth of the layer.

2.5.2 Parameterising the spatial and temporal distribution of meteorological variables

Since the thermal UAV surveys were conducted over periods of up to 2 hours, it was necessary to account for the changing spatial distribution of incoming shortwave radiation (SW_{in}) over the duration of each survey. Firstly, the 10 cm DEM of the glacier tongue (produced from the visible UAV imagery) was joined with the ALOS 30 m DEM of the surrounding topography. The resulting joined DEM was used to model the spatial distribution of solar radiation across the glacier surface for 5-minute periods at 30-minute intervals over the duration of each thermal survey. Through interpolation, a SW_{in} distribution map was produced for every 5-minute period of each thermal UAV survey. Each map was divided by its maximum value to produce fractional SW_{in} maps for every 5-minute period. The SW_{in} measurements recorded by Cuchillacocha weather station (Figure 1) at 30-minute intervals were also interpolated to each 5-minute period within each survey. Based on the assumption that SW_{in} measured at the weather station was equal to the maximum radiation across Llaca Glacier tongue, each modelled fractional SW_{in} map for every 5-minute period was multiplied by the corresponding weather-station-derived SW_{in} value for the same period, to produce weather-station-adjusted maps of SW_{in} for every 5-minute period. Each of the thermal survey areas were split into cross-sectional segments corresponding to 5-minute flight time blocks and each segment was assigned the spatially-distributed modelled SW_{in} values associated with the corresponding 5-minute flight time block. Finally, all cross-sectional segments were merged to produce a spatially-distributed maps of SW_{in}, adjusted for temporal changes in SW_{in}.

Weather station observations of air temperature (T_{air}) and relative humidity (RH) were used to model the temporal variations in incoming longwave radiation, LW_{in}, over the duration of the thermal UAV surveys, using the Stephan-Boltzmann law:

$$LW_{in} = \varepsilon_{eff} \sigma {T_{eff}}^4 \quad (4)$$

where ε_{eff} is the effective emissivity of the atmosphere, σ is the Stefan-Boltzmann constant (5.67 x 10^{-1} W m^{-2} K^{-4}) and T_{eff} is the effective air temperature. T_{eff} is represented by T_{air} at screen level. As there were clear weather conditions with no clouds during the thermal UAV surveys, the clear sky

For Peer Review

emissivity (ε_{clear}) was approximated using a parameterisation introduced by Dilley and O'Brian (1998) (equation 5). This approach has been found to provide the best parameterisation of LW_{in} over melting glaciers (Juszak and Pelliciotti, 2013).

$$\varepsilon_{clear} = \frac{a_{DO} + b_{DO}\left(\frac{T_{air}}{273.16}\right)^6 + c_{DO}\sqrt{\frac{4.65e_a}{25T_{air}}}}{\sigma {T_{air}}^4} \quad (5)$$

where e_a is the atmospheric vapour pressure (Pa), which was approximated from the altitude-corrected T_{air} and RH recorded at Cuchillacocha weather station (Figure 1), using the Magnus formula (Bell, 1996). a_{DO}, b_{DO} and c_{DO} are parameters from Dilley and O'Brien (1998) which have fixed values of 59.38, 113.7 and 96.96, respectively. Using this method, modelled LW_{in} values were produced at 30-minute intervals (corresponding to the frequency of weather station observations of T_{air} and RH), which were interpolated to produce modelled LW_{in} values for every 5-minutes of each thermal UAV survey. Each of these LW_{in} values was assigned to each of the corresponding cross-sectional segments of the thermal survey areas associated with each 5-minute flight time block of each survey. The cross-sectional segments produced were merged together to produce maps of LW_{in} which account for temporal variations in LW_{in} over the course of the thermal UAV surveys.

To account for altitudinal variations in T_{air} across the survey area, a spatially-dependent altitudinal correction was applied, using the UAV-derived DEM of the glacier tongue and a mean lapse rate derived from differences between values recorded at Cuchillacocha weather station (4630 m a.s.l.) and another weather station located further down the valley (3920 m a.s.l.). To account for temporal variations in T_{air}, wind speed and G_{ratio} over the duration of the thermal UAV surveys, the weather station observations (30-minute intervals) and modelled G_{ratio} (10-minute intervals) were again interpolated to every 5-minute flight time block of each thermal UAV survey. The resulting values were assigned to the cross-sectional segments corresponding to each 5-minute flight time block of each thermal survey, to produce temporally-corrected maps of T_{air}, wind speed and G_{ratio} for incorporation within the debris thickness model.

2.5.3 Producing modelled debris thickness maps

Using the calibrated UAV-derived surface temperatures, alongside the spatially and temporally distributed meteorological variables parameterised in Section 2.5.2, debris thickness maps were produced using surface energy balance modelling, which has previously been used to model debris thickness from coarser-resolution thermal satellite imagery (e.g., Foster et al., 2012; Rounce and McKinney, 2014). As the surface temperature data collected between 11.55 and 12.50 on 19 August (during survey S_{T3}) were most optimal for modelling debris thickness (as discussed further in Section 4.1), these data were used to model debris thickness across survey zone Z_{T2} (Figure 3a), which covers an area of ~137,000 m^2.

Firstly, the ground heat flux Q_c (W m^{-2}) was calculated as:

$$Q_c = R_n + H + LE \quad (6)$$

where R_n is the net radiation flux (W m^{-2}), H is the sensible heat flux (W m^{-2}) and LE is the latent heat flux (W m^{-2}). The net radiation flux was calculated as:

$$R_n = SW_{in}(1-\alpha) + \varepsilon\left(LW_{in} - \sigma {T_s}^4\right) \quad (7)$$

where SW_{in} is the incoming shortwave radiation (W m^{-2}), α is the albedo (dimensionless), ε is the emissivity (dimensionless), LW_{in} is the incoming longwave radiation (W m^{-2}), σ is the Stephan-Boltzmann constant (5.67 × 10^{-8} W m^{-2} K^{-4}) and T_s is the surface temperature (K). Debris emissivity

For Peer Review

and albedo values of 0.94 and 0.3, respectively, were assumed (Salisbury and D'Aria, 1992; Nicholson and Benn, 2012).

The sensible heat flux was calculated as:

$$H = \rho_{air}\left(\frac{P}{P_0}\right)c_{air}Au(T_{air} - T_s) \quad (8)$$

where ρ_{air} is the density of air (1.29 kg m^{-3}), P is the atmospheric pressure (Pa), P_0 is the atmospheric pressure at sea level (101 325 Pa), c_{air} is the specific heat capacity of air (1010 J kg^{-1} K^{-1}), A is the transfer coefficient (dimensionless), u is the wind speed recorded at the weather station (m s^{-1}) and T_{air} is the air temperature. The atmospheric pressure was computed using the barometric pressure formula and the transfer coefficient was calculated as:

$$A = \frac{{k_{vk}}^2}{\ln\left(\frac{z_h}{z_0}\right)\ln\left(\frac{z_h}{z_0}\right)} \quad (9)$$

where k_{vk} is the von Kármán's constant (0.41), z_h is the height of meteorological measurements (2 m) and z_0 is the surface roughness length, for which a value of 0.016 m was assumed (Rounce et al., 2014).

The latent heat flux was assumed to be zero, based on the assumption that the debris was dry.

The debris thickness d was calculated using a nonlinear model (Rounce and McKinney, 2014):

$$d = \frac{G_{ratio}k_{eff}(T_s - T_i)}{Q_c} \quad (10)$$

Where T_i is the temperature at debris-ice interface (assumed to be 273.15 K based on the thermistor measurements).

The three in-situ coupled GPS-debris-thickness measurements within the bounds of the thermal UAV survey were used as a guide to ensure that realistic debris thicknesses were being modelled. Negative modelled debris thickness values and values more than three median absolute deviations (MADs) from the mean were assigned as no data values.

2.5.4 Omitting supraglacial ice cliffs and ponds from the model

Cliffs and ponds were not included in the model since the modelling approaches used to estimate debris thickness cannot be applied to areas beneath supraglacial ponds or on the surface of supraglacial ice cliffs. Cliffs were semi-automatically classified using the DEM and orthomosaic derived from the visible UAV survey. Firstly, areas with a surface slope of >40° were isolated. To eliminate false detection areas, which primarily occur along the edges of large boulders where the surface gradient is high, areas with a maximum inter-pixel difference (between central pixel and surrounding pixels) of more than 40, in the brightness of the greyscale orthomosaic, were removed. Interconnected areas of less than 1 m^2 were also removed, in order to eliminate any remaining small rocks from the areas classified as ice cliffs. Finally, any boulder edges which were not successfully eliminated during the previous steps were removed manually from the ice-cliff-classified areas. As supraglacial ponds were relatively rare in comparison to ice cliffs, these features were classified using manual digitisation. Once ice cliffs and ponds had been classified, the areas covered by these features were removed from the model.

2.5.5 Alternative approach for mapping debris thickness from UAV-derived surface temperatures

For Peer Review

A simpler empirical method for modelling debris thickness from UAV-derived surface temperature data was also tested. This approach involved using the 22 TIR measurements collected between 13.25 and 15.05 on 21 August, alongside the debris thickness measurements acquired at each of the 22 sites, to find the second order polynomial relation between debris thickness and surface temperature on Llaca Glacier. Based on this relation, debris thickness was modelled from the calibrated surface temperature maps derived from UAV TIR imagery of Llaca Glacier tongue. This alternative approach is based on the assumption that the relation between surface temperature and debris thickness does not change significantly within the day, which is unlikely to be true. Furthermore, this approach does not take into account the spatially and temporally varying meteorological parameters that impact surface temperature. Therefore, this alternative method was only used for the purpose of testing how well debris thickness could be approximated using a simplified approach with fewer data requirements, as well as to allow comparison to the debris thicknesses modelled using the surface energy balance approach. A similar method was used by Mihalcea et al (2008) to model debris thickness from thermal satellite imagery (ASTER), based on the correlation between field-based debris thickness measurements and satellite-derived surface temperatures.

2.6 Modelling daily sub-debris melt rates

Distributed daily sub-debris melt rates were modelled based on the modelled debris thickness (derived from the surface energy balance modelling approach), following the method of Nicholson and Benn (2006). This method uses mean daily meteorological data, assuming that the daily mean temperature profile through the debris layer is linear and that net changes in heat storage are negligible on diurnal timescales. This method was chosen as it significantly reduces the computational resources needed to run the model and has been demonstrated to yield reliable sub-debris ablation rate estimates despite model simplification (Nicholson and Benn, 2006). Firstly, the distributed average daily surface temperatures were solved for iteratively, based on the polynomial:

$$-\varepsilon\sigma {T_s}^4 - \left(\rho_{air}\left(\frac{P}{P_0}\right)c_{air}Au + \frac{k_{eff}}{d}\right)T_s + SW_{in}(1-\alpha) + \rho_{air}\left(\frac{P}{P_0}\right)c_{air}AuT_{air} + \frac{k_{eff}T_i}{d} + \varepsilon\, LW_{in} = 0 \qquad (11)$$

Data from the Cuchillacocha weather station (Figure 1) were used to calculate mean daily meteorological parameters. Mean daily LW_{in} was calculated from T_{air} and RH (equations 4 and 5), while the spatial variability of meteorological parameters was accounted for using the following approaches. The spatial distribution of SW_{in} was modelled over a 24-hour period every 10 days between the 5 July and 5 October. Through interpolation, maps of average SW_{in} distribution were produced for every day during this 3-month period. For each day, the corresponding map of SW_{in} distribution was divided by its mean value, before being multiplied by the mean SW_{in} recorded at the weather station on that day. To account for spatial variations in T_{air}, the UAV-derived DEM was used to produce a map of altitude-dependent T_{air}, using an environmental lapse rate of 6.5 °C km^{-1}. u and LW_{in} were assumed to be spatially-homogeneous.

Using the resulting surface temperature map, the ground heat flux was computed using equation 6 and the distributed daily melt rate M (m d^{-1}) was computed as:

$$M = t\frac{Q_m}{\rho_{ice}L_f} \qquad (12)$$

Where t is time (seconds), Q_m is downward energy flux at the base of the debris layer (equal to Q_c), ρ_{ice} is the density of ice (assumed to be 900 kg m^{-3}) and L_f is the latent heat of fusion (334 kJ kg^{-1}). Negative values of M were set to 0, while values more than three standard deviations from the median were set to no data values.

For Peer Review

In order to investigate the impact of differing modelled debris thickness on modelled sub-debris melt rates, the model was run for a second time using debris thicknesses modelled from satellite data (Rounce et al., 2021) and the results were compared to the sub-debris melt rates modelled in this study.

3. Results

3.1 Vertical debris temperature profiles

The debris temperatures recorded by the thermistors at depths of 5, 10, 20, 30 and 40 cm (40 cm being the debris-ice interface) are shown in Figure 4. The variation in debris temperature decays with increasing depth, with an average range in daily temperature of 17.9 °C at 5 cm depth compared to 0.7 °C at the debris-ice interface (40 cm depth). As depth into the debris layer increases, the times of the diurnal peaks and troughs in debris temperature are increasingly lagged. For example, there is a lag of 6.83 hours between the average time of peak daily debris temperature at a depth of 5cm (14:17) and at a depth of 40cm (21:07).

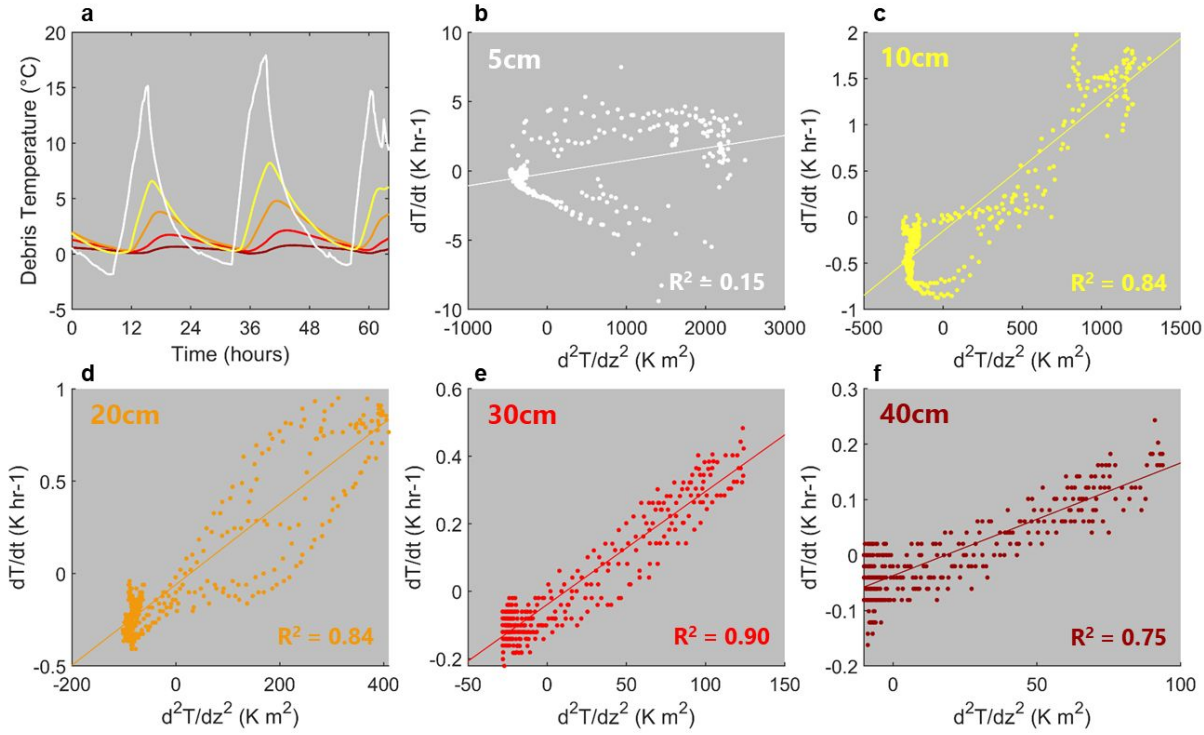

Figure 4. Thermal properties of the supraglacial debris layer at Llaca Glacier, derived from thermistors located at depths of 5, 10, 20, 30 and 40 cm (with the debris-ice interface being at 40 cm depth) within the debris layer. (a) shows the direct measurements that were recorded by each of the thermistors between 17 August 00:00 and 19 August 16:00, with lines colour-coded according to the debris thicknesses shown in (b)-(f). (b)-(f) show the relationship between the second derivative of debris temperature with respect to depth (d^2T/dz^2) and the first derivative of debris temperature with respect to time (dT/dt), derived from the time-series recorded by each of the thermistors. The gradient of this relationship, which was used to approximate the thermal diffusivity, is shown for each of the thermistors in (b)-(f), along with the R^2 value associated with each gradient.

3.2 Thermal conductivity

The effective thermal conductivity of the debris decreases by 0.963 W m^{-1} K^{-1} from near the surface of the debris layer (5 cm depth) to 30 cm depth (Table 2). However, the thermal conductivity appears to decrease

Table 2. Debris thermal properties on Llaca Glacier tongue. Thermal diffusivity and effective conductivity values, modelled from the thermistor measurements, are shown for each depth within the debris layer.

Debris thickness (cm)	Thermal diffusivity (mm^2 s^{-1})	Effective thermal conductivity (W m^{-1} K^{-1})
5	0.252	0.357
10	0.386	0.547
20	0.606	0.860
30	0.931	1.320
40	0.565	0.801

Cambridge University Press

below 30 cm, with a thermal conductivity 0.519 W m^{-1} K^{-1} lower at the ice-debris interface (40cm depth) than at 30 cm depth. R^2 associated with the gradients between $\frac{\partial T}{\partial t}$ and $\frac{\partial^2 T}{\partial z^2}$ are generally high (Figure 4c-f), except for at 5 cm depth, where the R^2 value is considerably lower (Figure 4b).

3.3 Modelled debris thickness

Figure 5 shows the debris thickness modelled across Llaca Glacier using the main workflow outlined in Figure 2. The results indicate a mean debris thickness of 0.20 m, with a variance of 0.03 m, across the survey area. Debris thickness generally decreases up-glacier, with the lowest debris thicknesses being found in the uppermost portion of the survey area, where the debris layer was ~ 1-7 cm thick. Over > 90% of the survey area (excluding supraglacial ice cliffs and ponds), the debris layer is thicker than the critical thickness required to reduce sub-debris melt rates through insulation of the ice surface (Östrem, 1959). Comparison against the three usable manually-acquired debris thickness measurements, coupled with accurate GPS locations, within the survey area indicates good agreement between measured and modelled values, with differences of < 6 % between modelled and measured debris thickness values (Figure 5b).

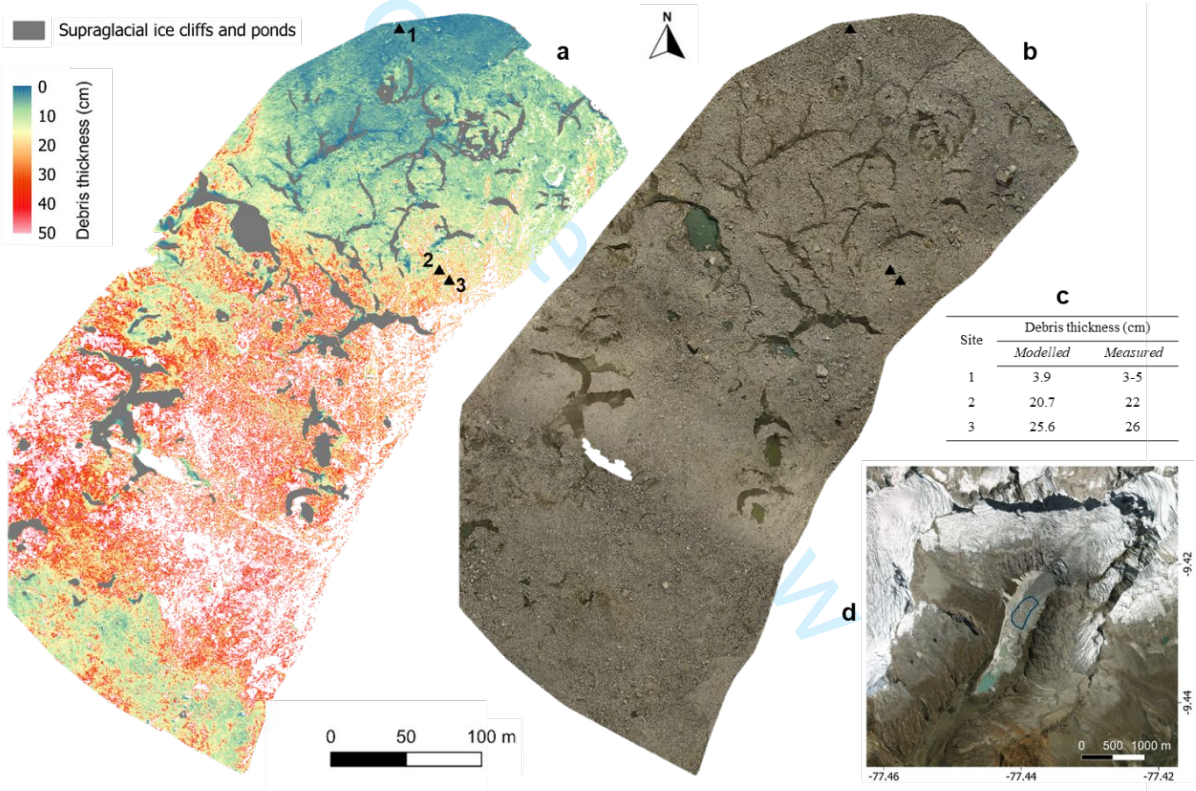

Figure 5. Spatially-distributed map of modelled debris thickness. Modelled debris thicknesses are shown in (a), with black triangles showing the locations of the in-situ debris thickness measurements within the survey area. White areas show the presence of no data values, where modelled values were negative or more than three MADs outside the mean (discussed in 2.5.3). Grey areas show the presence of supraglacial ice cliffs and ponds, which were not included in the model (discussed in 2.5.4). RGB orthomosaic for the modelled area is shown in (b). A comparison between the modelled and measured debris thicknesses at these three sites is shown in (c), while (d) shows the spatial coverage of the debris thickness map and RGB orthomosaic shown in (a) and (b), respectively.

3.4 Surface temperature

The results show that the spatial heterogeneity in surface temperatures is greatest during the middle of the day compared to early morning and late afternoon (Figure S1). More specifically, the surface temperatures derived from the thermal imagery collected between 11.55 and 12.50 (survey S_{T3}) show

a variance of 35.8 K across the survey area, while the surface temperatures derived from the thermal surveys of 16.25-17.20 (S_{T1}), 9.30-10.00 (S_{T2}) and 14.25-15.45 (S_{T3}) show lower variances of 14.2, 23.6 and 21.8 °C, respectively, across their survey areas. Meanwhile, the surface temperatures from S_{T3} have a standard deviation of 6.0, while the surface temperatures from S_{T1}, S_{T2} and S_{T4} have lower standard deviations of 3.8, 4.9 and 4.7 °C, respectively. Note that some of the differences in variance may be partially attributable to different areas being covered by thermal surveys conducted at different times of day (as described in Section 2.2.1).

3.5 Modelled sub-debris melt rates

The results indicate a mean sub-debris melt rate of 0.49 cm d^{-1} across the total survey area, over the entire 3-month model period between 5 July and 5 October (Figures 6-7), with high levels of spatial heterogeneity ranging from 0.00 cm d^{-1} to 1.91 cm d^{-1} across the study area (Figures 5d,6). Sub-debris melt rates also generally increase up-glacier through the survey area (Figure 6). Maximum sub-debris melt rates decrease as a function of debris thickness, with mean melt rates for the 93-day period of up to nearly 2 cm d^{-1} for thin debris layers of a few mm, compared to mean melt rates of up to ~0.5 cm d^{-1} where debris is 30 cm thick (Figure 7c). Figure 7b shows that mean sub-daily melt rate for the period 5 July – October has a skewed distribution, with a modal melt rate of ~0.25 cm d^{-1}.

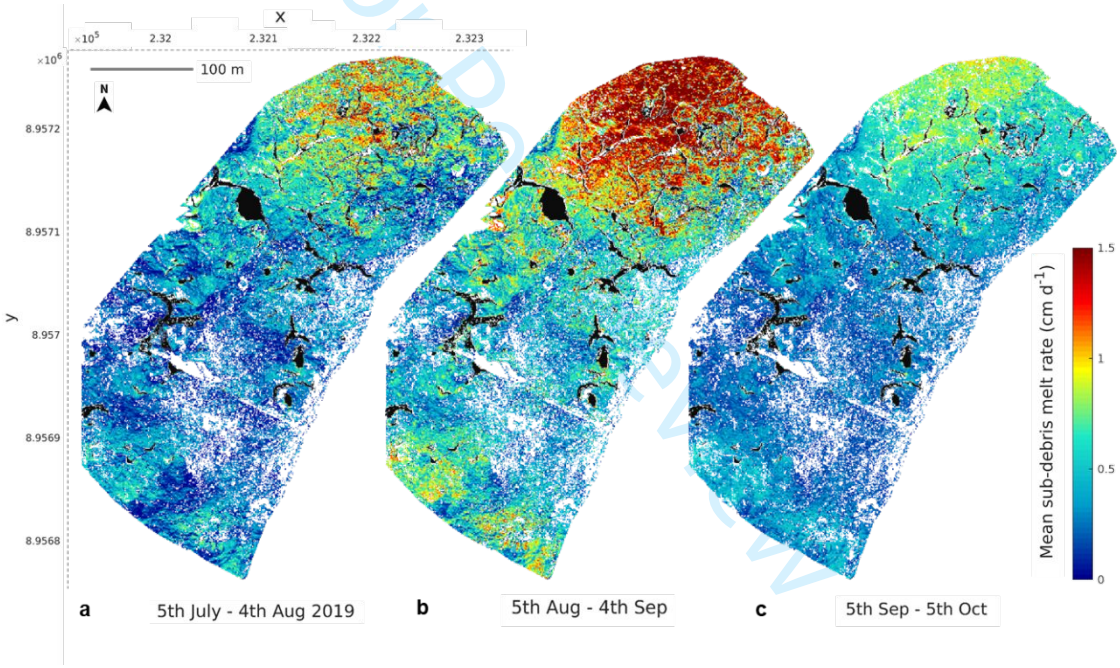

Figure 6. Spatially-distributed modelled sub-debris melt rates on Llaca Glacier tongue. Maps of the mean modelled melt rates (across the area shown in Figure 4c) are shown for three 31-day periods: 5 July – 4 August (a), 5 August – 4 September (b) and 5 September – 5 October (c). These values were modelled backwards and forwards in time from the date of thermal UAV data collection, 19 July 2019. Black shaded areas show the presence of supraglacial ice cliffs and ponds (which were not included in the model) and white areas show the presence of no data values.

There are high levels of temporal variability in the sub-debris melt rates on Llaca Glacier tongue, with modelled mean daily melt rates for the whole survey area ranging from 0.00 to 1.18 cm d^{-1} between 5 July and 5 October 2019 (Figure 7a). The results indicate that sub-debris melt rates are generally slightly greater during the middle of the three-month modelling period (see moving average in Figure 7a), with mean daily sub-debris melt rates of 0.69 cm between 5 August and 4 September, compared to 0.40 and 0.38 for the periods of 5 July – 4 August and 5 Sep – 5 Oct, respectively (Figure 6). Over the duration of the three-month modelling period, the mean incoming SW and LW radiation fluxes are 195 and 185 W m^{-2}, respectively (Figure 7d). The ranges in mean daily incoming SW and LW

radiation are 194 and 11 W m^{-2}, respectively, over the 93-day period, while the range in mean daily air temperature is 3.8 °C.

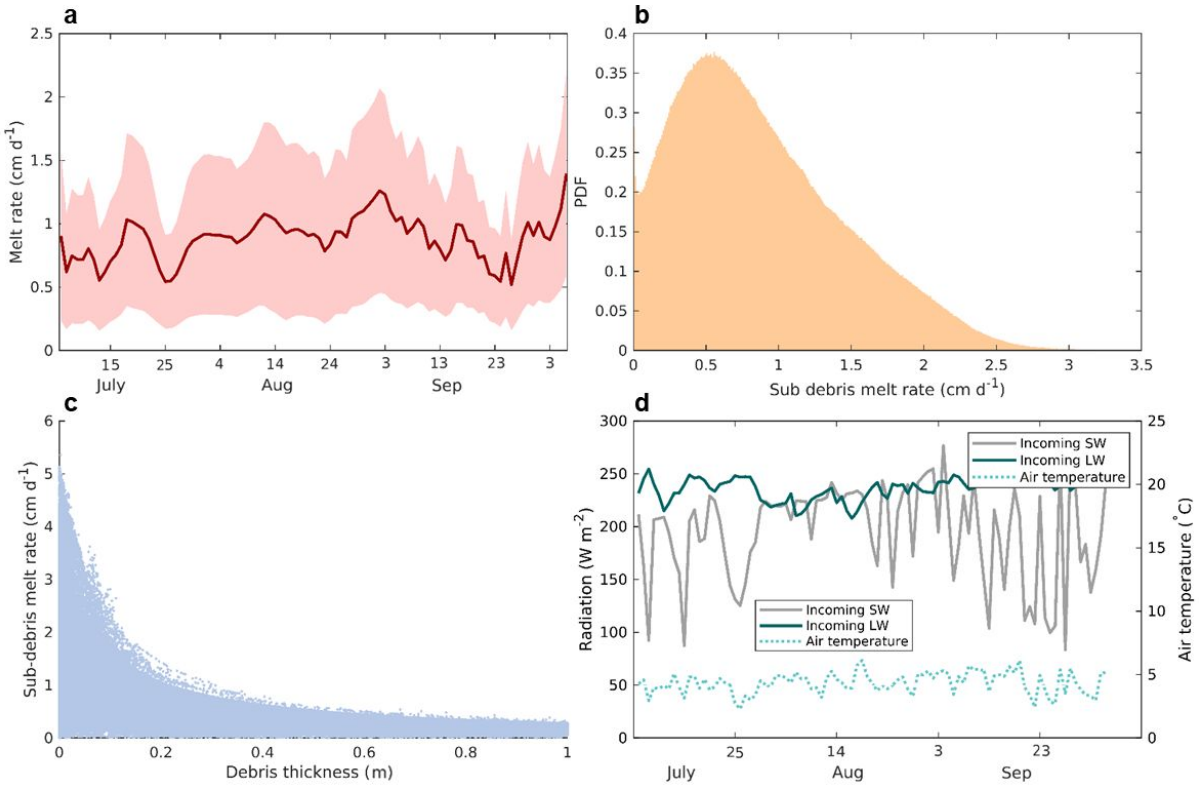

Figure 7. Modelled sub-debris melt rates on Llaca Glacier tongue between 5 July and 5 October 2019. (a) Temporal variations in the average sub-debris daily melt rates (red line with standard deviation shaded) and the 20-day moving average (yellow line) for the area shown in Figure 5c. (b) Probability density function (PDF) for the mean sub-debris melt rates of the period 5 July - 5 October for the survey area shown in Figure 5c. (c) Mean modelled sub-debris melt rates for the same area and period shown as a function of modelled debris thickness. (d) Mean daily air temperature and incoming shortwave (SW) radiation recorded at Cuchillacocha weather station and the mean daily modelled incoming longwave (LW) radiation between 5 July and 5 October).

4. Discussion

4.1 Modelling debris thickness from thermal UAV imagery

The results of this study demonstrate that thermal UAV imagery can be used to effectively model spatially-distributed supraglacial debris thicknesses. The results also demonstrated that, while high levels of precision can be gained from using such imagery, a number of calibrations and corrections are critical to ensure that (a) the thermal imagery is calibrated to account for biases associated with UAV-mounted thermal sensors, (b) the thermal imagery is corrected to account for the changing sensor-surface distance over the course of the thermal UAV flights (if terrain correction is not used), (c) the temporal changes in meteorological parameters over the course of the thermal surveys are accounted for, and (d) the spatial variations in meteorological parameters across the thermal survey area are accounted for. We recommend that future studies take the aforementioned steps in order to maximise the accuracy of debris thickness maps derived from thermal UAV imagery.

The results also show that thermal imagery acquired near the middle of the day is optimal for modelling debris thicknesses, due to (a) high spatial heterogeneity in surface temperatures, and (b) relatively low temporal variations in the modelled G_{ratio} and meteorological variables. As shown in Table S2, survey S_{T3} yielded a variance in surface temperatures 50 - 150 % greater, and a standard deviation 20 – 60 % greater, than the other three surveys. As a result, it is easiest to distinguish

between different debris thicknesses using thermal imagery collected during S_{T3}, which was conducted during the middle of the day (10.55 – 12.50). In contrast, debris-thickness-driven differences in surface temperatures are less pronounced in the early morning, since debris has not yet heated up sufficiently, resulting in cooler and more homogeneous debris temperatures (further demonstrated in Figure 4a). During the late afternoon, the debris has cooled significantly since the middle of the day (Figure 4a), again partially obscuring some of the debris-thickness-driven differences in surface temperatures. Furthermore, during the early morning and late afternoon, temporal variations in meteorological variables are high (Figure S1a,b,d,e), making it difficult to account for variability in meteorological parameters within the duration of the thermal UAV surveys, thereby impacting the accuracy of modelled debris thicknesses. Additionally, the G_{ratio} factor is highly unstable during the early morning (Figure S1c), making it more difficult to account for the complex and changeable debris temperatures. We therefore recommend that future studies collect thermal imagery near the middle of the day (e.g. between approximately 11.00 and 13.00), when surface temperature variations are greatest and temporal meteorological variability is likely to be relatively low (Figure S1).

Figure 8 demonstrates the improved level of detail obtained using UAV-derived surface temperatures to model debris thickness, compared to the use of thermal imagery derived from satellites. As demonstrated in Figure 5a, there are large variations in debris thickness over relatively small spatial scales, which can only be distinguished using the thermal UAV imagery, and not from the highest-resolution satellite imagery currently available (Figure 8). This provides further evidence that glaciological models which use satellite-derived debris thicknesses as input data are likely to be affected by 'inter-pixel mixing effects', as described by Rounce and McKinney (2014). Our UAV results indicate a mean debris thickness of 0.20 m across the survey area, which is 71 % less than the mean debris thickness modelled from thermal satellite data for the same area (0.70 m) (Rounce et al., 2021). This suggests that debris thicknesses on Llaca Glacier may be significantly overestimated by satellite-based models, with significant impacts on modelled sub-debris melt rates (as discussed further in Section 4.2). Further evidence is therefore required in order to confirm whether this could be indicative of a wider pattern.

The results also indicate that using a simpler method to model debris thickness, based on the polynomial relationship between surface temperature and debris thickness, similar spatial patterns of debris thickness can be detected in areas where the debris layer is less than ~20 cm in depth (Figure S3). However, when debris exceeds a thickness of around 20 cm, the polynomial-relation-based model appears to significantly underestimate debris thickness (Figure S2; Table S2). A potential explanation for this is that the polynomial relation method used to model debris thickness is based on a higher number of measurements at points where debris thickness is below 20cm (Figure S2), while there is only one measurement with a debris thickness of 25 cm, which may provide a poor representation of surface temperature for thicker debris. Additionally, the polynomial relation method does not account for the contribution of spatial variations in meteorological conditions towards the debris surface temperatures observed. As a result, the debris thickness accuracy is likely to be lower compared to the results derived from the surface energy balance modelling approach.

For Peer Review

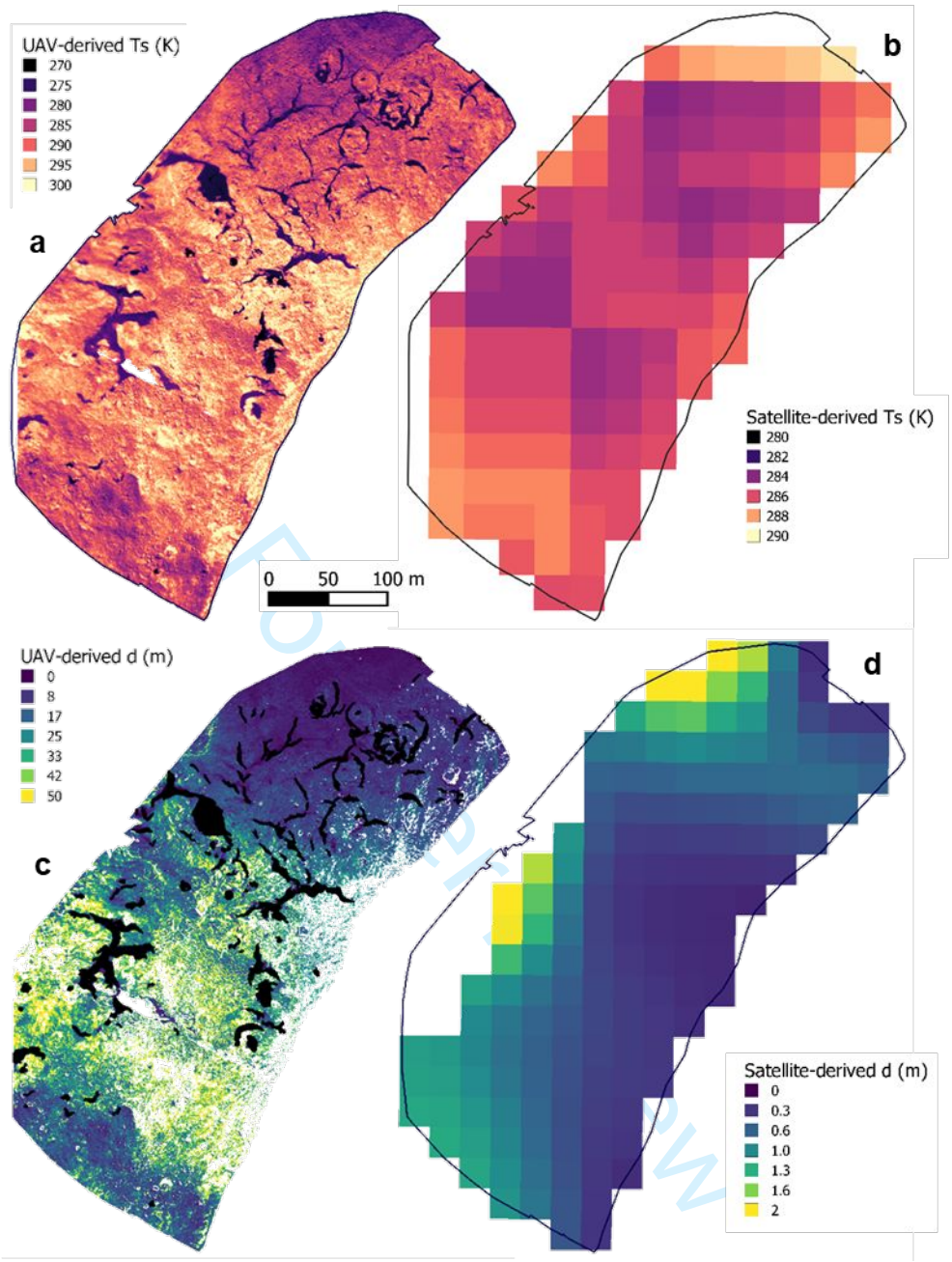

Figure 8. Comparison between UAV and satellite-derived surface temperature information and modelled debris thicknesses. (a) Calibrated surface temperatures derived from thermal UAV imagery, acquired between 10.55 and 12.50 on 19 August 2019. (b) Surface temperatures derived from the thermal band of the Landsat 7 satellite, acquired at 15.03 on 19 August 2019. (c) Debris thicknesses modelled in this study from thermal UAV imagery. Black shaded areas show the presence of ice cliffs and white areas show the presence of no data values. (d) Debris thicknesses modelled by Rounce et al. (2021). The black line surrounding each of the 4 maps shows the same reference area on Llaca Glacier, as shown in Figure 5c.

4.2 Modelling sub-debris melt rates from UAV-derived debris thickness maps

This study demonstrates that by using high-resolution maps of debris thickness derived from thermal UAV data, greater-precision estimates of sub-debris melt rates can be produced. As shown in Figure 6, high levels of spatial heterogeneity in ice surface melt rates over sub-metre scales can be detected across the survey area on Llaca Glacier tongue. Inputting the derived debris thicknesses modelled by Rounce et al. (2021) (which are nearly three times greater than our estimates) into our sub-debris melt model, we estimated a mean modelled melt rate of 0.17 cm d^{-1}, a value 65 % less than modelled in our

study (0.49 cm d^{-1}). This indicates that since the debris thicknesses modelled from satellite data appear to be considerably overestimated for Llaca Glacier tongue, this would lead to significant underestimation of sub-debris melt rates as a consequence. We therefore advocate for further high-precision studies of debris thickness, with better model validation, in order to better understand the uncertainties associated with satellite-derived debris thicknesses and more accurately calibrate regional-scale models of debris thickness and sub-debris melt rates.

4.3 Thermal properties of supraglacial debris

As shown by numerous previous studies (e.g. Conway and Rasmussen, 2000; Nicholson and Benn, 2012), our results further confirm that, during the daytime, the temperature of the supraglacial debris on Llaca Glacier is lowest at the debris ice interface and increases towards the surface of the debris layer (Figure 4a). The increasingly lagged peaks in debris temperature from the surface to the base of the debris layer indicate that, with increased debris thickness, there will be an augmented delay time in the melt response to meteorological forcing at Llaca Glacier.

The increase in thermal diffusivity from 30 cm depth to 40 cm depth indicates that moisture content likely plays an increasingly significant role near the debris-ice interface. The debris closest to the debris-ice interface is likely to be more moisture-saturated due to the accumulation of melted ice and, since thermal diffusivity is reduced where debris is more saturated (Juen et al., 2012), the thermal diffussivity of this layer is lower than the layer 10cm above. Furthermore, water-saturated debris loses energy to latent heat fluxes, resulting in a reduction in the amount of heat available to be transferred downwards to the ice surface (Giese et al., 2020).

The depth-averaged thermal conductivity of the debris layer at Llaca Glacier (0.78 W m^{-2} K^{-1}) appears to be slightly lower than the values generally reported by previous studies in the Himalaya. For example, at Ngozumpa Glacier in Nepal, Nicholson and Benn (2012) found thermal conductivities of $0{\cdot}95 \pm 0{\cdot}10$ W m^{-2} K^{-1} and $1{\cdot}29 \pm 0{\cdot}13$ W m^{-2} K^{-1} for dry debris in winter and summer respectively. This lower thermal conductivity could potentially be attributed to greater debris porosity, which results in more air being trapped within the debris layer and less heat being transferred downwards through the debris layer (Juen et al., 2012).

As a result of its relatively low thermal conductivity, the debris layer on Llaca Glacier is likely to be providing a greater insulative effect on the ice below than on glaciers where the debris thermal conductivity is greater. This suggests that the debris is having a relatively high inhibiting effect on melt rates at Llaca Glacier, in comparison to some of the well-studied glaciers in the Himalaya. This could be indicative of a higher regional importance of debris cover in controlling glacier melt rates in the Cordillera Blanca. However, further evidence is required in order to better understand the role of debris cover in controlling glacial melt rates and downstream hydrology in the Ancash region of Peru.

4.4 Model sensitivity and limitations

The sensitivity analysis results (Table S3) indicate that modelled debris thicknesses are most sensitive to incoming shortwave radiation and albedo. While incoming solar radiation recorded in the nearby valley is likely to be similar to Llaca Glacier (as there were cloud-free conditions during the thermal surveys), future studies could further minimise model uncertainties by gathering meteorological data on site. Additionally, ground-based pyranometer measurements of albedo could be collected and surface classification of albedo could be divided into a greater number of categories (e.g. corresponding to different debris lithologies). The model is relatively sensitive to surface temperature (Table S3), emphasising the importance of accurately calibrating the surface temperatures derived from UAV-mounted thermal cameras. While various calibration procedures were performed to correct for the effects of sensor biases, sensor drift, atmospheric signal attenuation and surface emissivity variations, future efforts could be made to further improve these calibration procedures. The model is

For Peer Review

also moderately sensitive to the nonlinear approximation factor. Since the parameterisation of the nonlinear approximation factor is affected by the debris temperatures recorded by the thermistors, setting up sequences of thermistors at multiple locations of varying debris thicknesses would help to ensure the accuracy of this parameter.

A key limitation associated with this study is the scarcity of debris thickness data suitable for validation (as discussed in Section 2.3.3), which results in some remaining uncertainty in the reliability of debris thicknesses modelled from thermal UAV data. In future, further thermal UAV surveys of debris-covered glaciers, coupled with a greater number of in-situ debris thickness measurements within surveyed areas, would be highly beneficial for establishing this technique as a viable method for obtaining high-precision estimates of supraglacial debris thickness with improved levels of accuracy. Furthermore, the collection of ablation-stake measurements at debris-thickness modelling sites would enable validation of modelled sub-debris melt rates produced using UAV-derived modelled debris thicknesses.

5. Conclusions

This study has presented an approach for modelling high-resolution, spatially-distributed supraglacial debris thicknesses and sub-debris melt rates from UAV-derived thermal imagery, in conjunction with local meteorological data, visible UAV imagery and vertically-profiled debris temperature measurements. We have demonstrated that by (a) effectively calibrating the radiometric thermal imagery, (b) accounting for the temporal variations in meteorological parameters over the UAV survey duration, (c) parameterising the spatial distribution of meteorological parameters across the survey area, and (d) modelling the thermal conductivity of the debris layer, surface energy balance modelling can be used to effectively to model the debris thickness and sub-debris melt rates of debris-covered glaciers. We have also demonstrated that by obtaining high-resolution (10 cm) UAV imagery, as opposed to using coarser (> 60 m) satellite imagery, the highly spatially-heterogeneous debris thickness across Llaca Glacier tongue can be significantly better represented, facilitating higher-precision sub-debris melt modelling. Our findings have indicated that the mean debris thickness across the survey area on Llaca Glacier tongue is ~ 71 % lower than the satellite-derived estimate, indicating that the accuracy of satellite-derived debris thicknesses are likely to be poor in some places. Further sub-debris melt modelling has indicated that this overestimation of debris thicknesses would have resulted in a ~ 65 % underestimation of sub-debris melt rates across the survey area. Our results also indicated that the debris layer on Llaca Glacier has an ~18 – 40 % lower thermal conductivity compared to the debris on previously-studied glaciers in the Himalaya, suggesting that the inhibiting effect of debris on melt rates may vary considerably between glaciers and/or regions. Overall, the results of this study emphasise the need for further high-precision UAV/ground-based studies of the thermal properties of supraglacial debris in the Cordillera Blanca, as well as in other mountain regions around the world, in order to better calibrate debris thicknesses within glaciological models and improve the accuracy of hydrological predictions.

Author contributions:

R.R.B. designed the study, with support from P.W.N., D.N.G. and R.G.B. The UAV surveys were planned and conducted by R.R.B., with advice from O.W. and field support from M.L.M. and R.A.L-M. All data were processed and analysed by R.R.B. and interpreted by R.R.B., R.G.B., P.W.N. and D.N.G. The manuscript was written by R.R.B. and edited by all co-authors.

Acknowledgements:

We would like to thank: Calum Reay for his support in the field; David Redpath, the founder of Sky Tech Ltd., for engineering the custom-built thermal UAV used in this study; the NERC Geophysical

For Peer Review

Equipment Facility (GEF) and NERC Field Spectroscopy Facility (FSF), both of which provided crucial equipment and support for the fieldwork component of this study; Claire Webster for UAV surveying advice; Magnus Hagdorn for advice on improving code efficiency; Bridgewater State University for providing open access to the meteorological data from Cuchillacocha and Casa de Agua weather stations which was used in this study; John Watt for providing vital safety equipment for fieldwork; and the School of GeoSciences equipment facility and Anthony Newton for providing the additional scientific equipment essential to the field data collection.

Funding:

This research was funded by the U.K. Natural Environment Research Council (NERC), through a studentship awarded to R.R.B. and R.G.B. by the University of Edinburgh NERC E^3 Doctoral Training Partnership (NE/L002558/1). The fieldwork formed part of the CASCADA project, a joint UK-Peruvian project researching the impacts of glacial retreat on water resources in the Ancash region of Peru, for which R.A.L.M. and J.L.W. are the PIs. CASCADA is funded by the Newton Paulet Fund, a UK/Peru collaboration led by NERC (NE/S013288/1) and the Consejo Nacional de Ciencia, Tecnología e Innovación Tecnológica, Perú (CONCYTEC). Additional funding support was received from the Scottish Alliance for Geoscience, Environment and Society (SAGES).

References

Anderson, L.S., Armstrong, W., Anderson, R.S., Buri, P. (2021) Debris cover and the thinning of Kennicott Glacier, Alaska: in situ measurements, automated ice cliff delineation and distributed melt estimates. *The Cryosphere*. 15(1), 265-282.

Bell, S.A., 1996. A guide to the measurement of humidity (NPL Guide 103*). Teddington: National Physical Laboratory*.

Buri, P., Pelliciotti, F., Steiner. J.F., Miles, E.S. (2016) A grid-based model of backwasting of supraglacial ice cliffs on debris-covered glaciers. *Annals of Glaciology*. 57(71), 199-211.

Clark, S.P. (1966) *Handbook of physical constants* (Vol. 97). Geological Society of America.

Conway, H., Rasmussen, L.A. (2000) Summer temperature profiles within supraglacial debris on Khumbu Glacier, Nepal. *Proceedings of a workshop held at Seattle, Washington, USA, September 2000.*

Dilley, A.C., O'Brien, D.M. (2013) Estimating downward clear sky long-wave irradiance at the surface from screen temperature and precipitable water. *Quarterly Journal of the Royal Meteorological Society*. 124(549), 1391-1401.

Fortner, S.K., Mark, B.G., McKenzie, J.M., Bury, J., Trierweiler, A., Baraer, M., Burns, P.J. and Munk, L. (2011) Elevated stream trace and minor element concentrations in the foreland of receding tropical glaciers. *Applied Geochemistry*. 26(11), 1792-1801.

Foster, L.A., Brock, B.W., Cutler, M.E.J., Diotri, F. (2012) A physically based method for estimating supraglacial debris thickness from thermal band remote-sensing data. *Journal of Glaciology*. 58(210), 677-691.

Giese, A., Boone, A., Wagnon, P., Hawley, R. (2020) Incorporating moisture content in surface energy balance modeling of a debris-covered glacier. *The Cryosphere*. 14, 1555-1577.

Guittard, A., Baraer, M., McKenzie, J.M., Mark, B.G., Wigmore, O., Fernandez, A., Rapre, A.C., Walsh, E., Bury, J., Carey, M. and French, A. (2017) Trace-metal contamination in the glacierized Rio Santa watershed, Peru. *Environmental monitoring and assessment*. 189(12), 1-16.

For Peer Review

Immerzeel, W.W., Kraaijenbrink, P.D.A., Shea, J.M., Shrestha, A.B., Pelliciotti, F., Bierkens, M.F.P., de Jong, S.M. (2014) High-resolution monitoring of Himalayan glacier dynamics using unmanned aerial vehicles. *Remote Sensing of Environment*. 150, 93-103.

Juen, M., Mayer, C., Lambrecht, A., Wirbel, A., Kueppers, U. (2012) Thermal properties of a supraglacial debris layer with respect to lithology and grain size. *Geografiska Annaler: Series A, Physical Geography*. 95(3), 197-209.

Juszak, I., Pellicciotti, F. (2013) A comparison of parameterizations of incoming longwave radiation over melting glaciers: Model robustness and seasonal variability. *Journal of Geophysical Research: Atmospheres*. 118, 3066-3084.

Kelly, J., Kljun, N., Olsson, P.O., Mihai, L., Liljeblad, B., Weslien, P., Klemedtsson, L., Eklundh, L. (2019) Challenges and Best Practices for Deriving Temperature Data from an Uncalibrated UAV Thermal Infrared Camera. *Remote Sensing*. 11(567), 1-21.

Kraaijenbrink, P.D.A., Shea, J.M., Pelliciotti, F., de Jong, S.M., Immerzeel, W.W. (2016) Object-based analysis of unmanned aerial vehicle imagery to map and characterise surface features on a debris-covered glacier. *Remote Sensing of Environment*. 186, 581-595.

Kraaijenbrink, P.D., Shea, J.M., Litt, M., Steiner, J.F., Treichler, D., Koch, I. and Immerzeel, W.W. (2018) Mapping surface temperatures on a debris-covered glacier with an unmanned aerial vehicle. *Frontiers in Earth Science*. 6, 64.

Maes, W.M., Huete, A.R., Steppe, K. (2017) Optimizing the Processing of UAV-Based Thermal Imagery. *Remote Sensing*. 9(476), 1-17.

Mark, B.G., Bury, J., McKenzie, J.M., French, A., Baraer, M. (2010) Climate Change and Tropical Andean Glacier Recession: Evaluating Hydrologic Changes and Livelihood Vulnerability in the Cordillera Blanca, Peru. *Annals of the Association of American Geographers*. 100(4), 794-805.

Mark, B.G., French, A., Baraer, M., Carey, M., Bury, J., Young, K.R., Polk, M.H., Wigmore, O., Lagos, P., Crumley, R., McKenzie, J.M. Lautz, L. (2017) Glacier loss and hydro-social risks in the Peruvian Andes. *Global and Planetary Change*. 159, 61-76.

Mihalcea, C., Brock, B.W., Diolaiuti, G., D'Agata, C., Citterio, M., Kirkbride, M.P., Cutler, M.E.J., Smiraglia, C. (2008a) Using ASTER satellite and ground-based surface temperature measurements to derive supraglacial debris cover and thickness patterns on Miage Glacier (Mont Blanc Massif, Italy). *Cold Regions Science and Technology*. 52(3), 341-354.

Nakawo, M., Rana, B. (1999) Estimate of Ablation Rate of Glacier Ice Under a Supraglacial Debris Layer. *Geografiska Annaler: Series A, Physical Geography*. 81(4), 695-701.

Nakawo, M., Young, G.J. (2017) Field experiments to determine the effect of a debris layer on ablation of glacier ice. *Annals of Glaciology*. 2, 85-91.

Nicholson, L., Benn, D.I. (2006) Calculating ice melt beneath a debris layer using meteorological data. *Journal of Glaciology*. 52(178), 463-470.

Nicholson, L., Benn, D.I. (2012) Properties of natural supraglacial debris in relation to modelling sub-debris ice ablation. *Earth Surface Processes and Landforms*. 38(5), 490-501.

Nicholson, L.I., McCarthy, M., Pritchard, H.D., Willis, I. (2018) Supraglacial debris thickness variability: impact on ablation and relation to terrain properties. *The Cryosphere*. 12(12), 3719-3734.

For Peer Review

Nicholson, L., Mertes, J. (2017) Thickness estimation of supraglacial debris above ice cliff exposures using a high-resolution digital surface model derived from terrestrial photography. *Journal of Glaciology*. 63(242), 989-998.

Östrem, G. (1959) Ice melting under a thin layer of moraine, and the existence of ice cores in moraine ridges. *Geografiska Annaler*. 41(4), 228-230.

Reid, T.D., Carenzo, M., Pelliciotti, F., Brock, W. (2012) Including debris cover effects in a distributed model of glacier ablation. *Journal of Geophysical Research*. 117(D18), 1-15.

RGI Consortium (2017) Randolph Glacier Inventory – A Dataset of Global Glacier Outlines: Version 6.0.

Rabatel, A., Francou, B., Soruco, A., Gomez, J., Cáceres, B., Ceballos, J.L., Basantes, R., Vuille, M., Sicart, J.E., Huggel, C., Scheel, M., Lejeune, Y., Arnaud, Y., Collet, M., Condom, T., Consoli, G., Favier, V., Jomelli, V., Galarraga, R., Ginot, P., Maisincho, L., Mendoza, J., Ménégoz, M., Ramarez, E., Ribtein, P., Suarez, W., Villacis, M., Wagnon, P. (2012) Current state of glaciers in the tropical Andes: a multi-century perspective on glacier evolution and climate change. *The Cryosphere*. 7 (1), 81-102.

Rounce, D.R., Hock, R., McNabb, R.W., Millan, R., Sommer, C., Braun, M.H., Malz, P., Maussion, J., Mouginot, J., Seehaus, T.C., Shean, D.E. (2021) Distributed Global Debris Thickness Estimates Reveal Debris Significantly Impacts Glacier Mass Balance. *Geophysical Research Letters*. 48(8), 1-12.

Rounce, D.R., McKinney, D.C. (2014) Debris thickness of glaciers in the Everest area (Nepal Himalaya) derived from satellite imagery using a nonlinear energy balance model. *The Cryosphere*. 8(4), 1317-1329.

Sakai, A., Takeuchi, N., Fujita, K., Nakawo, M. (2000) Role of supraglacial ponds in the ablation process of a debris-covered glacier in the Nepal Himalayas. *IAHS Publication*. 119-132.

Salisbury, J.W. and D'Aria, D.M. (1992) Emissivity of terrestrial materials in the 8–14 μm atmospheric window. *Remote sensing of Environment*. 42(2), 83-106.

Seehaus, T., Malz, P., Sommer, C., Lippl, S., Cochachin, A., Braun, M. (2019) Changes of the tropical glaciers throughout Peru between 2000 and 2016 - mass balance and area fluctuations. *The Cryosphere*. 13(10), 2537-2556.

Silverio, W., Jaquet, J.M. (2017) Evaluating glacier fluctuations in Cordillera Blanca (Peru). *Archives des Sciences*. 69, 145–62.

Steiner, J.F., Buri, P., Miles, E.S., Ragettli, S. Pellicciotti, F. (2019) Supraglacial ice cliffs and ponds on debris-covered glaciers: spatio-temporal distribution and characteristics. *Journal of Glaciology*. 65(252), 617-632.

Veettil, B.K. (2018) Glacier mapping in the Cordillera Blanca, Peru, tropical Andes, using Sentinel-2 and Landsat data. *Singapore Journal of Tropical Geography*. 39(3), 351-363.

Vincent, C., Wagnon, P., Shea, J.M., Immerzeel, W.W., Kraaijenbrink, P., Shrestha, D., Soruco, A., Arnaud, Y., Brun, F., Berthier, E., Sherpa, S.F. (2016) Reduced melt on debris-covered glaciers: Investigations from Changri Nup Glacier, Nepal. *The Cryosphere*. 10(4), 1845-1858.

Wigmore, O., Mark, B.G. (2017) Monitoring tropical debris-covered glacier dynamics from high-resolution unmanned aerial vehicle photogrammetry, Cordillera Blanca, Peru. *The Cryosphere*. 11(6), 2463-2480.

For Peer Review

816 Zhang, Y., Fujita, K., Liu, S., Liu, Q., Nuimera, T. (2011) Distribution of Debris Thickness and its
817 Effect on Ice Melt at Hailuogou Glacier, Southeastern Tibetan Plateau, Using In Situ Surveys and
818 ASTER Imagery. *Journal of Glaciology*. 57(206), 1147-1157.

819 Zhang, Y., Hirabayashi, Y., Fujita, K., Liu, S.Y. (2016) Heterogeneity in supraglacial debris thickness
820 and its role in glacier mass changes of the Mount Gongga. *Science China Earth Sciences*. 59(1), 170-
821 184.

For Peer Review